

Optical spectroscopy of earth-abundant zinc pnictides for photovoltaics

Présentée le 24 janvier 2022

Faculté des sciences et techniques de l'ingénieur
Laboratoire des matériaux semiconducteurs
Programme doctoral en science et génie des matériaux

pour l'obtention du grade de Docteur ès Sciences

par

Elias Zsolt STUTZ

Acceptée sur proposition du jury

Prof. Ph. Spätig, président du jury
Prof. A. Fontcuberta i Morral, directrice de thèse
Prof. I. Zardo, rapporteuse
Dr E. Alarcón Lladó, rapporteuse
Prof. R. Buonsanti, rapporteuse

Dans les champs de l'observation
le hasard ne favorise que les esprits préparés.
— Louis Pasteur

To my family.

Acknowledgements

This thesis has not been completed in a vacuum. Far from it, and thankfully so! I cannot be thankful enough for all the people who supported me over these more than four years. In particular, I would like to thank:

Anna Fontcuberta i Morral, for the support throughout this thesis and before. You have helped me get up at difficult times, and pushed me to become the best of me. Thank you for making LMSC a place to feel welcome and appreciated, for your patience and understanding, for emphasizing the importance of self-respect and mental well-being, and fostering the best research in the lab and from all of us. You have helped me grow as a scientist and as a person. Thank you, Anna.

Raffaella Buonsanti, Esther Alarcón Lladó, Ilaria Zardo and Philippe Spätig for your participation in my oral examination, the interesting discussions and taking the time to go through my thesis.

The II-V team for four years of exciting collaboration on zinc phosphide. Frustrating or rewarding, this work would never have been possible without you. Thank you for making all these samples for us to work with, and for the painstaking effort you put into the MBE. **Rajrupa Paul**, thank you for your unrelenting work, barely hampered by soot and ash; **Mahdi Zamani**, thank you for the wonderful structures you have grown, helping me advance my work, and accompanying me throughout my thesis, in the office and at conferences; **Jean-Baptiste Léran**, thank you for your relentless support. At the MBE, in the office, at conferences and beyond, you've helped us all grow, literally or figuratively. **Simon Escobar Steinvall**, I am so thankful for the many many things we've done together, in the lab, the office, in front of a beer, you name it! Thank you Simon.

Mirjana Dimitrievska, for helping me putting a conclusion to old projects, always being there for scientific discussions and showing me a new way of managing projects.

The LMSC spectroscopy team for fruitful discussions about this central aspect to my thesis and for helping me solve the many challenges accompanying it. **Luca Francaviglia**, you have taught me all I needed to start and the shown me rigor required; **Nicolas Tappy**, "coffee" chats with you were always a pleasure and your seemingly boundless understanding of optics has been invaluable; **Akshay Balgarkashi**, you have been with me for many of the optical challenges, and it was priceless to have you there for them; **Claire Blaga**, I have not had the chance to work with you for so long, but I have no doubt that you will be able to solve the challenges your work will and has already been giving you.

Acknowledgements

All LMSC group members, for the discussions, uplifting interactions, delightful social activities, whether with beers or with water, on the lakeshore or in the conference room, abroad or at home, alone or as a team, formally or informally. You have all made it a pleasure to come to the lab. **Didem Dede**, thank you for your boundless enthusiasm, for always bringing a cheer to everyone and everything and for sharing my appreciation for dancing. **Nick Morgan**, your just and measured ideas have made me a better person, and I will ever be thankful for having shared so much with you these past years. **Andrea Giunto**, we like to say that you are the worst, but your energy, your drive and your ideas bring more to the lab and the people around you than many can wish for. **Lucas Güniat**, thank you for helping make LMSC such a pleasant place to be. Your initiatives, inside and outside of the lab, help tighten the bonds that link us all. **Valerio Piazza**, thank you for your joviality, support and many a drinks shared. **Wonjong Kim**, thank you for the great time during our theses, in Korea or closer to the lab. **Martin Friedl**, more than the work we completed together, thank you for being a great office-mate and for the many pleasant times we've had. **Anna Kúkoľová**, we started almost at the same time, we finish nearly at the same time, sharing some of the good times like some of the more difficult ones. Thank you for the many great times spent together, at the mountain, the MBE, while dancing and many more. **Lea Ghisalberti**, thank you for sharing all those amazing experiences abroad, for helping me to become a better person and for helping me see how much more there is we can do. Thank you to the previous LMSC generation, **Heidi Potts**, **Francesca Amaduzzi**, **Dmitry Mikulik**, **Pablo Romero Gómez**, who have helped make the lab what it has become, the newer generation, **Santhanu Ramanandan**, **Michele Zendrini**, and many more I have not named directly.

I would also like to thank the students that I have supervised or worked with over my doctoral studies. Some have become much more than my students, and many have brought our work forward in ways I could not have done alone. All have helped me understand the differences of wishes, drives, skills and characters that make the pupil in each of us, and to become a better teacher and supervisor. Thank you **Capucine Molliex**, **Nicola Montanarella**, **Gladys Jaccard**, **Nicolas Humblot**, **Mevlûde Koçak**, **Léa Buswell**, **Julien Gay**, **Grégoire de Jerphanion**, **Nicole Shi**, **Benoît Reynier**, **Diego Sandoval-Salaiza**, **Iléane Lefevre** and **Mischa Flór**.

I would also like to thank our collaborators who have contributed to this work, and the people who helped me with different projects. From Kyoto University, **Ryoji Katsube** and **Yoshitaro Nose** for their samples and warm welcome in Kyoto. From the University of Manchester, **Djamshid Damry** and **Jessica Boland** for doing terahertz spectroscopy measurements on our samples. From the University of Houston, **Alexander Litvinchuk**, for doing density functional theory calculations. From within EPFL, I would also like to thank **Nicolò Oliva** and **Carlotta Gastaldi** for their assistance with electric measurements; **Linfeng Pan** and **Dan Ren** for their help with atomic layer deposition; **Pierre Mettraux**, may you rest in peace, for making the XPS measurements; **Paul Mural** and **Xiao Di** for our collaboration on pulsed laser deposition; and the **team of CIME** for their support for SEM and EDX.

Helping everything work so much smoother, I would also like to thank **Monika Salas Tesar** and **Laura Bischoff** for their relentless work, and **Jérôme Yerly** for helping me find many of

the old scientific literature on II-Vs.

Of course, many people outside LMSC have contributed to making these four years as enjoyable as they have been, at EPFL and beyond. **Sho Watanabe**, **Marica Giordano**, **Ping Che**, **Korbinian Baumgärtl** and all of **LMGN**, for the many joint events and wonderful social activities shared, **Mintae Chung**, for the countless drinks and events we've shared, including the weddings of our friends. **Amelia Estry**, for helping share veggie awareness, **Margaux Molinas** for the great discussions and dancing, and **Eva Kurisinkal** for your sunny presence. **Meg Escobar-Skipp**, of course, thank you for the countless times we've spent together, for celebrations or just because we were thirsty.

Thank you also to everyone who supported me through the last parts of my thesis and writing. **Lucie Godot**, for being there during some of the most difficult times, **Pascal** and **Cherry**, for supporting me during those long weeks of writing, **Sumiko**, **Simon** and **dad** for helping me improve my thesis, **Antonia** and **Mischa** for their feedback on my abstracts.

And to **my family**, merci du fond de mon coeur d'avoir toujours été là pour moi, de m'avoir soutenu toutes ces années, pendant les moments difficiles et les moments heureux. Merci papa, merci maman, merci **Yael**, merci **Leila**. Herzlichen Dank an die ganze Familie.

Enfin, merci à ma pépète d'or, **Kaori**. Merci de m'avoir soutenu à la fin de cette thèse. Tu es une personne extraordinaire et une danseuse merveilleuse. J'ai tant de la chance de t'avoir dans ma vie.

Lausanne, 5th of November, 2021

E. S.

Abstract

Zinc phosphide (Zn_3P_2) is an earth-abundant semiconductor with promising properties for applications as an absorber in photovoltaics. To beat the 40 years old record power conversion efficiency of solar cells made with this material, a deep understanding of the compound's electrical, optical, and crystal properties and their interplay with its growth conditions is required. In this thesis, we explore the crystalline and optical properties of zinc phosphide and the closely-related zinc arsenide (Zn_3As_2) by means of Raman and photoluminescence spectroscopy.

In the first part of this work, we establish that defect-free zinc arsenide nanosails grown by gold-catalyzed metal-organic vapor phase epitaxy display a metastable crystalline structure. The atomic lattice of these flat structures becomes isostructural to that of zinc phosphide likely due to the nanoscale nature of the system. We also determine that the nanosails are degenerate p-doped semiconductors with pure impurity band conduction at low temperatures.

The second part of this thesis is dedicated to establishing a thorough understanding of the dispersion and symmetries of the Raman-active lattice vibrational eigenmodes of zinc phosphide. We unambiguously identify most Raman-active phonons in the lattice and show the zinc- and phosphorus-dominated modes to be separated by a real phonon gap, establishing a reference Raman spectrum for zinc phosphide and its family of isostructural compounds.

In the final part of the thesis, we characterize the optical properties of zinc phosphide by photoluminescence of monocrystalline zinc phosphide grown by molecular beam epitaxy. We show that the photogenerated electron hole pairs experience two main radiative recombination mechanisms. Emission attributable to electronic transitions involving an impurity band is observed, and we show the first measurement by photoluminescence of the crystal field splitting of zinc phosphide.

Keywords

Zinc phosphide, zinc arsenide, earth-abundant, photovoltaics, II-V semiconductor, optical spectroscopy, Raman spectroscopy, photoluminescence, nanostructure, impurity band

Résumé

Le phosphure de zinc (Zn_3P_2) est un matériau semi-conducteur dont les composants sont abondants dans la croûte terrestre. Afin de dépasser le record de rendement photovoltaïque établi il y a 40 ans, une compréhension avancée des propriétés structurales et opto-électroniques est nécessaire, et cela compte tenu des conditions de croissance. Dans cette thèse, nous explorons les propriétés cristallines et optiques du phosphure de zinc et du matériau analogue qu'est l'arséniure de zinc (Zn_3As_2) en utilisant la spectroscopie Raman et la photoluminescence.

Dans la première partie de cet ouvrage, nous révélons que les nanovoiles d'arséniure de zinc crûes par épitaxie en phase vapeur aux organométalliques catalysées avec de l'or possèdent une structure cristalline métastable. Le réseau atomique de ces structures plates devient isostructural à celui du phosphure de zinc, certainement dû à l'échelle nanométrique du système. Nous montrons également que les nanovoiles sont des semi-conducteurs dégénérés de type p dont la conductivité électrique à basse température est exclusivement due à une bande d'impureté.

La deuxième partie de cette thèse est dédiée à la constitution d'une compréhension approfondie de la dispersion et des symétries des modes de vibration propres du réseau du phosphure de zinc actifs en Raman. Nous identifions sans ambiguïté la plupart des phonons actifs en Raman dans le réseau et montrons que les modes dominés par les vibrations des atomes de zinc et ceux dominés par celles du phosphore sont séparés par une véritable bande interdite phononique. Ces résultats établissent un spectre Raman de référence pour le phosphure de zinc et sa famille de composés isostructuraux.

Dans la dernière partie de cette thèse, nous caractérisons les propriétés optiques du phosphure de zinc par la spectroscopie de photoluminescence de phosphure de zinc monocristallin crû par épitaxie par jet moléculaire. Nous montrons que les paires électron-trou photogénérées sont principalement soumises à deux mécanismes de recombinaison radiatifs. Une émission associée à des transitions électroniques impliquant une bande d'impuretés est observée, et nous présentons la première mesure de la séparation de champ cristallin du phosphure de zinc par photoluminescence.

Résumé

Mots-clés

Phosphure de zinc, arséniure de zinc, abondance terrestre, photovoltaïque, semi-conducteur II-V, spectroscopie optique, spectroscopie Raman, photoluminescence, nanostructure, bande d'impureté

Zusammenfassung

Zinkphosphid (Zn_3P_2) ist ein auf der Erde reichlich vorhandener Halbleiter mit vielversprechenden Eigenschaften für die Anwendung als Absorber in der Photovoltaik. Um den 40 Jahre alten Rekord in der Leistungsumwandlungseffizienz von aus diesem Material hergestellten Solarzellen zu übertreffen ist ein tiefes Verständnis der elektrischen, optischen und kristallinen Eigenschaften der Verbindung und deren Zusammenspiel mit den Bedingungen, unter denen ihr Kristallwachstum stattfindet, erforderlich. In dieser Arbeit untersuchen wir die kristallinen und optischen Eigenschaften von Zinkphosphid und dem eng verwandten Zinkarsenid (Zn_3As_2) mittels Raman- und Photolumineszenzspektroskopie.

Im ersten Teil dieser Arbeit zeigen wir, dass defektfreie Zinkarsenid-Nanosegel, die durch goldkatalysierte metallorganische Gasphasenepitaxie gewachsen sind, eine metastabile kristalline Struktur aufweisen. Das Atomgitter dieser flachen Strukturen wird wahrscheinlich aufgrund der nanoskaligen Natur des Systems isostrukturell zu dem von Zinkphosphid. Wir stellen auch fest, dass es sich bei den Nanosegeln um entartete p-dotierte Halbleiter mit reiner Störstellenbandleitung bei niedrigen Temperaturen handelt.

Der zweite Teil dieser Dissertation widmet sich dem Aufbau eines gründlichen Verständnisses der Dispersion und der Symmetrien der Raman-aktiven Gitterschwingungseigenmoden von Zinkphosphid. Wir identifizieren eindeutig die meisten Raman-aktiven Phononen im Gitter und zeigen, dass die zink- und phosphordominierten Moden durch eine echte Phononenlücke getrennt sind, worauf wir ein Referenz-Raman-Spektrum für Zinkphosphid und seine Familie isostruktureller Verbindungen aufbauen.

Im letzten Teil der Arbeit charakterisieren wir die optischen Eigenschaften von Zinkphosphid mittels Photolumineszenzspektroskopie von monokristallinem Zinkphosphid, welches durch Molekularstrahlepitaxie gezüchtet wurde. Wir zeigen, dass die photogenerierten Elektronen-Loch-Paare zwei Hauptmechanismen der strahlenden Rekombination erfahren. Es wird eine Emission beobachtet, die elektronischen Übergängen in Verbindung mit einem Störstellenband zuzuschreiben ist, und wir zeigen die erste Messung der Kristallfelddaufspaltung von Zinkphosphid durch Photolumineszenz.

Stichwörter

Zinkphosphid, Zinkarsenid, auf der Erde reichlich vorhanden, Photovoltaik, II-V-Halbleiter, optische Spektroskopie, Raman Spektroskopie, Photolumineszenz, Nanostruktur, Störstellenband

Contents

Acknowledgements	i
Abstract (English/Français/Deutsch)	v
List of Figures	xvii
List of Tables	xxi
1 Introduction, Motivation & Literature review	1
1.1 The Terawatt Challenge	1
1.1.1 Electricity production with renewable sources	2
1.1.2 Solar photovoltaics	3
1.1.3 Photovoltaic solar cells	6
1.1.4 Material requirements and availability	8
1.1.5 Exaggerated claims of earth-abundance?	12
1.2 Earth-abundant photovoltaics	13
1.2.1 Material screening	14
1.2.2 Pnictides	15
1.2.3 Chalcogenides	16
1.2.4 Some relevant crystalline structures	17
1.2.5 Zinc-based pnictides	20
1.2.6 Zinc-based chalcogenides	22
1.2.7 Copper-based pnictides	23
1.2.8 Binary and ternary copper-based chalcogenides	23
1.2.9 Quaternary and higher-order copper-based chalcogenides	24
1.2.10 Earth-abundant perovskites	25
1.2.11 Bismuth-based materials	27
1.2.12 Silver-containing materials	29
1.2.13 Other cations	30
1.2.14 A case for zinc phosphide	31
1.3 Zinc phosphide	33
1.3.1 Structure	33
1.3.2 Current state of research	42
1.4 Outline of the thesis	43
	xi

2	Optical Spectroscopy	45
2.1	Raman spectroscopy	45
2.1.1	The Raman scattering process	45
2.1.2	Raman spectrometry, experimental details	55
2.1.3	Raman spectroscopy for research on semiconductors made of earth-abundant elements	58
2.2	Photoluminescence spectroscopy	59
2.2.1	Photoluminescence of solid semiconductors	60
2.2.2	Recombination mechanisms	60
2.3	Description of the photoluminescence spectroscopy setup	62
2.3.1	Photoluminescence for research on semiconductors made of earth-abundant elements	63
2.4	Spectroscopic ellipsometry	64
2.4.1	Introduction	64
2.4.2	Working principle	65
2.4.3	Applications	66
2.5	Summary	68
3	Nanosails showcasing Zn₃As₂ as an optoelectronic-grade earth abundant semiconductor	69
3.1	Accompanying information	69
3.2	Abstract	69
3.3	Introduction	69
3.4	Experimental Details	71
3.5	Structural properties	72
3.6	Electrical Properties	74
3.7	Conclusion	77
3.8	Supplementary information	77
3.9	Acknowledgements	78
4	Raman spectroscopy and lattice dynamics calculations of tetragonally-structured single crystal zinc phosphide (Zn₃P₂) nanowires	79
4.1	Accompanying information	79
4.2	Abstract	79
4.3	Introduction	80
4.4	Experimental details	82
4.4.1	Material preparation	82
4.5	Results and discussion	83
4.6	Conclusion	93
4.7	Supplementary information	93
4.8	Acknowledgements	94
5	Showcasing the optical properties of monocrystalline zinc phosphide thin films as	

an earth-abundant photovoltaic absorber	95
5.1 Accompanying information	95
5.2 Abstract	95
5.3 Introduction	96
5.4 Experimental section	97
5.5 Results and discussion	98
5.5.1 Crystalline properties	98
5.5.2 Photoluminescence spectroscopy	100
5.5.3 Optical pump terahertz probe spectroscopy	106
5.6 Conclusion	108
5.7 Acknowledgments	108
5.8 Supplementary information	108
6 Conclusion & Outlook	109
6.1 Future development	110
6.1.1 Crystal structure and properties	110
6.1.2 Measuring the dielectric function	110
6.1.3 Defects	111
6.1.4 Surfaces and interfaces	112
A Additional data	113
B Additional properties of zinc phosphide	115
B.1 Mechanical properties and structure	115
B.1.1 Vibrational modes	116
B.1.2 Unit cell size and bonding	116
B.1.3 Bonding	117
B.2 Optical and electronic properties	117
B.2.1 Band structure	117
B.2.2 Electronic properties	119
B.2.3 Optical properties	120
B.3 Defects	122
B.3.1 n-type zinc phosphide	122
B.4 Surfaces and interfaces	123
B.4.1 Etching	123
B.4.2 Materials joined with zinc phosphide	124
B.5 Other topics	126
B.6 Photoluminescence of zinc phosphide	126
B.6.1 1979-1996	126
B.6.2 2006-2021	127
C Optical anisotropy of zinc phosphide	131
C.1 Literature review of the anisotropic optical properties of zinc phosphide	131

Contents

C.1.1	Birefringence	131
C.1.2	Dichroism	131
C.1.3	Dielectric tensor	132
C.2	Determination of the optical anisotropy at all relevant energies	133
C.2.1	Correct identification of the band transitions	133
C.3	Polarization-resolved Raman spectroscopy of optically anisotropic zinc phosphide	134
C.3.1	Relative importance of birefringence	134
D	Additional zinc phosphide photoluminescence spectra	137
D.1	Changes due to composition	137
D.2	High-energy emission	138
D.3	Irreversible changes	139
D.4	Recommendations	141
E	Supplementary information for "Nanosails Showcasing Zn₃As₂ as an Optoelectronic-Grade Earth Abundant Semiconductor"	143
E.1	Nanosail growth parameters	143
E.2	Electrical contact fabrication and measurements	143
E.3	List of reported Raman peaks for α' -Zn ₃ As ₂	145
E.4	Simulation of electron diffraction from the α'' -Zn ₃ As ₂ phase	145
E.5	Fitting of the carrier concentration regime transition	147
F	Supplementary information for "Raman spectroscopy and lattice dynamics calculations of tetragonally-structured single crystal zinc phosphide (Zn₃P₂) nanowires"	149
F.1	Deconvolution procedure of Raman spectra	149
G	Supplementary information for "Showcasing the optical properties of monocrystalline zinc phosphide thin films as an earth-abundant photovoltaic absorber"	151
G.1	Additional RBS data	151
G.2	Summary of photoluminescence peak properties	152
G.3	Variability of the photoluminescence spectrum	152
G.4	Fitting of the photoluminescence spectra	153
G.5	Optical pump terahertz probe spectroscopy fitting	156
G.6	Optical pump terahertz probe spectroscopy fitting	158
G.7	Optical pump terahertz probe data analysis - calculation of photoconductivity	159
G.8	Photoconductivity decay within the thin film	160
H	Base concepts of solid-state physics	163
	Bibliography	165
	Glossaries	201

Curriculum Vitae	205
-------------------------	------------

List of Figures

1.1	2019 electricity production structure of Switzerland and other selected political entities.	5
1.2	Abundance of elements in the Earth's crust and their global production in 2010.	11
1.3	Illustrations of the unit cells of a face-centered cubic (FCC), a FCC crystal with four of the eight tetrahedral voids highlighted, a zincblende and a fluorite/anti-fluorite type structures.	18
1.4	Illustrations of two zincblende unit cells stacked on a face and the unit cells of chalcopyrite, kesterite and stannite type structures.	19
1.5	Illustration of the perovskite crystal structure.	19
1.6	Publication year histogram of the listings related to Zn_3P_2 on two major scientific work databases.	31
1.7	Zinc-rich side of the Zn-P binary phase diagram.	33
1.8	298 K section of the Zn_3P_2 - Cd_3P_2 - Cd_3As_2 - Zn_3As_2 pseudo-quaternary phase diagram.	36
1.9	Description of the crystalline structure of α - Zn_3P_2	38
1.10	Room temperature lattice parameter and bandgap of various semiconductors.	41
2.1	Schematics of the optical table for Raman spectroscopy.	56
2.2	Schematics of the spectroscopic measurement geometry.	57
2.3	Major radiative recombination mechanisms.	61
2.4	Schematics of the optical table for PL spectroscopy.	63
2.5	Side view schematics of an ellipsometric system.	66
3.1	Typical top-view scanning electron micrograph of the surface of a sample grown in the conditions described in the text.	71
3.2	Raman spectrum of a nanosail acquired at 12 K.	73
3.3	(a) Top-view colorized SEM image of a contacted Zn_3As_2 nanosail and (b) evolution of the conductivity of three nanosails with temperature.	75
3.4	(a) Variation of the Hall voltage with magnetic field applied on to the nanosail, (b) temperature dependence of the carrier concentration of three nanosails calculated using the measured Hall coefficients and (c) evolution of the hole mobility with the temperature.	75
4.1	Conventional unit cell representation of the tetragonal Zn_3P_2 structure.	84

List of Figures

4.2	Scanning electron micrographs of three different Zn_3P_2 nanowires grown vertically along the [001] direction.	85
4.3	High-angle annular dark-field scanning tunneling electron micrograph and accompanying energy-dispersive X-ray spectroscopy elemental maps of the top of a Zn_3P_2 nanowire	86
4.4	Raman spectra of Zn_3P_2 in polarized and unpolarized configurations measured at 12 K using 532 nm excitation wavelength.	88
4.5	Phonon dispersion along high-symmetry directions of the tetragonal Zn_3P_2 structure and partial phonon density of states calculated with density functional theory.	91
4.6	Calculated phonon displacements for several representative modes of Zn_3P_2 . .	92
5.1	Representative X-ray diffraction spectrum, tilted cross-section scanning electron micrograph and Raman spectrum of a Zn_3P_2 thin film on InP.	99
5.2	Representative composition along the depth of the sample, calculated from Rutherford back-scattering spectrometry.	100
5.3	Photoluminescence spectra of a monocrystalline Zn_3P_2 thin film.	102
5.4	Decay of excess charge carriers measured by optical pump terahertz probe spectroscopy at four pump fluences.	107
A.1	NREL Best Research-Cell Efficiency Chart	114
B.1	Thin film etched thickness.	124
C.1	Photodichroism coefficient calculated from the absorption measurements at 300 K.	132
C.2	Calculated birefringence and photodichroism coefficients	135
E.1	Simulated and experimental diffraction patterns of Zn_3As_2	146
E.2	Arrhenius-type plot of the carrier concentration in the three studied nanosails. .	147
F.1	Deconvoluted Raman spectra of Zn_3P_2 in polarized and unpolarized configurations.	150
G.1	Rutherford backscattering spectrum acquired with a grazing exit detector. . . .	151
G.2	Peak center positions of the gaussians best fitting the data.	152
G.3	Photoluminescence spectra acquired at 12 K at different positions.	152
G.4	Detailed fitting of the sub-1.36 eV peaks in the spectra acquired at 30 K.	153
G.5	Detailed fitting of the sub-1.36 eV peaks in the spectra acquired at 12 K.	154
G.6	Best fit parameters of spectra acquired at 100 K.	154
G.7	Best fit parameters of spectra acquired at 170 K.	155
G.8	Best fit parameters of spectra acquired at 230 K.	156
G.9	Decay of photoinduced carrier density as a function of time after photoexcitation. .	158

G.10 Maximum of the biexponential fit to the temporal OTP data, versus pump fluence.	158
G.11 Frequency-averaged photoconductivity of the Zn_3P_2 thin film	160
G.12 Calculated photoconductivity spectrum of the InP substrate	161
G.13 Change in photoconductivity as a function of distance within the Zn_3P_2 thin film and InP substrate.	162

List of Tables

1.1	List of phases synthesized by some authors investigating zinc oxynitrides. . . .	21
1.2	List of binary and ternary zinc pnictide semiconductors considered for applications as photovoltaic absorbers, as well as some closely related compounds. . .	22
1.3	List of copper pnictides investigated for photovoltaic applications.	23
1.4	List of binary and ternary copper chalcogenides.	24
1.5	List of quaternary and higher-order copper chalcogenides.	25
1.6	List of inorganic perovskites.	26
1.7	List of ferroelectric materials based on BiFeO_3	28
1.8	Selection of bismuth- and/or cesium-containing semiconductor compounds. .	28
1.9	Selection of silver-containing semiconductors.	30
1.10	Earth-abundant semiconductors not fitting any category discussed in the remainder of the chapter.	30
1.11	Reported binary phases in the zinc-phosphorus system.	35
2.1	D_{4h} point group symmetry character table	52
3.1	The different observed phases of Zn_3As_2 , their space group, stability in the bulk and number of atoms in the unit cell.	72
3.2	Deconvoluted peak positions of the high Raman shift stretching modes obtained by fitting with Lorentzians.	74
4.1	Angular dependencies of Raman modes intensity for tetragonal Zn_3P_2	87
4.2	Frequency of Raman peaks fitted by Lorentzians, their proposed symmetry assignment and previously reported values for the literature.	90
5.1	Best fit parameters of the low-energy PL emission at low temperatures.	104
5.2	Characteristic decay times of the best bi-exponential fits to the carrier decay data.	107
B.1	Properties of zinc phosphide	115
B.2	Coefficients of expansion of zinc phosphide. <i>l</i> : linear, <i>a</i> , <i>b</i> , and <i>c</i> : along the three (!) crystalline axes, <i>V</i> : volume.	115
B.3	Absorption coefficient and absorption length of light at different wavelengths in Zn_3P_2	120
B.4	List of the different etching solutions used on Zn_3P_2	123

List of Tables

C.1	Anisotropic optical properties of Zn_3P_2 at different energies.	136
E.1	Processing conditions of three nanosails.	144
E.2	Observed room-temperature Raman frequencies of $\alpha\text{-Zn}_3\text{As}_2$ reported in the literature.	145

1 Introduction, Motivation & Literature review

Ample energy supply is the key to solving most major current and future problems of our societies: water and food shortages, population increase, disease, degradation of the environment and lack of education. Low-cost and abundant energy is a direct solution to some of these problems or frees up crucial resources to tackle others. The United Nations predict a world population increase to about 11 billion people by the end of the century [1], and the biggest increases will occur in some of the poorest parts of the world [2]. Population and standard of living increases will lead to a vast increase in energy needs. How can we produce enough affordable and safe energy for everyone?

1.1 The Terawatt Challenge

Nobel laureate Richard Smalley called it the *Terawatt Challenge* [3]. In 2019, the world used about 21.0 TW of energy on average¹ [4]. With increases of population and standard of living, global energy needs will increase significantly during the next decades and throughout the century. The U.S. Energy Information Administration predicts that world energy consumption will be nearly 50% bigger in 2050 than in 2019, to an average of 30.4 TW [4], and it may well increase by another dozen terawatt by 2100 [5]. Which energy sources are going to sustain global prosperity at a low economical cost? Can it be done in a way as to minimize the coming effects of the climate crisis and our impact on the environment? We will have to find a way to produce, every day of every year, more energy than we do now, failing which the most critical global issues are bound to seriously increase. Which energy source can respond to the dozens of terawatts the world will ask for?

Energy production is only part of the issue. How can energy be transported to the places that need it, and how can it be stored to make up for intermittent production or drops in supplies? Broadly speaking, a strong contender for this role is electricity, which has long been the choice mean of energy transportation. Indeed, in terms of price and losses, electricity faces well against energy transport in the form of chemical energy as mass, which is done for some fossil

¹ 1 TW = 10^{12} watts = one terawatt (TW)

fuels [3]. Eventually, many of the energy sources are turned into electricity, either locally or in large plants, before being distributed to the consumer. Exceptions are some forms of heating, a large part of the transport industry and many industrial processes.

Which source, or more likely *sources*, of energy should we develop and expand to meet future demand? The energy sources with the biggest shares have long been the carbon-based fossil fuels, oil, natural gas, and the coal-related resources. In 2017, the share of carbon-based fossil fuels in Europe's primary energy consumption, its total energy demand, was 70.4%. That year, those same sources made up 81.3% of the world's total energy supply [6]. In 2018, carbon-based fossil fuels accounted for nearly half of the electricity production in Europe (fig. 1.1), With increasing energy needs and ever-rising environmental concerns, we need to develop more sustainable alternative energy sources.

Many of the most abundant energy sources are nuclear in nature. The fission of uranium in nuclear power plants already produces vast amounts of electricity with minimal impact on greenhouse gas concentrations. Geothermal technologies use the near endless supply of heat generated from nuclear decay deep in the Earth, and nuclear fusion in the Sun will produce solar and wind energy for a few billion years to come. The latter three energy sources still produce very small parts of today's energy, compared to the conventional non-renewable sources. New nuclear technologies are also being developed which may play major roles in energy production in the decades or centuries to come. For example, China announced in July 2021 their plan to build the very first commercial thorium molten salt nuclear reactor [7]. These reactors, using the more abundant thorium element instead of the more conventional uranium, are thought to be safer than uranium reactors in terms of operation, produce less harmful waste and do not require access to large sources of water. Based this time on nuclear fusion and not on fission, the international thermonuclear experimental reactor (ITER) in France brings great hopes for clean and abundant energy production from terrestrial fusion in the century to come [8].

Nonetheless, time remains an issue. The power scales involved are so large that even with the knowledge of some of the most perfect energy source, they would still take decades to build. We need vast amounts of new and sustainable energy sources.

1.1.1 Electricity production with renewable sources

Energy sources based fundamentally on nuclear reactions in the Sun or in the Earth's core could provide energy for as long as these processes are active, for up to billions of years. However, nuclear fission depletes the resources it depends on, as do all other fossil-fuel energy sources. Energy sources which are naturally replenishing, which do not deplete the resources they depend on, are *renewable*. They are virtually inexhaustible and much more sustainable than non-renewable resources [9].

Today's main renewable energy sources are geothermal, solar (photovoltaic, thermal and

photoelectrochemical), hydro (hydroelectric and tidal), wind and biomass.

Hydroelectricity, accounting for more than 55% of electricity production in Switzerland, and even larger fractions in a few other mountainous countries, requires specific topographical features. It has very limited potential for further expansion, but can be used for energy storage in addition to generation. Biomass could be a major player, but this technology has one of the worst land footprints of all energy production technologies, and its widespread development thwarts the efforts of resolving the two other global issues of food and water scarcity. Tidal and geothermal energy are remarkably stable and predictable sources. Some of their drawbacks include damaging the aquatic ecosystem or underground stability and waters [10]. Solar and wind energies vary in abundance across the world, but can be harvested with varying efficiency nearly everywhere on the planet.

There are ardent critics and proponents against and for each energy source type. Energy policy is a vast topic, and choosing the most suitable energy sources is very complex and depends greatly on geographic, economic and geopolitical factors. In my opinion, carbon-based fossil fuels should be quickly phased out and replaced by nuclear and renewable sources in the coming decade to slow greenhouse gas emissions. Then, through the next decades, tidal, geothermal, wind and solar energy production should be expanded where available and safe, perhaps complemented by nuclear fusion in the far future.

This thesis approaches the topic of solar energy conversion through photovoltaics, the transformation of light, usually directly from the Sun, into electricity. Considerations of material availability and abundance for sustainable development of the global electricity supply are discussed.

1.1.2 Solar photovoltaics

We are bathed in energy.

Richard E. Smalley [3]

Every instant, about 170 000 TW of energy reaches the planet's outer atmosphere from the Sun in the form of light, more than 8000 times the global energy production. Although some of the incident energy is released back into space without reaching Earth's surface [11], our planet's landmasses receive vastly more solar energy than we could use in the foreseeable future.

Solar photovoltaics is distinct from solar thermal and solar photoelectrochemical technologies. Solar thermal directly uses the heat of the Sun to heat up a fluid using mirrors. In photoelectrochemical technologies, the energy of the light is transformed into chemical energy by creating chemical compounds.

Solar energy conversion is evolving very fast. An important aspect of this technology is its

availability. Anywhere the light of the Sun reaches can in principle produce some solar energy. Dry areas far from the poles are generally preferred for their higher average irradiation, but electricity can even be generated under clouds and indoors to some extent. Solar irradiation is one of the most equitable energy sources. Average irradiance on a country has very little correlation with its economic wealth and all receive large amounts of it. What is more, areas with high population are correlated with areas of high solar irradiance [12].

An increasingly attractive advantage of photovoltaics is its low cost. The price of a unit of energy produced by PV has decreased dramatically over the last decades, especially compared to other energy sources [13, 14]. New PV is already more cost-effective than carbon fossil fuel power in many countries in the world, including western countries, China and India, and is the cheapest source of new electricity generation in most parts of the world [15]. The decrease of price is expected to continue in the near future, increasing the economical appeal of this technology [16, 17].

Closely interlinked with the price decrease of PV, installed solar production has been increasing nearly exponentially during the last decade. At the end of 2020, 0.76 TW of solar PV was installed cumulatively over the planet [18]. The milestone of one terawatt installed capacity is expected to be reached early this decade, 10 TW around 2030 and 30 TW to 70 TW by 2050 [16]. The shares of electricity production are still quite low today, however. In 2018, Switzerland produced 2.9% of its energy from photovoltaics, as illustrated in figure 1.1 [19], and the 0.62 TW of PV installed in 2019 [18] only account for about 3% of the 21 TW of power consumed on average that same year. PV price has been driven down by the intense scientific research efforts and the large technological improvements it prompted, as well as the benefits of large-scale production and political initiatives.

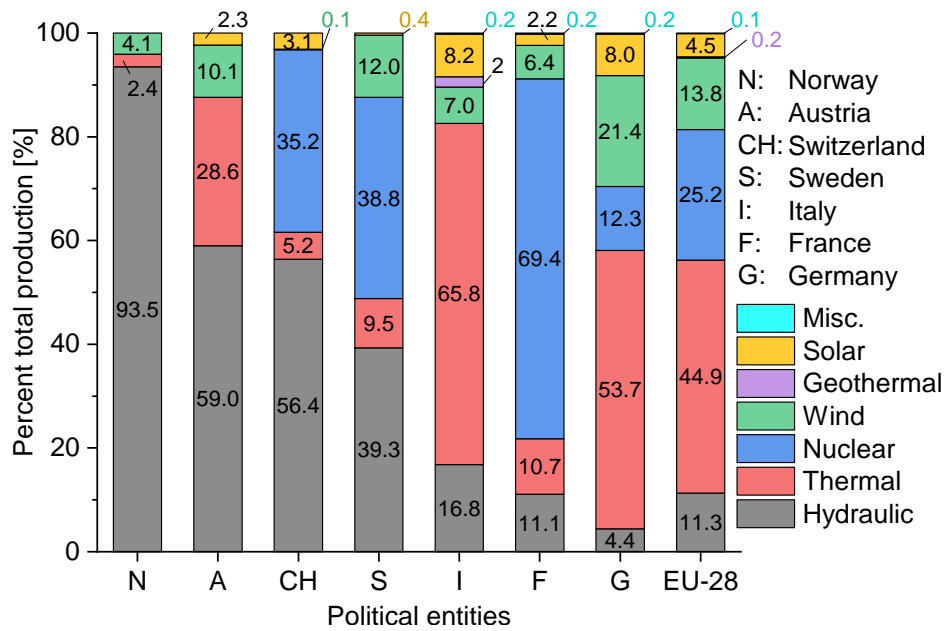


Figure 1.1 – 2019 electricity production structure of Switzerland, its major neighbors, two Scandinavian countries and the 28 European countries. Data from the 2020 Swiss electricity statistics [19].

Solar has a large footprint. Compared to fossil fuel power plants, it requires larger areas or land for the same energy production. The drawbacks of this characteristic can be minimized by integrating solar cells with other structures, such as roofs. Solar panels could also be placed in deserts and remote areas, transporting the energy to where it is needed [3]. Deserts also tend to have the highest irradiation, which is an added advantage. A study has found that all countries in mainland Europe, an area of high energy demand at relatively high latitudes, have the *potential* for autarkic electricity production using only wind and solar [20]. The authors took into account geographical and some environmental and social aspects, but acknowledge that their criterion is necessary but not sufficient for electric self-sufficiency. Interestingly, in this study, Switzerland consistently ranks among the countries with the least technical potential for PV and wind production based on PV and wind, though it still passes the threshold for autarky. This is likely due in part to the mountainous nature of a large part of the country, and the relative lack of land area for wind farms and open field PV. Although dense urban areas limit the use of PV, available land is not a limiting factor at larger scales. On a global scale, only 0.3% of the land area would have to be covered with solar PV to supply all the electricity needs of the planet [21].

PV generation is fundamentally intermittent. Some of the variability is completely predictable. Geographical effects such as seasonal differences at high latitudes, diurnal, panel orientation and climatic variability are all very predictable and can easily be accounted for in energy distribution. The stochastic variability of weather is not as foreseeable, but improved forecasting and generation across large geographical areas with a variety of technologies can smooth

out these effects [12]. Regardless, improvements to both energy storage and response to the variable electricity demand will need to be improved in the future [16].

A variety of means exist for storing energy, such as pumped-storage hydroelectric basins, which can double up as energy sources, or electrochemical batteries storing electricity as chemical energy [22]. Considerable research is being carried out to produce batteries with high energy densities, long lifetimes and free of critical or scarce elements.

Everything considered, photovoltaics is a mature technology ripe to become one of the main energy sources. To support it at the multi-terawatt scale, adequate electricity storage and transport solutions need to be determined. Careful modeling indicates that PV can play a major role in future cost-efficient and carbon-poor energy scenarios [21].

The quest for making PV a major energy source involves several fields of research. Current and future research in PV is directed towards cost reductions by increasing efficiency and reducing material use. Increasing reliability is also crucial, the previous two fields bringing their own shares of new failure mechanisms. Fields of research include material science and module design, integration, reliability and manufacturing.

1.1.3 Photovoltaic solar cells

Main commercial and research technologies

The different technologies of solar cells are often separated into separate generations somewhat based on the similarity of their challenges or properties. One such way of categorizing them is the following [12]: first generation solar cells are based on semiconductor wafers and most famously include monocrystalline and polycrystalline silicon cells. Second generation solar cells are the so-called thin-film technologies, where the active layers are very thin and may not make up the bulk of the cell. The most prominent commercial examples, with commercial applications, are amorphous silicon, CdTe and copper indium gallium sulfide (CIGS). Third generation solar cells generally include more novel and less-established technologies such as dye-sensitized, quantum dot, tandem, hot-carrier and others [23].

Commercially, the most important PV technology is based on silicon. In 2019, 94.5% of PV module production (measured in energy output) was based on crystalline silicon, about two-thirds of which were more specifically monocrystalline silicon. The 5.5% remaining are the second-generation thin film solar cells. Of those, the market share goes to CdTe (4.2% of total), copper indium gallium sulfide (1.2%) and amorphous silicon (~0.1%). The market share of thin film PV has been generally decreasing over the past years, since its peak at 17% in 2009, to the benefit of silicon [24]. No other technology owns any significant part of the market. Some have only an impact in some niche applications, such as the extremely efficient, lightweight and expensive solar cells for use in space.

Silicon-based solar cells are there to stay and are extremely unlikely to lose their majority

market share in the next decades, if ever. They have well-established supply and production chains, costs matching or beating other sources of energy, relatively good power conversion efficiencies and are based on the second-most abundant element on Earth. Pure silicon in fact happens to be the most earth-abundant semiconductor material among all, even those yet undiscovered. The more earth-abundant pure oxygen and silicon dioxide do not exhibit semiconducting properties at near-ambient conditions. Decades of research and abundant funding have lead silicon solar cell power conversion efficiency (PCE) quite close to its fundamental limit. The current record efficiency for single-junction non-concentrated homojunction silicon solar cell has been reached in 2018, and stands at 26.1% [25]. This cell, and the slightly more efficient silicon heterojunction solar cells standing at 26.7% [26], have reached to about 90-92% the way to the theoretical efficiency limit [27, 28]. Nowadays, a major part of the silicon photovoltaics research is devoted to reducing the price per unit of energy produced (usually measured in Watt-peak).

Nonetheless, compared to many other semiconductor materials, silicon absorbs light relatively poorly, an important drawback. It has an indirect bandgap², forcing photons to be absorbed with a fundamentally less efficient process than in direct bandgap semiconductors. For this reason, the absorbing layers are relatively thick, to allow a sufficient depth for most of the light shone on the cell to be absorbed. For comparison, silicon wafer thickness is about 170 μm , while the absorbing layers in thin film solar cells are typically around a few hundred nanometers thick, two to three orders of magnitude thinner. This relatively large thickness of the silicon layer requires the silicon to be extremely pure, to minimize losses to due impurities and to allow photoexcited charge carriers³ to diffuse to the contacts. The purification to electronic-grade silicon requires several expensive and energy-intensive processes. In nature, silicon is found in all silicate minerals, most notably in quartz, SiO_2 . In multiple purification stages, the concentration of impurities is lowered, some as low as 10^{-10} % [29].

In contrast, semiconducting compounds with a direct bandgap have much higher absorption coefficients. For that reason they tend to require very thin layers of material to absorb most of sunlight, and thus can in general be deposited with less regard for their quality and purity than silicon. A direct bandgap is a common property of second-generation solar cells.

On paper, a more optimal less-resource-intensive photovoltaic technology than silicon would thus combine the abundance and absence of toxicity exhibited by silicon with the thinness and the capability of cheap deposition processes of thin film and some other technologies. It is not to say that were such a technology proven to be reliable and cheap it would immediately replace silicon. After all, the investments put into silicon technologies are tremendous, and silicon PV has and is benefiting from the facilities and technologies put in place for CMOS fabrication processes. It would undoubtedly take immense effort, money and willingness to transition away from silicon. It is still possible in principle, and may end up having an important impact on the long term.

²A layperson explanation of *bandgap* is given in Appendix H: Base concepts of solid-state physics

³A layperson explanation of *carrier* is given in Appendix H: Base concepts of solid-state physics

The two major commercial thin film technologies do not unfortunately possess all of the above-mentioned qualities. The cadmium in CdTe is extremely hazardous for health and for the environment, and both CIGS and CdTe contain elements with very low abundance in Earth's crust, such as tellurium or indium. Amorphous silicon thin film solar cells possess the previously mentioned qualities, but have so far failed to overtake more than a fraction of a percent of the market. A variety of emerging materials are or have been investigated that promise the advantages of both silicon and second-generation solar cells. Section 1.2 is dedicated to an overview of such materials.

State of the art

Today, the efficiency of the best commercial solar cells is about 21%, with a maximum of 22.8% [30]. The cells, organized in modules, each size on the order of 100 cm^2 . In laboratories, the efficiencies vary much more and the cells are typically much smaller.

The latest most efficient solar cells and modules have been compiled by M. Green and co-authors [26] and data about the record research solar cells are gathered by the National Renewable Energy Laboratory (NREL) [31]. Frequently shown among researchers in the field of photovoltaic (PV), a chart by NREL graphically summarizing the progress in PV cell research since the end of the seventies until January 2021 is shown in the appendix (fig. A.1, p.114). Ehrler and co-authors compiled the latest records by placing the cell properties in perspective with the theoretical maximum of radiative recombination limit [32]. Their work also includes the records of different tandem structures, highlighting how these potentially higher efficiency cells bring additional challenges mostly absent in single-junction devices.

As of today, the most efficient laboratory-certified single-junction non-concentrated solar cell achieves an energy conversion efficiency of 29.1% using thin-film GaAs as the core absorbing layer [31, 33]. Light concentration and multi-junction solar cell technologies have been used to further increase the efficiency of solar cells, passing the fundamental efficiency limit of planar single-junction solar cells imposed by the Shockley-Queisser limit [34]. The current most efficient solar cell, among all categories, is made by a complex stacking of 140 layers of various III-V compounds in the (Al, Ga, In)(As, P) family [31, 35]. The six-junction solar cell converts 47.1% of all the concentrated light it receives (equivalent to the light of 143 Suns) into electricity.

1.1.4 Material requirements and availability

As PV production increases and new materials are being investigated for potential large-scale PV generation, concerns about the supply, use and recycling of materials used in the cells is gaining importance.

The supply of silicon will never run out. The supply of the higher-purity silicon ores may, which would induce additional processing costs, but our reserves of silicon are virtually infinite.

Silver, used for electrical contacts in those types of cells, is used in much larger proportions of our reserves, but could potentially be replaced if its price increased too significantly [36, 37].

Material availability is thus not an issue for silicon PV. However, as stated earlier, material availability is more of an issue in current commercial thin-film photovoltaics. PV absorbers should use earth-abundant and non-toxic elements with reserves distributed in various countries to avoid geopolitical supply difficulties and support multi-terawatt energy generation.

Distinction between critical and scarce materials

When making considerations about material sustainability, two types of classification come up: materials can be *critical* and they can be *scarce* or *earth-abundant*. Critical materials are material with high economic importance to a country or organization and whose unhindered and stable supply has been considered being at risk. This category is discussed in more details in section 1.1.4. Without an explicit definition, the term *earth-abundant* may be a bit misleading. In this work, when applied to a material, mineral or compound, it indicates that the elements forming the material have a high average concentration in Earth's crust. Earth-abundant compounds simply have a high average concentration in the crust. In the context of this thesis, when applied to materials, minerals, compounds and elements, *scarce*, or *earth-scarce*, means the opposite of *earth-abundant*. Based on this definition, let us note that earth-abundant compounds are not, in general, found anywhere naturally. Furthermore, the very few compounds that may be found naturally, usually oxides, are typically going to be of too low or unreliable quality to be usable without purification in semiconductor research and industries. Material abundance is discussed in more details in section 1.1.4.

Critical materials

The access to essential and critical raw materials is likely to become a major geopolitical issues of the century. The European Commission (EC) states that "Reliable and unhindered access to certain raw materials is a growing concern within the EU and across the globe." [38].

In 2008, the EC introduced its *Raw Materials Initiative* to tackle the issues of fair and sustainable supply of raw materials within and from outside of the EU, and to promote resource efficiency and recycling [39, 40]. In its most recent, 2020 communication, the Commission identified 30 raw material with "a high supply-risk and a high economic importance to which reliable and unhindered access is a concern for European industry and value chains" [41, 42]. The European Union is not alone in trying to ensure the supply of all raw materials critical to its economy. In 2018, the US Interior Department published a list of 35 critical mineral commodities, citing reasons of national security and economic prosperity [43]. In 2013, the Chinese government adopted their *Belt and Road Initiative* development strategy, one of the goals of which is securing supply to strategic raw materials for Chinese industries from African and Southeast Asian countries [44].

A number of materials on the EC list [42], such as gallium, germanium, indium and silicon metal have numerous uses in commercial or research photovoltaics. In addition to being abundant on average and easy to extract, elements in novel PV technologies should ideally also not be deemed critical and be widely available on most continents.

Elemental abundance

The Earth's crust has formed relatively early in the planet's existence, billions of years ago. Most of the crust has regenerated since, but its composition is relatively unchanged, and distinct from the deeper layers of the planet. Only the rocks and minerals remaining in the crust are reachable using current technology and its current contents are an upper limit to the reserves of elements we can expect to gather on our planet in the foreseeable future.

Abundant elements can be considered as elements that are found with high average concentrations within our reach, disregarding geopolitical issues. Abundance of elements in Earth's crust is one of today's most common measures of elemental abundance, but the ease of access of different parts of the crust for mining, such as the oceanic crust [45] may vary significantly. Asteroid mining is also being seriously considered for commercial mining [46], as minor planets may contain large masses of scarce elements such as platinum-family metals [47]. However, astronomical start-up costs and the high risks associated with these projects still make asteroid mining a process for the future[48].

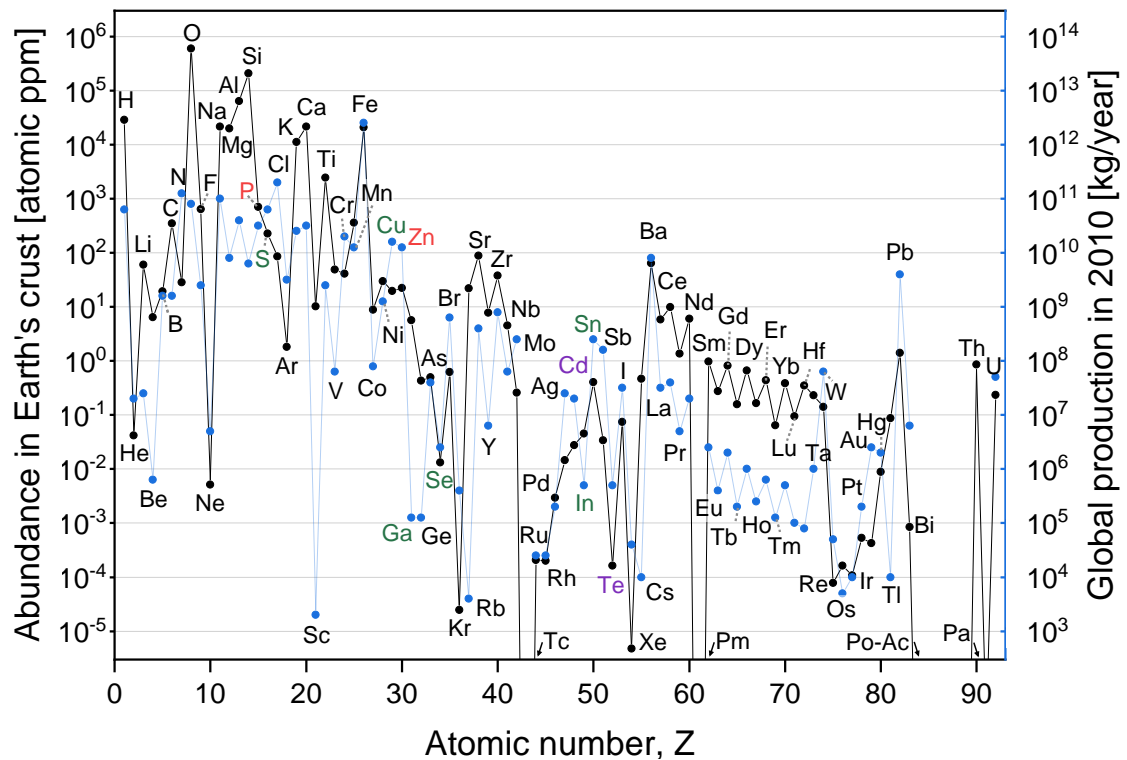


Figure 1.2 – Abundance of elements in the Earth's crust (black) and their global production in 2010 (blue). The units of atomic part-per-million are abbreviated as at-ppm in the text. In red, components of Zn_3P_2 , in green, components of CIGSse and CZTSe , in purple, components of CdTe . Abundance values for Tc, Pm, At and Fr, not available in the source, were arbitrarily set to a thousand times less abundant than Rn, the least abundant element in the reference dataset. Abundance data source: CRC Handbook of Chemistry and Physics [49]. Production data from Vesborg and Jaramillo [36].

The data points in black in figure 1.2 show the abundance in Earth's crust of most elements in parts per million of atoms (at-ppm). Relying only on average crustal abundance for judging the abundance of an element can be misleading. Actual material production is only somewhat related to element abundance. This fact is pictured by the production values of 2010, gathered by Vesborg and Jaramillo [36] and shown in blue in figure 1.2. The production is still scattered over multiple orders of magnitude for at least two reasons. One reason for this is that some elements are found in ores at concentrations orders of magnitude larger than their average concentration, making their extraction far more profitable and efficient once such ore pockets are found. A second reason is that the main extraction process of an element can be as a byproduct of another much more abundant and commercially significant material. In this case, the extraction of the main material results in the production of significant amounts of the more scarce element at relatively low added costs. This can be well illustrated with three elements very relevant for photovoltaics, silver, cadmium and indium. These three elements have very similar average concentrations in the crust, around $1 \cdot 10^{-2}$ at-ppm to

$4 \cdot 10^{-2}$ at-ppm. However, the production of indium is about two orders of magnitude lower than that of the two other elements, because it is usually found as low-concentration ores. Silver, on the other hand, is sometimes found in ores at a concentration orders of magnitude larger than its crustal average, making its mining much more viable commercially. Cadmium is produced as a byproduct of zinc production, and is present at 0.2% to 0.5% of the main zinc content. Zinc is among the 20 most produced elements, and is required in very large quantities, its main use being in galvanization of steel and iron to serve as a protective layer against corrosion. Cadmium supply thus follows the production of zinc, regardless of the demand for the scarcer element. Other relevant or somewhat relevant PV elements, bismuth and tellurium are produced at much larger rates than their average concentration would suggest. Again, this is due to these elements being the byproducts of the extraction of much more abundant and commercially relevant elements: lead and copper, for bismuth and tellurium, respectively. Other elements have the opposite trend of being produced much less than their abundance would suggest, such as scandium, rubidium or, more importantly for photovoltaics, gallium.

The previously-mentioned authors, Vesborg and Jaramillo, classified the elements in four categories depending on their production [36]. For the purposes of the discussions in this thesis, we will use the limit between their second and third categories to separate *earth-abundant* and *earth-scarce* elements, a limit at a production of 3.3×10^7 kg/year. According to the authors, elements produced at rates lower than this arbitrary threshold would require to be present in *very* low concentrations in renewable energy technologies to hope for terawatt energy production [36]. In this thesis, elements above this threshold will be considered as being earth-abundant. Some elements produced at rates lower than this threshold will also be discussed, either because they are close to the arbitrary boundary and may also be considered earth-abundant, or because they are present in compounds referred to as earth-abundant by the photovoltaics community.

1.1.5 Exaggerated claims of earth-abundance?

Some compounds using elements produced in very low quantities, or which are present in Earth's crust in very low average concentrations, are often labeled as being *earth-abundant*. One of the most striking example are compounds of selenium. This non-metal is both scarce on average and produced in very low quantities. A major example of such claims of earth-abundance of selenium compounds are the copper zinc tin sulfide/selenide (CZTSSe) kesterites [50]. These semiconductors are often regarded as the earth-abundant alternatives of the earth-scarce copper indium gallium sulfide/selenide (CIGSSe) technologies. The similar properties of sulfur and selenium mean that these elements are often studied in mixed forms, for increased tunability and customizability of material properties. Unfortunately, the label of earth-abundance, justly applicable to sulfur, is too often extended to its scarce partner.

Figure 1.2 highlights other elements that have average average crustal compositions, but that

are produced in very low volumes. Germanium and gallium are such examples. Gallium (5.66 at-ppm) is only about four times less abundant than zinc (22.2 at-ppm) in the crust on average, but is produced 100 000 times less every year. Germanium (0.43 at-ppm) has a similar average crustal abundance to arsenic (0.50 at-ppm), but is produced at rates nearly three order of magnitude smaller. According to Vesborg and Jaramillo, there is a potential for increased production of germanium, but the potential for increased production of gallium is limited [36].

A fourth element having questionably been labeled as earth-abundant is bismuth. Such designations can be found for example in reference [51]. Like gold, given its very low average crustal abundance, bismuth is produced in relatively large quantities. However, the absolute values of production are still quite low, and just above selenium or gold.

Whether compounds using the elements mentioned above should be qualified as earth-abundant remains debatable. They are nonetheless using components much scarcer than compounds with a universally-agreed "earth-abundant" label such as silicon, (selenium-free) copper zinc tin sulfide (CZTS), Cu_2O or FeS_2 [52]. They would require remarkably high rates of energy production per unit weight to allow sustainable production at global scales. Still, we will discuss these borderline "earth-scarce" materials in more details in this chapter, continuing in sections 1.2.2 and 1.2.3. They still represent major classes of semiconductors used in photovoltaics research, and are considered earth-abundant by a sufficiently large chunk of the research community. In section 1.2 below, we review earth-abundant (and some debatably so) semiconductor compounds investigated for applications as absorbers in photovoltaics.

1.2 Earth-abundant photovoltaics

In this section, we will discuss attempts of the PV community to find materials combining the abundance, and if possible the harmlessness, of the silicon material with the absorption efficiency of direct bandgap materials. Solar cells made from emerging semiconductor materials satisfying $>1\%$ efficiency and $>0.1\text{ cm}^2$ area have been listed in works such as the 2021 efficiency tables of Zakutayev et al. [53]. Let me remind the reader that the designation of an earth-abundant compound or semiconductor only indicates that its constituent element are abundant. The compounds themselves are not generally found in nature. The compounds covered in the remainder of this section will in general have applications as solar absorbers in photovoltaic devices. Other parts of photovoltaic devices can be made with earth-abundant compounds, and likely should if one is to produce the full devices on a very large scale. However, these will not be treated here. The review will be constrained to inorganic thin-film technologies. Organic or quantum dot technologies will be left out and hybrid organic-inorganic halide perovskites will only be briefly mentioned as a stepping stone towards fully inorganic perovskites.

This section is separated into different parts: subsection 1.2.1 covers the numerical ways new materials have been sought out; subsections 1.2.2 to 1.2.3 treat general aspects of compounds belonging to different families of element; subsection 1.2.4 summarizes some important

crystalline structures, and subsections 1.2.5 through 1.2.13 discuss different categories of earth-abundant, or closely related, semiconductor compounds. 1.2.5 contains pnictides based on zinc, the following section (1.2.6) chalcogenides based on zinc, then (1.2.7) pnictides based on copper, followed by (1.2.8) binary or ternary chalcogenides based on copper, after which (1.2.9) quaternary and higher-order copper chalcogenides are covered, followed yet again by (1.2.10) inorganic perovskites, then (1.2.11) bismuth compounds, (1.2.12) silver compounds and after that, (1.2.13) compounds not fitting in any previous category. Finally, in subsection 1.2.14, Zn_3P_2 is placed in perspective with the compounds examined in the previous subsections.

1.2.1 Material screening

Most materials used in photovoltaics have been discovered accidentally and were then improved over years of research. Before continuing towards describing materials that have been experimentally synthesized, let us briefly mention some ways which new materials are being explored using purely computational methods.

The 79 entirely-stable elements can combine with each other in an astronomic amount of combinations into an even much larger number of stable or metastable crystalline structures, each with different properties. It would be virtually impossible to synthesize and characterize all materials to find the one most suited to the application of choice. Simulation of material properties using computational methods help weed out unsuitable materials and focus our time and resources on investigating a small number of materials which have been predicted to exhibit promising properties.

An important step for computational screening of materials is choosing a selection metric for material "suitability". A simple one would be for example to look for materials with a direct bandgap close to the optimum of the Shockley-Queisser limit at ~ 1.3 eV [34], which is one of the most commonly used metric to judge the potential efficiency of absorber materials. This simple metric leaves a lot for improvement, however, because some direct bandgaps are symmetry-forbidden, while some materials with a too small fundamental indirect bandgap may have a suitable direct bandgap at higher energies. An example of a relevant PV material with a symmetry-forbidden direct bandgap is the ZnSiP_2 chalcopyrite, which has a 2.08 eV symmetry-forbidden absorption edge and a 2.9 eV allowed direct band transition [54, 55]. One approach for an improved suitability metric, used by Yu and Zunger and presented in reference [56], is to consider (i) the different allowed and forbidden direct and indirect bandgaps, (ii) the shape of the absorption curve near the bandgap energies and (iii) the radiative losses between the different lowest-energy band transitions. This metric captures the effects of the optical properties of the materials, but leaves out considerations of crystalline imperfections and economic factors. In their study, Yu and Zunger used a couple hundred already-predicted I_p - III_q - VI_r compounds as their initial set of materials to filter, then calculated their properties from first principles and applied their metric to compare the suitability of

these compounds.

Computational screening has been used for exploring a variety of classes of earth-abundant semiconductors, for photovoltaics and other applications. For example, a variety of previously unreported earth-abundant nitride semiconductor compounds with promising properties were presented in references [57] and [58], or chalcogenide perovskites (1.2.10) in reference [59].

Although high-throughput computational screenings provide relatively quick ways to find interesting materials, experimental synthesis and characterization are necessary steps to fully judge the suitability of the material. In computations, the mechanics of growth, the impact and densities of intrinsic and extrinsic defects and interactions at interfaces with other materials are not always fully taken into consideration, if at all. From 1.2.5 to 1.2.13, only experimentally-synthesized earth-abundant semiconductor compounds are presented, unless specified otherwise.

1.2.2 Pnictides

Pnictides are compounds of pnictogens, the nitrogen family of elements, or Group V on the periodic table. Elements in this family are nitrogen (N, 28.2 at-ppm), phosphorus (P, 704 at-ppm), arsenic (As, 0.5 at-ppm), antimony (Sb, $3.4 \cdot 10^{-2}$ at-ppm), bismuth (Bi, $8.45 \cdot 10^{-4}$ at-ppm) and moscovium (Mc, infinitesimal concentration). Elements of this family have similar chemical properties and can often be mixed and often occupy interchangeably the same sites in crystals. Nitrogen and phosphorus are undoubtedly earth-abundant, arsenic and antimony can be somewhat borderline but are only considered "low volume" and still suitable for terawatt energy production by Vesborg and Jaramillo [36].

Phosphides

Phosphorus is very abundant in Earth's crust and was the tenth most produced element in 2010 [36]. Phosphorus, as well as phosphate rock, is however considered a critical material by the European Union (EU) [41]. The most important use of phosphorus is as a fertilizer, in its P_2O_5 form, because it is an essential element for all living organisms. These quantities are magnitudes larger than those that would be needed for reaching TW levels of photovoltaic energy production, and phosphorus is considered a very attractive component of compounds for large-scale electricity production, in regards to its widespread availability and production [36, 52]. Zinc phosphide, specifically, is discussed in more details in 1.2.14 (p. 31), 1.3 (p. 33) and in the rest of this work.

Arsenides

Arsenic is a borderline abundant element (0.50 at-ppm). It is produced in moderate amounts directly from some ores and also as a byproduct of gold, copper and lead production. This element is an essential component of some of the most efficient solar cells, made with III-V semiconductor materials, bonded to the scarce gallium and indium. Arsenic can be harmful to health and to the environment when it leaks out of the compounds [60], but proper encapsulation and recycling techniques minimize this risk.

Bismuthides

Bismuth ($Z = 83$) is not an earth-abundant element. Its average crustal abundance of $8.4 \cdot 10^{-4}$ at-ppm make it more scarce than palladium ($2.9 \cdot 10^{-3}$ at-ppm) and neon ($5.2 \cdot 10^{-3}$ at-ppm) in the crust. Its production is high with respect to its very low abundance, and mostly bound to the production of lead. Nonetheless, Vesborg and Jaramillo qualified the element as "very low" on their scale of global element production in 2010. It would only be suitable for terawatt energy production if such solar cells would require 6 mg of bismuth per produced Watt or less, using the *whole* supply of 2010 bismuth production [36]. Furthermore, bismuth is one of the 30 raw materials listed by the European Commission as critical because of risks of supply shortage and impact on the economy [41, 42]. All these factors make terawatt-scale energy production with bismuth-containing materials very unlikely unless new large previously unknown deposits of commercially-suitable bismuth ores are found, or if these technologies could produce very large amounts of energy per unit weight of bismuth. Bismuthides are further discussed in section 1.2.11 (p. 27) in the framework of "earth-abundant" materials.

1.2.3 Chalcogenides

Chalcogenide are compounds of chalcogens, the oxygen family of elements, or Group VI on the periodic table. Elements in this family are oxygen (O, 599000 at-ppm), sulfur (S, 227 at-ppm), selenium (Se, $1.3 \cdot 10^{-2}$ at-ppm), tellurium (Te, $1.6 \cdot 10^{-4}$ at-ppm), polonium (Po, $1.99 \cdot 10^{-11}$ at-ppm) and livermorium (Lv, infinitesimal concentration). Like pnictides, elements of this family have similar chemical properties, can often be mixed and regularly occupy interchangeably the same sites in crystals. Mixtures of sulfur and selenium form an important part of the CIGS and CZTS compound families, the latter discussed in 1.2.9.

Oxides

Oxides tend to have very large bandgaps and are generally not suitable as absorber materials for photovoltaics, with a few exceptions. Photovoltaic cells have been made with ferroelectric oxides [61], for example, and with full-oxide nanostructures [62].

Selenides

The first ever solar cell, sparking the field of photovoltaics, was made in 1883 out of selenium [12, 63]. The current world record for power conversion efficiency with this 1.95 eV bandgap material, is of 6.5% [63]. This element is not so abundant in earth's crust ($1.3 \cdot 10^{-2}$ at-ppm), and compounds of selenium can in my opinion hardly be considered as *earth-abundant*. Vesborg and Jaramillo classified it as "very low volume", unlikely to allow TW-scale photovoltaic energy production, unless extremely low amounts of the elements could be used per watt of energy produced. Nevertheless, selenium is critical for the commercial CIGSSe and more sustainable CZTSSe technologies, and its compounds will be compared and treated as earth-abundant through the remainder of this work, as much of the research on sustainable photovoltaics includes selenium as a critical element.

Tellurides

As mentioned previously, tellurium is part of one of the few commercially-available thin film photovoltaic technologies, CdTe. Cadmium telluride cells have reached an impressive 22.1% energy conversion efficiency [31, 64], but tellurium is a very scarce element ($1.6 \cdot 10^{-4}$ at-ppm), and TW energy production is not realistic with these compounds [36, 52].

1.2.4 Some relevant crystalline structures

Here, the crystalline structures of some important compound families are compared and presented.

Zincblende, fluorite and wurtzite

The zincblende crystal structure is nearly ubiquitous among III-V semiconductors, such as GaAs, InGaAs and InP. This structure is the bi-atomic equivalent of the diamond structure famously exhibited by carbon and silicon. These group IV semiconductors can also crystallize in the more rare lonsdaleite (hexagonal carbon) structure, whose bi-atomic equivalent is the wurtzite structure. The zincblende and wurtzite structures are therefore very closely related, and in fact only vary in the stacking order along a (cubic) $\langle 111 \rangle$ direction [65]. The fluorite structure, like the zincblende structure, is made of a face-centered cubic (FCC) anion sublattice. Filling all of the 8 tetrahedral voids (forming the vertices of a cube) in the cubic unit cell with a cation produces the fluorite structure, while filling 4 of the 8 voids (with no filled spot on the same diagonal of the cube) produces the zincblende structure. Illustrations of these crystal structures are shown in figure 1.9a-e (p. 38). The structure of α - Zn_3P_2 , discussed in more detail in section 1.3.1, can be considered an alternated stack of zincblende and anti-fluorite structures (the anti-fluorite being the fluorite structure with cation and anion positions swapped).

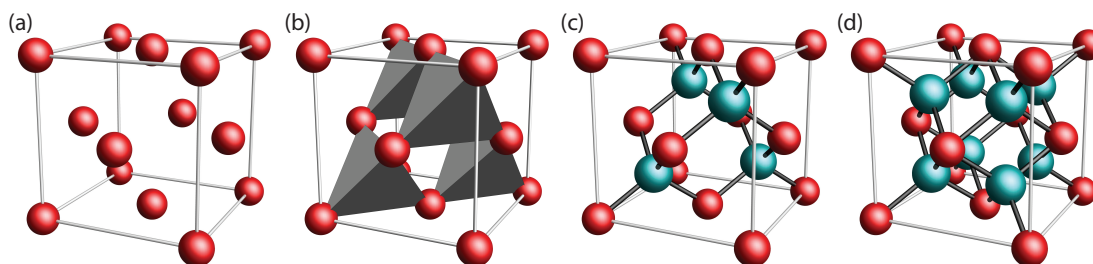


Figure 1.3 – Illustrations of the unit cells of (a) a face-centered cubic (FCC), (b) a FCC crystal with four of the eight tetrahedral voids highlighted, (c) a zincblende and (d) a fluorite/anti-fluorite type structures. The two differently colored spheres stand for two different atomic species.

Chalcopyrite

The chalcopyrite structure is closely related to the zincblende structure [66]. Compounds crystallizing in this structure are usually of the type II-IV-V₂. The unit cell of this structure (fig. 1.4b) can be viewed as two zincblende unit cells adjacent on a face (fig. 1.4a), where the cations (of group II and IV) alternate along the long axis of the unit cell. Electronically, a cation in group II and another in group IV replace two cations in group III, when compared to III-V zincblende compounds. In most real chalcopyrite structures, there are also slight distortions of the cell and slight displacements of the atoms.

Earth-abundant compounds exhibiting the chalcopyrite structure, such as ZnSnP₂ [67], are discussed in sections 1.2.5 and 1.2.8 below.

Kesterite and stannite

Compounds of the I₂-II-IV-VI₄ family crystallize in two main ways, in the kesterite and in the stannite structures (figures 1.4c,d) [68]. Like for the chalcopyrite structure, the kesterite and stannite unit cells can be thought of as two zincblende unit cells adjacent on a face. The differences lie again in the ordering of the cations, of groups I, II and IV. Electronically, two cations in group I replace one cation in group II, when compared to chalcopyrites.

In the kesterite structure, the stacking of cations along the long-axis of the tetragonal unit cell is I/II, followed by I/IV. In the stannite structure, the layers alternate as I/I and II/IV. A few other variations of the kesterite structure exist, differing further by their specific cation arrangement [68]. Earth-abundant compounds in the I₂-II-IV-VI₄ family are discussed in section 1.2.9.

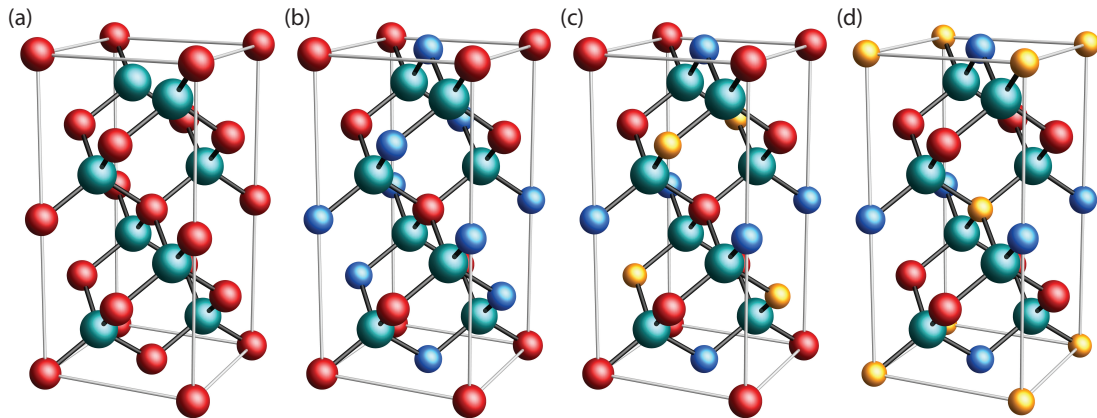


Figure 1.4 – Illustrations of (a) two zincblende unit cells stacked on a face and the unit cells of (b) chalcopyrite, (c) kesterite and (d) stannite type structures. The colored spheres correspond to different atomic species and are located at the equilibrium position of the atoms. The dark gray segments illustrate the bonds between neighboring atoms.

Perovskite

Perovskite designates a crystal lattice type, and by extension the whole class of compounds that crystallize exhibiting it or a related structure. Contrary to the crystalline structures discussed so far, the perovskite structure has very little in common with the zincblende structure. The highest-symmetry perovskites have fundamentally a simple cubic structure, and small distortions reduce the lattice to less-symmetric arrays.

According to Breternitz and Schorr, perovskites are compounds with an AMX_3 formula, or multiples of it, with regular or distorted octahedral coordination of cation M, and a corner-sharing 3D network of MX_6 octahedra [69]. Figure 1.5 shows an example of a cubic lattice with such a structure. Some non-cubic structures are also labeled as being perovskite, provided they exhibit the necessary characteristics.

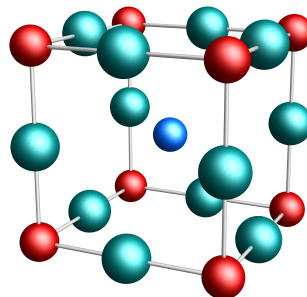


Figure 1.5 – Illustration of the perovskite crystal structure. Anion X is in turquoise, and cations A and M are in red and blue.

1.2.5 Zinc-based pnictides

The next series of sections discuss and list a selection of earth-abundant semiconductors, or closely related compounds.

Binary zinc pnictides

Earth-abundant binary zinc pnictides are zinc nitride, zinc phosphide and zinc arsenide. Arguably, antimonides and bismuthides may also be considered. **Zinc nitrides** appear to be extremely sensitive to their growth conditions and are discussed separately in a section below.

There are four established binary **zinc phosphides** phases [70], and only one phase, α -Zn₃P₂, is a serious contender for single-junction photovoltaics. The only other room-temperature-stable phase, α -ZnP₂, has an indirect bandgap of 2.1 eV [71]. α -Zn₃P₂ is discussed separately and in more details in section 1.2.14 (p. 31) and throughout this work.

Zinc arsenide has four known binary phases [72], two of which are stable at room temperature. At least one of the Zn₃As₂ phases has a bandgap of 1.0 eV [73, 74], which is slightly too low for photovoltaic applications. However, Im et al. have shown that the bandgap can be tuned continuously from 1.0 eV to 1.5 eV by alloying Zn₃P₂ and Zn₃As₂ [75], which form solid solutions over most of the compositional range, below 950 K [76], as illustrated in figure 1.8, p. 36).

The zinc-antimony binary system contains 6 binary phases [77]. The bulk of the work on **zinc antimonides** is in the field of thermoelectricity. Zn₄Sb₃ is one of the most efficient thermoelectrics [78, 79]. ZnSb, for example, has a bandgap of 0.5 eV [80], too low for photovoltaics. To the best of my knowledge, there are no known binary **zinc bismuthides** [81].

Zn-IV-V₂ compounds

Zn-IV-V₂ chalcopyrite compounds have attracted attention as earth-abundant semiconductors with many similarities to III-V compounds. For example, Zn-IV-N₂ compounds have similar electronic and optical properties to InGaN [82, 83].

Similarly to III-V compounds, the properties of Zn-IV-V₂ compounds, including their bandgap, can be tuned by alloying with different elements [82]. A wide range of II-IV-V₂ compounds have been synthesized experimentally, and are reviewed for example in reference [84]. Many of these compounds have a relatively large bandgap in the range from 1.5 eV to 2.5 eV [84], too large or on the larger side of suitable bandgaps for photovoltaics. Interestingly, cation disorder in these compounds has a major impact on their electronic properties. For example, the fundamental band edge energy of ZnSnN₂ was found to be tunable between 1.0 eV and 2.0 eV [83]. This indicates that an additional degree of freedom, besides alloying, is available to optimize the properties of these compounds.

Zinc nitrides and oxynitrides

Zinc nitride (Zn_3N_2), has been considered for a variety of applications in optoelectronics and electronics, in part thanks to the good charge carrier mobility ($\sim 100 \text{ cm}^2 \text{ V}^{-1} \text{ s}^{-1}$) of even amorphous or nanocrystalline films [85, 86]. A very large range of bandgap energies of Zn_3N_2 have been reported [87], ranging from about 1.0 eV [88, 89], through 1.23 eV [90] and 2.12 eV [91], until a maximum of 3.2 eV [92, 93]. This large range of values is likely due to differences in processing conditions, with defects such as nitrogen interstitials, forming N-N bonds and embedded N_2 species, or unintentional oxygen doping⁴/alloying. One may think that the "true" bandgap energy of Zn_3N_2 corresponds to the largest reported values (3.2 eV), and that high concentrations of defects create bands within the original bandgap, which make it appear as if the bandgap of the semiconductor is smaller. This, however, appears not to be the case. Density-functional theory (DFT) calculations place the bandgap of this compound at 0.84 eV [87] or 0.70 eV [94]. Some of the apparent bandgap increase has been explained by Kumagai et al. [87], but the authors were unable to provide a conclusive answer to the many differences of reported bandgap values. If one could reliably control the bandgap of Zn_3N_2 to remain in the range from 1.0 eV to 2.0 eV, this n-type⁵ semiconductor could be a suitable option for earth-abundant photovoltaics.

Several attempts have been made to reliably produce and study compounds intermediate between ZnO and Zn_3N_2 , in the hopes of controlling the bandgap between the high-energy bandgap of ZnO at 3.37 eV [95] and the low-energy bandgap of Zn_3N_2 . So far, results are very varied. Bandgap energy control and understanding has not been achieved yet. Compounds with zinc and mixtures of oxygen and nitrogen have been synthesized in ZnO, Zn_3N_2 or amorphous structures, sometimes with bandgaps close to the optimum for photovoltaics. Some examples of such compounds are summarized in table 1.1.

Material	Composition	Structure	Bandgap	Refs
ZnO:N	$\leq 10\% \text{ N}$	ZnO	2.30 eV to 3.26 eV	[96]
Zn-O-N	undetermined	am.	undetermined	[85]
"ZnON"	56:22:22 (atomic)	am.	1.3 eV	[97]
"ZnON"	1:0.73:0.27	am. + ZnO	1.8 eV or 2.4 eV	[86]
"ZnON"	1:0.51:0.49	am. + nanocryst.	1.5 eV to 2.0 eV	
"ZnON"	1:0.14:0.86	am. + Zn-O + Zn-N	1.3 eV	
$\text{Zn}_3\text{N}_{2-x}\text{O}_x$	$x = 0.11 \text{ to } 0.19$	Zn_3N_2	2.3 eV to 2.6 eV	[98]

Table 1.1 – List of phases synthesized by some authors investigating zinc oxynitrides. *am.*: amorphous, *nanocryst.*: nanocrystals.

Zinc oxynitrides may be suitable candidates for at least n-type semiconductor absorbers in photovoltaics. However, a good control of the defect structure and the significant changes it

⁴A layperson explanation of *doping* is given in Appendix H: Base concepts of solid-state physics

⁵A layperson explanation of *n-type* is given in Appendix H: Base concepts of solid-state physics

induces to the electronic band structure is imperative, and remains missing to this day.

Other zinc pnictides

A multitude of compounds with zinc and pnictogens exist, most of which have not been discussed here. Some have been investigated for different applications, some have been synthesized but their optical properties are still unknown, others have been predicted theoretically without ever being synthesized, while others remain still completely unknown.

A few of those compounds, with a measured bandgap, are listed in the last section of table 1.2. Other little studied compounds are BaZnBi₂ [99], BaZnSb₂ [99], Ca₉Zn₄Bi₉ [100], LiZnBi [101], SrZnBi₂ [102], and there are many more.

Material	Structure	bandgap	PCE	Refs
Zn ₃ N ₂	II ₃ -V ₂	1.0 eV to 3.2 eV	5.96% [104]	[98]
Zn ₃ P ₂	II ₃ -V ₂	~1.5 eV[103]		
Zn ₃ As ₂	II ₃ -V ₂	1.0 eV[73, 74]		
ZnSiN ₂	II-IV-V ₂	1.0 eV [106], 1.7 eV [107] and 2.0 eV [82] ≥2.0 eV to 3.1 eV (p1) 1.38 eV & (p2) 1.68 eV[67]	3.44% [109]	[105]
ZnSnN ₂	II-IV-V ₂			[108]
Zn(Sn, Ge)N ₂	II-IV-V ₂			[82]
ZnGeAs ₂	II-IV-V ₂			[84]
ZnSnP ₂	II-IV-V ₂			[110]
Ca ₂ ZnN ₂	II' ₂ -II''-V ₂	1.6 eV (i) 1.9 eV (d)	-	[57]
Zn ₂ SbN ₃	II ₂ -V'-V'' ₃	1.55 eV to 1.71 eV		[111]
LiZnN	I-II-V	1.91 eV		[112]
CaZn ₂ N ₂	II'-II'' ₂ -V ₂	1.9 eV	-	[57]

Table 1.2 – List of binary and ternary zinc pnictide semiconductors considered for applications as photovoltaic absorbers, as well as some closely related compounds.

1.2.6 Zinc-based chalcogenides

Binary zinc and chalcogenide compounds have large bandgap that make them unsuitable as absorbers in photovoltaics as such. ZnO has a bandgap of 3.37 eV [95], ZnS 3.66 eV [113] and ZnSe 2.81 eV [114]. When grown in low-resistive ways, these compounds have applications as transparent conductive layers and buffer layers in photovoltaic devices. Some variations based on zinc oxide used as transparent conductive earth-abundant layers are zinc tin oxide (Zn_xSn_{1-x}O_{2-x}) [115] and aluminum-doped zinc oxide (AZO) [116].

Owing to their similar chemical properties, these compounds can be alloyed together or with similar copper or cadmium [117] chalcogenides. Zinc and copper sulfides and selenides are closely related to the important CIGS and CZTS compound families discussed in section 1.2.9, which have more suitable properties as solar absorbers.

1.2.7 Copper-based pnictides

Cu_3N stood out in the search for defect tolerant semiconductor for solar energy conversion. Similarly to CIGSSe, the optoelectronic properties of this semiconductor, and hence its energy conversion efficiency, are relatively unaffected by defects, point-like, dislocations or 2D stacking faults and interfaces [118]. This defect tolerance property is desirable because it reduces the need for the expensive, slow or small-area growth and processing techniques required for high-quality structures. Its 1.0 eV indirect bandgap and 1.4 eV onset of absorption place this material in the lower-bandgap range of potentially suitable materials for photovoltaics, and hence effort has been spent to find other copper nitrides with closer to optimal properties [119]. Delafossite nitride compounds, AMN_2 , have shown some potential in this regard [120, 121]. CuTaN_2 and CuNbN_2 are such compounds.

CuTaN_2 has a calculated indirect bandgap of 1.3 eV and a calculated direct bandgap of 1.4 eV with an experimentally-determined onset of absorption at 1.5 eV and a very high above-bandgap absorption coefficient ($\alpha_{\text{calc}} = 10^5$ to 10^6 cm^{-1}) [122]. CuNbN_2 has a calculated indirect bandgap of 0.9 eV and a calculated direct bandgap of 1.4 eV, and an experimental optical bandgap of 1.3 eV with low calculated carrier effective masses [120].

Material	Bandgap					Reference
	Calculated		Experimental			
	indirect	direct	Indirect	abs. onset	optical	
Cu ₃ N			1.0	1.4		[118]
CuTaN ₂	1.3	1.4		1.5		[122]
CuNbN ₂	0.9	1.4			1.3	[120]

Table 1.3 – List of copper pnictides investigated for photovoltaic applications. *abs. onset* is the experimentally-measured onset of absorption.

1.2.8 Binary and ternary copper-based chalcogenides

Copper chalcogenides form a prevalent class of materials in the field of earth-abundant photovoltaics. In this section, such binary and ternary compounds are discussed. The quaternary and higher-order compounds, which include the kesterite-structured CZTSSe compounds are discussed in section 1.2.9.

Binary copper chalcogenides have received considerable attention in the field of earth-abundant photovoltaics. The two copper-oxygen binary compounds, CuO and Cu_2O [123], and Cu_2S are some of the very few compounds that have a potential for global photovoltaic energy production matching Zn_3P_2 and amorphous silicon [52]. This is in part due to their high abundance in the crust (O: 59.9 at-%, Cu: 19.6 at-ppm, S: 227 at-ppm) and in part to their suitable bandgaps. Cuprous oxide (Cu_2O) and cupric oxide (CuO) have bandgaps of 2.0 eV and 1.2 eV, respectively. Cu_2S has a satisfactory bandgap of 1.21 eV and has received a lot of

attention, especially a few decades ago in thin film structures, in conjunction with CdS [124]. Cu_xSe , although having a bandgap in the 1.0 eV to 1.3 eV range [125], has received much less attention for applications in photovoltaics than its oxygen or sulfur alternatives.

The binary copper chalcogenides, though simple in their structure and attractive in their abundance have so far failed to become dominant absorber materials for different reasons. The formation of phase-pure structures of Cu_2O has been a challenge because it tends to decompose into the more stable CuO [126]. As for the sulfide compound, a vigorous research effort on the well-studied $\text{Cu}_2\text{S}/\text{CdS}$ planar solar cells dwindled during the 1980s due to the negative effects of copper diffusion into CdS [124]. Renewed efforts in the growth of this system in nanoscale form in the recent decades encounters new sets of challenges.

Material	bandgap	PCE	Reference
CuO	1.2 eV	8.1%	[127]
Cu_2O	2 eV [128]		[129]
$\text{Cu}_2\text{S}^{(1)}$	1.21 eV		[117, 130]
Cu_xS			
Cu_xSe			
CuSbSe_2	1.04 eV to 1.2 eV	4.7%	[131, 132]
CuSbS_2		1.8%	[133]
Cu_3AsS_4			[134–137]
$\text{Cu}_2(\text{Ge, Sn})(\text{S, Se})_3$			
Cu_2SnS_3	0.93 eV, 1.06 eV		
Cu_2GeS_3			[137]

Table 1.4 – List of binary and ternary copper chalcogenides. (1): typically paired with CdS.

1.2.9 Quaternary and higher-order copper-based chalcogenides

The commercial success and remarkable efficiency of $\text{Cu}(\text{In, Ga})(\text{S, Se})_2$, CIGSSe, and CdTe semiconductors as solar absorbers has prompted research to find compounds with similar structures and properties using more sustainable elements. Kesterite-type $\text{Cu}_2\text{ZnSnS}_4$, $\text{Cu}_2\text{ZnSnSe}_4$ and their alloys $\text{Cu}_2\text{ZnSn}(\text{S, Se})_4$ have emerged in this search and serve as the basis of a wide set of materials aimed at bypassing the shortcomings of CIGSSe. Some of the challenges brought by these materials include a very narrow range of phase stability, a comparatively high volatility of tin compounds with respect to other species and easy formation of point defects [138].

The biggest factor holding back the power conversion efficiency of CZTSSe cells, compared to the theoretical maximum, is a small open-circuit voltage. This unexpectedly low voltage has been attributed to the band tailing caused by the presence of defects. A variety of studies have shown that anti-site defects are prevalent, especially between Cu-Zn and Sn-Zn, when these atoms are present [139], owing in big part to the similar radii and chemical behavior. Three

directions are being explored to reduce the impact of disorder on the photovoltaic properties of these compounds: (i) studying the effect of growth conditions, (ii) atomic substitution to introduce atomic size mismatches, thus reducing the likelihood of anti-site defects and (iii) searching for other, less defect-sensitive crystalline structures. A comprehensive 2017 review covering these efforts was for example published by Shin et al. [138]. In addition to the many compounds resulting from atomic substitutions that are presented in that work, we may also add $(\text{Ag}_x\text{Cu}_{1-x})_2\text{ZnSnSe}_2$ [140] and $\text{BaCu}_2\text{Sn}(\text{S}, \text{Se})_4$ [139]. The small quantities of silver added in the first compound ($x = 0.03$) decreased the density of Cu_{Zn} antisite defects and improved the PCE by 3 points. Also, the crystalline structure of the $\text{BaCu}_2\text{Sn}(\text{S}, \text{Se})_4$ compound deviates from the abundant zincblende-related structures, and takes a trigonal structure instead.

Material	bandgap	PCE	Reference
$\text{Cu}_2\text{ZnSnSe}_4$	(1.02 eV ref 11-12 [141])		[142]
$\text{Cu}_2\text{ZnSnS}_4$			[143, 144]
$\text{Cu}_2\text{FeSnS}_4$			
CuPbSbS_3	1.3 eV	2.65%	[145, 146]
$\text{Cu}_2\text{SrSnS}_4$			[147]
$\text{CuZn}_2\text{AlS}_4$			[148]
$\text{Cu}_2\text{Sn}_{1-x}\text{Ge}_x\text{S}_3$	0.92 eV to 1.6 eV (over x)	6.7%	[137]
$\text{BaCu}_2\text{SnS}_4$	2.05 eV [149]	1.62% [139]	[139, 147, 149]
$\text{BaCu}_2\text{SnSe}_4$	1.72 eV		
$\text{SrCu}_2\text{SnS}_4$			
$\text{Ag}_2\text{ZnSnSe}_4$			
$\text{Cu}_2\text{Zn}(\text{Sn}_{1-x}\text{Ge}_x)\text{Se}_4$	0.99 eV to 1.35 eV [150]	9.1% [151]	[141]
$\text{Cu}_2\text{ZnSn}(\text{S}, \text{Se})_4$	~ 1.15 eV [50]	12.6% [50]	[50, 138, 142]
CZFeTS			
$\text{BaCu}_2\text{Sn}(\text{S}, \text{Se})_4$	1.5 eV to 2 eV [139, 152]	5.2% [152]	[139, 152, 153]
$(\text{Ag}_x\text{Cu}_{1-x})_2\text{ZnSnSe}_4$	1.02 eV to 1.33 eV	10.2%	[140]
$\text{CuGa}(\text{Ge}, \text{Sn})(\text{S}, \text{Se})_4$			
$\text{Cu}_2\text{Ba}(\text{Sn}, \text{Ge})(\text{S}, \text{Se})_4$			
$(\text{Ag}_x\text{Cu}_{1-x})_2\text{ZnSn}(\text{S}, \text{Se})_2$	1.04 eV to 1.13 eV	10.36%	[154]
$\text{Cu}_2\text{Zn}(\text{Sn}, \text{Ge}, \text{Si})(\text{Se}, \text{S})_4$			[141, 142]

Table 1.5 – List of quaternary and higher-order copper chalcogenides.

1.2.10 Earth-abundant perovskites

Perovskite compounds have gained an enormous notoriety in the photovoltaic community with the advent of hybrid organic-inorganic lead-halide perovskites in the first half of the 2010s (●, in NREL efficiency chart, p. 114). The crystal structure of these compounds, discussed in section 1.2.4, differs from most compounds reviewed until here, and does not have tetrahedral coordination.

The perovskite crystalline structure is in itself a reason for the remarkable properties of these compounds [155]. In methylammonium lead iodide perovskites, for example, the high ionicity of the compound has been found to be a major factor of the low formation energy of shallow defects and the high formation energy of deep defects [156]. Phases without the sought-after corner-sharing structures, with *needle-like* or *hexagonal* structures are thought to have more massive carriers, and thus lower mobility, owing to more localized band edges [157].

The great success of hybrid halide perovskites has prompted efforts to find materials maintaining the good optoelectronic properties of the hybrid compounds while simultaneously avoiding the two major issues of these compounds, namely toxicity and instability [158]. Indeed, lead (Pb) has been a major component of these crystals, and the compounds tend to decompose when stored in ambient conditions [157].

A fully-inorganic perovskite family that has been the subject of inquiries is for example the $(\text{Ba}, \text{Ca})(\text{Zr}, \text{Hf})\text{S}_3$ compounds. However, among those, the compound with the lowest bandgap is BaZrS_3 , at 1.73 eV [158]. This remains slightly too large for single-junction photovoltaics, but substitution with isovalent elements, such as Ti for Zr, were shown to decrease the bandgap to optimal values. $\text{BaZr}_{0.9}\text{Ti}_{0.1}\text{S}_3$ has a bandgap of 1.47 eV, for example, though it appears to be metastable in decomposition into more titanium-rich phases [157].

These inorganic compounds appear to be very stable [159] in ambient conditions, and transition metal perovskite chalcogenides also have large density of states in the conduction band [159]. This property of the bands leads to very large absorption coefficients near the bandgap energy [160]. Currently, a lot of work is still being done on, in one of the broadest designations, $(\text{Ba}, \text{Sr}, \text{Ca})(\text{Ti}, \text{Zr}, \text{Hf})(\text{O}, \text{S}, \text{Se})_3$ perovskites to explore the compositional space and the properties of these fully-inorganic mostly earth-abundant semiconductors.

Material	bandgap	PCE	Reference
BaZrS ₃	1.73 eV [158]		[158–160]
BaHfS ₃			[160]
SrZrS ₃			[158–160]
SrHfS ₃			[160]
SrTiS ₃			[158]
CaZrS ₃			[158]
Ba(Zr, Ti)S ₃	1.90 eV		[59, 157, 160, 161]
BaZr(S, Se) ₃			[160]
BaZr(O, S) ₃			[59]
SrZr(O, S) ₃			[59]

Table 1.6 – List of inorganic perovskites.

1.2.11 Bismuth-based materials

We now make a brief parenthesis to talk about a niche set of photovoltaic materials based on bismuth. Bismuth-containing materials have come up in the search for a replacement for the unstable and toxic hybrid lead-halide perovskites [162–166]. The ferroelectric perovskite BiFeO_3 forms the basis to a set of bismuth-containing ferroelectric compounds with a relatively large bandgap investigated for photovoltaic applications. Ferroelectric materials have interesting properties for photovoltaic applications thanks to the bulk photovoltaic effect [167]. Contrary to regular semiconductors used for photovoltaics, materials exhibiting the bulk photovoltaic effect can separate solar-generated charges in homogeneous materials thanks to their built-in polarization and can achieve open-circuit voltages much larger than the band gap [168]. These effects make such materials interesting for photovoltaics, but the large bandgap of well-studied materials such as BaTiO_3 limit absorption to the ultraviolet (UV) part of the solar spectrum. Promising results with BiFeO_3 [168, 169], with its direct bandgap of approximately 2.52 eV to 2.75 eV [168–171], have sparked interest for further study of this material and its alloys. Various attempts to shift the bandgap to more suitable lower values were attempted by alloying with different elements. Attempts have been performed with manganese ($\text{BiFe}_{0.9}\text{Mn}_{0.1}\text{O}_3$, 2.79 eV bandgap [171]), strontium ($\text{Bi}_{0.9}\text{Sr}_{0.1}\text{FeO}_3$, 2.76 eV bandgap [170]), scandium ($\text{BiFe}_{0.6}\text{Sc}_{0.4}\text{O}_3$, 2.76 eV bandgap [172]), cerium ($\text{Bi}_{0.88}\text{Ce}_{0.12}\text{FeO}_3$, 2.66 eV bandgap [171]), sodium ($\text{Bi}_{0.8}\text{Na}_{0.2}\text{FeO}_3$, 2.52 eV bandgap [173]), titanium ($\text{Bi}_{0.92}\text{Ti}_{0.08}\text{FeO}_3$, 2.38 eV bandgap [174]), silicon ($\text{BiFe}_{0.95}\text{Si}_{0.05}\text{O}_3$, ~ 2.30 eV bandgap [175]) and neodymium ($\text{Bi}_{0.9}\text{Nd}_{0.1}\text{FeO}_3$ 2.22 eV [176] or 2.71 eV [177] bandgap). Co-doping of some of these elements was also investigated: neodymium and vanadium ($\text{Bi}_{0.95}\text{Nd}_{0.05}\text{Fe}_{0.97}\text{V}_{0.03}\text{O}_3$, 2.51 eV bandgap [178]), manganese and cerium ($\text{Bi}_{0.88}\text{Ce}_{0.12}\text{Fe}_{0.9}\text{Mn}_{0.1}\text{O}_3$, 2.81 eV bandgap [171]), samarium and cobalt ($\text{Bi}_{0.9}\text{Sm}_{0.1}\text{Fe}_{0.95}\text{Co}_{0.05}\text{O}_3$ [179]), and lanthanum and nickel ($\text{Bi}_{0.975}\text{La}_{0.025}\text{Fe}_{0.975}\text{Ni}_{0.025}\text{O}_3$ [180]). The most successful attempt at making an efficient solar cell out of variations of BiFeO_3 was achieved by Nechache et al., who built a solar cell made with different layers based on $\text{Bi}_2\text{FeCrO}_6$, reaching a very respectable 8.1% power conversion efficiency [61]. In general, photovoltaic devices made with these materials tend to have large open-circuit voltages and low short-circuit currents.

Material	bandgap	PCE	Reference
BiFeO ₃	2.52 eV to 2.75 eV		[168–171]
BiFe _{0.9} Mn _{0.1} O ₃	2.79 eV		[171]
Bi _{0.9} Sr _{0.1} FeO ₃	2.76 eV		[170]
BiFe _{0.6} Sc _{0.4} O ₃	2.76 eV		[172]
Bi _{0.88} Ce _{0.12} FeO ₃	2.66 eV		[171]
Bi _{0.8} Na _{0.2} FeO ₃	2.52 eV		[173]
Bi _{0.92} Ti _{0.08} FeO ₃	2.38 eV		[174]
BiFe _{0.95} Si _{0.05} O ₃	~2.30 eV		[175]
Bi _{0.9} Nd _{0.1} FeO ₃	2.22 eV		[176]
	2.71 eV		[177]
Bi _{0.95} Nd _{0.05} Fe _{0.97} V _{0.03} O ₃	2.51 eV		[178]
Bi _{0.88} Ce _{0.12} Fe _{0.9} Mn _{0.1} O ₃	2.81 eV		[171]
Bi _{0.9} Sm _{0.1} Fe _{0.95} Co _{0.05} O ₃			[179]
Bi _{0.975} La _{0.025} Fe _{0.975} Ni _{0.025} O ₃			[180]
Bi ₂ FeCrO ₆		8.1%	[61]

 Table 1.7 – List of ferroelectric materials based on BiFeO₃

Material	bandgap	PCE	Reference
BiSI	1.57 eV (i)		[181, 182]
Bi ₁₃ S ₁₈ I ₂	0.75 eV	0.85%	[181]
SrBi ₂ Nb ₂ O ₉ : Ni	>2.25 eV		[183]
Cs ₂ NaBiI ₆	1.5 eV to 2.3 eV		[184]
Cs ₃ Bi ₂ I ₉	2.01 eV[185], 1.94 eV [186]	0.07%	[185, 187]
	~2.1 eV [187]	3.20% [188]	[188]
Cs _{3-x} Bi ₂ I ₉	1.77 eV to 2.01 eV	≤0.62%	[185]
CsBi ₃ I ₁₀	1.77 eV[189]	0.77% [190]	
	1.75 eV	0.63%	[191]
BiI ₃	1.80 eV[185], 1.69 eV [192]	0.36% [185]	[185, 193–195]
CsPbBr ₃	2.3 eV		ref:[196]
Cs ₃ Bi _{2-x} Pb _x Br ₉	2.23 eV to 2.62 eV		[197]
α-CsPbI ₃	1.73 eV	4.13%	ref:[196]
α-CsPb _{1-x} Bi _x I ₃		≤13.21%	[196]
γ-CsPbI ₃	1.71 eV to 1.73 eV	12.1%	[198]
CuBiI ₄	~1.81 eV	1.12%	[199]
	2.67 eV	0.82%	[200]
BiI _{3-x} Cl _x	1.75 eV to 1.78 eV		[201]
BiI _{3-x} Br _x	1.75 eV to 2.06 eV		[201]
Cs ₃ Sb ₂ I ₉	2.05 eV		[202]

Table 1.8 – Selection of bismuth- and/or cesium-containing semiconductor compounds.

1.2.12 Silver-containing materials

Silver ($Z = 47$) has an average crustal abundance of $1.4 \cdot 10^{-2}$ at-ppm and is just about as scarce as cadmium ($2.8 \cdot 10^{-2}$ at-ppm) and indium ($4.5 \cdot 10^{-2}$ at-ppm). Its production is relatively high, compared to its low abundance in the crust, and it is considered an element with "very low" production in 2010 and that it is "overproduced" with respect to the known reserves. An increase of production would likely only be possible with substantial increases in prices, if demand was to increase dramatically [36]. A significant part of silver use in industry comes from silver-paste usage in silicon photovoltaics. A 2019 study attempting to predict the upcoming demand and use of silver concluded that the current increase in silicon solar cell deployment was not constrained by silver availability provided that the decrease in silver-paste use per silicon panel continued at the current rate [203]. The study did not however consider a potential increase in silver use stemming from the development and increased production of silver-containing semiconductors as photovoltaic absorbers. Given the previous constraints and limitations, it seems that terawatt-scale energy production with silver-containing solar absorber materials is a very unlikely scenario.

Let us still briefly review recent developments in silver-based solar absorber materials. AgBiS_2 , a material containing both silver and bismuth, and thus extremely unlikely to ever reach a production scale of any significance, attained the respectable power conversion efficiency of 6.3% [204]. A standout property of these solar cells is their very thin active layer thickness of 35 nm, which means that relatively low volumes of silver and bismuth are needed. Their requirements of indium and silver in the contacting layers used in their prototype solar cell still need to be addressed before considering large-scale production, however. AgNbN_2 and AgTaN_2 , delafossite nitrides structurally similar to the CuNbN_2 and CuTa_2N_2 described earlier, have also been predicted as promising by first-principles computation [121], but have not been produced experimentally.

Material	bandgap	PCE	Reference
AgBiS ₂		6.3%	[204]
AgBi ₂ I ₇	1.87 eV	1.22%	[205]
Ag(Bi, Sb) ₂ I ₇	indirect 1.61 eV to 1.98 eV direct 1.79 eV to 2.23 eV	≤1.76%	[206]
AgBi ₂ (I, Br) ₇	indirect 1.59 eV to 1.95 eV direct 1.78 eV to 2.28 eV	≤1.02%	[207]
Cs ₂ AgBiBr ₆	1.95 eV to 2.19 eV		[208, 209]
Cs ₂ AgBi _{1-x} Sb _x Br ₆	1.6 eV to 2.0 eV		[209]
Cs ₂ AgBiCl ₆	2.77 eV		ref:[208]
	2.5 eV		[208]
AgBiI ₄	(i) 1.79 eV, (d) 1.94 eV	2.50%	[210]
AgBi ₃ I ₁₀	1.8 eV	2.73%	[211]
Ag ₃ BiI _{6-2x} S _x		≤5.44%	[212]
(Ag _{1-x} Cs _x) ₂ BiI ₅	1.88 eV to 1.97 eV	≤0.73%	[213]
Ag ₂ (Bi _{1-x} Sb _x)I ₅	1.86 eV to 1.97 eV	≤1.06%	[213]
Ag ₂ BiI ₅	1.97 eV	0.42%	[213]

Table 1.9 – Selection of silver-containing semiconductors.

1.2.13 Other cations

The compounds discussed so far have been grouped according to the characteristics of their constituents or their crystal structure. The table below contains a list of compounds with either constituent atoms not included in the previous categories, or that can hardly be considered earth-abundant but that may still deserve a mention.

Material	bandgap	PCE	Reference
Se	1.95 eV	6.5%	[63]
FeS ₂			[214]
SnS			[215–217]
Ca ₃ N ₂	1.7 eV		[218] & [57] SI
Sb ₂ Se ₃			
Sb ₂ S ₃			
CdGeP ₂			[84]
CdSnP ₂			[84]
MgSnAs ₂			[84]
CdSiAs ₂			[84]

Table 1.10 – Earth-abundant semiconductors not fitting any category discussed in the remainder of the chapter.

1.2.14 A case for zinc phosphide

Research carried out on zinc phosphide is limited, when compared to other earth-abundant semiconductors with a high potential for PV energy production such as iron, copper, nickel or lead sulfides and copper or zinc oxides [52]. At the time of writing, a quick search on a major database search engine, webofscience.com⁶ for papers on each of the previously mentioned compounds⁷ yields approximately 2600, 3400, 1900, 2100, 13800 and 56800 results, respectively. This is in comparison with the same search for "zinc phosphide", yielding only 433 results overall.

Historically, research on zinc phosphide peaked in the 1980s, with a new acceleration of activity in the early 2010s. Figure 1.6 shows a histogram charting the publication year of scientific works related to zinc phosphide listed on two major scientific work databases, scholar.google.com⁸ and webofscience.com. The data covers the range from the first report of materials properties of zinc phosphide by Stackelberg and Paulus [220] (in 1933, not included in either databases) to 2020.

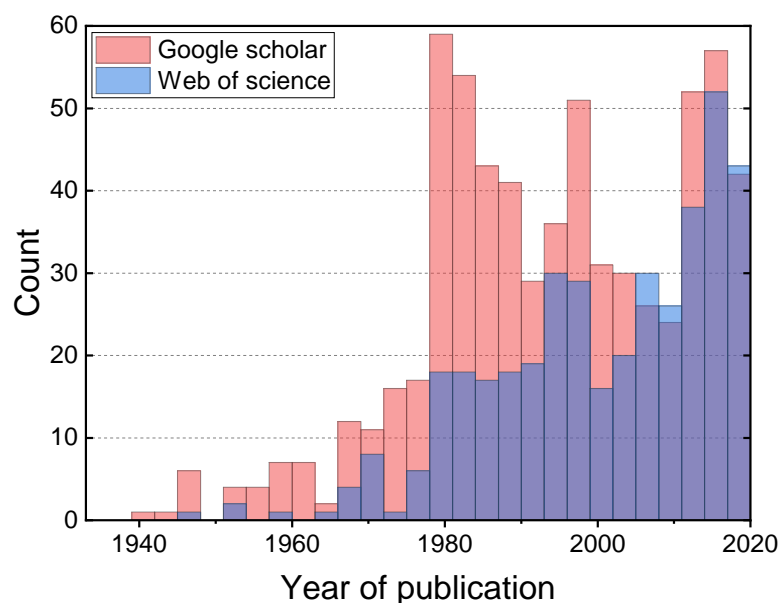


Figure 1.6 – Publication year histogram of (in blue) the listings on webofscience.com on the topic of "zinc phosphide" and (in red) the papers listed by Google Scholar with a title containing "zinc phosphide", from 1933 to 2020. Bin size is 3 years.

Compared to the compounds discussed until here, Zn_3P_2 has several positive aspects. Its components are very abundant. The binary phase diagram of zinc and phosphorus is relatively simple, and the cation only exhibits a single oxidation number, +II. The latter implies that

⁶<https://clarivate.com/webofsciencegroup/solutions/web-of-science/>

⁷ Searching for papers on the *topic* of, for example, "iron sulfide" (with quotation marks).

⁸ Listings recovered using the *Publish or Perish* software [219].

phase transitions such as the transitions observed between Cu(I) oxide and Cu(II) oxide are avoided. This phosphide has a near-ideal direct bandgap of 1.5 eV resulting in a penetration depth (63% absorbed) of less than 1 μm for red light, and less than 100 nm for yellow and more energetic light. Its carrier diffusion length of a few micrometers means that all light can be absorbed and most photogenerated carriers can be collected with films of a few hundred nanometers.

The record power conversion efficiency of a zinc phosphide solar cell, about 6% has been reached in 1981 [104], near the peak of research activity for this compound. The record is thus still standing 40 years after being set. This is certainly due in part to the few challenges this material brings up, which have not fully solved: (i) the "inconvenient" properties of the crystalline lattice, and (ii) the doping self-compensation of intrinsic acceptor defects. The inconveniences of the crystalline lattice are covered in more details in section 1.3.1.

1.3 Zinc phosphide

This section contains a discussion of the properties of the Zn_3P_2 crystal and related phases, as well as the current state of research on the material. The reader is directed to such works as the doctoral theses of Drs. Mahdi Zamani [221], Simon Escobar Steinvall [222], Ryoji Katsube [223], Timothy Burgess [224], Jeffrey Bosco [225] and Gregory Kimball [226] for other detailed perspectives on zinc phosphide and closely related materials.

1.3.1 Structure

Phases of the Zn-P system

There are four stable binary phases in the zinc-phosphorus system at standard pressure: $\alpha\text{-Zn}_3\text{P}_2$, $\beta\text{-Zn}_3\text{P}_2$, $\alpha\text{-ZnP}_2$ and $\beta\text{-ZnP}_2$ [70]. These are phases #1 to 4 in table 1.11, and the binary compounds in the atmospheric-pressure Zn-P phase diagram in figure 1.7. The β phases are high-temperature phases, while the α phases are stable at more moderate temperatures.

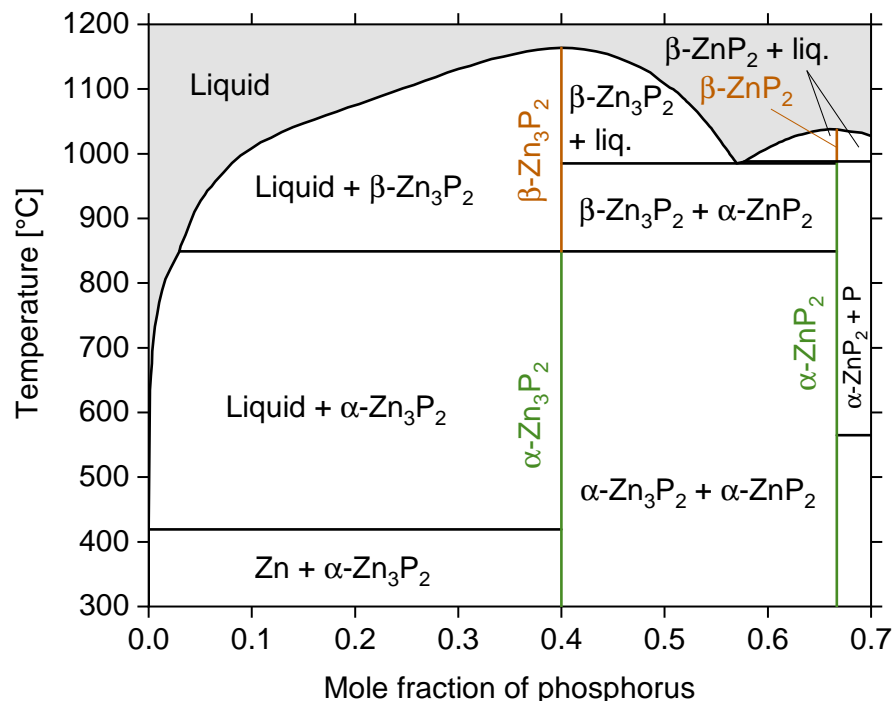


Figure 1.7 – Zinc-rich side of the Zn-P binary phase diagram. Exponential model from reference [70].

The tetragonal phase $\alpha\text{-Zn}_3\text{P}_2$ is the most interesting phase of this system for light absorption in photovoltaics, because it is the only established phase that is both stable below 850 °C and with a bandgap close to the optimum for single-junction photovoltaics. Unless specified

otherwise, all mentions of *zinc phosphide* and Zn_3P_2 , in this work, refer to the α - Zn_3P_2 phase.

Other binary phases besides the four aforementioned phases have been reported in the zinc-phosphorus system. At high pressure, other polymorphs with Zn_3P_2 and ZnP_2 formula units have been observed (#5-7), and also compounds with unusual Zn:P ratios of 1:4 and 7:10 (#8-9) [227–230]. At least some of these compounds synthesized at high pressure (#6-9) do not appear to exhibit a phase transition when brought back to atmospheric pressure. Those phases are likely metastable at standard temperature and pressure, although this has not been reported or verified.

Finally, there are a few reports of odd Zn-P phases. The first is in reference [228], where the authors report the synthesis of a previously-unreported phase (#10) during the *decompression* of a high-pressure Zn_3P_2 orthorhombic phase. This metastable phase transforms into stable phases when stored for less than a month in standard conditions. The second one is in reference [227], where the authors claim that the tetragonal α - Zn_3P_2 transforms into an orthorhombic phase (#11) when cooled below room temperature. This unexpected claim has unfortunately not been supported by providing the measured X-ray diffraction spectra. The third and fourth odd reports are the claims that Zn_3P_2 can be found in the same body-centered cubic anti-bixbyite phase as Zn_3N_2 (#12) [231] or in a cubic $\text{Pn}\bar{3}m$ phase with 10 ordered atoms in the unit cell (#13) [94]. No experimental result support these claims. Finally, computations predict that 2D crystals of Zn_3P_2 may be stable (#14) [232].

#	Phase	Symmetry	Space gr.	Zn:P	Press. & Temp.	Refs
1	α Zn_3P_2	tetragonal	$\text{P4}_2/\text{nmc}$	3:2	Std	[233]
2	β Zn_3P_2	cubic (FCC)	$\text{Fm}\bar{3}\text{m}$	3:2	High T	[234] ([235])
3	α ZnP_2	tetragonal	P4_12_12	1:2	Std	[236]
4	β ZnP_2	monoclinic	$\text{P2}_1/\text{c}$	1:2	High T	[236]
5	Zn_3P_2	orthorhombic	Pmmn	3:2	High P	[227, 228]
6	γ ZnP_2	(pseudo?-)cubic	?	1:2	High P	[229]
7	ZnP_2	orthorhombic	P2_12_12	1:2	High P	[230]
8	ZnP_4	tetragonal	P4_12_12	1:4	High P ⁽²⁾	[230]
9	Zn_7P_{10}	orthorhombic	Fdd2	7:10	High P ⁽²⁾	[230]
10	Zn_3P_2	cubic (SC)	P4_232	3:2	Std (metast.)	[228]
11	Zn_3P_2	orthorhombic	?	3:2	Low T	[227]
12	Zn_3P_2	cubic (BCC)	$\text{Ia}\bar{3}$	3:2	Std (comput.) ⁽¹⁾	[231]
13	Zn_3P_2	cubic (SC)	$\text{Pn}\bar{3}\text{m}$	3:2	Std (comput.)	[94]
14	Zn_3P_2	2D	$\text{P}\bar{3}\text{m}1$	3:2	? (comput.)	[232]

Table 1.11 – Reported binary phases in the zinc-phosphorus system. Phases 1 to 4 are all the experimentally-observed and commonly-accepted phases that are stable at standard pressure, phases 5 to 9 are experimentally-observed phases that are stable at high pressure and phases 10 to 14 are other phases. *Std*: stable at standard pressure and temperature, *High T*: stable at standard pressure and higher than standard temperature, *High P*: stable at higher than standard pressure. *Low T*: detected at standard pressure and lower than standard temperature. (1): Pressure and temperature conditions not clearly specified, assumed to be standard. (2): created at high pressure, studied at standard pressure, decomposed when heated above about 670 K. Phases #6 and #7, reported in different works, could be one and the same.

Phases related to $\alpha\text{-Zn}_3\text{P}_2$

Binary compounds in the Cd-P, Cd-As and Zn-As systems have many similarities to those in the Zn-P system. This is due to the close chemical similarities of cadmium and zinc and of arsenic and phosphorus. For example, $\alpha''\text{-Cd}_3\text{As}_2$ is isostructural to $\alpha\text{-Zn}_3\text{P}_2$. In fact, $\alpha\text{-Zn}_3\text{P}_2$ has the name α for historical reasons, but it is isostructural to $\alpha''\text{-Cd}_3\text{As}_2$, so $\alpha''\text{-Zn}_3\text{P}_2$ can be considered as an alternative designation for $\alpha\text{-Zn}_3\text{P}_2$.

Incidentally, there is full miscibility of the $\alpha''\text{-(Cd}_x\text{Zn}_{1-x})_3(\text{As}_y\text{P}_{1-y})_2$ compounds over the full compositional range between $\sim 750^\circ\text{C}$ and $\sim 910^\circ\text{C}$, according to reference [76]. The temperature range may be approximate, because the phase transition temperatures are sometimes inaccurate, but very good miscibility of the compounds is still a fact.

Nonetheless, at most of the temperatures below the $\alpha'' \rightleftharpoons \beta$ transitions, the $\alpha''\text{-(Cd}_x\text{Zn}_{1-x})_3(\text{As}_y\text{P}_{1-y})_2$ phase is the most stable phase over almost all the compositional range. Pure Zn_3As_2 and Cd_3As_2 are in the α , α' or α'' phases, but transform into solely the α'' phase with a substitution of a few percents of phosphorus or cadmium. Between very approximately

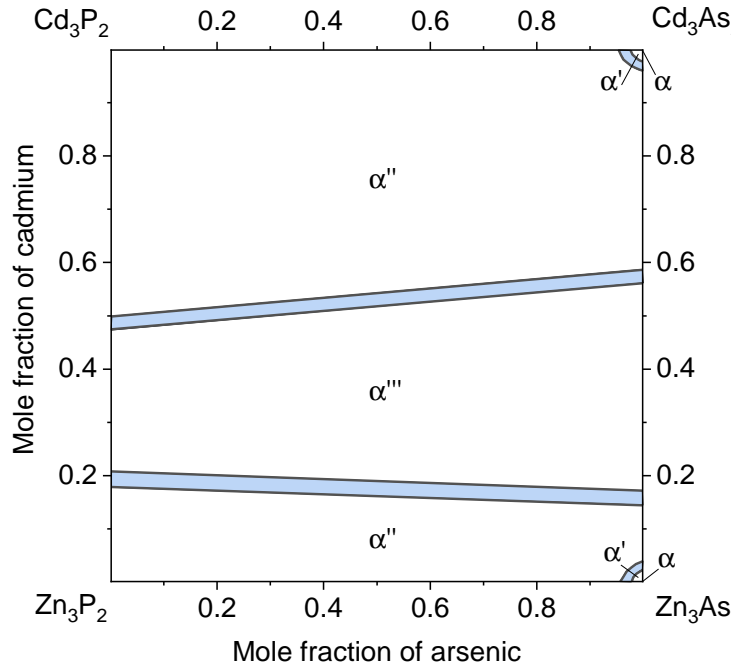


Figure 1.8 – 298 K section of the Zn_3P_2 - Cd_3P_2 - Cd_3As_2 - Zn_3As_2 pseudo-quaternary phase diagram. Shaded areas are two-phase areas. Data from reference [76].

$y = 0.5$ and $y = 0.8$ and below approximately 700°C , another phase, α''' , is the most stable. The phase diagram of the $(\text{Cd}_x\text{Zn}_{1-x})_3(\text{As}_y\text{P}_{1-y})_2$ compounds at 298 K, from reference [76] is shown in figure 1.8.

The good miscibility properties of this material system allow for continuous bandgap and lattice parameter tuning, though not necessarily both independently. This could be used to tune the bandgap for specific applications, for example to optimize double- or higher-number-junction tandem solar cells. The solid-solutions have not been much studied, however, in comparison to the pure binary compounds. For example, according to reference [75], the bandgap of the $\text{Zn}_3(\text{As}_y\text{P}_{1-y})_2$ solid-solution and the position of its absorption edge vary monotonically and continuously between the binary extremes of 1.0 eV and 1.5 eV. The much older and lower-quality measurements of [237] show a non-monotonous change in bandgap, however. The crystallographic and electronic properties of the solid solutions in bulk form were investigated in [237] (with a follow-up in [238]) and the elastic and dielectric permittivity were studied in [239]. Solid-solutions of $\text{Zn}_3(\text{As}_y\text{P}_{1-y})_2$ in the form of nanowires were even grown in reference [75].

Tetragonal phases of the $(\text{Zn}, \text{Cd})_3(\text{P}, \text{As})_2$ system

In all $(\text{Cd}, \text{Zn})_3(\text{As}, \text{P})_2$ phases, the anions form a slightly distorted face-centered cubic sublattice (fig. 1.9a), and the differences between phases arise from the orderings of the cations

in the tetrahedral voids of the sublattice (some of those voids are shown in fig. 1.9b). In the high-temperature β - Zn_3P_2 phase, all the tetrahedral sites are filled equivalently (6 atoms distributed randomly between 8 sites), making the symmetry cubic, but the lower-temperature phases are less disordered, and the specific orderings differentiate the phases and determine their space group/symmetries. The different symmetries will change the volume of the unit cell of the crystal. The unit cell of α - Zn_3P_2 and the α'' phases is four times as big as the "cubic" building block, while the other α phases and the α' phases have unit cells 16 times larger than the cubic building blocks [240]. Displacements of only a few cations can be sufficient to change symmetry entirely [241]. In fact, displacements of as little as one in every twenty metal atoms are required for the $\alpha \rightleftharpoons \alpha'$ and $\alpha' \rightleftharpoons \alpha''$ phase transitions [242, 243].

In Cd_3As_2 and Zn_3As_2 , for example, at least 3 (α , α' and α'') [240, 244] and 2 (α and α') [72, 240] such tetragonal phases with different orderings have been detected, respectively, and four have been observed in the full the $(\text{Cd}, \text{Zn})_3(\text{As}, \text{P})_2$ system (α , α' , α'' and α'''). Zn_3P_2 has only been detected in a single low-temperature, tetragonal, phase.

As evidenced by the two phase transitions occurring when substituting a few percent of the anion or cation of both α - Cd_3As_2 and α - Zn_3As_2 , $\alpha \rightleftharpoons \alpha'$ and $\alpha' \rightleftharpoons \alpha''$ (see fig. 1.8), small lattice distortions can induce cation reordering and thus phase changes. It is therefore not unlikely that phases with different cation orderings than those already known can exist under specific circumstances, in conditions close to standard or even in standard conditions. They may not yet have been observed, due to their similarities to the known phases or them having small ranges of stability. Evidence of such fleeting phases have been observed in Zn_3As_2 . Studying the phase transitions of Zn_3As_2 , Pietraszko and Lukaszewicz [240] hypothesized the existence of an intermediate, thermodynamically unstable phase of Zn_3As_2 . Some other evidence has been discovered by Pangilinan et al. [241, 245]. They discovered that the Raman spectra of micrometer-thick layers of Zn_3As_2 , grown on nearly-lattice-matched substrates InP and GaAs, do not match the symmetry of the known phases. These differences are also discussed in chapter 3. In the work described in that chapter, like in that of Pangilinan et al., the Raman spectrum of Zn_3As_2 does not match a known thermodynamically-stable phase of Zn_3As_2 . It is therefore quite possible that currently unknown tetragonal phases of in the quaternary system may be discovered in the future, including new tetragonal phases of Zn_3P_2 .

The α - Zn_3P_2 (or α'' - Zn_3P_2) phase

The structure of α - Zn_3P_2 can be understood as an ordered stacking of (slightly distorted) zincblende-type (figures 1.9d,e) and anti-fluorite-type cells (fig. 1.9c), as schematized in figure 1.9. Zincblende unit cells in two different orientations are stacked in alternate ways, interleaved with anti-fluorite cells (fig. 1.9f), making the α - Zn_3P_2 structure. α - Zn_3P_2 is primitive tetragonal, and its unit cell is half of such a stack, as indicated by the blue lines in figure 1.9f. The unit cell with all 40 atoms (16 phosphorus and 24 zinc) and bonds is shown in figure 1.9g.

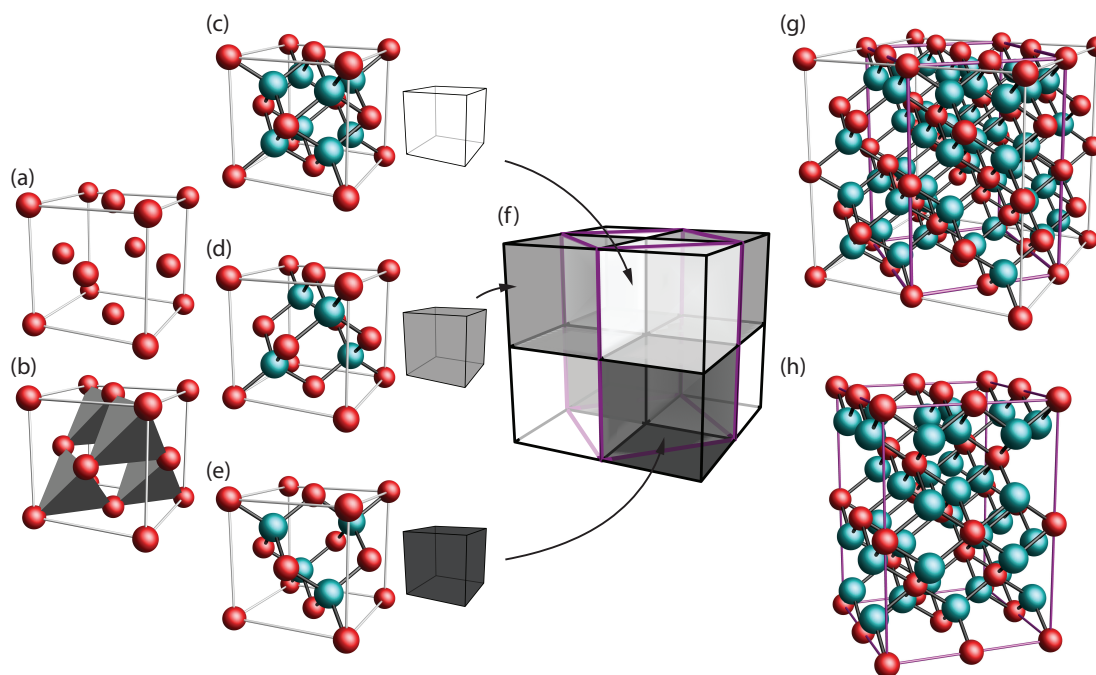


Figure 1.9 – Description of the crystalline structure of α - Zn_3P_2 (and all α'' -($\text{Cd}_x\text{Zn}_{1-x}$) $_3(\text{As}_y\text{P}_{1-y})_2$ compounds) [245, 246]. The unit cubic cells (a-e) have a lattice parameter a' , the stack of cubes (f & g) has an edge length of $2a'$. Disregarding the tetragonal distortion, the lattice parameters of the tetragonal unit cell (h), highlighted in purple, are $c = 2a'$ and $a = \sqrt{2}a'$. See the text for detailed descriptions.

This arrangement makes the crystal structure of the multiple α phases of Zn_3P_2 somewhat intermediate between the (anti-)fluorite structure and the zincblende structure, nearly ubiquitous in III-V semiconductors. 75% of the tetrahedral voids are filled with a cation, as opposed to 100% in (anti-)fluorite and 50% in zincblende. In the particular case of α - Zn_3P_2 , the unoccupied tetrahedral sites are aligned in lines along [100] and [010] directions (or diagonally across a face of the cubic building blocks), alternating between the two directions along [001]. The tetragonal nature of the lattice has two causes. It is due in part to the slight distortion of the nearly cubic building blocks, and in part to their ordering.

As stated earlier, the anion sublattice of the $(\text{Cd},\text{Zn})_3(\text{As},\text{P})_2$ compounds is face-centered cubic, barring the slight distortion. This is a necessary condition for semiconducting properties. However, unlike in more conventional III-V compounds, not all atoms are tetrahedrally coordinated. Only the cations are. The anions are bonded to six cations, located at the corners of a distorted cube centered around the anion. The structure, more filled with metal atoms than the zincblende structure, will have an enhanced metallic bonding character. The bonding type is thus a complex mixture of covalent, ionic and metallic-type bonding [247]. The bonds are slightly electron-deficient, compared to bonds in zincblende, and exhibit a variety of lengths. They range from 2.3320 Å to 2.7676 Å [248], for lattice parameters $a = 8.0785$ Å and

$c = 11.3966 \text{ \AA}$ [249].

In some regards, zinc phosphide behaves like a cubic material, and is thus sometimes considered a pseudo-cubic material. As shown in figure 1.9, barring the tetragonal distortion and the non-ideal positions of the atoms exhibited by the wide range of bonds, the lattice can be considered as being cubic. As can be understood by looking at the blue tetragonal cut in fig. 1.9f, the lattice parameters ratio of Zn_3P_2 should be exactly $\frac{c}{a} = \sqrt{2} \approx 1.4142$, if there was no tetragonal distortion. However, this ratio has been experimentally measured as being 1.4102 [235], 1.4107 [249], 1.4108 [227], 1.4119 [228] and 1.4141 [233], or no less than 99.7% of $\sqrt{2}$. In certain situations, the crystal behaves like an isotropic cubic crystal, while in others, like a uniaxial tetragonal crystal. In the following discussion, crystallographic planes and directions in the tetragonal point of view are labeled with an index t , and they are labeled with an index pc when considering the pseudo-cubic geometry.

Zinc phosphide generally behaves as a pseudo-cubic material during growth. The structural differences of crystallographic planes that are equivalent in the pseudo-cubic view, but different in the tetragonal view, are very small, and the surface energy differences of these planes is very small. Such behavior is for example displayed in zinc phosphide heterotwin nanowires. These nanowires grow along an axis perpendicular to a $\{101\}_t$ plane, with a three-fold rotational symmetry [250]. Tetragonal unit cells do not have any three-fold symmetry axis, but cubes do. This means that the nanowires only appear to have three-fold symmetry. In reality, the side facets, which appear to be equivalent crystalline planes, are not totally equivalent in the tetragonal lattice. The three-fold symmetry can be understood when considering the lattice in the pseudo-cubic view. The $(101)_t$ plane perpendicular to the nanowire axis is equivalent to one of the $\{111\}_{pc}$ planes, making a $[111]_{pc}$ direction the nanowire axis. These planes (almost) have the three-fold rotational symmetry observed in the nanowire. In III-V semiconductors, nanowire growth is easiest, and thus most commonly observed, along a $\langle 111 \rangle$ direction [65, 251]. The tetragonal phase also behaves in an isotropic way in regards of its distortion under high isotropic pressures. Its compressivities along the $[100]$ and $[001]$ directions are similar, with no major anisotropic compression behaviors [228].

The true uniaxial, tetragonal, symmetry of the crystal is revealed in other properties of the crystal. For example, the crystal is birefringent and dichroic, two properties of anisotropic crystals. Its Raman spectrum, the topic of chapter 4, has unmistakable tetragonal D_{4h} symmetry.

The "inconveniences" of the $\alpha\text{-Zn}_3\text{P}_2$ crystal lattice

Zinc phosphide has a relatively large primitive unit cell, compared to the common III-V zincblende structures and those discussed in section 1.2.4. This does not in itself constitute an issue for growth and interface mismatch, because a large cell could be perfectly matched to a substrate with a smaller unit cell if their crystalline plane separations have simple rational ratios in some orientations. When determining the lattice mismatch between zinc-phosphide-

type and zincblende materials, it is important to use the size of the 10-atom defective anti-fluorite pseudo-cubic cell of the tetragonal material, its reduced unit cell. Comparing the lattice parameter of this cell, the reduced lattice parameter, with the lattice parameter of zincblende materials is more or less equivalent to comparing their bond lengths.

As discussed above and illustrated in figure 1.9, the lattice parameter a' of this reduced cell is approximately equal to $\frac{1}{2}c \approx \frac{\sqrt{2}}{2}a$. This definition gives $a' = 5.693 \text{ \AA}$ to 5.725 \AA , depending on the source [227, 228, 233, 235, 249]. Using this definition, zinc phosphide has an average lattice parameter, compared to III-V and II-VI semiconductors. Its properties place it well in the cluster of materials in figure 1.10, between GaAs and InP, with which it has lattice mismatches of 0.8% to 1.3% and -2.4% to -2.9%, respectively. Here, the lattice mismatch is calculated as follows

$$\frac{a'_{\text{Zn}_3\text{P}_2} - a_{\text{sub}}}{a_{\text{sub}}} \quad (1.1)$$

where $a'_{\text{Zn}_3\text{P}_2}$ is the lattice parameter of the reduced cell of Zn_3P_2 , and a_{sub} is the lattice parameter of the substrate. The exact mismatch values depend on the specific lattice dimensions of Zn_3P_2 taken from the different references, and whether a' is defined using the a or c lattice parameter. Positive (negative) values of mismatch indicate that Zn_3P_2 would be in compression (traction). The shaded grey area in figure 1.10 highlights the compounds with which Zn_3P_2 would have a lattice mismatch smaller or equal to 1%.

A perfectly matched substrate could therefore be produced for zinc phosphide, if really required. $\text{Al}_x\text{In}_{1-x}\text{P}$ with $x \approx 0.4 - 0.5$ would likely be lattice-matched to Zn_3P_2 . So may the metastable $\text{Ga}_x\text{In}_{1-x}\text{P}$, forming a miscibility gap. Zn_3P_2 growth on these two substrate would probably not induce the formation of a layer with a different composition at the interface, like it does for growth on GaAs [252], but the two proposed substrate still contain an earth-scarce element. $\text{Zn}_x\text{Cd}_{1-x}\text{S}$ may also form lattice-matched material to Zn_3P_2 .

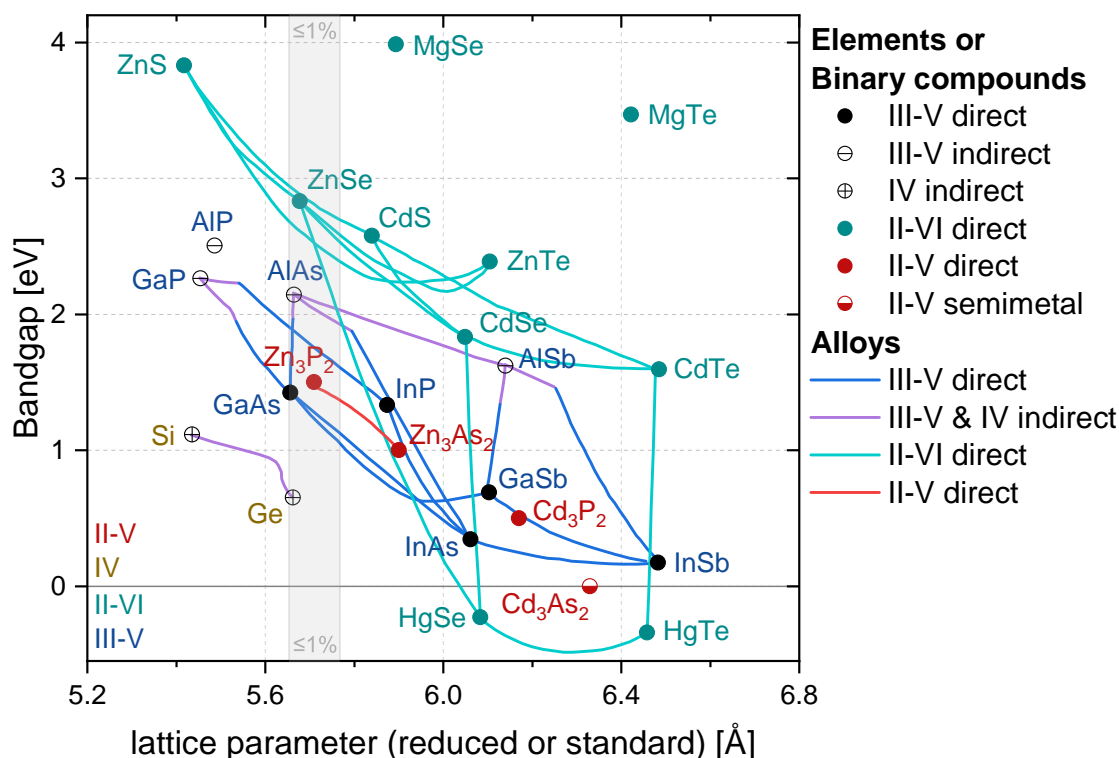


Figure 1.10 – Room temperature lattice parameter and bandgap of various semiconductors. The grey shaded area highlights the materials with which Zn_3P_2 has a lattice mismatch smaller or equal to 1%. Data for III-V, II-VI and IV-IV materials from references [253] and [254].

Zinc phosphide is also said to have a relatively large coefficient of thermal expansion. The linear coefficient of thermal expansion of zinc phosphide reported in the literature varies from $8.33 \times 10^{-6} \text{ K}^{-1}$ to $14 \times 10^{-6} \text{ K}^{-1}$ [227, 243, 255]. To put these values into perspective, let us compare them to the experimental values of the coefficient of thermal expansion (CTE) of 11 tetrahedrally-coordinated zincblende II-VI and III-V compounds gathered in reference [256]. The average CTE⁹ of the 4 II-VI and 7 III-V materials listed is $5.70 \times 10^{-6} \text{ K}^{-1}$, with a standard deviation of $1.33 \times 10^{-6} \text{ K}^{-1}$. Zn_3P_2 does therefore indeed appear to have a relatively large CTE, in comparison to zincblende semiconductors. Without proper handling, this may become an issue. Stress may build up at the interface when the temperature is changed, which can lead to crack formation. There are several ways to minimize interface defects and cracking, such as growing on CTE-matched substrates or at relatively low temperature, to minimize CTE-mismatch strain during cooling. Steel has for example been found to be a substrate with a CTE well-matched to Zn_3P_2 [257], and reports of iron making ohmic [258] and Schottky [259] junctions with Zn_3P_2 have been published. In the Laboratory of Semiconductor Materials, we have tackled the issue of CTE-mismatch in a variety of ways. One way is to grow Zn_3P_2 on one of the best lattice- and CTE-matched substrates with a relatively low temperature deposition process, molecular beam epitaxy [260]. The chosen substrate is InP(100). Growing Zn_3P_2

⁹When two different values are given for the same material, their average is used to calculate the final mean CTE.

solar cells at large scales on InP would defeat the purpose of working with earth-abundant elements, but the development stage of Zn_3P_2 solar is still in its infancy. It is currently still as important to understand the growth mechanism and parameters to synthesize Zn_3P_2 as to explore and find the most suitable earth-abundant materials to use in conjunction with the semiconductor. InP thus serves as a suitable first substrate to study the growth of Zn_3P_2 .

Another way is to grow Zn_3P_2 on a substrate without forming covalent bonds at the interface at all, thus getting completely rid of any impact of the CTE-mismatch. This can be achieved for example by growing on graphene [261]. Another way is to minimize the interface area by growing Zn_3P_2 in the form of nanowires [262]. The nanowire geometry provides a relaxation mechanisms for the interfacial stress, and may prevent the formation of mismatch dislocations. A second way to minimize the defects in a grown film is by minimizing the interfacial area by selective area epitaxy and complete the growth of a film by lateral epitaxial overgrowth, as done in reference [263].

1.3.2 Current state of research

With photovoltaic applications in mind, one of the most important research questions about zinc phosphide is how to achieve the best solar cells using zinc phosphide as an absorber material. Going slightly more in depth, the question can be separated into, on one hand, determining which are some of the most efficient solar cell structures, selecting the materials, their properties and their structural geometries, and on the other hand, how to synthesize them. To answer these questions, one needs to delve into the material science relationships between structure, growth and processing methods, and properties.

Some of the effort into understanding the growth mechanisms and the impact of the growth parameters has been mentioned above. This thesis is dedicated to understanding some functional properties of Zn_3P_2 and the closely related material Zn_3As_2 . The Raman and photoluminescence spectra of Zn_3P_2 are investigated in detail, both as detailed references on high-quality samples for further research and to understand some of the underlying properties of the materials, some of their electronic states and the types and amounts of defects in the crystals. This work will serve to better understand the properties of the highest-quality zinc phosphide and to start understanding the relationships between the parameters of growth and the properties of the created crystals. Better knowledge and understanding of the crystals allows the creation of accurate models of photovoltaic cells and the selection of the most suitable growth conditions for tailoring of properties in the creation of photovoltaic solar cells.

1.4 Outline of the thesis

This thesis is divided into six chapters:

Chapter 1: Introduction, Motivation & Literature review

In the first chapter, the topic of the thesis is introduced and placed into its broader context. Emerging earth-abundant semiconductors for photovoltaics are reviewed, and the properties of zinc phosphide are presented.

Chapter 2: Optical Spectroscopy

The second chapter presents an introduction to the two major optical spectroscopy techniques used in this work, as well as a brief introduction to spectroscopic ellipsometry. In particular, the origin of the Raman selection rules is discussed.

Chapter 3: Nanosails showcasing Zn_3As_2 as an optoelectronic-grade earth abundant semiconductor

This chapter presents the first part of the main results. The electronic and crystalline properties of zinc arsenide nanosails are characterized. The nanostructures are shown to exhibit a metastable crystalline structure and to be degenerate semiconductors.

Chapter 4: Raman spectroscopy and lattice dynamics calculations of tetragonally-structured single crystal zinc phosphide (Zn_3P_2) nanowires

The fourth chapter continues the presentations of the results. The Raman spectrum of zinc phosphide is described in full, using polarized Raman spectroscopy and density functional theory calculations.

Chapter 5: Showcasing the optical properties of monocrystalline zinc phosphide thin films as an earth-abundant photovoltaic absorber

This chapter contains the last part of the results. The photoluminescence spectrum of monocrystalline zinc phosphide is studied. We show emission attributable to a defect band and a doublet resulting from the peak crystal field splitting.

Chapter 6: Conclusion & Outlook

In the last chapter we conclude the work and discuss an outlook for the future of research in this topic.

2 Optical Spectroscopy

Historically, spectroscopy is the study of absorption and emission of the electromagnetic spectrum by matter. Nowadays, spectroscopy also includes the study of interactions between particles other than photons, such as electrons and neutrons, as a function of their energy. In this chapter, I will introduce two spectroscopy techniques central to the work performed during my doctoral studies, Raman spectroscopy and photoluminescence (PL) spectroscopy, as well as briefly introduce spectroscopic ellipsometry.

2.1 Raman spectroscopy

Raman spectroscopy is a technique used in studying materials by using the Raman scattering process, also called the *Raman effect*. This is an inelastic scattering effect in which photons lose or gain energy by creating or destroying various quasi-particles in a material. It was first reported in 1928 by C. V. Raman and K. S. Krishnan, who studied the phenomenon in liquids and gases [264]. The first report of the effect in crystals, specifically on quartz and calcite, occurred shortly after, during the same year, by G. Landsberg and L. Mandelstam [265]. In this section, I will describe the Raman scattering process using classical physics and explain the origin of its spectroscopic selection rules using the mathematical group theory and a partial quantum mechanical description of scattering. I will then discuss Raman spectrometers, and in particular the one used for this work. Finally, I will describe some uses of this technique in the field of earth-abundant photovoltaics.

2.1.1 The Raman scattering process

The Raman effect is an inelastic scattering process during which photons propagating within a material exchange energy (hence inelastic) and momentum with intrinsic excitations of the medium through the annihilation or creation of one or more (quasi-)particles. In this work, the created/annihilated quasi-particles are phonons, vibrational excitations of the crystal lattice, but they could also be magnetic (magnons, and magnetic excitons [266]), plasmonic

(coupled phonon-plasmons [267]), excitonic (coupled phonon-excitons [268]), polaritonic (phonon polaritons [269, 270]), etc.

Classical description

Raman scattering can be described using classical physics. Chapter 3 of *Raman spectroscopy*, by D. A. Long [271], contains a detailed description of this development. Here, I elucidate it by showing only what I consider necessary to understand the phenomenon, in a manner not dissimilar to Long. One of the main differences is that I use here relations and properties of crystals, namely by using the electrical susceptibility χ to relate the polarization with the electric field, as opposed to Long, who uses the polarizability α to describe molecular systems.

In solids, the *polarization density* describes the local volume density of electric dipoles, $\frac{dp}{dV}$. Some materials can exhibit a permanent polarization, and it will in general depend on the material chosen. All materials will also exhibit an additional component to the polarization, induced by local electric fields such as the electric field of an electromagnetic wave traveling through the medium. This *induced polarization*, \mathbf{P} , is related to the local electric field \mathbf{E} through the following equation:

$$\mathbf{P} = \bar{\chi}\epsilon_0\mathbf{E}, \quad (2.1)$$

where $\bar{\chi}$ is the electric susceptibility tensor, a property of the crystal, and ϵ_0 the vacuum permittivity. This relation can be expanded into a Taylor series:

$$\mathbf{P} = \epsilon_0\overline{\chi^{(1)}}\mathbf{E} + O(E^2). \quad (2.2)$$

Here, the tensor $\overline{\chi^{(1)}}$, hereafter described by dropping the exponent, is the linear electric susceptibility, and the higher-order terms in $O(E^2)$ contain nonlinear susceptibilities, such as $\overline{\chi^{(2)}}$, which become important for nonlinear optical applications [272], but which will not be relevant for this work and will therefore be neglected. Under this assumption, the relation can be rewritten as such:

$$P_i = \epsilon_0 \sum_j \chi_{ij} E_j. \quad (2.3)$$

where P_i and E_j are components of the \mathbf{P} and \mathbf{E} vectors, respectively, χ_{ij} is an element of the $\bar{\chi}$ tensor and the summation is done over the components along the three directions of space. This equation is valid for any configuration of a crystal, but the electric susceptibility depends on the positions of atoms in the lattice, and will therefore be modulated by lattice vibrations around its value at the equilibrium lattice position. The effect of the vibrations can

be described by expanding around the equilibrium lattice position:

$$\chi_{ij} = (\chi_{ij})_0 + \sum_k \left(\frac{\partial \chi_{ij}}{\partial Q_k} \right)_0 Q_k + \frac{1}{2} \sum_{k,l} \left(\frac{\partial^2 \chi_{ij}}{\partial Q_k \partial Q_l} \right)_0 Q_k Q_l + \dots \quad (2.4)$$

where Q_k is the k^{th} normal coordinate of vibration and is associated with vibration frequency ω_k . $(\chi_{ij})_0$ is the susceptibility of the lattice at the equilibrium position and the subscript 0 on the derivatives indicates that the derivative is taken at the equilibrium position of the lattice. The coordinates of vibration represent displacements along the normal modes of vibration and represent different ways the structure can be displaced from the equilibrium position. The quantized quasi-particles of the normal modes (which only formally appear when considering a quantum-mechanical description of the material), and thus of the lattice vibrations, are called phonons [273]. The specific values of the Q_k displacements changes with time as the lattice vibrates. Assuming harmonic motion, the displacement caused by a single phonon with circular frequency ω_k can be described as:

$$Q_k = Q_{k0} \cdot \cos(\omega_k t + \delta_k) \quad (2.5)$$

where Q_{k0} is the amplitude of the oscillation, and δ_k its phase, which will be set to zero as it is not relevant in our discussion. Substituting equation 2.5 into equation 2.4 and neglecting the second- and higher-order terms yields:

$$\chi_{ij} = (\chi_{ij})_0 + \sum_k \left(\frac{\partial \chi_{ij}}{\partial Q_k} \right)_0 Q_{k0} \cdot \cos(\omega_k t). \quad (2.6)$$

To simplify the problem, let us only consider that a single normal mode k is relevant. This assumption does not remove any validity to the calculations; the additional modes simply add other similar terms. Then

$$\chi_{ij} = (\chi_{ij})_0 + \left(\frac{\partial \chi_{ij}}{\partial Q} \right)_0 Q_0 \cdot \cos(\omega_k t). \quad (2.7)$$

Substituting 2.7 into 2.3, we obtain

$$P_i = \epsilon_0 \sum_j \left((\chi_{ij})_0 + \left(\frac{\partial \chi_{ij}}{\partial Q} \right)_0 Q_0 \cdot \cos(\omega_k t) \right) E_j. \quad (2.8)$$

Furthermore, let us consider an isotropic material, meaning that $\chi_{ij} = \chi_c$ if $i = j$ and $\chi_{ij} = 0$ if

$i \neq j$:

$$P_i = \epsilon_0 \left((\chi_c)_0 + \left(\frac{\partial \chi_c}{\partial Q} \right)_0 Q_0 \cdot \cos(\omega_k t) \right) E_i. \quad (2.9)$$

Then, substituting E_i with the time-dependent form of the electromagnetic wave $E_i = E_{i0} \cdot \cos(\omega t)$ (setting the phase to zero) and expanding:

$$\begin{aligned} P_i &= \epsilon_0 \cdot (\chi_c)_0 \cdot E_{i0} \cdot \cos(\omega t) \\ &+ \epsilon_0 \left(\frac{\partial \chi_c}{\partial Q} \right)_0 Q_0 \cdot E_{i0} \cdot \cos(\omega_k t) \cdot \cos(\omega t) \end{aligned} \quad (2.10)$$

Finally, simplifying the second right-hand-side term using the trigonometric identity $2 \cos(\theta) \cos(\phi) = \cos(\theta - \phi) + \cos(\theta + \phi)$, one obtains the sought after time-dependence expression of the induced polarization:

$$\begin{aligned} P_i &= \epsilon_0 \cdot (\chi_c)_0 \cdot E_{i0} \cdot \cos(\omega t) \\ &+ \epsilon_0 \frac{1}{2} \left(\frac{\partial \chi_c}{\partial Q} \right)_0 Q_0 \cdot E_{i0} \cdot \cos((\omega - \omega_k) t) \\ &+ \epsilon_0 \frac{1}{2} \left(\frac{\partial \chi_c}{\partial Q} \right)_0 Q_0 \cdot E_{i0} \cdot \cos((\omega + \omega_k) t). \end{aligned} \quad (2.11)$$

The time-varying polarization described in this equation will cause light to be radiated from local dipoles in the material at the frequencies of the oscillation. The first term on the right hand side of equation 2.11 is the Rayleigh term [274, 275]. The radiation emitted from that component will have the same frequency as the incident radiation (ω) and corresponds to an elastic scattering mechanism, changing the polarization and propagation direction of light but not its frequency, or energy.

The two other terms on the right hand side of equation 2.11 correspond to oscillations with frequencies different from that of the incident radiation, and are both Raman terms. The first component has a frequency shifted down from ω by ω_k , the frequency of the oscillating normal mode, or phonon. This component is called the Stokes Raman term. The last component, with a frequency shifted up from ω by ω_k , is the anti-Stokes Raman term.

The Rayleigh term oscillates with an amplitude of $\epsilon_0 \cdot (\chi_c)_0 \cdot E_{i0}$, while the two Raman terms have an amplitude of $\epsilon_0 \frac{1}{2} \left(\frac{\partial \chi_c}{\partial Q} \right)_0 Q_0 \cdot E_{i0}$. While the specific amplitude of the different terms depend on many factors and will be different from every material, the intensity of Raman scattering will be roughly one thousandth of the intensity of Rayleigh scattering, itself about one thousandth the intensity of the incident radiation [271]. Thus, a typical spectrum in the neighborhood of the incident light wavelength is composed of a very intense Rayleigh emission line at ω , and smaller Raman emission lines on either side of it, equally spaced by ω_k .

The simplification applied to equation 2.6, to consider only a single normal mode, resulted in only one component in each of the Stokes and anti-Stokes terms. Usually, there are more than one phonon/normal mode, and the Raman/Rayleigh spectrum will consist of several peaks, shifted $\pm\omega_i$, $\pm\omega_j$, $\pm\omega_k$, etc. from the unique Rayleigh line. Usually, when displaying a Raman spectrum, we do not plot the light intensity versus its wavelength. Instead, the difference in the radiation energy with respect to the Rayleigh peak energy is displayed (usually in units of cm^{-1}), where Stokes Raman shifts are positive and anti-Stokes Raman shifts negative. This highlights the symmetry of the spectrum around the Rayleigh peak and provides a quick read of the energy of the quasi-particles involved in the scattering event.

Raman spectra are central to the work performed in this thesis. In particular, the Raman spectrum of $\alpha''\text{-Zn}_3\text{As}_2$ is discussed in chapter 3 and shown in figure 3.2 on page 73, while the Raman spectrum of $\alpha\text{-Zn}_3\text{P}_2$ is discussed in chapter 4 and shown in figure 4.4 on page 88. In most of the scientific literature, only the Stokes side of the Raman spectra will be shown, if not also captured in the spectrometer. This is due to the Stokes side containing most of the information contained in the full Stokes/anti-Stokes spectrum, while being more intense than the anti-Stokes side. The Rayleigh peak is also often not included in the spectra, since it usually overshadows the Raman peaks only seldom contains relevant information.

As shown by equation 2.11, Raman scattering only occurs for a given vibration (phonon) if the susceptibility of the lattice changes as a result of the displacements around the equilibrium position caused by that vibration. In the situation described in this section, this means $\left(\frac{\partial\chi_c}{\partial Q}\right)_0 \neq 0$. In general, if all $\left(\frac{\partial\chi_{ij}}{\partial Q_k}\right)_0$ for a given k are zero, the phonon will not be allowed to contribute to Raman scattering. In such a case, the phonon is called *Raman inactive*. In cases where $\left(\frac{\partial\chi_{ij}}{\partial Q_k}\right)_0 \neq 0$ for at least one $i j$ index, the mode is called *Raman active*.

Furthermore, in some measurement geometries, a Raman active phonon can still be absent from the spectrum. This can occur if in the current measurement geometry is chosen such that only $\left(\frac{\partial\chi_{ij}}{\partial Q_k}\right)_0 = 0$ components come into play for the calculation of the polarization. In such a case, the transition is called *forbidden*, otherwise it is *allowed*.

The rules describing under which conditions some modes are forbidden and some are allowed are called the *selection rules* of the scattering process. Similar considerations provide indications about how the intensity of a given mode will change when the measurement geometry is changed. These rules, central to the work presented in chapter 4, only strictly arise when considering a quantum-mechanical description of the scattering process. The next section will introduce such a description, and introduce more formally the selection rules using aspects of the mathematical group theory.

Partial quantum mechanical description and selection rules

As shown in the previous section, Raman emission can be understood using only classical physics as a low-frequency modulation to the vibration of light-induced dipoles in materials.

Phonons, briefly introduced in the previous section, are not issued from classical physics. Their inclusion in the explanation served to highlight the relationship between classical lattice vibrations and the quantized vibrations, but was not necessary for the development. A more in-depth understanding of the scattering process can be acquired by incorporating quantum mechanics in the description. The following development follows in broad lines from chapter 4 of Long's detailed *Raman spectroscopy* [271], but aims at only bringing the physics and group theory knowledge necessary to understand the selection rules of the Raman spectroscopy scattering process.

Transitions between energy levels of the system take place if the transition moment \mathbf{P}_{fi} , related to the initial (i) and final (f) states of the system, is non-zero.

$$\mathbf{P}_{fi} = \langle \Psi_f | \mathbf{P} | \Psi_i \rangle \quad (2.12)$$

where Ψ is the state wavefunction, either of the final or the initial state. \mathbf{P} is the dipole moment operator, which depends on the process being described. For light scattering, \mathbf{P} is the *induced* dipole moment operator, and for absorption processes, it is the *permanent* dipole moment operator. Similarly to equation 2.2 for the classical description, the linear term of the induced dipole moment is

$$\mathbf{P}_0 = \epsilon_0 \bar{\chi} \mathbf{E} \quad (2.13)$$

The $\bar{\chi}$ tensor will simply be described as χ in the remainder of the text.

The amplitude of the transition moment associated with a transition from initial state i to final state f is

$$[\mathbf{P}_0]_{fi} = \epsilon_0 \cdot \langle \psi_f | \chi | \psi_i \rangle \cdot \mathbf{E} \quad (2.14)$$

where ψ_i and ψ_f are the initial and final stationary states, respectively. In the above equation, it is assumed for simplification that the electric field is uniform over the scattering volume. This assumption is not necessary a good one for absorbing crystals, but the electric quadrupole and magnetic dipole contributions that are neglected when using this assumption do not play a major role in this development [271]. Implicit in equation 2.14, where $[\mathbf{P}_0]_{fi}$ and \mathbf{E} are vectors and χ is a tensor, are the following equations:

$$\begin{aligned} [P_{x_0}]_{fi} \cdot (\epsilon_0)^{-1} &= [\chi_{xx}]_{fi} E_{x_0} + [\chi_{xy}]_{fi} E_{y_0} + [\chi_{xz}]_{fi} E_{z_0} \\ [P_{y_0}]_{fi} \cdot (\epsilon_0)^{-1} &= [\chi_{yx}]_{fi} E_{x_0} + [\chi_{yy}]_{fi} E_{y_0} + [\chi_{yz}]_{fi} E_{z_0} \\ [P_{z_0}]_{fi} \cdot (\epsilon_0)^{-1} &= [\chi_{zx}]_{fi} E_{x_0} + [\chi_{zy}]_{fi} E_{y_0} + [\chi_{zz}]_{fi} E_{z_0} \end{aligned} \quad (2.15)$$

where $[\chi_{yx}]_{fi} = \langle \psi_f | \chi_{yx} | \psi_i \rangle$ (and similarly for the others) are the matrix elements of the susceptibility tensor component χ_{yx} for the transition i to f. For a transition to be allowed, at least one of the matrix elements needs to be nonzero.

For a vibrational transition, at the end of which a single quantum of vibration (a phonon) in

the normal vibrational mode k is created, the matrix elements are of the form:

$$[\chi_{xy}]_{fi} = \langle \phi_f(Q_k) | \chi_{xy} | \phi_i(Q_k) \rangle \quad (2.16)$$

where $\phi_i(Q_k)$ and $\phi_f(Q_k)$ are the harmonic oscillator wavefunctions associated with the initial and final states of the normal coordinate Q_k , respectively. They can be for example the ground state with no quantum of vibration and the first excited state with a single quantum of vibration. The analysis of equation 2.16 contains the basic elements to understand the selection rules of the scattering process. If all of the matrix elements are zero, the transition is forbidden. It is possible to evaluate whether the the right-hand-side of 2.16 is zero or non-zero without evaluating it, by considering the symmetry of its constituents. The right-hand-side of equation 2.16 is a shorthand for

$$\iiint_{\mathbb{R}^3} \phi_f^*(Q_k) \cdot \chi_{xy} \cdot \phi_i(Q_k) dV \quad (2.17)$$

where the integration is taken over all space. The symmetry of the functions represented by the three multiplied functions determines whether the integral is zero or finite.

To give a very simple example, let's consider the following real integral, where m and n are real numbers:

$$\int_{-\infty}^{\infty} \sin(mx) \cos(nx) dx$$

The function $\sin(mx)$ is odd, meaning that $f_o(-x) = -f_o(x)$, when the sign of x is changed, the absolute value of the function remains the same, but its sign changes. $\cos(nx)$ is an even function, meaning that $f_e(-x) = f_e(x)$, the value of the function remains the same as the sign of x is flipped. The symmetry of the functions can also be described using the transformations that map the graph of the function onto itself. $\sin(mx)$ remains unchanged under inversion around the origin, and $\cos(nx)$ stays the same under a mirror reflection across the abscissa. Then, consider the following definite integral of the product of an odd and an even function:

$$\begin{aligned} \int_{-\infty}^{\infty} f_o(x) f_e(x) dx &= \int_{-\infty}^0 f_o(x) f_e(x) dx + \int_0^{\infty} f_o(x) f_e(x) dx \\ &= \int_0^{\infty} -f_o(x) f_e(x) dx + \int_0^{\infty} f_o(x) f_e(x) dx \\ &= \int_0^{\infty} f_o(x) f_e(x) - f_o(x) f_e(x) dx \\ &= \int_0^{\infty} 0 dx \\ &= 0 \end{aligned}$$

hence

$$\int_{-\infty}^{\infty} \sin(mx) \cos(nx) dx = 0$$

for all m and n .

Using only considerations of symmetry, we were able to show that the value of these definite integrals is zero. Similar considerations can be done for equation 2.17. The possible types of symmetries (in the same way as functions can be odd, even or neither) of the three functions $\phi_1^*(Q_k)$, χ_{xy} and $\phi_0(Q_k)$ depend on the crystal. The types of symmetries that can be exhibited by the susceptibility tensor elements depend only on the symmetry of the crystalline unit cell, its *point group*, while the symmetry species of the normal coordinates and wavefunctions depend on the crystal under study. The different types of symmetries, or irreducible representations, and the different symmetry operations of an object with D_{4h} symmetry are summarized in the D_{4h} character table shown in table 2.1. α - Zn_3P_2 and α'' - Zn_3As_2 are examples of semiconductors exhibiting the D_{4h} symmetry.

D_{4h}	E	$2C_4$	C_2	$2C'_2$	$2C''_2$	i	$2S_4$	σ_h	$2\sigma_v$	$2\sigma_d$	linear, rotations	quadratic
A_{1g}	1	1	1	1	1	1	1	1	1	1		$x^2 + y^2, z^2$
A_{2g}	1	1	1	-1	-1	1	1	1	-1	-1	R_z	
B_{1g}	1	-1	1	1	-1	1	-1	1	1	-1		$x^2 - y^2$
B_{2g}	1	-1	1	-1	1	1	-1	1	-1	1		xy
E_g	2	0	-2	0	0	2	0	-2	0	0	(R_x, R_y)	(xz, yz)
A_{1u}	1	1	1	1	1	-1	-1	-1	-1	-1		
A_{2u}	1	1	1	-1	-1	-1	-1	-1	1	1	z	
B_{1u}	1	-1	1	1	-1	-1	1	-1	-1	1		
B_{2u}	1	-1	1	-1	1	-1	1	-1	1	-1		
E_u	2	0	-2	0	0	-2	0	2	0	0	(x, y)	

Table 2.1 – D_{4h} point group symmetry character table [276, 277]. The first row contains all symmetry elements of the point group. In order: the identity, four-fold rotation axes around the z -axis, three different kinds of two-fold rotation axes, the central inversion, a four-fold rotation-reflection axis, a horizontal mirror plane, two vertical mirror planes and two dihedral mirror planes. The first column lists the name of the different irreducible representations. The two rightmost columns indicate to which irreducible representation belong some important linear and quadratic functions, as well as the three rotations around the axes.

Without going into a deep course on group theory, the *representations* of a symmetry group are sequences of matrices that have the same multiplication tables as the group. For example, if matrix A is associated with the identity transformation E , and matrix B is associated with the inversion i , then the matrix multiplication AB must give a matrix that is associated to the result of $E \cdot i$, in this case i . A set of such matrices satisfying all the multiplications rules of the group is a representation of the group. Among the infinite number of representations of the finite groups encountered in materials science and crystallography, there is a finite

number of representations that cannot be simplified¹, called the *irreducible representations*. The first column of table 2.1 contains the labels of the 10 irreducible representations of the symmetry group D_{4h} . Irreducible representations with dimension 1 have labels A or B, those with dimension 2, E and those with dimension 3, T. Indices u and g are given to representations that are asymmetric and symmetric with respect to inversion, respectively. The A and B labels are given to irreducible representations that are symmetric and anti-symmetric with respect to the rotation around the principal axis, respectively [278]. The first row of the table contains the 10 classes of symmetry operations of the D_{4h} symmetry group, from the identity E to dihedral reflection σ_d . The square array of integers, forming the major part of the table, contains the *characters* of the irreducible representations for the different classes of symmetry operations. These characters are the traces of the matrices of the irreducible representations. They indicate, among other things, in which way an object is modified (inverted or not) as the symmetry operations of the group are applied on it. The first irreducible representations, A_{1g} , is the fully symmetric irreducible representation, the one where the object remains completely unchanged under all symmetry operations of the crystal.

Coming back to equation 2.17, all the functions $\phi_1^*(Q_k)$, χ_{xy} and $\phi_0(Q_k)$ transform as one of the irreducible representations, and can thus be assigned their labels. Group theory allows us to determine whether or not the integral in 2.17 is zero by looking at which irreducible representations the functions belong. By multiplying the functions in the integral in 2.17, which are described by one irreducible representation each, one creates a new function which can be described with a (generally different and reducible) representation. This new representation could in general be simplified/reduced, and will be composed of some number of each of the irreducible representations. Say for example that the wavefunction of the ground state, $\phi_0(Q_k)$, which transforms according to the fully symmetric irreducible representation A_{1g} is multiplied with an element of the susceptibility matrix with irreducible representation B_{1g} (one of the four possible irreducible representations of phonons involved in Raman scattering in zinc phosphide). Group theory tell us that the resulting function will contain the irreducible representation B_{1g} only:

$$A_{1g} \otimes B_{1g} = B_{1g}$$

In this specific example, the resulting representation only contains the B_{1g} already present among the two original representations, but in general the new representation can be reduced in a variety of irreducible representations.

One of the most important results of group theory regarding spectroscopic selection rules is that the integrals in equations 2.16 and 2.17 will be zero only if the representation obtained by direct product of the irreducible representations of the three functions contains the fully symmetric irreducible representation A_{1g} . This rule is general and does not only apply to transitions starting in the ground state [271, 279]. Very simply, this rule can be understood

¹How this simplification occurs is outside the scope of this description.

as follows: the function in the integral will have different components each transforming according to different irreducible representations. Since the integration is done over all space, the components that are anti-symmetric with respect to at least one symmetry operation will vanish. Only the components which are fully symmetric (thus belonging to the fully symmetric irreducible representation A_{1g}) will be nonzero.

This gives us a very powerful tool to quickly know whether an electronic transition between state i to state f , mediated by an operator is allowed or forbidden, by looking at the irreducible representations of the functions. Making these calculations for Raman scattering between all states, with all phonons in a crystal and in all geometries, one creates the selection rules of Raman scattering. In practice, this process rarely needs to be done, because the rules are similar for a given scattering process and a crystal of a given symmetry. In Raman spectroscopy, these rules are summarized in the so-called Raman tensors. For Zn_3P_2 and other D_{4h} (or $4/mmm$) crystals, they are:

$$\begin{aligned} \mathfrak{R}_{A_{1g}} &= \begin{pmatrix} a & 0 & 0 \\ 0 & a & 0 \\ 0 & 0 & b \end{pmatrix}; \quad \mathfrak{R}_{B_{1g}} = \begin{pmatrix} c & 0 & 0 \\ 0 & -c & 0 \\ 0 & 0 & 0 \end{pmatrix}; \\ \mathfrak{R}_{B_{2g}} &= \begin{pmatrix} 0 & d & 0 \\ d & 0 & 0 \\ 0 & 0 & 0 \end{pmatrix}; \quad \mathfrak{R}_{E_g} = \begin{pmatrix} 0 & 0 & e \\ 0 & 0 & e \\ e & e & 0 \end{pmatrix} \end{aligned} \quad (2.18)$$

These tensors, one for each Raman active irreducible representation, have different nonzero elements for each crystal. In practice, one may use these tensors to quickly obtain information about the selection rules of the crystal. Indeed, the intensity of a Raman transition will be proportional to

$$|\nu_i \cdot \mathfrak{R}_\alpha \cdot \nu_s|^2 \quad (2.19)$$

In this equation, ν_i and ν_s represent unit vectors parallel to the polarization axis of the incident and scattered radiation, respectively, and \mathfrak{R}_α is the Raman tensor of a phonon with irreducible representation α , one of the tensors in 2.18.

The considerations developed in this section are central to the work presented in chapter 4. The Raman active modes of Zn_3P_2 are expressed there in equation 4.1 (p. 84, and the selection rules for a back-scattering measurement carried out perpendicularly to a (010) plane of Zn_3P_2 are listed in table 4.1 (p. 87).

This was a quick and to the point introduction to the selection rules of Raman scattering. For more rigorous definitions of the group theory concept introduced in this chapter and

books on group theory applied to solids and to Raman spectroscopy, the avid reader is pointed towards section 2.3 of Yu and Cardona's *Fundamentals of Semiconductors: A Pedestrian's Guide to Group Theory* [280] or towards a simple and well-written appendix by Piela [279], and also towards Dresselhaus [281], Bradley [282] or Bishop [283].

2.1.2 Raman spectrometry, experimental details

Carrying out high-quality Raman spectroscopy requires two conditions to be met. First, the sample needs to be illuminated by an intense beam of light with a very narrow range of wavelengths, and second, the constituents of the scattered light need be separated. The high intensity is required because Raman scattering is a rare event, when compared to Rayleigh scattering. High incident light intensities are required in order to produce sufficient Raman scattering events to be detected. A small range of wavelengths (bandwidth) is important for two reasons. First, because of the small wavelength shifts involved in Raman scattering, Raman scattering usually involves energy shifts in the $0\text{--}3500\text{ cm}^{-1}$ range, or $0\text{--}434\text{ meV}$ [271], and if the elastically-scattered Rayleigh peak is too broad, it will overlap with the lowest-shift Raman peaks, hiding them because of the large differences in intensity. This phenomenon plays a small role in the work presented in chapter 4, where the measurement of all the Raman peaks of the Zn_3P_2 lattice was sought for comparison with theoretically-predicted peaks. This is illustrated in figure 4.4 (p. 88) and table 4.2 (p. 90), where the positions of the experimentally-observed and theoretically-predicted peaks are compared side-by-side. The peaks with a shift lower or equal to 42 cm^{-1} (approx. 5.2 meV) are not observed, because they are hidden in the edge of the Rayleigh peak (centered at 0 cm^{-1} not shown in figure 4.4). The second reason why a narrow excitation bandwidth is sought is that the width of the Raman peaks will be at least as large as the width of the incident light. Large-bandwidth excitation sources may artificially widen Raman peaks, thus making it more difficult to resolve them. This is not an issue nowadays, as the width of Raman peaks is generally limited by spectrometer broadening and fundamental material-dependent broadening effects.

Historically, the development of Raman scattering was first much slower than that of, for example, infrared (IR) absorption spectroscopy, because of the lack of suitable light sources. The first reports of Raman spectroscopy used "a beam of sunlight" converged with optical elements [264] or mercury arc lamps [265]. Mercury lamps were the only viable sources of monochromatic light, and their few lines, the strongest at 435.83 nm and 253.65 nm , restricted the use of Raman spectroscopy to samples that did not absorb at these wavelengths. The low irradiance of mercury arc lamps (compared to lasers) limited the applications where the weak Raman signal was produced strongly enough to be detectable. This slow development remained until the mid-sixties, when the advent of the gas laser led to substantial advances in the field thanks to its desirable properties as a strong monochromated light source [271].

Description of the Raman optical setup

Nowadays, Raman spectroscopy can be carried out in its simplest form by illuminating a sample with a visible- or near-visible-light narrow-band laser and dispersing the scattered light with a spectrometer. During most of my doctoral studies, I used a fully-modifiable non-commercial triple-spectrometer Raman system, located in one of the rooms of our laboratory, at EPFL. The system was originally designed and installed by Dr. Bernt Ketterer prior to my arrival, and then passed on to Dr. Francesca Amaduzzi, Prof. Esther Alarcón Lladó, Dr. Luca Francaviglia, who trained me for its use, and finally me, for the duration of my thesis. A schematic description of the optical setup is shown in figure 2.1.

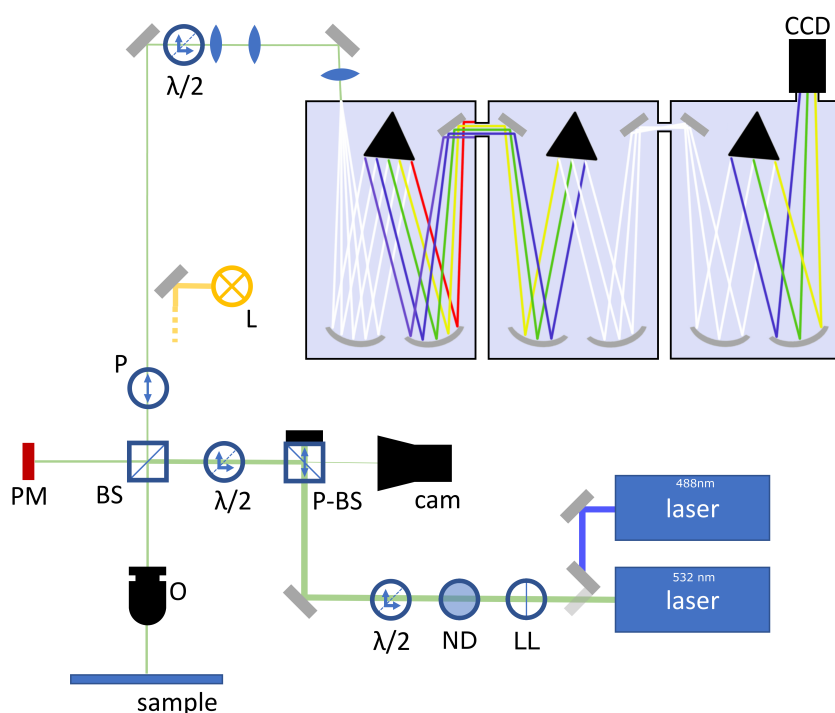


Figure 2.1 – Schematics of the optical table for Raman spectroscopy. *LL* stands for laser line filter, *ND* for neutral density filter, $\lambda/2$ for a half-waveplate, *P-BS* for polarizing beamsplitter, *cam* for camera, *BS* for (non-polarizing) beamsplitter, *PM* for power-meter, *O* for microscope objective, *L* for a white light source, *P* for a linear polarizer and *CCD* for the charge-coupled device, serving as detector. The sample is located at the bottom left. Mirrors are in gray and convergent lenses are dark blue rugby-ball-shaped elements. The light paths inside the spectrometers schematize the effects occurring in the subtractive mode configuration, and only approximate real ray paths. White rays represent undispersed polychromatic light, while colored rays represent dispersed light.

The system is attached to an optical table with screws, for stability, and in a room surrounded by dark curtains to prevent parasitic light to enter the spectrometers from the outside and to protect outside users from the lasers.

The system starts with two continuous-wave lasers (bottom right of the figure), both regularly used throughout my thesis work. Their light is inherently polarized linearly. The gray rectangular elements in fig. 2.1 represent mirrors. A flipping mirror controls which of the 488 nm or 532 nm laser is allowed through into the rest of the setup. Then a laser line filter (LL) ensures that only the main line of the laser continues through the optical path. The next three major elements (ND, $\lambda/2$ and P-BS), control the laser intensity. Neutral density filters (ND) serve to change the laser power by discrete factors, and the half-waveplate ($\lambda/2$) works in conjunction with the polarizing beamsplitter (P-BS) to finely adjust the power. The polarizing beamsplitter only lets through vertically-polarized light (in the frame of reference of the table), and the rotation of the half-waveplate changes the fraction of the beam that is in that state of polarization. After that, the beam passes through another half-waveplate ($\lambda/2$), this time to set the polarization direction of the beam by rotating the fixed polarization of the light exiting the polarizing beamsplitter. At the next (non-polarizing, 50:50) beamsplitter (BS), approximately 50% of the light is sent to a photodiode power sensor/power-meter (PM), to measure the beam intensity, and the remained of the beam is sent to a microscope objective (O), to be focused onto the sample of interest. The geometry of the interaction between the laser and the sample is shown in figure 2.2.

At that point, the laser light interacts with the sample, and many effects occur simultaneously, when possible: Raman/Rayleigh scattering, surface scattering, photoluminescence (discussed in section 2.2), plasmonic excitations, heating/annealing, sample destruction (if the sample cannot handle the high power density), etc. Light is scattered in many directions, diffusively for most processes processes, and the microscope objective collects a small fraction of it, the part that went back up parallel but in the opposite direction as the incident laser beam. This measurement geometry is called the back-scattering geometry.

The light collected by the objective is sent further towards the spectrometers, first passing back through the beamsplitter (BS) and then continuing either towards the photoluminescence spectrometer (described in more details in section 2.3) or towards the Raman triple spectrometers. When fully polarized Raman measurements are done, such as in the work described in chapter 4 for the identification and separation of Raman modes, the light passes through a linear polarizer (P) and another half waveplate, to first select the desired polarization orientation, and then orient the light polarization to be constant and independent of the polarizer orientation at the entrance of the spectrometers [284]. Finally,



Figure 2.2 – Schematics of the spectroscopic measurement geometry. Not to scale.

before entering the first of three spectrometers in series, the beam is collimated with two convergent lenses, and finally focused onto the entrance slit of the spectrometer with a last convergent lens.

As shown on figure 2.1, the optical table is also equipped with a white light source (L), illuminating the sample through the beamsplitter and the objective, and a camera (cam) for imaging the sample surface. These elements are necessary to accurately focus the laser onto a structure of interest on the sample.

Modes of the triple-spectrometer

There are two main ways to use a triple spectrometer for Raman spectroscopy, the additive mode, and the subtractive mode. The subtractive mode is schematized in figure 2.1. In this mode, the first two spectrometers act as a tunable bandpass filter, and the third spectrometer disperses the polychromatic beam that enters it. To act as a bandpass filter, the first spectrometer disperses light as would any spectrometer, which is passed through a wide aperture into the second spectrometer, where the dispersion of the first spectrometer is canceled (subtracted), recombining the beams into a polychromatic beam. A specific range of wavelength is chosen by changing the size of the intermediate slit and rotating the diffraction gratings. In the additive mode, the three spectrometers add their contributions to the dispersion of light, each further dispersing the light that passes through it.

The additive mode has the advantage of having a high resolution (0.22 cm^{-1} per pixel, or $27 \text{ } \mu\text{eV}$ per pixel, in the setup used during the doctoral work), at the expense of being able to detect only a small range of wavelengths. The subtractive mode has a reasonably good resolution (about three times worse than in the additive mode), and a much wider range of observable wavelength. Examples of spectra taken in the subtractive mode are shown in figures 3.2 and 4.4. The main advantage of the subtractive mode of a triple spectrometer over a single spectrometer is the superior stray light rejection, allowing for cleaner spectra.

2.1.3 Raman spectroscopy for research on semiconductors made of earth-abundant elements

Raman spectroscopy has many useful applications for the research field of earth-abundant photovoltaics. One of the main applications is its ability to measure the characteristic spectrum of a material, and thus to identify the presence or absence of specific phases. Such identifications are also commonly done by X-ray diffraction (XRD) and TEM methods, but Raman spectroscopy has the advantage over X-ray techniques as requiring only very small volumes of active material, thus allowing small structures to be studied, or large structures to be mapped in a non-destructive manner.

One earth-abundant material system where Raman spectroscopy has been proved useful is the relatively complex CZTSSe material system. The identification of secondary phases by XRD is

challenging in this system of materials, due to the similarities between the secondary phases such as ZnS and Cu_2SnS_3 and the kesterite [285]. Nonetheless, detailed multi-wavelength characterization of the Raman fingerprints of these earth-abundant kesterites have allowed the modes to be well-understood and characterized [286, 287]. Raman spectroscopy has now regularly been used to check for the presence or absence of secondary phases Cu_2SnS_3 , $\text{Zn}(\text{S}, \text{Se})$, $\text{Cu}_{2-x}(\text{S}, \text{Se})$, $\text{Sn}(\text{S}, \text{Se})$ or ZnO [288–293].

Another important application is the study of defects, as Raman spectroscopy is affected by the specific arrangement of atoms in the lattice. Atomic substitutions, displacements or vacancies will change the phonon dispersion relations, and careful investigation of the differences can teach a lot about the changes caused by defects. This is proving useful in the CZTSSe system again, where disorder has been attributed to the lag in power conversion efficiency as compared with CIGSSe devices [138]. To investigate the Cu/Zn disorder, Cu and Zn occupying equivalent sites, Scragg et al. used near-resonant Raman scattering to investigate the order-disorder transition [294]. Their use of Raman spectroscopy over other techniques such as XRD, neutron diffraction and nuclear magnetic resonance (NMR), is that it can distinguish the Cu and Zn atoms, and it is sensitive enough to measure thin films. In their study, they were able to determine the critical temperature of this second-order phase transition by measuring the intensity ratio of Raman peaks belonging to modes sensitive to the cation ordering. Grading of the bandgap through continuous changes in the [S] to [S]+[Se] ratio of CZTSSe compounds is also thought to be key in maximizing the power conversion efficiencies of such solar cells. Yang et al. used changes in the intensity ratio of peaks associated with the two chalcogens to quantitatively map their ratio along the depth of a film [289]. They benefited here from the higher spatial resolution of Raman as compared to XRD.

2.2 Photoluminescence spectroscopy

Here, I will describe photoluminescence spectroscopy. The *luminescence* part of PL indicates that it is a luminescent process, meaning that it emits light. In PL spectroscopy, the spectrum of the emitted light is measured and interpreted to learn about the emitting material properties.

Light emission occurs when an excited electronic state releases energy by releasing a photon. There are many types of luminescence, depending on the system and the cause of the existence of the excited state. In chemiluminescence, for example, light is emitted by chemical reactions, when a chemical species is produced in an excited state. Living organisms can bioluminesce, as a special form of chemiluminescence. Materials and molecules can also luminesce. In these cases, the reason for the existence of the excited electronic state can be temperature (thermoluminescence), where excited states are generated randomly and follow the Boltzmann distribution, externally incident high-energy electrons (cathodoluminescence) or photons (photoluminescence). Photoluminescence is the emission of light, after absorption.

2.2.1 Photoluminescence of solid semiconductors

In solid semiconductors, the most common way to excite an electron using light is by absorption of a photon to excite an electron from the valence band to the conduction band. Unless the exciting photon has one of a few specific material-dependent energies, the electron will be excited to a state in the conduction band, away from the conduction band minimum (CBM). The system is then brought out of equilibrium, and the light emission occurs as the system goes back towards equilibrium. The electron in the excited state quickly releases some of its energy, until it ends up at the one of the local minima of the conduction band. The electron will then release its excess energy by a variety of competing processes.

The excited electron can also be created by exciting it not from the valence band, but from a defect state [295]. The result is similar, as the electron will also stay at the CBM until it recombines or gets trapped. The differences are that smaller energies are needed to excite the electron, because defect states occupied by electrons are generally closer to the CBM than the valence band states, and also the probability of the event, which needs the existence of an occupied defect state.

Light absorption and photoluminescence are closely related phenomena. The former involves the excitation of an electron by absorption of a photon, and the latter the opposite process. In nanostructures, light coupling effects can affect dramatically the spatial distribution and wavelength-dependence of emission and absorption [296]. The wavelength of the incident light may also play an important role as it may change the penetration depth of the light into a the material, and if the sample is inhomogeneous in depth, the energy of the light may be distributed differently between the phases and change the measured spectra.

At the CBM, the electron will lose energy through a variety of paths, by either emitting a photon, a radiative way whose occurrence can be detected by PL, emitting phonons in different ways, non-radiative pathways which are detected indirectly, or by transferring its energy to free charge carriers, to raise them higher in their bands, a process called Auger recombination [297].

2.2.2 Recombination mechanisms

Radiative recombination comes in five major types [297]. The first is the recombination between a free carrier, in one of the band extrema, and a carrier bound at a defect state (fig. 2.3a). The second one is the transition between nearby acceptor and donor defects, which becomes more relevant as the density of defect increases and the likelihood of two defect being close enough to exchange electrons becomes relevant (fig. 2.3b). The third one is the transition between different levels within a single impurity, generally between an excited state and the ground state (fig. 2.3c). When conditions allow for the existence of excitons, such as at low temperature in semiconductors with few defects, a few other recombination mechanisms involving them can take place [295]: free and bound excitons can recombine and annihilate, releasing energies close to the bandgap energy (fig. 2.3d). Finally, commonly observed in direct

bandgap semiconductors, band-to-band radiative recombinations result in the annihilation of an electron in the conduction band with a hole in the valence band (fig. 2.3e) [298].

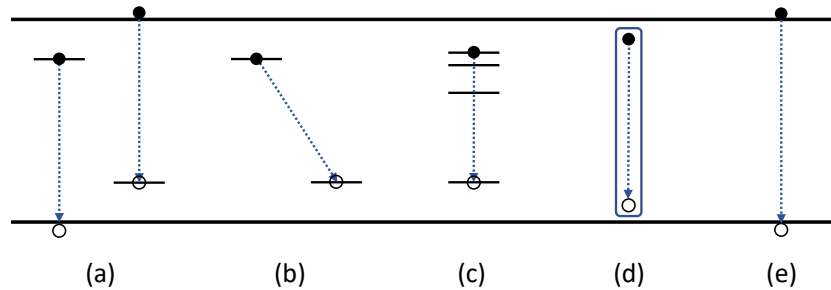


Figure 2.3 – Major radiative recombination mechanisms. (a) recombination between a free and a localized carrier (b) recombinations between an acceptor and a donor, or pair recombination, only possible if the defects are close to each other, (c) recombinations between the levels of a single impurity, (d) recombination of free or bound excitons and (e) band-to-band recombination.

Non-radiative recombinations are not directly measured in PL spectroscopy. Their existence can be observed by the lowering of the material luminescence. The temperature of the sample can also have a large influence on the photoluminescence spectrum. Temperature can change the distribution of carriers in different bands, thermally exciting carriers from shallow defect states into the bands, for examples, which changes the occurrence probability of the recombination pathways.

Because the internal energy release processes depend on the specifics of the illuminated material, its band levels and defect levels, PL spectra contain a wide range of information about the material's electronic structure. The set of PL peak positions, characteristic of the energy differences between energy levels, is a characteristic fingerprint of the material and its quality. Then, the peak widths are closely related to the quality of the material. Disorder, and the bond distortions it creates, locally shifts the positions of the energy bands, broadening the PL peak detected, which is an aggregated measure of that specific transition, now subject to different small perturbations. The last major characteristic of the PL peaks, their intensity, is a measure of the amount of material measured and the efficiency of light outcoupling from nanostructures. As explained above, other processes may change peak intensities, but all characteristics of the material kept equal, larger amounts of it provides a larger number of identical recombination events and thus a more intense luminescence. Changes in the peak characteristics described until here provide information about changes to their original sources. Peak shifts, for example, are generally due band fillings or to shifts in the energy levels, as a result of lattice expansions/contraction due to temperature changes, or stress, isotropic or anisotropic.

Further than that, the polarization of the emitted photons can provide information about the symmetry and orientation of the crystal. Similarly to the transitions involved in Raman

scattering, and described previously in *Partial quantum mechanical description and selection rules*, on pages 49 to 55, each individual radiative recombination event is the result of a transition between two states with specific symmetry, two electronic bands/orbitals with different shapes. Because of the requirement for overlap between the states and particles involved in the process, only photons with a specific polarization allow the transition to occur, and thus are emitted. When a collection of emitters is composed of randomly oriented events, the resulting observed light will be the average of the individual polarizations and may be completely depolarized. This could be the case in gases, for example, where the emitting species are free to move in all directions. In single-crystals, the radiative transitions occur between finite sets of bands with well-defined symmetries. Since the crystal is fixed in space, the polarized emission is not randomly distributed and remains fixed in space as well, and thus emission spectra with well-defined polarizations may be measured. Filtering the emitted light to only allow some polarizations to be detected allows these effects to be measured.

The photoluminescence process is a major characterization technique in the field of optoelectronics. Lasers and light emitting diodes (LEDs) do not typically rely much on photoluminescence in their working principles, but these devices and other optoelectronic devices can be characterized with photoluminescence spectroscopy to study or verify their properties. Lasers rely instead on the emission of light stimulated by other photons, a phenomenon from which they take their name, but also somewhat on spontaneous emission to provide the initial "seed" photons. LEDs emit light by an applied electrical current, and exhibit therefore electroluminescence. These structures are optimized to emit light at specific wavelengths and high intensities.

There are also two closely related techniques to standard photoluminescence spectroscopy. One is time-resolved photoluminescence (TRPL) spectroscopy, where instead of studying the radiative recombinations in steady-state, the sample is excited by pulses of light, leaving time for the carriers to decay completely before re-exciting, to study their dynamics. The lifetime of carriers in the different levels, such as exciton lifetimes, can be measured this way. The other is photoluminescence excitation (PLE), a technique in which the intensity of a given PL peak is measured as the wavelength of the incident excitation radiation is modified. The measured intensity is small for excitations below the bandgap, because few excited electrons are produced in the CBM, but it increases near the bandgap and above as the light is efficiently converted to excited carriers.

2.3 Description of the photoluminescence spectroscopy setup

The photoluminescence setup used during the course of my thesis has a lot of elements in common with the Raman spectroscopy setup described earlier. A schematic of the setup is shown in figure 2.4.

2.3. Description of the photoluminescence spectroscopy setup

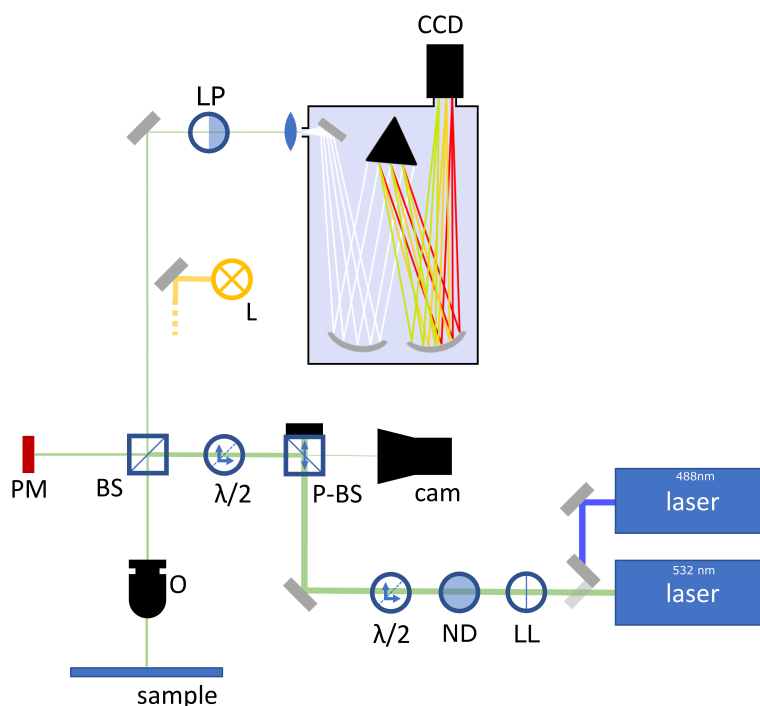


Figure 2.4 – Schematics of the optical table for PL spectroscopy. *LL* stands for laser line filter, *ND* for neutral density filter, $\lambda/2$ for a half-waveplate, *P-BS* for polarizing beamsplitter, *cam* for camera, *BS* for (non-polarizing) beamsplitter, *PM* for power-meter, *O* for microscope objective, *L* for a white light source, *LP* for a longpass filter and *CCD* for the charge-coupled device, serving as detector. The sample is located at the bottom left. Mirrors are in gray and convergent lenses are dark blue rugby-ball-shaped elements. White rays represent undispersed polychromatic light, containing only the PL signal, and colored rays represent dispersed light.

The lower half of figure 2.4 is the same as that of figure 2.1 described above. The description of the optical elements and components of the setup until the light exits the beamsplitter (BS) towards the spectrometer, already done in *Description of the Raman optical setup*, starting on page 56, is here left out. The interested reader is referred to it for details. The differences, starting at the exit of the beamsplitter, are that the beam is filtered through a longpass filter (LP). This is to remove the very intense laser emission, only letting through the longer wavelength (and lower energy) photoluminescence signal. The signal is then dispersed by a diffraction grating and collected on a CCD camera (CCD).

2.3.1 Photoluminescence for research on semiconductors made of earth-abundant elements

Photoluminescence spectroscopy is a commonly used technique in semiconductor research, because it gives information about the purity and crystalline quality of semiconductors and the electronic levels. In many of the studies about novel earth-abundant semiconductors

discussed in chapter 1, a simple PL spectrum is shown as an indicator of crystal quality. Photoluminescence can also be the main investigative tool in the study of the optical properties and quality of earth-abundant solar absorbers.

PL can be used as a tool for investigating the position of energy levels in the bandgap, crucial knowledge to quantify the impact of specific defects on the electronic properties. This has for example been done in the study of earth-abundant CuSbSe_2 . Building up on works modeling the electronic states of defects and determining their activation energies experimentally with electrical conductivity measurements, Penezko and co-authors studied the photoluminescence spectrum of the semiconductor [132]. By combining power-dependent and temperature-dependent steady-state PL measurements, they measured experimentally the activation energies of defect and identified the likely origins of the radiative recombination transitions. Such information can then be used to further identify the exact defect responsible for the emissions and to tune the defect densities to optimize the material properties for specific applications, such as removing deep defect harmful in photovoltaic applications.

In lesser studied material systems, PL can also be used to measure the bandgap value, so critical in PV. For example, Cu_2SnS_3 and Cu_2GeS_3 can be mixed to tune the bandgap from one extreme to the other (0.92 eV to 1.6 eV). It is however necessary to verify this and to determine in which way the bandgap changes, in order to target specific compositions for different applications. Aihara and Tanaka have used temperature-dependent and power-dependent PL to identify the radiative PL transitions of $\text{Cu}_2\text{Sn}_{1-x}\text{Ge}_x\text{S}_3$ and to measure the bandgap variation with x [137].

2.4 Spectroscopic ellipsometry

Here, I will describe spectroscopic ellipsometry, a technique commonly used to study the complex refractive index of thin films.

2.4.1 Introduction

Spectroscopic ellipsometry is a technique used to study the optical constants, also called dielectric function, thicknesses and surface roughnesses of planar thin films. The studied structures are generally thin film stacks on a substrate, assumed to be homogeneous and isotropic [299].

In this technique, light with a known polarization state (linear or elliptic) and wavelength/energy is shone onto the surface of a sample at a given angle. The polarization state of the reflected beam (as the complex reflectance ratio, ρ) is recorded:

$$\rho = \frac{r_p}{r_s} \quad (2.20)$$

where r_p and r_s are the complex Fresnel reflection coefficients of the p and s components of the beam, respectively, the p component being within the plane on incidence formed by the incident and reflected beams, and s being perpendicular to the plane of incidence. Generally, ρ is described by the amplitude ratio Ψ and phase difference Δ , defined as follows:

$$\rho = \frac{r_p}{r_s} = \tan(\Psi) \cdot e^{i\Delta}. \quad (2.21)$$

Ψ and Δ are energy-dependent quantities. In spectroscopic ellipsometry, their values are measured over a range of energies from the infrared to the ultraviolet, depending on the capabilities of the measurement system. On its own, knowledge of the reflectance ratio can only be used to calculate the dielectric function of the sample in specific conditions, for example for very thick (semi-infinite, as far as light is concerned) isotropic substrates with no additional layer, or for a single non-absorbing layer on a known substrate [299]. In all other cases, data analysis relies on models and more complex data analysis methods.

In general, the measured complex reflectance ratio is interpreted by (i) building a model of the analyzed stack of thin film and by (ii) calculating the reflectance ratio in the experimental conditions. Almost always, one or more parameters of the model (such as the layer thickness or dielectric function of one of the layers) are unknown. The model is modified to match the calculated reflectance ratio to the experimentally measured values. The ellipsometric model is composed of a stack of layers of thicknesses and dielectric functions matching those of the physical sample. When the dielectric functions of all the layers are known, tabulated values are used, but when some are not, their dielectric properties are modeled using dispersion laws, such as damped oscillators (Lorentz) or oscillators combined with realistic near band edge densities of states (Tauc-Lorentz) [299].

2.4.2 Working principle

A working spectroscopic ellipsometer needs to be able to characterize the ellipticity of the reflected light at all wavelength and can do so in several configurations. A general schematic of an ellipsometer is shown in figure 2.5.

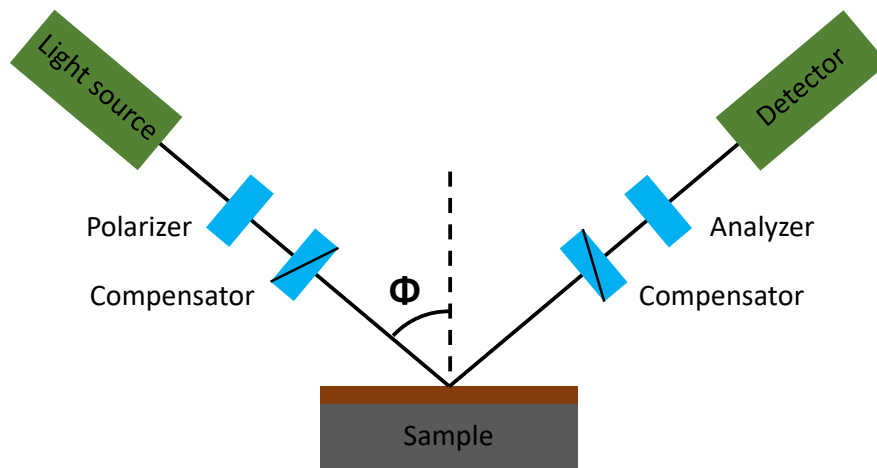


Figure 2.5 – Side view schematics of an ellipsometric system. The p-plane is parallel to the figure, and the s direction is perpendicular to the figure. Usually, the compensator is either before or after the sample, not both simultaneously.

The simplest way to measure the polarization state of the light after reflection on the sample is by rotating a linear polarizer (the analyzer) in front of the detector. For improved accuracy, however, today it is more common to add a waveplate (retarder plate, designated here as a compensator) between the sample and the analyzer or just before the sample, and to rotate it instead of the analyzer. These configurations are called rotating-compensator ellipsometers [300]. In spectroscopic ellipsometer, the light source is a broadband source. Since the interactions with the compensator and the sample are wavelength-dependent, the polarization state of all wavelengths needs to be measured. In these cases, the detector typically includes a dispersion grating and a one- or two-dimensional detector to measure the state of the light with all wavelengths simultaneously [299].

2.4.3 Applications

Spectroscopic ellipsometry is a commonly available characterization tool in laboratories working with thin film, in the semiconductor and microelectronic industries and research laboratories, in big part thanks to it being very sensitive and non-destructive. It is a very useful tool for PV cell engineering and research. spectroscopic ellipsometry (SE) can be used to measure layer thicknesses, optical constants, optical band gaps, film compositions, interface thicknesses, surface roughness thicknesses and crystallinities, locally with a focused ray of light, or mapped over large areas. As stated earlier, the films are often assumed to be homogeneous and isotropic, but the technique can be generalized to study anisotropic films or graded layers [299, 301, 302].

The most straightforward application of SE, probably after measuring the thickness of a single layer with known optical properties, is certainly the determination of the complex refractive

index of a deposited film. In reference [303], for example, the authors calculated the optical parameters of polycrystalline thin films of the well-studied CdTe semiconductor, determining that the low index of refraction, as compared to single crystal CdTe, was due to a non-negligible pore fraction in the film. They also deduced the presence of an interface layer of different composition. Deducing the existence of a previously unknown layer is not a straightforward task. Having at least a partial prior knowledge of the sample structure is of tremendous help in making accurate models, and the trial and error nature of guessing the existence of unknown phases requires a good understanding of the possible growth and mixing processes that may have occurred during growth.

SE also has the advantage of being able to measure the optical properties and absorption coefficients of layers in device structures [304, 305]. This helps in device modeling, since close-to-real optical parameters can be used by including in the measurement the effects of layer intermixing, interfaces and effects due to the growth process. In addition to that, real time SE allows for the monitoring and controlling of growth, to study dynamics or changes in the phases [306, 307]. Defect levels in semiconductors, critical elements to control in optoelectronic and electronic devices, can be detected and studied through their effects on the structure of the dielectric function [308]. The speed of SE measurements also allows mapping of production-scale areas to generate maps of chemical composition and film and roughness layer thicknesses for rapid large-scale evaluation [309].

Ellipsometry of zinc phosphide

Zn₃P₂ has been reportedly studied twice using spectroscopic ellipsometry. Pascual et al. measured the ellipsometric spectrum in the range from 1.7 eV to 4.4 eV. The authors compared the spectra taken on samples with different surface treatments and did not model the optical properties of zinc phosphide. Instead, they calculated a pseudodielectric function associated with the whole structure (glass substrate/p-Zn₃P₂/degraded overlayer) [310].

Other than the previous paper, Kimball et al. studied polycrystalline Zn₃P₂ wafers grown by physical vapor transport in carbon-coated Bridgman quartz ampoules [311] in the range 0.56 eV to 4.13 eV [103]. The authors do not explain in detail their procedure for calculating the optical properties of their zinc phosphide samples and they do not explicitly report a model of the dielectric function of zinc phosphide.

To the best of my knowledge, our laboratory was the first to measure the ellipsometric spectrum of monocrystalline thin films and to create an ellipsometric model to calculate the optical properties of zinc phosphide and build more complex multi-layered models.

2.5 Summary

In summary, this chapter presents the basics of Raman spectroscopy and a description of the origin of its selection rules. Then experimental aspects of Raman spectrometry and applications of this techniques are reviewed. In the second part, the basics of photoluminescence spectroscopy, some experimental aspects and applications are presented. Finally, spectroscopic ellipsometry is introduced and its applications in photovoltaics research are discussed.

3 Nanosails showcasing Zn_3As_2 as an optoelectronic-grade earth abundant semiconductor

3.1 Accompanying information

This work has been published in the peer-reviewed journal *physica status solidi (RRL) - Rapid Research Letters*, volume 13, issue 7, p. 1900084 in 2019 [312]. The work is presented in this chapter with permission. Its digital object identifier is 10.1002/pssr.201900084. The list of authors is as follows: Elias Z. Stutz, Martin Friedl, Tim Burgess, Hark Hoe Tan, Philippe Caroff, Chennupati Jagadish and Anna Fontcuberta i Morral. Martin Friedl and I have contributed equally to this work. My contributions to this work include the spectroscopic analysis and the creation of the manuscript, with feedback from the co-authors. Included is the acquisition of part of the scanning electron micrographs, analysis and acquisition of the Raman spectrum, and simulation and comparison of XRD diffraction patterns.

3.2 Abstract

Zn_3As_2 is a promising earth-abundant semiconductor material. Its bandgap, around 1 eV, can be tuned across the infrared by alloying and makes this material suited for applications in optoelectronics. Here, we report the crystalline structure and electrical properties of strain-free Zn_3As_2 nanosails, grown by metal-organic vapor phase epitaxy. We demonstrate that the crystalline structure is consistent with the $\text{P4}_2/\text{nmc}$ (D_{4h}^{15}) α'' - Zn_3As_2 metastable phase. Temperature dependent Hall effect measurements indicate that the material is degenerately p-doped with a hole mobility close to $10^3 \text{ cm}^2 \text{ V}^{-1} \text{ s}^{-1}$. Our results display the potential of Zn_3As_2 nanostructures for next generation energy harvesting and optoelectronic devices.

3.3 Introduction

The increasing production of high-performance electronic devices and the push towards generating energy in a sustainable manner leads to sustainability challenges for optoelectronic

Chapter 3. Nanosails showcasing Zn_3As_2 as an optoelectronic-grade earth abundant semiconductor

and PV technologies. Particularly affected are devices using atomic elements of scarce abundance in the earth's crust, which prevents their widespread deployment. In this context, highly functional materials made of earth-abundant elements are being sought for both PV and optoelectronic applications. The second most abundant element in the earth's crust, silicon, is a semiconductor very successfully deployed in the PV market. It suffers nonetheless from its indirect bandgap and the consequently high purity required for the production of efficient solar cells. Both characteristics increase the energy needs for silicon PV device production. The so-called 'second generation' solar cells, built with much thinner, direct bandgap active layers, could in principle solve these two issues. Still, these thin film solar cells exhibit either a long energy payback time (amorphous silicon) or they use scarce and expensive elements (ex: copper, indium, gallium, selenium, cadmium, tellurium).

Direct bandgap semiconductors employing earth-abundant elements could combine the advantages of all these material families. They would enable efficient light collection in a thin film of easily available materials. CZTS and zinc phosphide (Zn_3P_2) have received increasing attention as materials satisfying these criteria for efficient and sustainable light conversion discussed so far. Belonging to the same family, zinc arsenide (Zn_3As_2) is a p-type semiconductor structurally similar to Zn_3P_2 . It exhibits a band gap around 1.0 eV [313] and potentially high hole mobilities [314]. The stoichiometry of this material can be transformed continuously into Cd_3As_2 [315] or Zn_3P_2 [75] by appropriate atomic substitutions, shifting its bandgap energy towards 1.5 eV and 0 eV, respectively. $(\text{Zn}_{1-x}\text{Cd}_x)_3\text{As}_2$ transforms from a semiconductor to a three-dimensional Dirac semimetal as x reaches 0.62 [316]. The ability to tune its direct bandgap energy makes this material system very attractive for long-wavelength optoelectronics and as a constituent in multi-junction solar cells.

$\text{M}_3^{\text{II}}\text{X}_2^{\text{V}}$ compounds crystallize in a structure akin to the anti-fluorite structure, with the difference being that 25% of the cation sites are empty. In turn, this causes a slight tetragonal distortion. Barring the minute deformation, their anion sublattice is face-centered cubic. Historically, the progress in the use of II-V materials has been hindered by a lack of suitable substrates matched in terms of their lattice constants and large CTE. InP and GaAs have shown to be the most suited substrates for the growth of Zn_3As_2 , with lattice mismatches of 0.35% and 4% at 300 K, respectively [317]. One should note here however that using InP and GaAs defies the purpose of achieving a sustainable technology with earth abundant elements. Epitaxial thin films of Zn_3As_2 have been obtained by metal-organic vapor phase epitaxy [74], molecular beam epitaxy [318], and liquid phase epitaxy [319]. In all these reports, misfit dislocations and cracks at the interface of thin films seem to be unavoidable [320]. The resulting interface defects drastically impair the electrical properties of the heterostructures.

One solution to both the lattice mismatch and CTE difference problems constitutes the use of freestanding nanostructures rather than thin films. In this case, the nanoscale contact area with the substrate allows for very efficient elastic strain relaxation [321]. Examples of heterogeneous integration of materials in the form of nanoparticles or nanowires are numerous [322–325]. Until now there are only a few publications demonstrating synthesis

of Zn_3As_2 and Zn_3P_2 nanostructures [314, 326–328], including simple device demonstration such as field-effect transistors and photodetectors [314].

Other kinds of free-standing structures include two-dimensional nanoscale objects such as nanosails or nanoscale membranes [329–332]. Thanks to their potentially equally efficient relaxation of mismatch strain, they provide a perfect platform for the study of two-dimensional structures which are free from any dislocations or cracks. They thus provide information on the intrinsic properties of the material and a path for their realistic use in applications.

3.4 Experimental Details

The Zn_3As_2 nanosails were grown by horizontal flow gold-catalyzed metal-organic vapor phase epitaxy (MOVPE) on a GaAs (111)B substrate by the vapor-liquid-solid method, as in ref. [328]. The growth time was 10 min. Details of the growth are described in the supplementary information. The morphological properties of the nanosails were characterized by scanning electron microscopy (SEM) and by atomic force microscopy (AFM). Figure 3.1 shows a typical SEM picture of the as-grown sample.

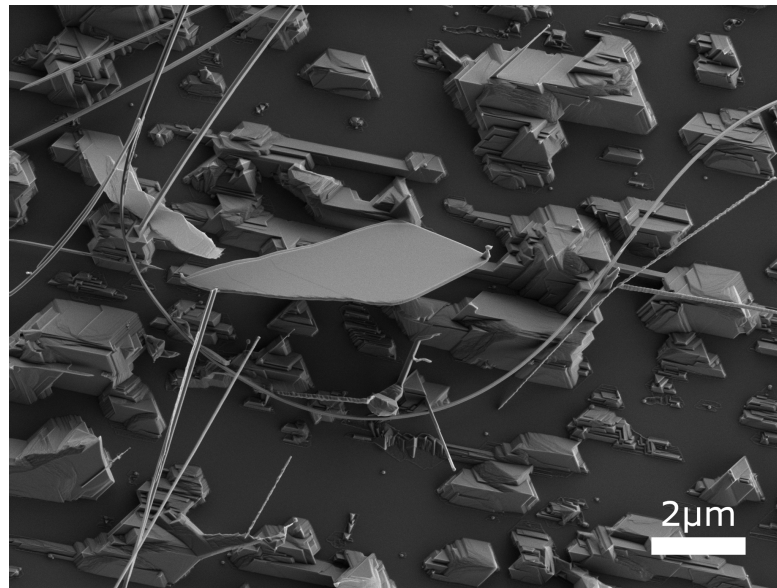


Figure 3.1 – Typical top-view scanning electron microscopy image of the surface of a sample grown in the conditions described in the text. Nanosails, nanowires, and gold nanoparticles can be seen.

Micro-Raman scattering measurements were performed on individual nanosails at 12 K with a single-frequency optically pumped semiconductor laser at 532 nm wavelength as an excitation source. The laser, with a power of 140 μW at the sample surface, was focused on the sample with a microscope objective ($\text{NA} = 0.75$). The polarization of the incident laser was controlled by a linear polarizer. The scattered light was collected in backscattering geometry through the

same objective and recorded by a TriVista triple spectrometer with gratings of 900, 900 and 1800 lines/mm, respectively, and a Princeton Instruments liquid nitrogen cooled multichannel CCD PyLoN camera. For the device fabrication, the nanosails were detached from the growth substrate by sonication in isopropanol and drop cast onto a thermally oxidized silicon wafer. The contacts were then patterned with aligned e-beam lithography [333] followed by wet etching in a buffered hydrogen fluoride solution with one chip additionally being Ar milled in-situ before metal deposition (see supplementary information for details). The contacts were then deposited by sputtering 20 nm of Cr and 150 nm of Au. The conductivity of the nanosails was measured by applying the van der Pauw method [334] while the thickness of the nanostructures was determined by AFM. The Hall mobility of the nanostructures was measured employing the same four contacts while sweeping a perpendicular magnetic field from -5 T to 5 T.

3.5 Structural properties

We start by reporting the structural properties of the nanosails. In bulk form, pure Zn_3As_2 exists in three different polymorphs named α , α' and β [243]. This material can also be found in a fourth crystalline structure when 2-4% of zinc or arsenic atoms are substituted with cadmium [335] or phosphorus [336], respectively. Table 3.1 lists the four polymorphs along with their characteristics in terms of symmetry, stability and number of atoms in the unit cell.

Name	Space group	Stability in bulk	# of atoms
α	$I4_1cd$	Stable: ≈ 300 K	160
α'	$P4_2/nbc$	Stable: 457-945 K	160
β	$Fm\bar{3}m$	Stable: > 945 K	10
α''	$P4_2/nmc$	Metastable	40

Table 3.1 – The different observed phases of Zn_3As_2 , their space group, stability in the bulk and number of atoms in the unit cell.

The thermodynamically stable Zn_3As_2 phase at room temperature is the so-called α phase. At temperatures between 457 and 945 K, typically used for growth, the α' phase with a different symmetry becomes stable. At higher temperatures, the β phase becomes stable. The loss of order of the cations increases the symmetry of this phase and makes it face-centered cubic. Pangilinan et al. [245] have observed a strained phase whose symmetry could not be matched with any known pure phase of Zn_3As_2 . They have not identified it as such at that time but given that the symmetry of their phase matches that of the α'' phase, this is the first observation of stoichiometrically pure α'' - Zn_3As_2 . To the best of our knowledge, this phase has otherwise never been synthesized and identified before.

Raman spectroscopy is a non-destructive technique that provides information not only on the structure, but also on the orientation and symmetry of the material. Figure 3.2 shows a

representative Raman spectrum of a Zn_3As_2 nanosail. The spectrum exhibits a dozen peaks separated in two sets: one at low energy ascribed to bending vibrations of the X-Zn-X systems (X = As, P) and the other at high energy, attributed to fundamental stretching vibrations of the Zn-X bonds [337]. The exact position of the deconvoluted stretching mode peaks along with their symmetry are reported in Table 3.2. The bending mode peaks acquired under our measurement conditions overlap too much to be reliably deconvoluted. One peak (*) could be the reportedly anomalous peak also observed by Pangilinan [245]. A similar Raman spectrum to the one presented here is observed in α - or α'' Zn_3P_2 [246], another compound of the α'' -($\text{Zn}_{1-x}\text{Cd}_x$)₃($\text{P}_{1-y}\text{As}_y$)₂ quaternary phase. This structure of the Raman spectrum is not observed in a lower symmetry phase of Zn_3As_2 such as α [338]. The Raman shift of the peaks identified in that article are listed in table E.2 in the supplementary information for comparison.

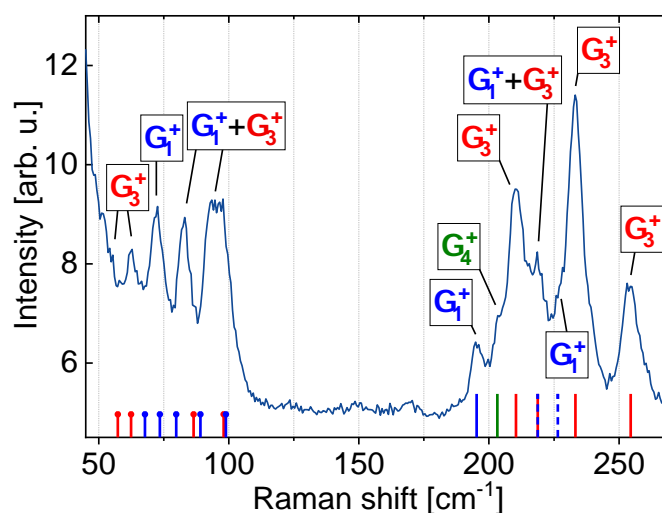


Figure 3.2 – Raman spectrum of a nanosail acquired at 12 K in backscattering geometry. The incident 532 nm laser light at approx. 150 μW was linearly polarized along the main axis of the nanostructure while the scattered light was unpolarized.

Position	Mode representation	Position in [245]
195.3	Γ_1^+	196.7
203.2	Γ_4^+	204.9
210.3	Γ_3^+	210.6
218.8	$\Gamma_1^+ \& \Gamma_3^+$	215.4
226.5	$\Gamma_1^+ (*)$	225.7
233.2	Γ_3^+	232.4
254.5	Γ_3^+	252.1

Table 3.2 – Deconvoluted peak positions of the high Raman shift stretching modes obtained by fitting with Lorentzians. The peak positions are matched with the corresponding peak and their symmetry determined by Pangilinan et al. [245].

In a previous study, Burgess et al. [328] assigned the α' phase of Zn_3As_2 to the nanosails obtained in extremely similar conditions (400 °C on GaAs(110)). The crystal structure was assigned by comparing electron diffraction patterns to simulated diffraction patterns of the α - and α' - Zn_3As_2 structures, and the latter seemed to be the most suitable. We simulated the diffraction pattern of α'' - Zn_3As_2 in equivalent zone axes to compare with their experimental diffraction patterns. The zinc ordering in the α'' phase does not match the crystalline structure of their nanostructures. Details of the simulation are shown in the supplementary information.

Prior to the growth described here, the metal-organic chemical vapor deposition (MOCVD) system had been used to grow zinc phosphide on indium phosphide substrates. It is possible that there was some residual phosphorus originating from the precursor or from the substrate in the growth chamber which could have been incorporated in the nanosails. Slight phosphorous contamination is possible in MOCVD, if the system is used both for phosphides and arsenides or if the substrate contains phosphorus. This would explain the growth of the α'' phase [336]. Further evidence indicating that our nanosails belong to this phase is that its crystal structure exhibits a relatively small unit cell with 40 atoms, four times less than the α and α' phases. This is consistent with the reduced number of observed first-order phonons in our structures. In conclusion, Raman spectra indicate are consistent with the crystalline phase of the nanosails being α'' - Zn_3As_2 .

3.6 Electrical Properties

Figure 3.3a shows a nanosail device, with its four electrical contacts. The thickness of the characterized devices, determined with AFM, ranged from 80 to 160 nm. We start by reporting on the temperature dependence of the electrical conductivity, between 4 and 300 K. The measurements of three different nanosails obtained in the same batch are shown in figure 3.3b. The conductivity increases at lower temperatures. Such a behavior is only expected in metals or in semiconductors with degenerate doping.

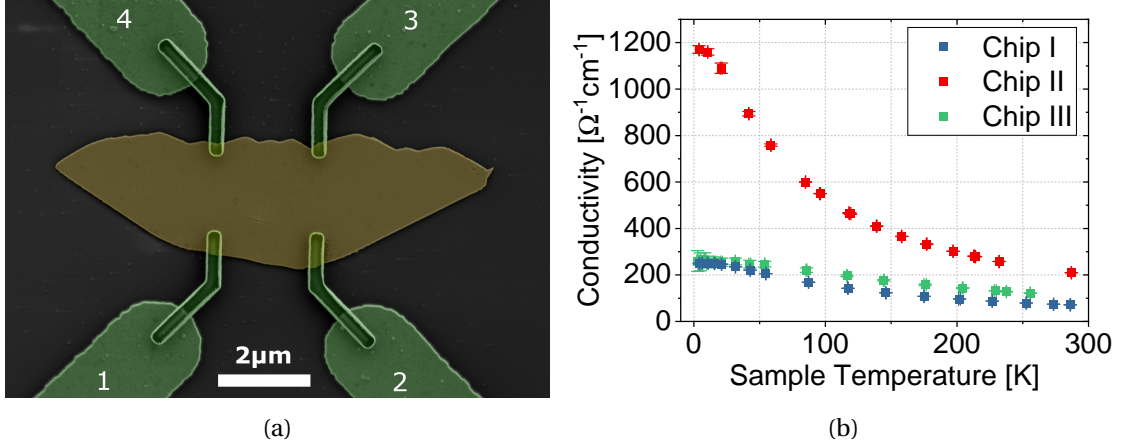


Figure 3.3 – a) Top-view colorized SEM image of a Zn₃As₂ nanosail (yellow) and the four contacts used for electrical characterization (green). b) Evolution of the conductivity of three nanosails with temperature, measured with the van der Pauw method.

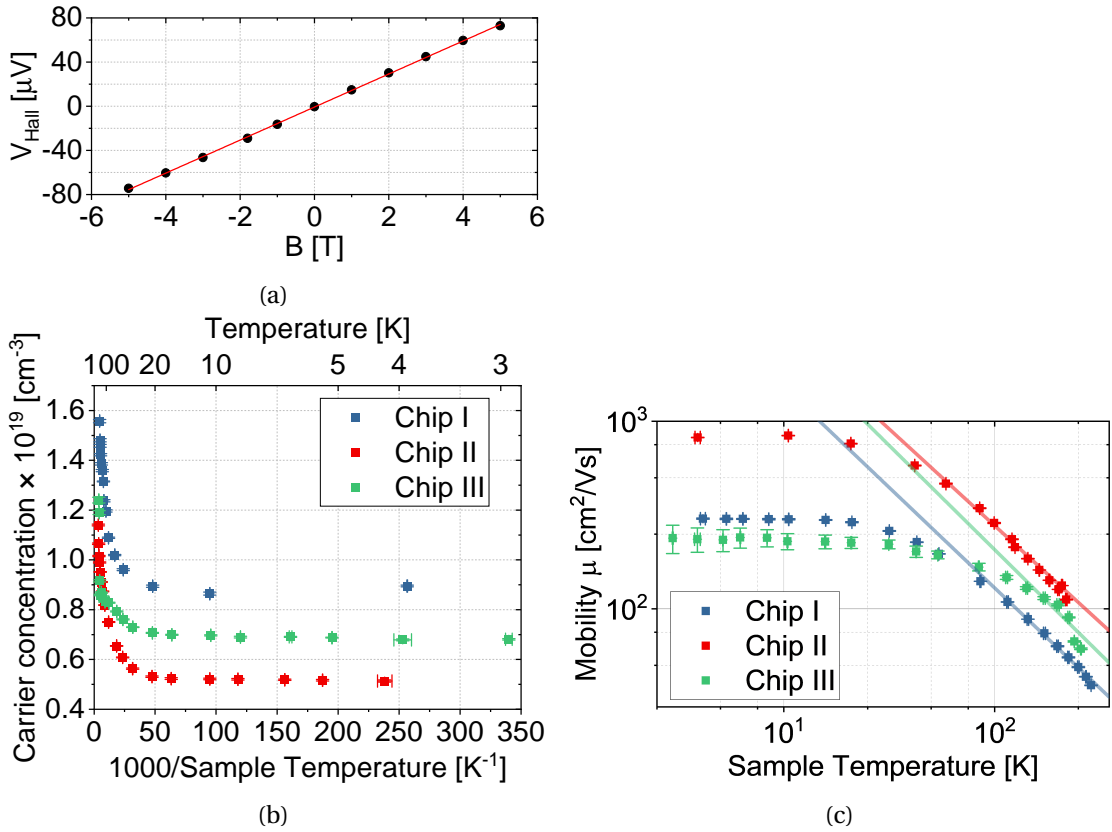


Figure 3.4 – a) Variation of the Hall voltage with magnetic field applied on to the nanosail and (in red) a linear fit to the data. b) temperature dependence of the carrier concentration of three nanosails calculated using the measured Hall coefficients and c) evolution of the hole mobility with the temperature (points). A fit to the linear high-temperature regime (solid lines) provides the temperature dependence of lattice scattering in Zn₃As₂.

Chapter 3. Nanosails showcasing Zn_3As_2 as an optoelectronic-grade earth abundant semiconductor

Figure 3.4a shows an example of a typical relationship between the measured Hall voltage and the applied magnetic field. The positive slope of the curves indicates a positive Hall coefficient, and hence confirms that the material is p-type, as reported extensively in the literature. The data follows the linear dependence of the Hall voltage as a function of the magnetic field: $V_H = \frac{IB}{pte}$ with a regression close to 1 ($\rho^2 = 0.9997$).

We use the conductivity measurements and the Hall voltage to determine the carrier concentration and mobility as a function of temperature. The concentration of free carriers and mobility is shown in figure 3.4b,c, respectively. The carrier concentration increases at high temperatures but does not freeze out at low temperatures, remaining above $4 \times 10^{18} \text{ cm}^{-3}$.

In all nanosails studied, the mobility of the carriers is constant below 10 K and decreases at higher temperatures. Linear fits to the high-energy parts of the curves reveal that the mobility is nearly proportional to the inverse of the temperature. This dependence is typical of metals and degenerate semiconductors, for which lattice vibrations are the dominant sources of scattering above their Debye temperature.

The three nanosails characterized have qualitatively very similar properties. The most striking difference between the three is the approximately threefold increase in carrier mobility measured in Chip II with respect to the other two. This in turn could explain most of the 4.5-fold increase in conductivity in that same nanosail. The reasons why this nanostructure exhibits increased mobility and conductivity with respect to the other two could be due to local differences of the growth conditions and environment during growth.

Overall, the electrical measurements indicate that the Zn_3As_2 nanosails are degenerately doped. Our results are consistent with some of the prior works on epitaxial Zn_3As_2 [73, 313, 317, 339]. The Zn_3As_2 material in this study is found to be unintentionally p-type. The unintentional p-doping is attributed to shallow [318] native defects [340]. Acceptor levels within a few dozen meV from the valence band maximum (VBM) have been detected in Zn_3As_2 by electrical, absorption [73] and photoluminescence [74, 341] spectroscopy measurements. Using the tight-binding method, Szatkowski et al. calculated the energy levels of vacancies [342]. They determined that zinc vacancies induce levels within 20 meV of the VBM. These findings are supported by DFT computations of the point defect energy levels of Zn_3P_2 [343], which exhibits the same short-range order as Zn_3As_2 . Finally, the presence of an impurity band (IB) in Zn_3As_2 due to the degenerate doping was proposed by Iwami et al. [339] and Sujak-Cyrul et al. [73].

The temperature dependence of the carrier concentration of our nanosails also shows two different regimes: below about 30 K, the concentration is nearly constant, and at higher temperatures, or only until about 80 K in Chip III, the concentration increases considerably. The transition temperature has been obtained by fitting the two regimes, as shown in figure E.2 in the supplementary information. The constant low-temperature regime indicates that pure impurity band conduction occurs up to these temperatures, at which point thermal carrier generation initiates, leading to a further increase of the carrier concentration. The spacing

between the VBM and the IB has been determined from the onset of thermal carrier generation to be 2.5 meV, a value consistent with previous observations. Whether the IB carrying the conduction carriers at the lowest temperature is degenerate with the top of the valence band or separated from it remains to be determined.

Based on the literature describing the low-temperature carrier properties of Zn_3As_2 , the presence of an IB seems to be ubiquitous in this kind of material, whether synthesized by the Bridgman method [339], by resublimation [73] or pseudomorphically on InP by MBE [317].

Comparison of the conductivities measured in the different works shows striking differences. For example, Szatkowski obtained $7 \Omega^{-1} \text{cm}^{-1}$ at 5 K, Sujak-Cyruł $35 \Omega^{-1} \text{cm}^{-1}$ (calc.) at 5 K and Chelluri $220 \Omega^{-1} \text{cm}^{-1}$ (calc.) at 10 K. This is to be compared with our results of at least $250 \Omega^{-1} \text{cm}^{-1}$ at 5 K. Szatkowski et al., reporting the lowest measured conductivity in single crystals at 5 K. This might be due to the presence of a higher density of defects associated with the growth method. Similarly, a reduction of the carrier mobility in Zn_3As_2 thin films with decreasing material quality has been reported by Kolodka [344].

Overall, the high values of mobility obtained by this work indicates the high potential of nanosails to investigate the intrinsic properties of materials bypassing lattice constant and CTE mismatch challenges. In addition, we believe our results show Zn_3As_2 has excellent potential for photovoltaic applications. For this to be possible, junctions should be created by also growing n-type regions or by heteroepitaxy of a second material yielding a type-II band alignment. Further work could also aim at optimizing the growth conditions to increase the yield of nanosails as in refs. [345, 346].

3.7 Conclusion

In conclusion, we have shed light on the electrical properties of $\alpha''\text{-Zn}_3\text{As}_2$ nanosails, whose crystalline structure has been demonstrated by polarized Raman spectroscopy. The temperature dependence of the conductivity, majority carrier concentration and carrier mobility between 4 and 300 K are consistent with a high-quality degenerately doped p-type semiconductor. This work demonstrates the potential of Zn_3As_2 as an earth-abundant semiconductor for next generation energy harvesting or optoelectronic applications.

3.8 Supplementary information

The supplementary information is presented in appendix E and includes growth parameters, details on the electrical contact fabrication, lists of reported Raman peaks for $\alpha''\text{-Zn}_3\text{As}_2$, simulations of electron diffraction patterns and fitting details of the carrier concentration regimes.

3.9 Acknowledgements

EZS and MF have contributed equally to this work. ME, EZS, and AFiM thank financial support by the Swiss National Science Foundation (SNSF) through the QSIT network and consolidator grant Easeh (grant nr BSCGI0_157705), as well as initial discussions with Andreana Daniil and Simon Escobar Steinvall. We acknowledge the Australian National Fabrication Facility, ACT Node for access to the MOCVD facility.

4 Raman spectroscopy and lattice dynamics calculations of tetragonally-structured single crystal zinc phosphide (Zn_3P_2) nanowires

4.1 Accompanying information

This work has been published in the peer-reviewed journal *Nanotechnology*, volume 32, number 8, p. 085704 in 2021 [347]. Its digital object identifier is 10.1088/1361-6528/abc91b. The work presented in this chapter has been originally published under the terms of the Creative Commons Attribution 4.0 licence. The list of authors is as follows: Elias Z. Stutz, Simon Escobar Steinvall, Alexander P. Litvinchuk, Jean-Baptiste Leran, Mahdi Zamani, Rajrupa Paul, Anna Fontcuberta i Morral and Mirjana Dimitrievska. My contributions to this work include the acquisition and analysis of the Raman spectroscopic data and the acquisition of part of the scanning electron micrographs. I contributed significantly to the writing of the manuscript.

4.2 Abstract

Earth-abundant and low-cost semiconductors, such as zinc phosphide (Zn_3P_2), are promising candidates for the next generation photovoltaic applications. However, synthesis on commercially available substrates, which favors the formation of defects, and controllable doping are challenging drawbacks that restrain device performance. Better assessment of relevant properties such as structure, crystal quality and defects will allow faster advancement of Zn_3P_2 , and in this sense, Raman spectroscopy can play an invaluable role. In order to provide a complete Raman spectrum reference of Zn_3P_2 , this work presents a comprehensive analysis of vibrational properties of tetragonally-structured Zn_3P_2 (space group $\text{P4}_2/\text{nmc}$) nanowires, from both experimental and theoretical perspectives. Low-temperature, high-resolution Raman polarization measurements have been performed on single-crystalline nanowires. Different polarization configurations have allowed selective enhancement of A_{1g} , B_{1g} and E_g

Raman modes, while B_{2g} modes were identified from complementary unpolarized Raman measurements. Simultaneous deconvolution of all Raman spectra with Lorentzian curves has allowed identification of 33 peaks which have been assigned to 34 ($8 \text{ A}_{1g} + 9 \text{ B}_{1g} + 3 \text{ B}_{2g} + 14 \text{ E}_g$) out of the 39 theoretically predicted eigenmodes. The experimental results are in good agreement with the vibrational frequencies that have been computed by first-principles calculations based on density functional theory. Three separate regions were observed in the phonon dispersion diagram: (i) low-frequency region ($<210 \text{ cm}^{-1}$) which is dominated by Zn-related vibrations, (ii) intermediate region ($210\text{--}225 \text{ cm}^{-1}$) which represents a true phonon gap with no observed vibrations, and (iii) high-frequency region ($>225 \text{ cm}^{-1}$) which is attributed to primarily P-related vibrations. The analysis of vibrational patterns has shown that non-degenerate modes involve mostly atomic motion along the long crystal axis (c -axis), while degenerate modes correspond primarily to in-plane vibrations, perpendicular to the long c -axis. These results provide a detailed reference for identification of the tetragonal Zn_3P_2 phase and can be used for building Raman based methodologies for effective defect screening of bulk materials and films, which might contain structural inhomogeneities.

4.3 Introduction

Among the II–V compounds, zinc phosphide ($\alpha\text{-Zn}_3\text{P}_2$, hereafter referred to as Zn_3P_2), an earth-abundant, environmentally friendly and low-cost semiconductor, has gained attention as a promising absorber candidate for the next generation of thin-film photovoltaics (PV) [32, 52, 348]. With merits such as a direct band gap of 1.5 eV, a high absorption coefficient of $10^4\text{--}10^5 \text{ cm}^{-1}$, and carrier diffusion lengths of $10 \mu\text{m}$, zinc phosphide is a very suitable material for solar energy applications [103, 247, 349–352]. However, even with all these benefits, the conversion efficiencies are still far from reaching the 31% predicted from the Shockley–Queisser limit [34]. In fact, the record solar cell, with a conversion efficiency of 6%, was produced 40 years ago [104], and since then there has not been any significant scientific breakthrough. Despite the highly promising result at that time, research on Zn_3P_2 recessed mostly due to technical challenges in fabricating high-quality material with controllable doping, surface passivation and clean interfaces, all of which are crucial for high-efficiency devices.

One major challenge in the synthesis of high-quality Zn_3P_2 is its rather large crystallographic unit cell [104] when compared to other PV materials, along with its high coefficient of thermal expansion [257, 353]. All of these increase heterointerface defect densities when grown epitaxially on commercially available substrates. Major progress has recently been made in this regard, where growth of highly crystalline Zn_3P_2 was achieved using innovative nanofabrication methods (i.e. selective area epitaxy) [261–263]. However, fine-tuning of the material's functional properties through doping and defect engineering still remains a challenge. This is mostly due to the complex structure of Zn_3P_2 characterized by empty sites in the cubic zinc sublattice dispersed throughout a tetragonal lattice, which, besides providing ample opportunities for material design, also results in a higher probability for formation of intrinsic defects

during synthesis (i.e. phosphorus interstitials in the empty zinc sites). While some amounts of intrinsic defects are beneficial for the doping and recombination characteristics of the Zn_3P_2 , large concentrations of defect complexes can lead to limiting minority charge carrier lifetimes and enhance recombination processes [351, 354, 355]. Defects can also have an effect on the net band gap variations and cause localized band gap or electrostatic potential fluctuations, which can lead to a change in the bulk diffusivity and indirectly affect the optoelectronic properties [355, 356]. This is why controlled defect engineering and doping play a significant role in achieving high-efficiency devices based on Zn_3P_2 . Thus, a thorough assessment of Zn_3P_2 , in terms of crystalline quality, defect identification and quantification, and homogeneity is of the foremost importance for the future development of this technology. In particular, developing predictive synthesis–structure–property relationships are crucial for effective design of materials with enhanced functional properties as absorbers for high-efficiency devices.

Raman spectroscopy can play an important role in this context. Besides being a fast and non-destructive technique, it is also one of the most suitable tools for determining the crystal structure and quality of semiconductors. This is due to the intensity, shape and position of Raman peaks being strongly influenced by the presence of structural inhomogeneities in the material. These include both point defects, such as vacancies, interstitials, and anti-sites, and other structural disorders, like dislocations or grain boundaries. Clear variations in Raman spectral features with the changes in the composition, processing conditions and doping can be observed for many materials [287, 357–362]. However, in order to be able to use Raman spectroscopy as a suitable tool for defect identification, it is necessary to have reliable reference Raman spectra of the material, with detailed identification of all peaks and their vibrational origin. This can greatly help in building Raman based methodologies which can be later used for further development of materials in the PV field.

In this work, we provide a reference Raman spectrum of single-crystalline Zn_3P_2 , with a complete analysis of all Raman active modes from both experimental and theoretical perspectives. To the best of our knowledge, this is the first comprehensive theoretical analysis of the lattice vibrations in Zn_3P_2 along with a concise comparison with experimental results in terms of phonon symmetries and frequencies. So far, the most complete experimental Raman analysis of Zn_3P_2 was performed by Pangilinan et al [246]. However, this work contained a few inconsistencies in terms of the number of observed modes and their symmetry assignment. Later on, Hanuza et al provided data on the vibrational modes in zinc phosphide by reflectance spectroscopy [337]. The identification of the modes was supported by a molecular model of a simplified Zn_3P_2 structure with 18 atoms out of the 40 present in the Zn_3P_2 unit cell, which resulted in a somehow qualitative assessment of the vibrations in the structure. On the other hand, density functional theory (DFT) calculations of Zn_3P_2 have primarily been dealing with the prediction of the electronic band structure [232], defects [343, 363] and growth mechanisms [364, 365], rather than the phonon analysis.

This work provides high-resolution polarization-resolved Raman scattering measurements. The experiments have been performed on the basal (010) plane of single crystal nanowires

in high-symmetry polarization conditions. Together with the detailed deconvolution of the Raman spectra with Lorentzian curves, this has allowed the identification of 33 Raman peaks. The experimental results are consistent with the vibrational frequencies that have been computed by first-principles calculations based on DFT. Furthermore, calculations of the phonon density of states (PDOS) (elemental and total), as well as the phonon dispersions provide a microscopic understanding of the experimentally observed phonon lines, in addition to the assignment to the specific lattice eigenmodes. These results can be used as a reference for identification of the Zn_3P_2 phase, as well as for building Raman based methodologies for effective defect screening of bulk materials and films that might contain structural inhomogeneities.

4.4 Experimental details

4.4.1 Material preparation

The Zn_3P_2 nanowires were epitaxially grown in a Veeco GENxplor molecular beam epitaxy (molecular beam epitaxy (MBE)) system on InP (100) substrates. They were grown via a In-catalyzed vapor–liquid–solid method. The In was generated through a 5 min Zn pre-deposition prior to growth, which reacted with the substrate to form the catalyst droplet. The analyzed samples were then grown at a manipulator temperature of 250 °C and a P/Zn ratio of 1.45 for four hours (Zn base flux 3.4×10^{-7} Torr). Additional details on the growth can be found in [70, 262].

Characterization

The morphological properties of the nanowires were characterized by scanning electron microscopy (SEM) with a Zeiss Merlin microscope operated at 3 kV. (Scanning) Transmission electron microscopy (S/TEM) and energy-dispersive x-ray spectroscopy (EDX) studies were performed using an FEI Talos transmission electron microscope operating at 200 kV. For transmission electron microscopy (TEM) analysis, the nanowires were transferred to a copper grid covered by holey-carbon by gently scraping it across the substrate surface with a cotton swab.

Micro-Raman spectroscopy was realized in the back-scattering configuration on a Zn_3P_2 nanowire at 12 K. The 532 nm line of a Coherent Sapphire SF optically pumped semiconductor laser was used for excitation. The beam was focused on the sample with a microscope objective with a numerical aperture of 0.75, resulting in around 1 μm diameter spot size, and reached radiant fluxes on the order of 150 μW at the surface. A linear polarizer and a half-waveplate were used to control the polarization of the incident beam, while the scattered light was filtered through a linear polarizer. Before entering the spectrometer, a half-waveplate oriented the light polarization parallel to the entrance slit. The signal was analyzed with a TriVista triple spectrometer with 900, 900 and 1800 mm^{-1} gratings in subtractive mode and a Princeton Instruments liquid nitrogen cooled multichannel CCD PyLoN camera. The polarization

direction is described by the angle it makes with the direction of the long axis of the nanowire. For Raman analysis, the nanowires were transferred to a silicon wafer by gently brushing the growth substrate against it.

Lattice dynamics calculations

The first-principles calculations of the electronic ground state of the tetragonally structured Zn_3P_2 were performed within the local density approximation using Ceperly–Adler functional [366, 367], as implemented in the CASTEP code [368]. Norm-conserving pseudopotentials were used. The cutoff energy for the plane wave basis was set to 600 eV. A self-consistent-field (SCF) tolerance better than 10^{-7} eV per atom and the phonon SCF threshold of 10^{-12} eV per atom were imposed. Prior to performing calculations, the structure was relaxed so that forces on atoms in the equilibrium position did not exceed $2 \text{ meV}\text{\AA}^{-1}$ and the residual stress was below 5 MPa. Experimentally determined lattice parameters from [249] were used as a starting point. An integration over the Brillouin zone was performed over a $3 \times 3 \times 2$ Monkhorst–Pack grid in reciprocal space.

4.5 Results and discussion

A sketch of the crystal structure of Zn_3P_2 is depicted in figure 4.1. It exhibits tetragonal symmetry with the space group $P4_2/nmc$ (D_{4h}^{15}), which contains 8 formula units, resulting in a total of 40 atoms per unit cell. The packing of atoms in the structure takes place in a layered lattice along the [001] direction (c -axis), with alternating layers of cations (Zn) and anions (P). The cations are placed at four nearly equidistant planes occupying three distinct 8g ($1/4, y, z$) symmetry positions. The anions are located between the cation planes, with P atoms occupying three inequivalent Wyckoff positions at 4c ($-1/4, 1/4, z$), 4d ($-1/4, 1/4, z$) and 8f ($x, -x, 1/4$). The Zn and P atoms form a tetrahedral arrangement like in zinc-blende and fluorite type structures. Based on this arrangement P atoms form a face-centered cubic sublattice with Zn atoms filling $3/4$ of the tetrahedral voids. Each P atom is surrounded by 6 Zn atoms at the corners of a distorted cube while the metal atoms are surrounded by 4 P atoms at the vertices of a distorted tetrahedron. The ordered unoccupied tetrahedral voids lead to a decrease in lattice symmetry and the significant extension of Zn_3P_2 unit cell when compared to the zinc-blende or fluorite building blocks. The experimentally determined lattice parameters are $a = b = 8.0785 \text{\AA}$ and $c = 11.3966 \text{\AA}$ [249].

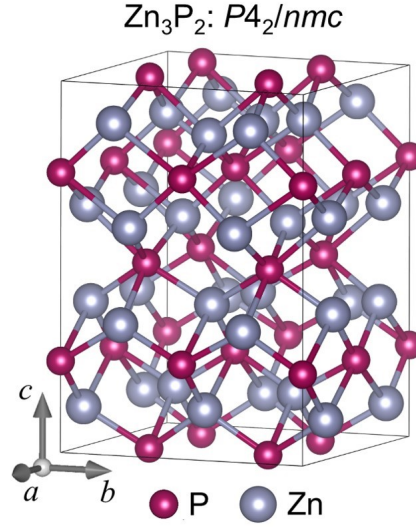


Figure 4.1 – Conventional unit cell representation of the tetragonal Zn_3P_2 structure.

Group theory analysis predicts the following set of irreducible representations for the structure $P4_2/nmc$ (D_{4h}^{15}) at the Γ point of the Brillouin zone [369–371]:

$$\begin{aligned} \Gamma_{total} = & 9A_{1g} + 5A_{2g} + 10B_{1g} + 4B_{2g} + 16E_g \\ & + 4A_{1u} + 10A_{2u} + 5B_{1u} + 9B_{2u} + 16A_u \end{aligned}$$

from which the Raman and infra-red active modes are:

$$\Gamma_{Raman} = 9A_{1g} + 10B_{1g} + 4B_{2g} + 16E_g, \quad (4.1)$$

$$\Gamma_{IR} = 9A_{2u} + 15E_u, \quad (4.2)$$

while the other modes are silent. Note also that the A and B modes are non-degenerate, while the E modes are doubly degenerate. The Raman tensors for $P4_2/nmc$ space group are defined as follows:

$$\begin{aligned} \Re_{A_{1g}} &= \begin{pmatrix} a & 0 & 0 \\ 0 & a & 0 \\ 0 & 0 & b \end{pmatrix}; & \Re_{B_{1g}} &= \begin{pmatrix} c & 0 & 0 \\ 0 & -c & 0 \\ 0 & 0 & 0 \end{pmatrix}; \\ \Re_{B_{2g}} &= \begin{pmatrix} 0 & d & 0 \\ d & 0 & 0 \\ 0 & 0 & 0 \end{pmatrix}; & \Re_{E_g} &= \begin{pmatrix} 0 & 0 & e \\ 0 & 0 & e \\ e & e & 0 \end{pmatrix} \end{aligned} \quad (4.3)$$

where a , b , c , d , and e are the Raman tensor elements.

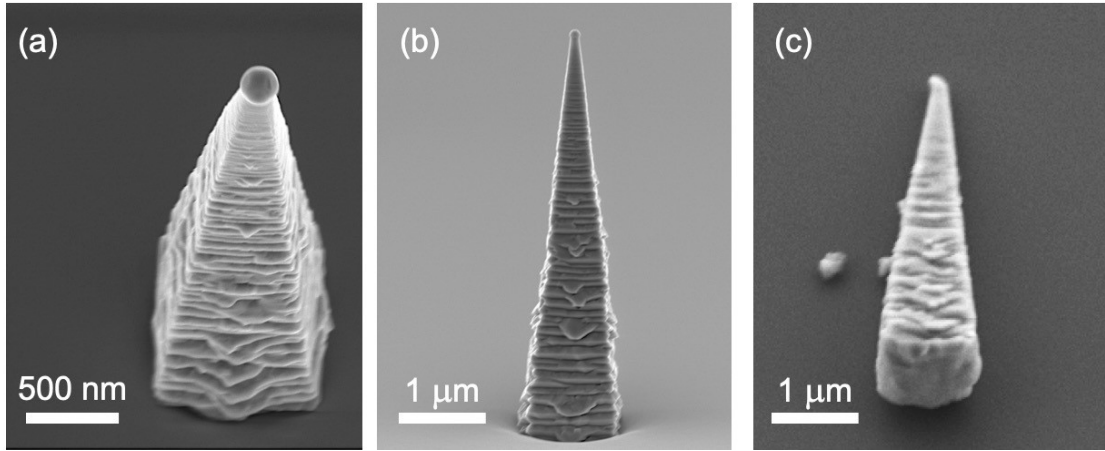


Figure 4.2 – SEM micrographs of three different Zn_3P_2 nanowires grown vertically along the [001] direction. The images are taken in different configurations, with the nanowire orientation being (a) and (b) perpendicular and (c) parallel to the substrate (transferred for the optical measurements). The Raman spectra presented in this study were acquired from the wire shown in (c).

In order to experimentally determine the positions of the Raman active modes, high-resolution Raman polarization measurements were performed on a Zn_3P_2 nanowire, of which SEM micrographs are presented in figure 4.2. The nanowires present a square cross-section that decreases in area along the nanowire axis. At the top we find the indium droplet that catalyzes the growth. The Raman measurements were carried out at approximately one-third of the length of the nanowire from the wide base. The nanowire width is at least 100 nm along the whole structure and more than 600 nm at the location of the measurement. Consequently, phonon confinement effects are negligible, and the measured spectrum is equivalent to that of the bulk material.

Selective area electron diffraction measurements on the nanowires in TEM have confirmed the formation of monocrystalline Zn_3P_2 phase with $P4_2/nmc$ tetragonal symmetry, and allowed identification of the nanowire growth orientation as [001], with the c crystal axis perpendicular to the substrate [262]. It should be noted that the roughness on the nanowire surface is not due to crystallographic defects but rather microfaceting as the (101) facets have a lower surface energy than (100) facets, and thus the surface has the same crystalline orientation as the core of the nanowire and does not affect the Raman spectrum. The compositional assessment, performed by STEM-EDX, indicated the formation of Zn-rich wires with $\text{Zn}/\text{P} = 2.3$ compared to stoichiometric $\text{Zn}/\text{P} = 1.5$. The extra Zn is probably accommodated at the empty Zn sites in the lattice, and therefore it should not affect the positions of the main Raman modes expected for this crystal structure. Further, a homogenous distribution of Zn and P with no phase segregation is observed from the compositional maps shown in figure 4.3. This confirms that only peaks from the Zn_3P_2 phase are expected in the Raman spectra.

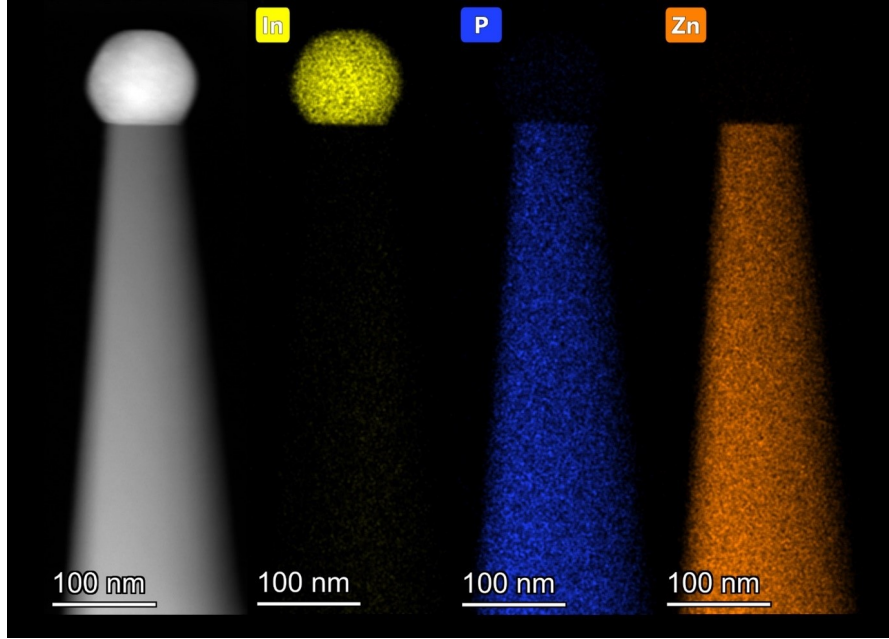


Figure 4.3 – High-angle annular dark-field STEM image and accompanying EDX elemental maps of the top of a Zn_3P_2 nanowire with composition corresponding to $\text{Zn}/\text{P} = 2.3$.

Raman measurements were performed on a nanowire with the $[001]$ growth direction being parallel to the substrate (figure 4.2c), indicating (010) crystallographic plane as the basal plane.

Based on these conditions, the angular dependence of the Raman mode intensity is given by:

$$I \propto |\nu_i \cdot \mathfrak{R}_{xyz} \cdot \nu_s|^2, \quad (4.4)$$

$$\begin{aligned} \nu_i &= (\cos(\theta) \quad 0 \quad \sin(\theta)); \\ \nu_s^{\parallel} &= \begin{pmatrix} \cos(\theta) \\ 0 \\ \sin(\theta) \end{pmatrix}; \\ \nu_s^{\perp} &= \begin{pmatrix} -\sin(\theta) \\ 0 \\ \cos(\theta) \end{pmatrix}, \end{aligned} \quad (4.5)$$

where ν_i and ν_s are the unit polarization vectors of the electric field for the incident and scattered light, respectively, and \mathfrak{R}_{xyz} is the Raman tensor, while θ is the angle between the $[100]$ nanowire direction and the electric field of the incident light. The superscripts \parallel and \perp correspond to the parallel and perpendicular polarization configurations. Substitution of Raman tensors from equation 4.3 into equations 4.4 and 4.5 yields general angular dependencies

of the intensities of the Raman modes, which are presented in table 4.1.

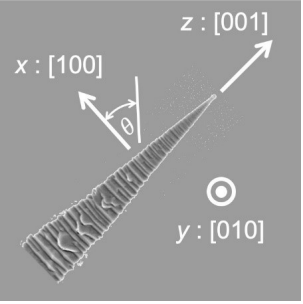
Polarization geometry	Mode	Parallel configuration	Perpendicular configuration
	A_{1g}	$ a \cos(\theta)^2 + b \sin(\theta)^2 ^2$	$ \frac{1}{2}(b - a) \sin(2\theta) ^2$
	B_{1g}	$ c \cos(\theta)^2 ^2$	$ \frac{1}{2}c \sin(2\theta) ^2$
	B_{2g}	0	0
	E_g	$ e \sin(2\theta)^2 ^2$	$ e \cos(2\theta)^2 ^2$

Table 4.1 – Angular dependencies of Raman modes intensity for tetragonal Zn_3P_2 in case of a (010) basal plane, and with the incident and scattered light parallel to the [010] direction.

Based on the angular dependencies of Raman modes intensity from table 4.1, three polarization geometry configurations were chosen for selective activation of specific phonon symmetries in the Raman spectra, thus allowing easier identification of the peak characteristics. The chosen polarization geometries correspond to the maximum or minimum Raman response of the lattice, in terms of the A_{1g} , B_{1g} and E_g modes. Raman measurements in parallel configuration with $\theta = 90^\circ$ allow selective enhancement of only the A_{1g} modes, while for $\theta = 0^\circ$ both A_{1g} and B_{1g} modes are expected. On the other side, polarization measurements in the perpendicular configuration with $\theta = 90^\circ$ will selectively enhance only the E_g modes. Finally, unpolarized Raman measurements were performed in order to identify B_{2g} vibrations.

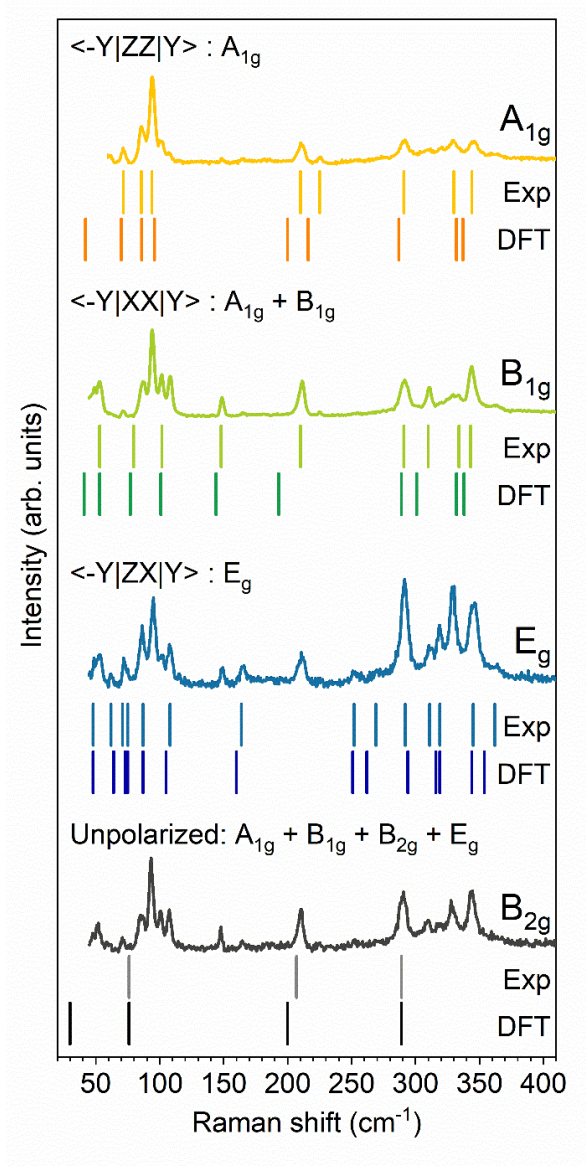


Figure 4.4 – Raman spectra of Zn_3P_2 in polarized and unpolarized configurations measured at 12 K using 532 nm excitation wavelength. The polarization geometry is indicated above each spectrum, along with the labels of the specific phonons that are allowed in these conditions. The lines under each spectrum show comparison between the Raman peak positions obtained experimentally by the deconvolution of the spectra with Lorentzian curves (labeled Exp), and from the lattice dynamics calculations based on DFT (labeled DFT).

Figure 4.4 presents the Raman spectra of Zn_3P_2 measured at 12 K under different polarization configurations using 532 nm excitation. Low-temperature measurements were chosen due to the increase in the phonon lifetime in the material, which results in better defined Raman peaks. This allows for a repeatable and reliable spectrum deconvolution as it decreases the overlap between Raman lines. The standard Porto notation has been utilized for labeling of

the measurements, where $\langle -Y|ZX|Y \rangle$ denotes the incoming radiation along the $-y$ -axis being polarized along the z -axis with the backscattered (y) light polarized along x . It should be noted that in case of the $\langle -Y|ZX|Y \rangle$ polarization configuration, besides the allowed E_g modes, the appearance of extra peaks is observed with closely matching positions and characteristics of A_{1g} modes. The activation of forbidden A_{1g} modes under this measurement geometry can be explained by a possible breakdown of selection rules. For example, planar native defects in the form of stacking faults with the direction of growth in the c axis, which are often found in layered materials due to very low formation energy, could activate forbidden modes [250, 361, 372, 373]. Additionally, the breakdown of selection rules can be activated by the photonic nature of the light–nanowire interaction, which can modify the light polarization inside the nanowire [267, 374–376].

Raman spectra were deconvoluted with a minimum number of Lorentzian components, allowing identification of a total of 33 peaks from the four different Raman measurement configurations. A representative deconvolution of the Raman spectra of Zn_3P_2 , along with details regarding the deconvolution procedure and identification of the peaks can be found in the supporting information (see appendix F, p. 149). It should be noted that all linewidths of the peaks are narrow and similar in values, pointing to their nature as one-phonon modes. Table 4.2 lists the Raman frequencies of all peaks obtained from the deconvolution, the symmetry assignment based on the polarization conditions, comparison with calculated phonon modes, as well as previously reported experimental results [246]. Table 4.2 indicates an excellent agreement (within 2% difference) between the experimentally observed peaks and the theoretically predicted Raman frequencies. Minor disagreement in the Raman peak positions between the experimental and the theoretical results is expected, due to approximations applied during the calculations.

Chapter 4. Raman spectroscopy and lattice dynamics calculations of tetragonally-structured single crystal zinc phosphide (Zn₃P₂) nanowires

This work			Reference [246]
ν_{exp} (cm ⁻¹)	ν_{theory} (cm ⁻¹)	Symmetry assignment	ν_{exp} (cm ⁻¹)
	14	E _g	
	30	B _{2g}	
	30	E _g	
	41	B _{1g}	41 (E _g)
	42	A _{1g}	
48	48	E _g	48 (B _{2g})
53	53	B _{1g}	53 (A _{1g})
62	64	E _g	62
71	70	A _{1g}	
72	73	E _g	71
75	75	E _g	
76	76	B _{2g}	
79	77	B _{1g}	
86	86	A _{1g}	87
87	87	E _g	88 (B _{1g})
94	96	A _{1g}	94
102	101	B _{1g}	101 (A _{1g})
108	105	E _g	108 (B _{1g})
148	144	B _{1g}	148
164	160	E _g	164
209	193	B _{1g}	
207	200	B _{2g}	
211	200	A _{1g}	210
225	216	A _{1g}	225
252	251	E _g	251
269	262	E _g	
291	287	A _{1g}	290
289	289	B _{1g}	292
	289	B _{2g}	
292	294	E _g	
309	301	B _{1g}	309
311	316	E _g	310 (A _{1g})
319	319	E _g	319
330	332	A _{1g}	323
334	332	B _{1g}	329 (E _g)
344	337	A _{1g}	333
343	338	B _{1g}	344
345	344	E _g	346
362	354	E _g	362 (A _{1g})

Table 4.2 – Frequency (in cm⁻¹) of peaks from Lorentzian fitting of Raman spectra measured with 532 nm and proposed mode symmetry assignment compared with theoretical predictions and reported experimental data from the literature.

While the peak positions have shown excellent agreement between this work and the results reported in the literature, we would like to point out several inconsistencies regarding their symmetry assignment. In particular, 9 modes out of 26 modes from [246] do not match the proposed symmetry assignment with the identification performed in this work. These peaks are highlighted in table 4.2 by providing the literature's symmetry assignment in parenthesis next to the peak position. One possible reason for the mismatch could be closeness in peak position for different types of modes, which, along with some breakdown in selection rules due to the defects present in the crystal, as reported in [246], could result in the appearance of forbidden modes in the Raman spectra, and consequently lead to misinterpretation. Additionally, we also point out that the proposed mode assignment in [246] is based solely on experimental results, while this work is supported by both theoretical calculations and polarization measurements.

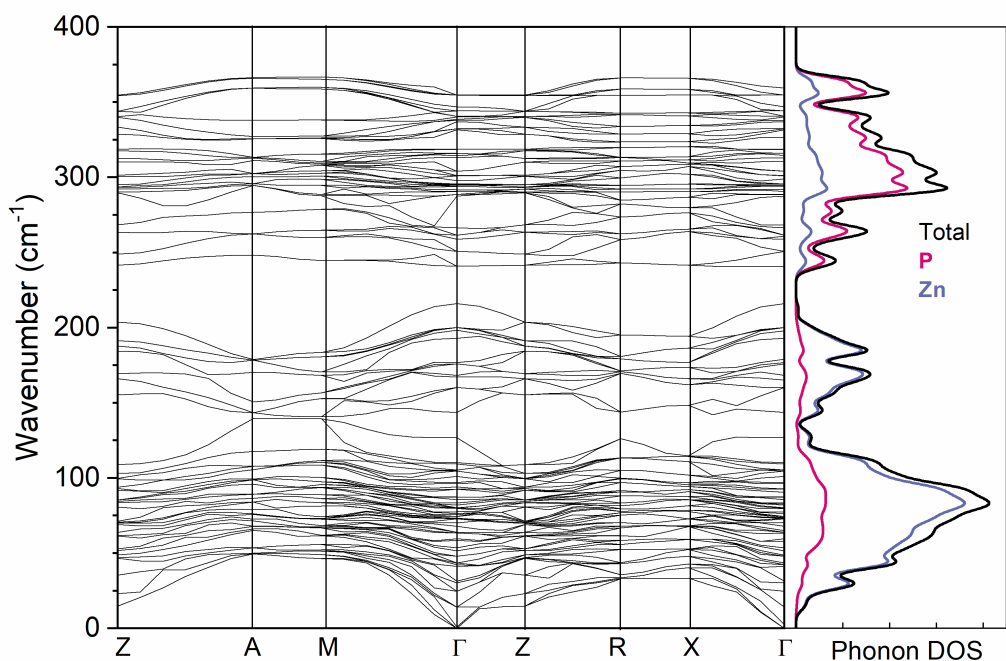


Figure 4.5 – DFT-calculated phonon dispersion along high-symmetry directions of the tetragonal Zn_3P_2 structure. On the right the partial phonon density of states is presented: zinc atoms in blue-gray, phosphorous in pink, and total in black.

A more detailed analysis of the Zn_3P_2 phonons can be obtained from the calculated phonon dispersion along high-symmetry directions of the Brillouin zone, which is presented in figure 4.5, along with the total and elemental PDOS. Three separate regions can be identified in

Chapter 4. Raman spectroscopy and lattice dynamics calculations of tetragonally-structured single crystal zinc phosphide (Zn_3P_2) nanowires

the phonon dispersion diagram: (i) a low-frequency region ($<210\text{ cm}^{-1}$) which is dominated by Zn-related vibrations, (ii) an intermediate region ($210\text{--}225\text{ cm}^{-1}$) which represents a true phonon gap with no observed vibrations, and (iii) a high-frequency region ($>225\text{ cm}^{-1}$) which is attributed mainly to P-related vibrations. The observation of the phonon gaps seems typical for II–V compounds, as similar features were observed for ZnP_2 and CdP_2 [377]. Additionally, it was noted that the position and shape across the Brillouin zone of those phonon bandgaps seems virtually independent of the cations (Zn or Cd). This feature could be further exploited for thermoelectric applications, for example. It is also important to point out that the tetragonal Zn_3P_2 does not possess any optical phonons above 365 cm^{-1} . This is the consequence of Zn_3P_2 being structurally more similar to ternary and quaternary chalcogenides where anions, similar to cations, are all tetrahedrally coordinated [287, 362, 378].

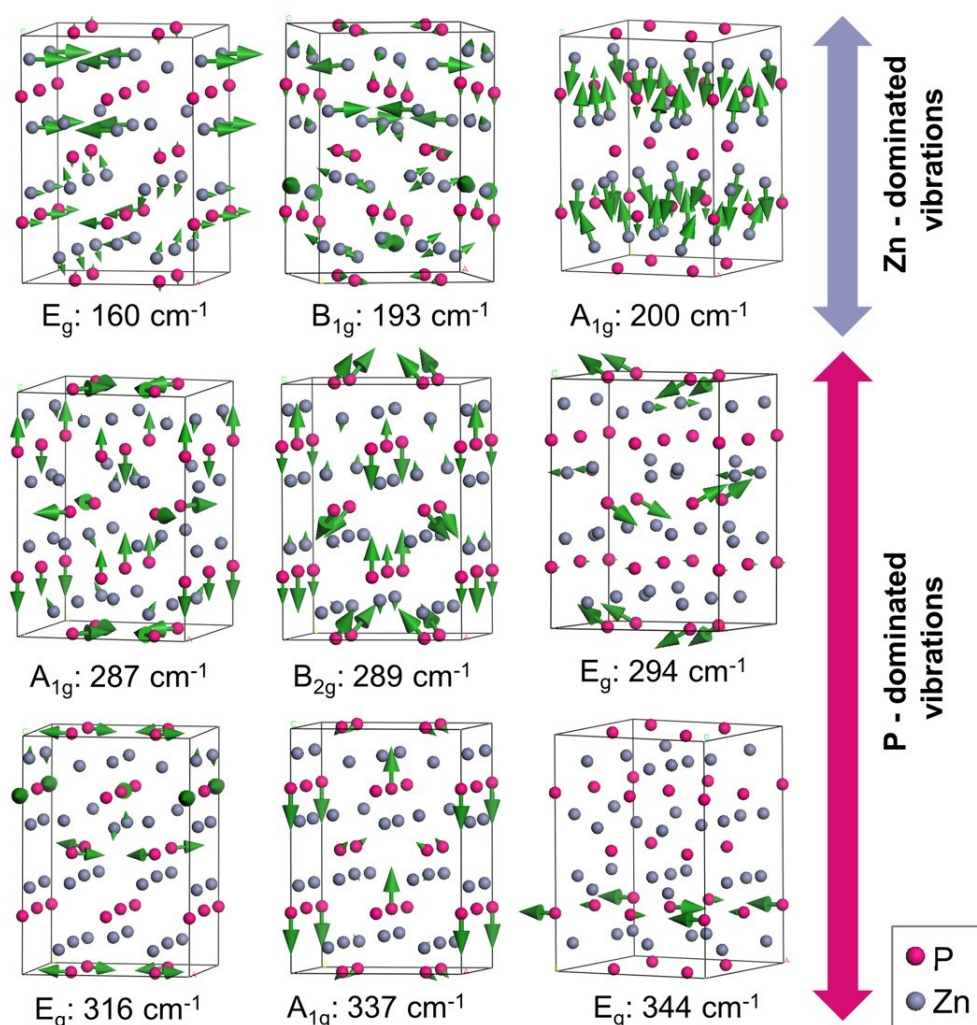


Figure 4.6 – Calculated phonon displacements for several representative modes of Zn_3P_2 . Mode symmetries and frequencies (in cm^{-1}) are listed under each picture.

Finally, atomic displacements of the Raman modes were calculated to provide the visualization of the corresponding atom motions. Figure 4.6 shows representative vibrational patterns. As expected from the PDOS, the vibrational patterns are mostly dominated by either Zn ($<200\text{ cm}^{-1}$) or P motions ($>225\text{ cm}^{-1}$). E_g -symmetry modes represent primarily in-plane vibrations, perpendicular to the long c -axis of the crystal lattice ($160, 316$ and 344 cm^{-1}). On the other hand, non-degenerate modes involve mostly atomic motion along the c -axis. The A_{1g} mode centered at 200 cm^{-1} , for example, corresponds to compression of Zn layers towards P atoms at 4c and 4d Wyckoff positions. The A_{1g} mode at 287 cm^{-1} involves breathing-like vibrations of P atoms around the vacancy at 8e Wyckoff position. On the other hand, the A_{1g} mode at 337 cm^{-1} involves asymmetric stretching vibrations along the c crystal axis of P atoms at 4c and 4d positions. Other modes exhibit more complicated vibrational patterns, which can involve both in and out of plane motions of atoms, as shown in figure 4.6.

4.6 Conclusion

In conclusion, this work provides a reference Raman spectrum of tetragonally-structured Zn_3P_2 , with the complete analysis of all Raman active modes from both experimental and theoretical perspectives. High-resolution Raman scattering measurements that were performed under different polarization configurations on the basal (010) plane of single crystal nanowires, together with the detailed deconvolution of the Raman spectra with Lorentzian curves, have allowed identification of 33 Raman peaks out of 39 even parity vibrational modes. The experimental results are in good agreement with the vibrational frequencies that have been computed by first-principles calculations based on DFT. Further calculations of the PDOS (elemental and total), as well as the phonon dispersions allowed for a better understanding of the experimentally observed phonon lines, as well as the assignment to the specific lattice eigenmodes. In particular, three separate regions were observed in the phonon dispersion diagram: (i) a low-frequency region ($<210\text{ cm}^{-1}$) which is dominated by Zn-related vibrations, (ii) an intermediate region ($210\text{--}225\text{ cm}^{-1}$) which represents a true phonon gap with no observed vibrations, and (iii) a high-frequency region ($>225\text{ cm}^{-1}$) which is attributed to primarily P-related vibrations. These results can be used as a reference for identification of the Zn_3P_2 phase, as well as for building Raman based methodologies for effective defect screening of bulk materials and films, which might contain structural inhomogeneities.

4.7 Supplementary information

The supplementary information is presented in appendix F and includes growth parameters, details on the electrical contact fabrication, lists of reported Raman peaks for $\alpha''\text{-Zn}_3\text{As}_2$, simulations of electron diffraction patterns and fitting details of the carrier concentration regimes.

4.8 Acknowledgements

The authors gratefully acknowledge support from the Swiss National Science Foundation (SNSF) through project BSCGI0_157705 and by the Max Planck-EPFL Center for Molecular Nanoscience and Technology.

5 Showcasing the optical properties of monocrystalline zinc phosphide thin films as an earth-abundant photovoltaic absorber

5.1 Accompanying information

This work has been submitted to a peer-reviewed journal and is under review at the time of writing. The list of authors is as follows: Elias Z. Stutz, Mahdi Zamani, Djamshid A. Damry, Léa Buswell, Rajrupa Paul, Simon Escobar Steinvall, Jean-Baptiste Leran, Jessica L. Boland, Mirjana Dimitrievska and Anna Fontcuberta i Morral. My contributions to this work include writing the manuscript and the acquisition and analysis of the photoluminescence and Raman data.

5.2 Abstract

Zinc phosphide, Zn_3P_2 , is a semiconductor with a high absorption coefficient in the spectral range relevant for single junction photovoltaic applications. It is made of elements abundant in the Earth's crust, opening up a pathway for large deployment of solar cell alternatives to the silicon market. Here we provide a thorough study of the optical properties of single crystalline Zn_3P_2 thin films grown on (100) InP by molecular beam epitaxy. The films are slightly phosphorus-rich as determined by Rutherford backscattering. We elucidate two main radiative recombination pathways: one transition at approximately 1.52 eV attributed to zone-center band-to-band electronic transitions; and a lower-energy transition observed at 1.3 eV to 1.4 eV attributed to a defect band. We believe phosphorus interstitials are likely at the origin of this band.

5.3 Introduction

Direct-bandgap solar absorbers with non-toxic components that are abundant in the Earth's crust are essential for replacing photovoltaic technologies using scarce and toxic materials. Earth-scarce indium, gallium, selenium or tellurium are all part of commercially-available CIGSSe (copper indium gallium sulfide selenide) and CdTe photovoltaic solar cells. Technologies based on these elements are precluded from ever reaching the terawatt energy production scales needed to sustainably supply renewable energy without using vanishingly small amounts of material [36, 379]. A semiconductor with non-toxic components satisfying both the needs for abundance and suitable properties for light absorption in photovoltaics is zinc phosphide, α -Zn₃P₂ [52], hereafter referred to as Zn₃P₂. This semiconductor has a direct 1.5 eV bandgap, strongly absorbs visible light ($>10^4$ - 10^5 cm⁻¹) [349, 380] and exhibits carrier diffusion lengths of several micrometers [103]. However, two challenges have been holding back the power conversion efficiency of zinc phosphide solar cells, with the record standing at 6% for the past 40 years [104]. First, Zn₃P₂ has a relatively large coefficient of thermal expansion (CTE), compared to conventional III-V semiconductors [227]. Combined with the absence of commercially-available lattice-matched substrates, this can induce large thermal-mismatch strain during cooling after processing and the formation of mismatch dislocations and cracks. Several successful workarounds have been shown in the past years. For example, the growth of Zn₃P₂ on graphene completely removes the influence of lattice- and CTE-mismatch by removing the formation of covalent bonds at the interface [261]. Whereas, the growth of nanostructures, either vapor-liquid-solid-grown nanowires [262] or by selected area epitaxy limiting growth to nanoscale areas [263] allows the formation of higher-quality crystals with their increased control of mismatch strain and defects close to the interface. The second main challenge in the development of zinc phosphide is doping. This semiconductor has almost always been found to be intrinsically p-doped, due to the small formation energy of intrinsic acceptor defects such as phosphorus interstitials [363, 381]. Doping engineering is critical for the formation of homo- and heterojunctions with properties tailored for photovoltaic applications and reaching the expectations of this promising PV material. Defects can also influence other electronic properties, such as carrier lifetimes [382], and can lead to localized bandgap fluctuations [383], all of which contribute to the efficiency of electronic devices [287]. Therefore, a thorough understanding of the defects, their electronic properties and their interplay with the growth conditions is crucial for the development of photovoltaic cells with this earth-abundant absorber.

Photoluminescence (PL) spectroscopy can provide relevant information on the material properties. It is highly sensitive to the presence of defects and the electronic band structure, as they are often involved in radiative recombination processes [384]. This non-destructive and contactless technique is commonly used to characterize the optoelectronic properties of semiconductors. The different characteristics of the PL peaks are related to the average properties of defects or electronic bands, such as their relative positions and their concentrations [385, 386]. Uncontrolled growth and poor crystalline quality can increase the complexity

and variability of the PL spectra, making their interpretation more challenging and less reliable. To date, some of the most complete PL studies of this semiconductor were done by Briones et al., who studied the details of pair transitions at low temperatures [351], and by Kimball et al., investigating the PL emission of polycrystalline Zn_3P_2 wafers from 5.9 K to 310 K [103].

In this work, we investigate the steady-state PL spectrum of monocrystalline zinc phosphide thin films grown by molecular beam epitaxy on one of the best lattice-matched substrates, (100) InP. Temperature-dependent measurements are complemented by power-dependent PL measurements to study the electronic transitions involved in the radiative emission pathways. We also characterize the carrier dynamics via another non-contact technique, optical-pump terahertz-probe optical pump terahertz probe (OPTP) spectroscopy and demonstrate long lifetimes suitable for photovoltaic applications. To the best of our knowledge, this is the most thorough description of the PL spectrum of a high-quality Zn_3P_2 thin film, and one of the most thorough PL studies of zinc phosphide overall. Our results can be used as a basis of comparison for the defect characterization of more complex and disordered Zn_3P_2 structures, leading to the characterization of the interplay between the processing conditions and optoelectronic properties of the semiconductor.

5.4 Experimental section

The thin films studied here were prepared following reference [260]. X-ray diffraction measurements were performed using a Panalytical Empyrean diffractometer operating in Goni scan configuration with a copper (K_α) X-ray source with 1.54 Å wavelength, operating at 35 keV and 40 mA. The scanning electron microscopy images were taken in a Zeiss MERLIN™ field emission scanning electron microscope (SEM) with a 20° tilt and an Inlens detector. The micro-Raman spectrum has been acquired using a TriVista triple spectrometer with 900, 900 and 1800 mm^{-1} gratings in subtractive mode and a Princeton Instruments liquid nitrogen cooled multichannel CCD PyLoN camera. The excitation light was the 532 nm line of a Coherent Sapphire SF optically pumped semiconductor laser and was focused onto the sample in back-scattering geometry with a microscope objective (numerical aperture: 0.75), reaching spot diameters of about 1 μm . A gaussian filter with a standard deviation of 1.5 pixels (approximately 0.88 cm^{-1}) was used to smooth the Raman spectrum. The measurement was carried out at 12 K in a cryostat pumped to roughly 5×10^{-7} mbar. The same cryostat and focusing objective were used to carry out the micro-photoluminescence measurements. Those were captured with an Andor iDus DV420A-OE detector, illuminated with the 488 nm line of a Coherent Sapphire laser. The photoluminescence spectra were corrected for the spectral sensitivity of the detection system and transformed to the energy scale with the Jacobian transformation. Parasitic features of the spectra, such as cosmic rays and a diffracted peak of the laser at 1.27 eV have been replaced with artificial data points for clarity and are shown as different color shades in the figures. Rutherford backscattering spectrometry measurements, carried out by EAG Laboratories, were taken with a nearly-normally-incident beam of 2.275 MeV alpha particles. The normal detector angle collected particles scattered by 160°, and the grazing

Chapter 5. Showcasing the optical properties of monocrystalline zinc phosphide thin films as an earth-abundant photovoltaic absorber

detector was set at 104° . Assumptions of 6.61×10^{22} atoms/cm³ in the zinc phosphide layer and 5.26×10^{22} atoms/cm³ in the indium phosphide were used, and the atomic concentration uncertainty is $\pm 1\%$.

Optical-pump terahertz-probe spectroscopic measurements were carried out using a spectrometer based on an ultrafast Ti:Sapphire amplifier (Newport Spectra Physics Spitfire Ace, 13 mJ, 1 kHz, 40 fs) described in reference [387]. The terahertz probe was generated by optical rectification in a GaP crystal, before being focused onto the sample. The reflected THz beam was then detected by electro-optic sampling in ZnTe using a balanced photodiode scheme and a high-precision, high-resolution oscilloscope (Pico Technology PicoScope 4262) for data acquisition. To measure in reflection, a silver-coated prism was placed near the focus of the OPTP spectrometer. The THz beam reflected from one side of the prism, onto the sample, off the second face of the prism and subsequently continued along the initial THz beam axis. The angle of incidence was $<15^\circ$ from normal incidence. The sample was photoexcited with a pulse centered at 750 nm ($E_{\text{photon}} = 1.65$ eV) and pulse duration of 40 fs at fluences between 12 and 128 $\mu\text{J cm}^{-2}$. Photoexcitation at this wavelength generates electron-hole pairs within the Zn₃P₂ thin films modifying the dielectric landscape of the sample and inducing a change, ΔE , in the reflection of the electric field of the terahertz probe pulse, E . This value of $\Delta E/E$ is proportional to the photoconductivity of the sample and thus to the free carrier concentration [388]. The temporal evolution of this response therefore provides information on the carrier lifetime and mobility of the sample [389].

5.5 Results and discussion

5.5.1 Crystalline properties

First, the crystalline structure of the thin film is characterized. The X-ray diffraction pattern measured in goni geometry from the thin-film and substrate structure is shown in figure 5.1a. As elucidated in reference [260], this pattern is a characteristic fingerprint of monocrystalline thin films on InP. The monocrystallinity of the film is also verified by transmission electron microscopy selected area diffraction patterns of thin film cross-sections in data presented in references [260] and [390]. Figure 5.1b shows a tilted scanning electron micrograph of a cleaved cross-section. The film surface is slightly undulated due to the uneven growth of a thin layer of native oxide [310]. At about 800 nm, the Zn₃P₂ film is thick enough to absorb most of the incident laser light. The 99% attenuation length in zinc phosphide for the light of the two lasers used for optical spectroscopy in this study is approximately 280 nm and 200 nm, for 532 nm and 488 nm wavelength, respectively [391]. This is 2.8 to 4.0 times shorter than the 800 nm film thickness, about 660 nm. The contribution of Zn₃P₂ to the optical spectra is thus expected to dominate the contribution of the InP substrate. It is shown below that this is true, except for low-temperature photoluminescence spectroscopy. Topographical ridges can be seen crossing the cleaved cross-section and substrate. These are attributed to the strain at the interface and are sometimes observed after cleaving.

The unpolarized Raman spectrum of the film is shown in figure 5.1c. The spectrum is a clear fingerprint of the D_{4h} α - Zn_3P_2 lattice [245, 347] and does not show any contribution from the substrate. The peak positions of all phonons in the wavenumber range, determined experimentally in reference [347], are shown with symbols under the spectrum.

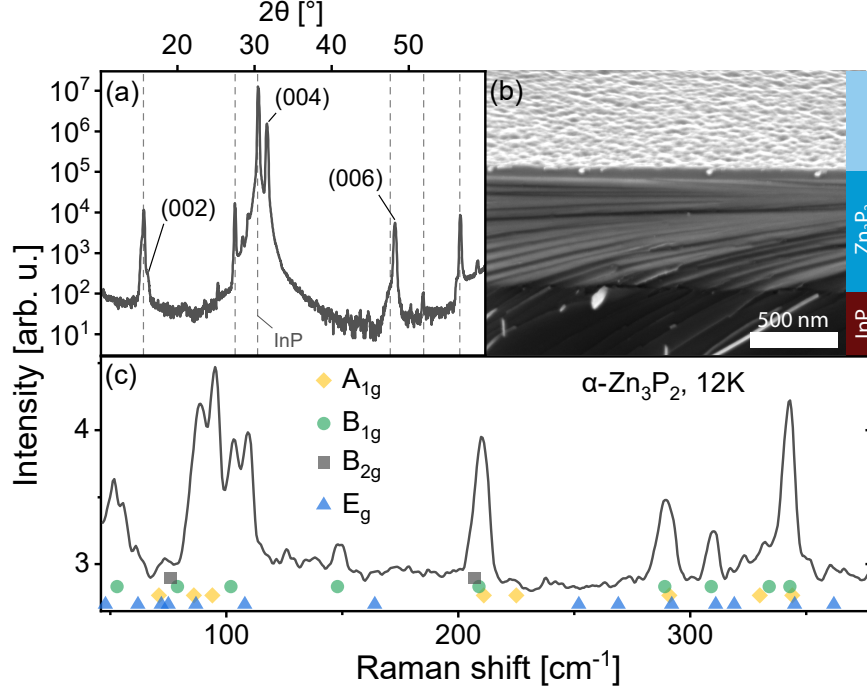


Figure 5.1 – Representative (a) X-ray diffraction (XRD) spectrum, (b) tilted cross-section scanning electron micrograph and (c) Raman spectrum of a Zn_3P_2 thin film on InP. XRD peaks assigned to the InP substrate are shown with dashed lines. The experimentally-determined peak positions of the phonons of Zn_3P_2 , from reference [347], are shown with colored symbols.

The film is oriented with the c -axis perpendicular to the (100) InP substrate surface, as seen in the XRD pattern. The (004) peak of Zn_3P_2 is located at $2\theta = 31.61 \pm 0.026^\circ$ in the pattern. Lattice parameter c calculated from the XRD pattern is equal to $11.67 \pm 0.15 \text{ \AA}$. This is about $2.4 \pm 1.3\%$ larger than the lattice parameters of bulk crystals [249]. Considering uniaxial elongation of the crystal uniformly across the film, we estimate the other lattice parameter using Poisson's ratio ν , calculated from the elastic moduli in reference [243]. With $\nu = \frac{E}{2G} - 1 = 0.32$, where E and G are the Young and the shear moduli, respectively, the lattice parameter a is $8.02 \pm 0.03 \text{ \AA}$, or about $0.8 \pm 0.4\%$ smaller than measured in reference [249]. The lattice of this compound can be viewed as a stack of defected and slightly distorted anti-fluorite cubic cells. The reduced lattice parameter of the tetragonal lattice, a' , is related to the standard tetragonal lattice parameters a_t and c_t in the following way: $2a' \approx \sqrt{2}a_t \approx c_t$ [240]. Comparing the parameter $a' = 5.67 \pm 0.02 \text{ \AA}$, calculated from a_t , with the lattice parameter of InP, 5.8687 \AA , gives a lattice mismatch of $3.4 \pm 0.4\%$ between the Zn_3P_2 thin film and the InP substrate. The film is thus mostly relaxed overall, with a small uniaxial distortion along the c -axis. These values are also

very similar to the lattice mismatch of $\sim 2\%$ determined on other monocrystalline thin films by selected area electron diffraction (SAED) in transmission electron microscopy [260].

The lattice of zinc phosphide can accommodate relatively large compositional variations away from stoichiometry while maintaining the crystalline structure of Zn_3P_2 [262]. The composition of our film across the depth, measured with Rutherford backscattering spectrometry (RBS), is shown in figure 5.2. The analysis of the data is consistent with a uniform composition of 55% of zinc and 45% of phosphorus, making the compound slightly phosphorus rich, compared to the 60:40 composition of stoichiometric Zn_3P_2 .

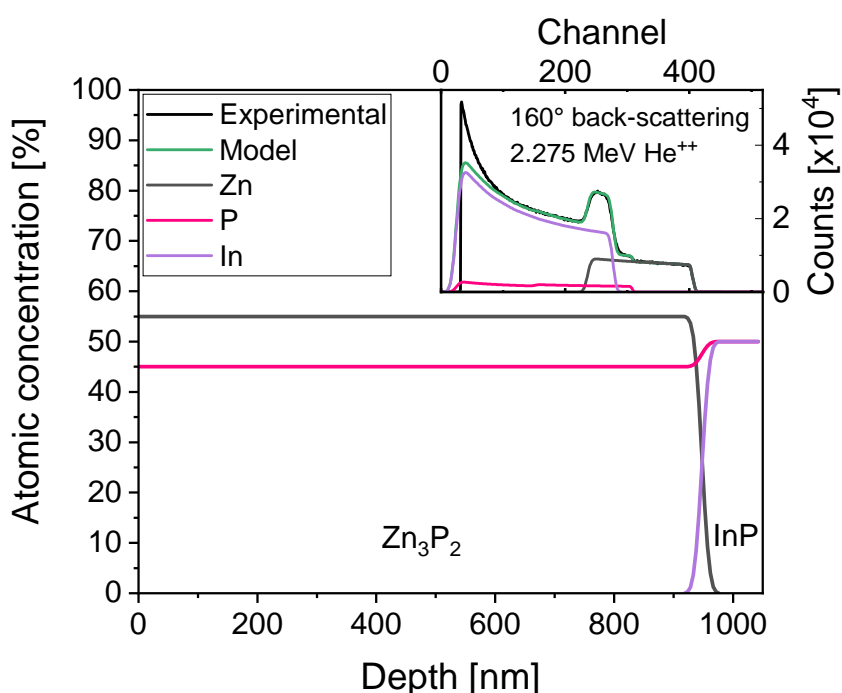


Figure 5.2 – Representative composition along the depth of the sample, calculated from Rutherford back-scattering with 2.275 MeV He^{++} . The inset shows the measured RBS spectrum in back-scattering (160°) and the fit of the spectrum. The spectrum at grazing exit (104°) is shown in the supplementary information (fig. G.1).

5.5.2 Photoluminescence spectroscopy

Now that we have established the structural and compositional characteristics of our film, we turn to the optical properties by means of steady-state photoluminescence spectroscopy. The PL spectra of zinc phosphide, acquired with a 488 nm laser at different temperatures and excitation power densities, are shown in figure 5.3. The spectra are well described with two stable and consistent radiative contributions, one shifting significantly with temperature, and the other, at higher energies, with minimal shift. In addition to these consistent sources, the spectra also exhibit some irregular emissions only observed sporadically.

At 12 K and 30 K, two sets of peaks originating from the InP substrate can be observed, one series of defect-related peaks near 1.377 eV, and their phonon replicas 0.042 ± 0.002 eV lower [392]. The positions of these peaks are indicated with grayed out areas. At temperatures of 100 K and higher, only emission from the film is observed. As discussed above, the light reaching the substrate is more than 6 orders of magnitude less intense than the excitation light contributing to the photoluminescence of zinc phosphide. We think that the observation of InP photoluminescence in our spectra is due to the diffusion of photoexcited charges from Zn_3P_2 to InP, where they would recombine. This hypothesis is supported by the fact that InP photoluminescence is not observed at higher temperatures, where carrier mobility is decreased by scattering effects and carrier recombination dynamics in Zn_3P_2 are altered.

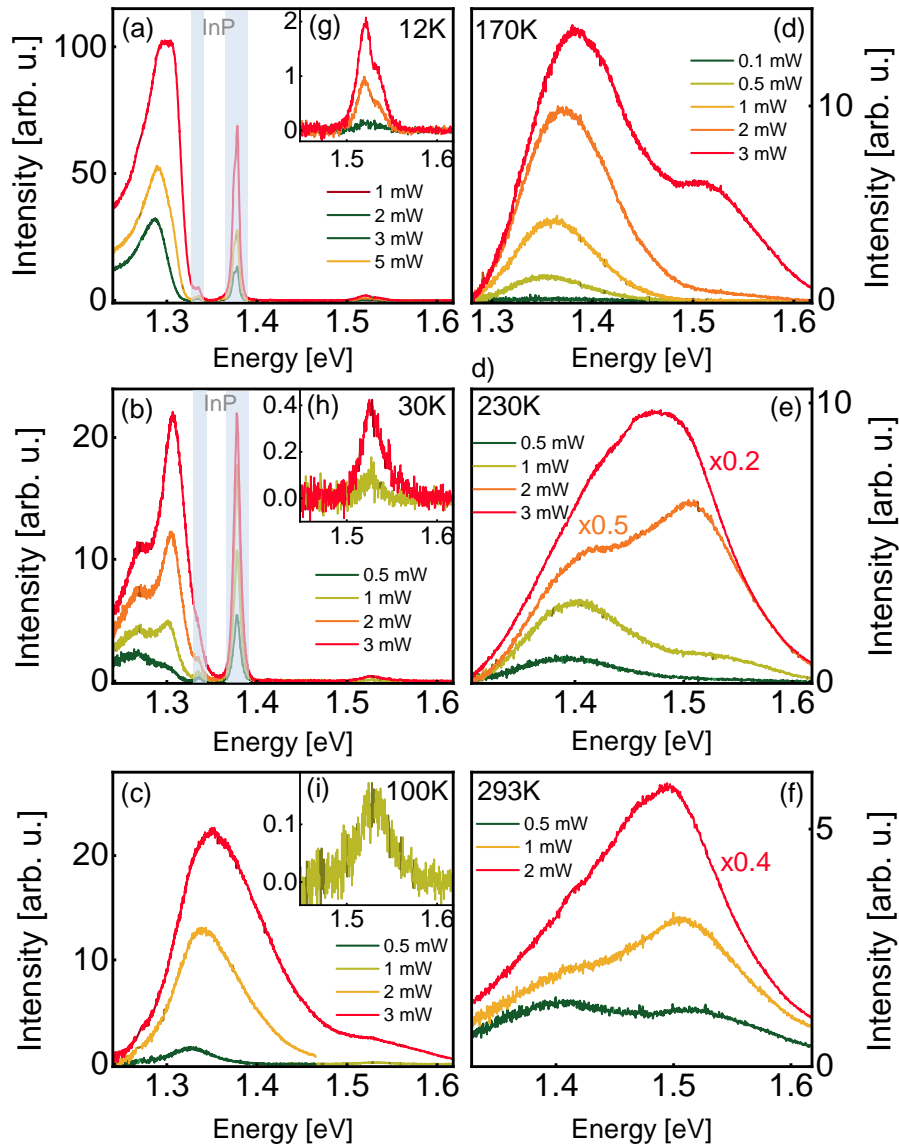


Figure 5.3 – Photoluminescence spectra of a monocrystalline thin film acquired with a 488 nm laser at (a) 12 K, (b) 30 K, (c) 100 K, (d) 170 K, (e) 230 K and (f) 293 K. Insets (g-i) show magnified views of the peaks near 1.52 eV. Photoluminescence peaks assigned to the InP substrate are shown with grayed out areas. Shade differences in the graphs indicate that the data was altered for readability, as described in the main text.

At low temperatures (12 K to 30 K, figs. 5.3a, 5.3b), the zinc phosphide spectrum consists of a set of very intense peaks in the 1.26-1.31 eV range, and a set of much weaker peaks in the 1.52-1.54 eV range, close to the direct bandgap energy of zinc phosphide [393]. We designate these two sets of peaks as low-energy (LE) and high-energy (HE) peaks, respectively. Low-temperature spectra with intense peaks at energies of 1.41 eV and lower appear to be common in zinc phosphide [103, 351, 394, 395].

At higher temperatures (100 K to 293 K, figs. 5.3c-5.3f), the LE and HE peaks in the spectra are not only wider, making them more overlapped, but the broad LE peak is found at higher energies, centered in the range from 1.32 eV to 1.4 eV approximately. To the best of our knowledge, only two other groups published near-room-temperature photoluminescence spectra of this material until today [103, 255, 311]. The results compare relatively well. A peak near the bandgap energy of zinc phosphide is always observed, albeit sometimes without being accompanied by a second peak at lower energy.

We have determined the nature of the transitions involved in the recombination processes for Zn_3P_2 by investigating the excitation intensity dependence of the PL spectra. Models of the different recombination processes in semiconductors indicate that when the incident excitation power (P) is varied over a range of at least two orders of magnitude, the relationship between the intensity of a single PL peak (I) is related to it by a power law of the form: $I \sim P^k$, where k is a coefficient depending on the nature of the transition [295, 396]. Values of k smaller than 1 are interpreted as a recombination involving localization of the carriers at defects with levels inside the band gap. On the other hand, values of k greater than 1 are related to free- and bound-exciton emission. Figure G.2 summarizes the k coefficient of the different observed peaks, wherever it can be estimated. All peaks observed in the PL spectra exhibit power dependency behavior with $k > 1$, excluding the possibility of localized defect levels inside the band gap. Furthermore, some of the PL peaks observed in this study appear to have very high power coefficients (k), such as the peak at approximately 1.31 eV observed at 12 K (fig. 5.3a), which appears to have a coefficient $k=4.2$. It must be noted that this peak is not clearly resolved, and it is currently unclear how many and exactly what kind of radiative electronic transitions contribute to the detected signal in the energy range near this peak. The apparent dramatic intensity increase could be caused by the interplay of multiple peaks.

Low-energy radiative transitions

In the lowest-temperature spectra, acquired at 12 K and 30 K (figs. 5.3a, 5.3b), the LE emission is composed of multiple peaks. The position of these peaks is quite consistent over the film, with some occasional shifts or new peaks close in energy. Figure G.3 in the supplementary information shows different spectra acquired in the same conditions at different locations on a sample at 12 K.

At 30 K (fig. 5.3b), the LE emission can be separated into two contributions, a symmetric peak near the high-energy edge and a wider symmetric peak at lower energies. The spectrum can be very well fitted with two gaussians exhibiting regular and monotonous changes with increasing irradiance (fig. G.4). At 12 K, the LE peaks on the low-energy side are more asymmetric and those on the high-energy side are more difficult to resolve (fig. G.5). Nonetheless, the spectrum can be well described with an asymmetric and a symmetric peak. At 100 K, the LE and HE peaks are separated at low power, and overlap at higher powers. At low power, the LE peak is symmetric and becomes asymmetric at higher powers. Obtained peak properties from the fits are listed in Table 5.1. Both contributions shift to higher energy side with increasing laser power

Chapter 5. Showcasing the optical properties of monocrystalline zinc phosphide thin films as an earth-abundant photovoltaic absorber

at rates in the range from 3 to 6 meV mW⁻¹. These kinds of shifts, along with its asymmetric shape at low temperatures, may be related to band tail recombination mechanisms [396, 397]. High concentrations of randomly distributed charged defects can cause spatial potential fluctuations which in turn create tails in the electron and hole densities of states, at energies below the conduction band minimum, or above the valence band maximum. This might be the case in phosphorus-rich Zn₃P₂, due to the high concentration of phosphorus interstitials.

At temperatures of 170 K and above, the LE and HE peaks are overlap even at low power. They can be well described with one gaussian describing each of the LE and HE peaks. Figures G.7 and G.8 show the variation of the peak parameters with the laser power. Overall, as the temperature increases, the LE peaks shift to higher energies, while the HE peaks do not exhibit a noticeable shift in energy. In figure G.2, the position of the LE (single or double) and HE peaks (single or averaged) are shown for the different temperatures.

Temperature	Note	First LE peak		Second LE peak	
		Position [eV]	Shift	Position [eV]	Shift
12K		1.283 (a)	3.3	1.306-1.310 (s)	
30K		1.262 (s)	5.6	1.299 (s)	3.5
100K	Low power	1.326 (s)			
	High power	1.324 (a)	6.2		

Table 5.1 – Best fit parameters of the low-energy emission at low temperatures. (s) and (a) indicate that the corresponding peak is symmetric or asymmetric, respectively. All peaks shift towards higher energies with increasing power

There has long been a lack of consensus about the nature of the fundamental band transition of zinc phosphide [103], with claims of it being direct [247, 398] and other of it being indirect [399, 400]. Recently, valence electron energy-loss spectroscopy performed on Zn₃P₂ nanowires and spectroscopic ellipsometry on Zn₃P₂ monocrystalline thin films have reported Zn₃P₂ being a direct band gap semiconductor [393]. An explanation to the apparent presence of a fleeting and unpredicted indirect fundamental band edge could be the existence of a defect band or band tails. The presence of an impurity band has already been shown to exist in Zn₃As₂, a II-V semiconductor structurally and electronically very similar to Zn₃P₂ [312]. The critical defect concentration for the Mott transition in Zn₃P₂ and Zn₃As₂ are similar and may be around $2 \times 10^{16} \text{ cm}^{-3}$ [401].

One of the most common defects in zinc phosphide, and most especially in phosphorus-rich crystals, are phosphorus interstitials. These defects are commonly designated as the main reason for the nearly ubiquitous intrinsic p-type doping of zinc phosphide. When charged, these defects could facilitate the formation of defect bands or band tails due to their large delocalization [363]. Such bands or degenerate doping have never been reported in zinc phosphide. However, given the very phosphorus-rich nature of our films and the aforementioned properties of the most common defects, the presence of an impurity band or

band tails is a real possibility.

The existence of a defect band can explain the LE peak observed in these samples. Let us assume that the high concentration of defects, likely phosphorus interstitials acting as acceptors, creates an impurity band (IB) close to the valence band maximum (VBM), peaking in the center of the Brillouin Zone. Direct transitions between the conduction and the valence band are at the origin of the HE ~ 1.5 eV peak in the photoluminescence spectrum, while indirect transitions between the conduction band and the impurity band result in the other main peak at lower energies. The HE peak does not shift significantly with temperature, while the LE peaks appear to blueshift with increasing temperature (fig. G.2), at a rate of approximately $4.0 \times 10^{-4} \text{ eV K}^{-1}$, consistent in magnitude with band shifts reported in the literature for zinc phosphide [351, 398, 402, 403]. The VBM and the IB maximum would thus have different temperature dependences. This is consistent with some observations. Bands with temperature shifts of opposite signs have been observed experimentally in zinc phosphide [351, 403].

The energy levels involved in the observed LE PL emission may also have a yet undiscussed origin. It has recently been shown that rotated crystallites with interfaces free of dangling bonds can be formed during growth [404]. DFT calculations have shown that the electronic bandgap at these interfaces is significantly decreased compared to the bulk, on the order of 0.1 eV smaller, and new localized acceptor levels are formed. The existence of these 2D defects also appears to have near to no additional energetical cost compared to their absence, though their dependence on temperature is still unknown. Additionally, the nanoscale growth process leading to the formation of these defects, i.e., the growth and merger of differently-oriented Zn_3P_2 nuclei on (100) InP, is likely to have also occurred in the growth of the thin films discussed in this work. For these reasons, the presence of these defects in our thin films is likely, but their density and impact are undetermined. It is challenging to observe these rotated domain interfaces and additional work would be needed to quantify them in monocrystalline thin films and to experimentally verify their properties. Radiative recombination across the reduced bandgap at these interfaces could potentially be an origin of some or most sub-bandgap radiative transitions observed in this work.

High-energy radiative transitions

Contrary to the LE peaks discussed in the previous section, the position of the HE peaks at about 1.5 eV is only weakly affected by temperature (fig. G.2). At 12 K and 30 K, the HE peaks are about 50 to 100 times less intense than the LE peaks for all powers, but the intensities of the two sets of peaks become more balanced at higher temperatures. This kind of peak behavior suggest band to band transitions, between the valence and conduction bands. Furthermore, the position of the peaks matches well previously reported results for direct band gap of Zn_3P_2 at around 1.5 eV [103, 393].

At 12 K, the HE peak is a doublet (fig. 5.3g). The lineshape is well fitted with two gaussians

with a separation of 18.1 meV to 18.6 meV and an intensity ratio of 3 to 4. At 30 K (fig. 5.3h), the peaks are not well resolved, and can tentatively be assigned a splitting of 27 meV. At higher temperatures, the doublet cannot be resolved. The higher-energy peak is smaller than the lower-energy peak, like in Cd_3P_2 [405]. Contrary to the PL peak splittings reported until now for Zn_3P_2 , this doublet cannot be due to a phonon replica since the lower intensity peak is at a higher energy. The measured splitting of the doublet is close to the crystal field splitting of zinc phosphide, reported to be around 0.02 eV [406] to ~ 0.04 eV [247, 398]. This is the first time the crystal field splitting of this semiconductor is observed in a photoluminescence spectrum, a testament to the exceptional crystalline quality of these structures.

5.5.3 Optical pump terahertz probe spectroscopy

To further characterize the temporal dynamics of photoexcited carriers, we studied the film with optical-pump terahertz-probe (OPTP) spectroscopy in reflection mode at room temperature. OPTP spectroscopy is sensitive to both radiative and non-radiative recombination processes, so the photoinduced response probes the temporal evolution of any conductive or polarizable charge species, including excitons, plasmons and free charges. The thin films were photoexcited at a center wavelength of 750 nm, corresponding to a photon energy of 1.65 eV. This photon energy is above the expected direct bandgap of Zn_3P_2 , and hence should inject free electron-hole pairs within the thin film at room temperature⁴⁴. As the thickness of the thin film is greater than the absorption depth of Zn_3P_2 at 750 nm, the photoinduced THz response is dominated by the contribution from the Zn_3P_2 thin film with a negligible response from the InP substrate (see SI). Using the value of the absorption coefficient at this photoexcitation wavelength [407], the photoinduced carrier densities within the film were calculated to be between $4.9 \times 10^{17} \text{ cm}^{-3}$ and $5.17 \times 10^{18} \text{ cm}^{-3}$ for the fluence range.

Photoexcitation leads to a sharp rise in the THz photoconductivity followed by a biexponential decay on a nanosecond timescale. Figure 5.4 shows the change in photoconductivity with time after photoexcitation at photoexcitation fluences of 12, 28, 57 and $128 \mu\text{J cm}^{-2}$. Stronger pump fluences will photodope higher carrier densities into the conduction band. For the fluences used in this study, the peak photoconductivity and thereby excited carrier density is linearly related to the laser fluence (fig. G.10). The decay curves displayed a biexponential behavior at all fluences, and the solid black lines in figure 5.4 show the fitted plots through the experimental data. The extracted characteristic decay constants of the biexponential fits are listed in table 5.2.

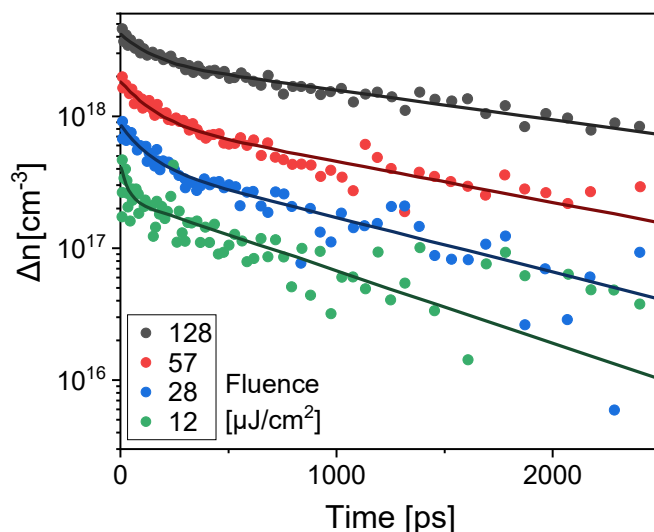


Figure 5.4 – Decay of excess charge carriers measured by terahertz probe spectroscopy at four pump fluences. Decay is biexponential.

Pulse fluence [$\mu\text{J cm}^{-2}$]	τ_1 [ns]	τ_2 [ns]
128	0.12	1.94
57	0.12	1.40
28	0.10	1.01
12	0.03	0.79

Table 5.2 – Characteristic decay times of the best bi-exponential fits to the carrier decay data.

At the timescales of this experiment, the carrier dynamics are dominated by a fast decay process (τ_1) with a time constant of ~ 0.1 ns, followed by a longer decay process (τ_2) with a time constant of ~ 1 ns. Both decay times increase slightly with increasing laser fluence and are likely attributable to surface and bulk recombination effects. The monoexponential behavior of the fast and slow decay components suggests that the recombination is dominated by monomolecular recombination. Both bulk band-edge and surface recombination pathways have been attributed to low-nanosecond range decay phenomena in zinc phosphide [408, 409], and exciton recombination times are in the order of 0.1 ns [410].

The native oxide of zinc phosphide passivates more than 90% of electrically active surface recombination states [408]. Given that our samples have not been treated since their growth, the 0.1 ns fast decay component cannot be on account of surface recombination processes. We therefore attributed the 1 ns slow decay component instead to recombination through surface states. This is further supported by the increasing decay times with increasing fluence. Surface states become saturated at high carrier injections, slowing the recombination rate at the surface. On the other hand, the faster recombination pathway is attributed to band-

edge recombination. This is consistent with the direct nature of the transition and the minor changes in recombination rates at higher fluences. Still, further studies are recommended to separate the effects of bulk and surface recombination more reliably and to identify the major bulk recombination pathways observable in OPTP spectroscopy.

5.6 Conclusion

In this work, we characterize the crystalline and photoluminescence properties of monocrystalline Zn_3P_2 thin films grown on (100) InP by molecular beam epitaxy. The films are phosphorus-rich and are oriented with the c-axis perpendicular to the substrate. The thin films exhibit two main radiative recombination pathways. A transition at approximately 1.52 eV is attributed to zone-center band-to-band electronic transitions. At 12 K and 30 K, the peak forms a doublet owed to the crystal field splitting of the tetragonal material. A second, lower-energy transition is observed at 1.3 eV to 1.4 eV and is attributed to a defect band or band tail transition. Phosphorus interstitials are likely at the origin of this band. Further studies should aim to more reliably separate surface and bulk effects with suitable surface treatments and to refine the identification of the specific defects involved in radiative recombination. The effect of the precise stoichiometry on the optical properties of thin films, in contrast to nanowires [262, 349], should also be studied in the future.

5.7 Acknowledgments

The authors gratefully acknowledge support from the Swiss National Science Foundation (SNSF) through project BSCGI0_157705 and by the Max Planck-EPFL Center for Molecular Nanoscience and Technology. M.D. thanks funding from H2020 through SMARTCELL project (project number: 101022257). The authors also thank EAG Laboratories for performing the Rutherford backscattering spectrometry measurements. J.L.B also gratefully acknowledges support from EPSRC via project EP/S037438/1 and from the Leverhulme Trust via the Philip Leverhulme Prize. She would also like to thank the University of Warwick for providing access to the Warwick Centre for Ultrafast Spectroscopy (WCUS) facility and Dr Michael Staniforth for conducting the THz spectroscopy measurements during the COVID lockdown period. J.L.B also thanks Dr Christopher Beckerleg for fruitful discussions.

5.8 Supplementary information

The supplementary information is presented in appendix G. It includes a RBS at grazing exit, additional PL data and fits to the spectra, and complementary OPTP data.

6 Conclusion & Outlook

In this thesis we investigated the electronic properties of zinc phosphide and zinc arsenide as well as the properties of their crystalline lattices. Our results contribute to establishing a detailed understanding of the fundamental properties of these semiconductors and their relationship with their structure and conditions of growth. This work paves the way towards the fabrication of efficient zinc phosphide solar cells with controlled and optimized electronic and optical properties.

In chapter 3, we showed that zinc arsenide nanosails exhibit a crystalline structure that is metastable in bulk form, only observed previously in thin films. We also showed that the nanostructures are degenerate p-type semiconductors with pure impurity band conduction at low temperature. Next steps to develop this work further would understanding the mechanisms leading to the change of phase and being able to control the phase at will. This would require new MOVPE growths of Zn_3As_2 with systematic change in the growth conditions and structural analysis with X-ray and microscopy techniques. This work is not planned currently.

In the second publication, chapter 4, we studied the Raman spectra of zinc phosphide. We identified 34 of the 39 Raman-active phonon peaks, and assigned their symmetry. The DFT calculations match well with the peaks acquired by deconvolution of the experimental spectrum, and we reveal that zinc- and phosphorus-dominated vibrational modes are separated by a real phonon gap. This work provides a reference Raman spectrum for zinc phosphide and isostructural compounds such as $\alpha''\text{-Zn}_3\text{As}_2$ and $\alpha''\text{-Cd}_3\text{P}_2$.

Then, in chapter 5, we demonstrated that monocrystalline Zn_3P_2 thin-films grown by molecular beam epitaxy also contain a defect band, and that the quality of the grown structures is high enough to observe band splitting due to the crystal field. Currently ongoing work not presented in this thesis is aiming at understanding and identifying the photoluminescence emission peaks of thin-films and other structures grown under different conditions and with other defect structures to identify the electronic transitions occurring in the material and advancing towards a complete understanding of the electronic structure of Zn_3P_2 and the ability to use photoluminescence as a tool for assessing the quality and defect concentrations

of this material.

6.1 Future development

Given the current state of research on zinc phosphide and the results presented in this thesis, a number of potential research directions are offering themselves to us along the way to the fabrication of efficient Zn_3P_2 solar cells. The sections below discuss different proposed new steps of zinc pnictide research.

6.1.1 Crystal structure and properties

There is still a lot left to do regarding the identification and characterization of the less common phases in the Zn-P and Zn-Cd-P-As systems, as discussed in section 1.3.1. As listed in table 1.11 (p. 35), besides the four established atmospheric-pressure Zn-P phases, at least six other zinc-phosphorus phases appear to have been synthesized, and three more have been shown computationally to be at least metastable. The Zn-Cd-P-As is even far more complex, exhibiting at least one phase not observed in any of its binary constituents (α'''). The $\text{A}_3^{\text{II}}\text{X}_2^{\text{IV}}$ compound family especially appears to show several polymorphs at near standard temperature and pressure (α , α' , α'' , α''' and maybe more?), as already discussed in this thesis (see section 1.3.1 and chapter 3). These phases only differ in their ordering of cations and have relatively similar diffraction patterns, as illustrated by figure E.1. I suspect that the structural similarities of these phases and the still nascent understanding of their properties likely has and is going to cause them to be confused one for another. The structural transitions between these phases is relatively simple, with only a fraction of the metal atoms shifting to the nearest tetrahedral void [242, 243]. Apparently, the relative stability of these phases is fragile and can be affected by moderate phenomena, as evidenced by two phenomena. The first is the appearance of an uncommon phase of Zn_3As_2 when grown under strain on a mismatched substrate [245] or as nanostructures [312]. The second being the two phase transitions occurring when substituting small fractions of the cations or anions in α - Zn_3As_2 and in α - Cd_3As_2 by the other cation or by phosphorus, respectively (fig. 1.8, p. 36). Imperfectly controlled growth of these phases may end up with mixtures of different α phases unbeknownst to the growers, and it could turn out that only careful studies of the characteristics of the phases of even the most pristine structures may tell them apart. I think it likely that other unexpected or even new phases in the $\text{A}_3^{\text{II}}\text{X}_2^{\text{IV}}$ system will turn up as the study of these compounds moves forward. Future work will likely confirm or invalidate the existence of the less explored phases in this material system.

6.1.2 Measuring the dielectric function

A near-perfect control and knowledge of the dielectric function of Zn_3P_2 is necessary to reach its peak potential of energy conversion as a solar cell absorber. Knowledge of these prop-

erties helps understanding light propagation in the material and devices it is used in, and is necessary to tune anti-reflection coatings, layer thicknesses and light trapping structures. The idealized isotropic index of refraction and extinction coefficient are starting to be relatively well known over large energy ranges, thanks in part with the recent determination of these properties from below-bandgap energies up to 20 eV by valence electron energy loss spectroscopy (VEELS) [393]. The anisotropic dielectric function of Zn_3P_2 is slightly less studied. Zn_3P_2 is moderately birefringent, compared to other uniaxial materials listed in reference [411]. It is also slightly photodichroic, i.e. its absorption coefficient depends on the travel direction and polarization of the light propagating in the crystal. This effect appears to be quite pronounced at energies close to the bandgap, as shown by Misiewicz and co-authors in different works, and is observed by offsets in the onset of light absorption of a few hundred meV [247, 412]. These effects are ultimately related to the details of the band structure of the material. It has been proposed that the fundamental CBM to VBM transition is forbidden for light polarized perpendicularly to the c-axis of the crystal [247]. As far as I am aware, some work is still required to unambiguously determine the symmetries of the bands near the CBM and the VBM, helping to elucidate the selection rules for the near-bandgap optical transitions. Especially, the reports about the symmetries of the lowest conduction bands and the highest valence bands have sometimes contained conflicting information and would require some attention [413–419]. The symmetry of the band extrema change from the high-symmetry zincblende structures through both the effects of the spin-orbit interactions and the tetragonal distortion of the lattice, its crystal field splitting. In addition to shedding new light on the fundamental properties of pristine Zn_3P_2 , such an investigation would also be closely related to the study of crystalline defects and their effects on the optoelectronic properties of the material.

6.1.3 Defects

The work presented in this thesis has shown progress towards the description of certain optical and lattice properties of high-quality zinc phosphide and zinc arsenide, in thin-film or nanostructure forms. Description of the defects in "lower" quality structures and their impact on all properties of the crystals is the next step towards the description of materials synthesized with cheap and scalable growth techniques. The location of the main intrinsic and some extrinsic point defects has been established computationally [343, 363]. Nonetheless, establishing the concentrations of the different types of defects is rarely done and challenging. Establishing experimentally the relationships between processing conditions and the concentration of different defects, the microscopic and local properties of the defects and their impact on the macroscopic properties of the bulk material will certainly be an important research topic for the creation of optoelectronic devices made with these zinc pnictides.

6.1.4 Surfaces and interfaces

The understanding of the structure of Zn_3P_2 surfaces and interfaces and their electronic passivation have improved over the past decade. The Mg- Zn_3P_2 interface at the heart of the record solar cell and the disputed reasons for the relatively good efficiencies of these cells are now well understood [420–423]. When it was previously thought that magnesium diffusion into Zn_3P_2 doped the semiconductor, it is now established that a ternary Mg-Zn-P compound formed at the interface contributes to the rectifying behavior of the cell. It has also been shown that the growth of Zn_3P_2 on the nearly lattice-matched GaAs forms up to a few monolayers of GaP at the interface [252]. New general considerations about metal- Zn_3P_2 interfaces have been established [424], and the passivation of films [311, 408], nanowires [425] and nanoparticles [426] have been investigated. DFT computations have revealed the intimate details of the energetics and geometry of small molecule adsorption on Zn_3P_2 [364, 365, 427] and the surface energies of different crystalline planes [263]. Furthermore, two new types of 2D defects have been discovered in this crystal system: heterotwins, containing a monolayer of indium [250], and rotated domain interfaces (Spadaro & Escobar Steinvall, submitted).

Nonetheless, a stable and inorganic electric passivation scheme of zinc phosphide surfaces compatible with the processing of zinc phosphide and its preparation into a solar cell is still needed. Some of the current proposed mechanisms may satisfy all these conditions. This has yet to be verified.

A Additional data

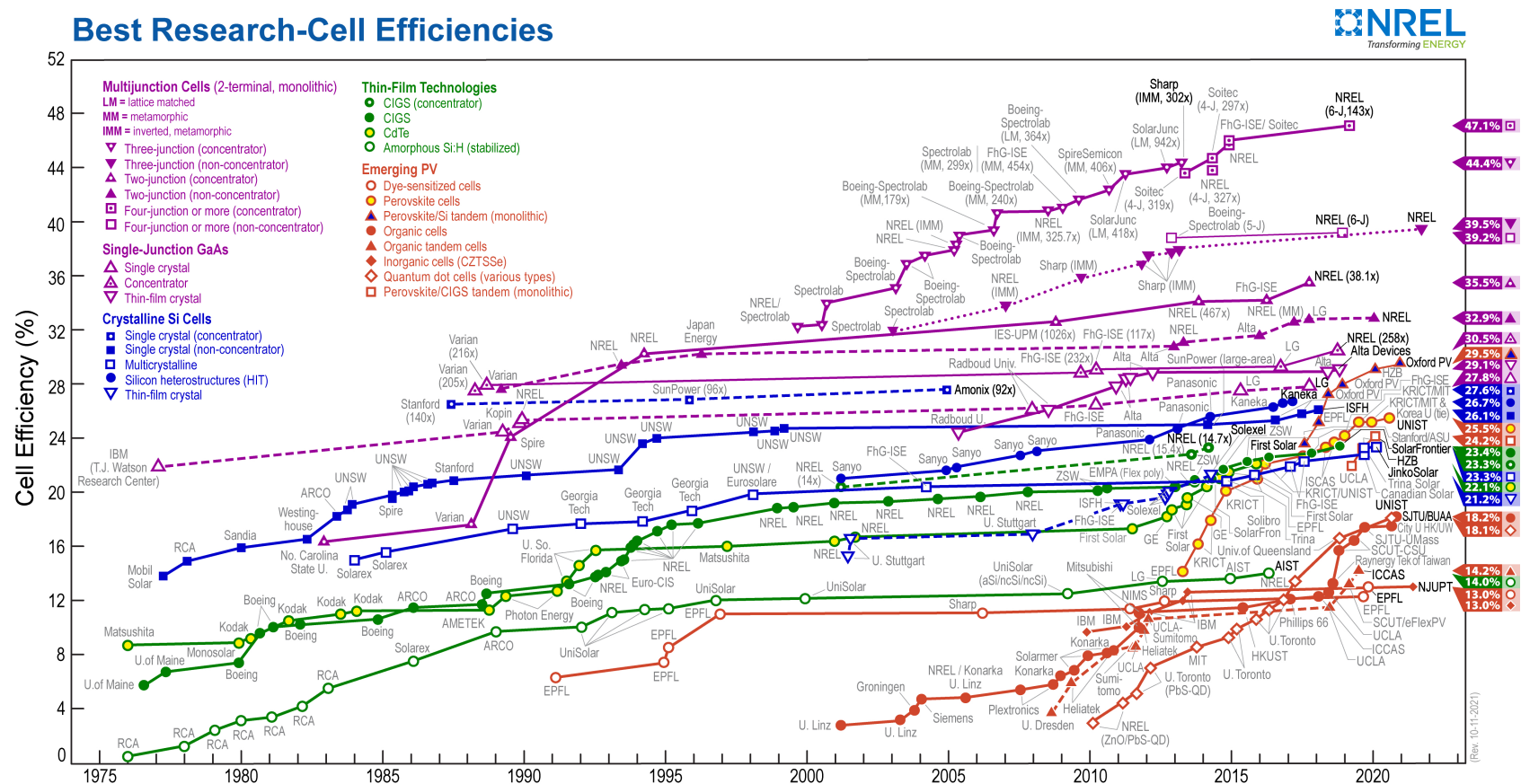


Figure A.1 – Chart of research-quality solar cells by highest confirmed energy conversion efficiency. Chart version: 11th of October 2021. Full details and legends are available at www.nrel.gov/pv/cell-efficiency.html. This plot is courtesy of the National Renewable Energy Laboratory, Golden, CO, USA [31].

B Additional properties of zinc phosphide

B.1 Mechanical properties and structure

Property		value	unit	source
Density	ρ	4485	kg m^{-3}	[243]
Horizontal sound velocity	V_L	5290	m s^{-1}	[243]
Vertical sound velocity	V_t	2000	m s^{-1}	[243]
Coefficient of elasticity (Young?)	ε	$9.8 \cdot 10^{-10}$	N m^{-2}	[243]
Coefficient of elasticity (Shear)	G	$3.7 \cdot 10^{-10}$	N m^{-2}	[243]
Poisson's ratio	ν	0.32	-	calc.
Coefficient of adiabatic compression	χ	$0.9 \cdot 10^{11}$	m^2N^{-1}	[243]
Debye temperature	θ_D	320	K	[243]
Static dielectric constant	ε_0	12	[TBD]	[428]
Optical limit of dielectric constant	ε_∞	2	[TBD]	[428]

Table B.1 – Properties of zinc phosphide

Some remaining properties are listed in reference [243]

α_l	8.33×10^{-6}	K^{-1}	[243]
α_l	14×10^{-6}	K^{-1}	[255]
α_a	12.4×10^{-6}	K^{-1}	[227]
α_b	12.3×10^{-6}	K^{-1}	[227]
α_c	10.2×10^{-6}	K^{-1}	[227]
α_V	34.7×10^{-6}	K^{-1}	[227]

Table B.2 – Coefficients of expansion of zinc phosphide. l : linear, a , b , and c : along the three (!) crystalline axes, V : volume.

In [227], the lattice appears to be orthorhombic at low temperatures.

B.1.1 Vibrational modes

References

- [429]: IR
- [430]: absorption, Raman and reflectivity
- [431]: reflectivity, transmissivity and Raman (related to [430])
- [246]: Raman and resonant Raman
- [432]: reflectance
- [337]: reflectance

Techniques

- Reflectance: [337, 430–432]
- IR spectroscopy: [429, 433]
- Raman spectroscopy: [246, 430, 431]
- Absorption: [430, 433]
- Transmittance: [431, 433]

Phonons in indirect optical transitions

Energy of (25 ± 5) meV [400]

B.1.2 Unit cell size and bonding

Lattice parameters:

- $a=8.092 \text{ \AA}$ and $c=11.425 \text{ \AA}$ [228]
- $a=8.0851 \text{ \AA}$ and $c=11.4065 \text{ \AA}$ [227]
- $a=8.0785 \text{ \AA}$ and $c=11.3966 \text{ \AA}$ [249]
- $a=8.097 \text{ \AA}$ and $c=11.45 \text{ \AA}$ [233]
- $a=8.0889 \text{ \AA}$ and $c=11.4069 \text{ \AA}$ [235]

B.1.3 Bonding

Bond ionicity, $f_i = 0.17$ to 0.19 [247]

B.2 Optical and electronic properties**B.2.1 Band structure**

Some relevant references: [398, 402, 416] Many different values are given for the bandgap energy. Reference [434] reviews some of them. Reference [246] also makes a small summary (pp. 2586)

A detailed discussion about the two types of bandgaps (direct and indirect) is given in [400]. The authors also discuss whether the indirect extrema is in the conduction or the valence band, with details given in [435]. Some authors think that the *indirect* fundamental absorption edge is different for parallel and perpendicularly polarized light [412] [418] but that the anisotropy of the direct gap is small or absent [418]. The indirect bandgap is fitted in [400]. Band edges appear clearly exponential in [398]

Electron affinity

By UV photoemission spectroscopy: 3.2-3.5 eV [436]

Work function

Calculated with DFT for (001), (101) and (110) surfaces [365].

Valence band splitting

A detailed theoretical description of the inclusion of crystal field and spin-orbit splitting into models of the Γ point is given by Dowgiallo-Plenkiewicz in [413].

From: [402], at 77 K to 293 K

$\Delta_{so} = 0.3$ eV to 0.4 eV and $\Delta_{cf} = 0.17$ eV to 0.26 eV

[413], referenced in Pawlikowski's Kane model fitting [437]

$\Delta_{so} = 0.11$ eV and $\Delta_{cf} = 0.03$ eV

From: [438], at unclear temperature (it is unclear how they got the values)

Appendix B. Additional properties of zinc phosphide

$\Delta_{so} = 0.125 \text{ eV}$ and $\Delta_{cf} = 0.03 \text{ eV}$

From: [416], at 77 K

$\Delta_{so} = 0.08 \text{ eV}$ to 0.1 eV and $\Delta_{cf} = 0.02 \text{ eV}$ to 0.03 eV

From: [437], at an undetermined temperature

$\Delta_{so} = 0.17 \text{ eV}$ to 0.18 eV or 0.21 eV and $\Delta_{cf} = 0.04 \text{ eV}$

From: [247], at (potentially) room temperature

$\Delta_{so} = 0.09 \text{ eV}$ to 0.11 eV and $\Delta_{cf} = 0.03 \text{ eV}$ to 0.04 eV

Quite convincing experimental result

From: [406], at an unspecified temperature

$\Delta_{so} = 0.16 \text{ eV}$ and $\Delta_{cf} = 0.02 \text{ eV}$

From: [398], at an undetermined temperature

$\Delta_{so} = 0.2 \text{ eV}$ to 0.243 eV and $\Delta_{cf} = 0.043 \text{ eV}$

Temperature coefficient of bandgap energy

- $-10^{-4} \text{ eVK}^{-1}$ to $-7 \times 10^{-4} \text{ eVK}^{-1}$ [402]
- $\frac{d\alpha_{\parallel}}{dT} \cong 0$ and $\frac{d\alpha_{\perp}}{dT} \cong 15.5 \times 10^{-4} \text{ eV/K}$ [412]⁽¹⁾
- $\frac{d\alpha_{\parallel}}{dT} \cong 0$ and $\frac{d\alpha_{\perp}}{dT} \cong 1.8 \times 10^{-4} \text{ eV/K}$ [403]⁽¹⁾
- $-3.2 \times 10^{-4} \text{ eVK}^{-1}$ [351]
- 10^{-4} eVK^{-1} [398]

⁽¹⁾ Note that the same authors published very different values of $\frac{d\alpha_{\perp}}{dT}$ one year apart. Their absorption measurements look nearly identical.

Positive temperature coefficient bands

- Possible band in CL (referenced by [351]) by [439]
- High-temperature (50 K+) PL band [351]

Carrier effective masses

Lin-Chung's simplified ab initio band diagram calculations [440]:

- Electron in CBM: $m_{\Gamma}^* = 0.128 m_0$

Pawlikowski's Kane model fitting [437]:

- Holes in VBM: $m_{\nu_1}^* = 0.22 m_0$
- Electrons in CBM: $m_c^* = 0.2 m_0$

Valence density of states: [441]. From ab initio: [343, 364, 365, 419, 442]

Band diagram

Pseudopotential energy band calculations of the simplified crystalline structure [440]. Tight-binding band structure of the zinc-blende approximate structure [443] have been done, and the band structure of Cd_3P_2 with the real D_{4h}^{15} symmetry have been done with the pseudopotential method [414] albeit with the neglect of the spin-orbit interaction.

Full crystalline structure DFT calculated band structure are presented in [419], [363] and [343]. The presented DFT diagrams agree quite well. See also [363].

Contrary to reference [247], reference [413] states that the valance bands are split into Γ_7^- , Γ_6^- and Γ_6^- bands after taking into account spin-orbit interaction and the tetragonal distortion. And again, from Andrzejewski's ab initio band structure calculations [419]: the valence bands are Γ_2^- , Γ_5^- and Γ_5^- while the three lowest conduction bands are Γ_5^+ , Γ_5^+ and Γ_3^+ . See also references [414, 415] for comparison. Also reference [418] corrects the level ordering of [416]. A discussion of the level ordering at the Γ point is presented in [417].

Reference [73] discusses in details the band structure of Zn_3As_2 (in 1982). Important band structure parameters are discussed in [413]. Reference [444] discussed the band structure of II_3V_2 compounds. See also [55].

B.2.2 Electronic properties

First measurement of the mobility in Zn_3P_2 , in 1955, by [445], and some old mobility data in [446] with the thermal dependence. See also [439] with mobilities $10 \text{ cm}^2 \text{ V}^{-1}$ to $50 \text{ cm}^2 \text{ V}^{-1}$ at 290 K and 78 K

Also, reference [395] shows mobilities in the order of $2000 \text{ cm}^2 \text{ V}^{-1} \text{ s}^{-1}$ to $7000 \text{ cm}^2 \text{ V}^{-1} \text{ s}^{-1}$ for very low room temperature carrier concentrations on the order of $3 \times 10^{10} \text{ cm}^{-3}$ to $9 \times 10^{10} \text{ cm}^{-3}$.

Appendix B. Additional properties of zinc phosphide

Reference [447] $12 \text{ cm}^2 \text{ V}^{-1}$ for 10^{16} cm^{-3} . The authors hypothesize an activation energy coming from transport across grain boundaries with or without tunneling (see [448] for modelling of grain boundary scattering in Zn_3P_2).

Reference [410] also studied carrier transport and their mechanisms in Zn_3P_2 nanowires. They find a thermal activation energy for resistance at high temperatures 197 meV, but the resistance seems to be influenced by a different mechanism at low temperatures ($T < 200 \text{ K}$).

Diffusion length

Diffusion length is discussed in [104, 352, 449]. Also in reference [348], finding $8 \mu\text{m}$ to $13 \mu\text{m}$. Minority diffusion length of $4.5 \mu\text{m}$ mentioned in reference 1 of [435]. Reference [353] finds $0.5 \mu\text{m}$ to $0.8 \mu\text{m}$.

Carrier lifetime

First (and rough) lifetime measurement in Zn_3P_2 : [450]. More detailed studies in references [434] and [451].

Grain-boundaries

Grain boundary effects approached in references [104, 448].

B.2.3 Optical properties

Absorption

A graph of the absorption coefficient of Zn_3P_2 is shown for example in reference [391]. Absorption in polycrystalline thin films is similar [452].

λ [nm]	α [cm^{-1}]	α^{-1} [nm]
785 (NIR)	7030	1422
532 (green)	165000	61
488 (blue)	234000	43

Table B.3 – Absorption coefficient and absorption length of light at different wavelengths in Zn_3P_2

Dielectric constant

- 0 eV to 6 eV from K-K analysis of reflectivity [453] and [454]
- 0 eV to 7.5 eV from K-K analysis of reflectivity [428]

- 1.3 eV to 11 eV from K-K analysis of reflectivity [455]
- 0.5 eV to 3 eV [433]
- 0.5 eV to 4.1 eV [103]
- 1.4 eV to 3.2 eV [456]
- 1 eV to 10 eV (1-6 at 80 K and 6-10 at 300 K) from K-K analysis of reflectivity [398]

Reflectivity spectrum extrapolation for the application of the Kramers-Kronig relations are discussed in [455].

Reflectance/Transmittance

- [402] to identify band transitions
- [457] with surface quality
- [380] on different quality surfaces
- [400] to study the band transitions
- [428] to calculate dielectric function
- [399]
- [458] to study surface quality
- [455] to calculate dielectric function
- [247] with different polarizations
- [433] amorphous and crystalline

The effect of surface roughness on the sample reflectivity is discussed in refs 6 to 8 of [459]. Such imperfections can be characterized by means of the precise ellipsometric determination of the dielectric response at photon energies well above the fundamental absorption edge (refs 9 and 10 of [459]).

Optical anisotropy

This topic is covered in more details in appendix C (p. 131).

Dichroism and birefringence studied in some details in [412] but only in the range 1.3 eV to 1.55 eV at 300 K (800 nm to 950 nm) and 1.32 eV to 1.63 eV at 80 K (760 nm to 940 nm). Also in

[452] and in great details in [460]. And in [247], using the measurement technique described in [460]. In [418] they use the two types of minority carries detected in [352] as an argument for the existence of two indirect CB minima and hence mobilities/effective masses. **Dichroism** of the optical properties of Zn_3P_2 is shown or dicussed in [380], [412], [418], [452], [399], [247], [246] and [348]. The anisotropy of Zn_3P_2 comes from three contributions, which must all be taken into account when considering the problem of anisotropy of Zn_3P_2 [417]:

1. The metal-ion "vacancy" arrangement is different between the real and the anti-fluorite structures
2. Atoms (mostly the metal atoms) are displaced from their idealized lattice sites (i.e. they are not at simple fractions of the lattice parameters)
3. There is a slight distortion along the c-axis between the cubic and tetragonal structures. Zn_3P_2 is slightly compressed along the c-axis.

B.3 Defects

Photovoltage polarity inversion was observed at Au- Zn_3P_2 junctions, but not at Mg- Zn_3P_2 or In- Zn_3P_2 junctions [355]

B.3.1 n-type zinc phosphide

1. n-type above 340 K[461]
2. Claiming n-type Zn_3P_2 formation due to Mg diffusion: [462] & [463]. Likely disproved (e.g. [423]).
3. A Varanasi-based team (Saha, Singh, Basak) report having made n-type Zn_3P_2 . [464] refer to [465] where the n-type claim is based upon Mott-Schottky plots. Reference [448] models the electrical conduction and refers to (Saha & Singh, *Physica Status Solidi*, 1993). The same year [466] uses capacitance-voltage measurements in an electrolyte, during which Zn_3P_2 is quickly degraded. They fail to provide the thermo-power measurement evidence they claim to have.
4. Reference [395] claims to have Hall-effect measurements demonstrating n-type doping, but does not show the relevant data.

B.4 Surfaces and interfaces

B.4.1 Etching

Br ₂ [%]	other components	references
TBD	water	[424]
2	ethanol	[467] ⁽⁴⁾
5	alcohol ^[sic]	[400]
unkn	alcohol ^[sic]	[429, 468]
unkn	methanol	[259, 381, 434, 447, 469] [399, 430, 452, 470, 471]
0.05	methanol	[422] ⁽¹³⁾
0.1	methanol	[310] ⁽⁸⁾
0.25	methanol	[472] ⁽²⁾
0.5	methanol	[436] ⁽⁶⁾
1	methanol	[473, 474] ⁽¹⁾ [104, 449, 463]
1-1.5	methanol	[475] ⁽³⁾
1-2	methanol	[356]
1.5-2	methanol	[247, 355] ⁽⁷⁾
2	methanol	[408] ^{d(12)} [476, 477]
1-3	methanol	[311] ⁽¹¹⁾
2.5	methanol	[428]
2-3	methanol	[420] ⁽¹¹⁾
3	methanol	[478][479] ⁽¹⁾
2-5	methanol	[480]
5	methanol	[481–483][484] ⁽⁹⁾ [485] ⁽⁹⁾⁽¹⁰⁾
2-40	methanol	[486] ⁽⁵⁾
-	10% HF - 0.25% H ₂ O ₂	[408] ^d
-	30% H ₂ O ₂ with citric acid 5.2M	[352] ⁽¹⁴⁾
-	saturated solution	[487]
-	1:25 HF:HNO ₃	[394]
-	36% HCl	[380]
-	1:20 HCl:methanol	[488]

Table B.4 – See full caption below.

Appendix B. Additional properties of zinc phosphide

Caption of table B.4 above:

Nearly-exhaustive list of different etching solutions used on Zn_3P_2 reported in the literature.

Notes: (1): sputter cleaned, (2): jet of etchant, (3) degreased in acetone and methanol, (4) 10min etch, (5) etch rinsing procedure: MeOH, EtOH and dried by N_2 . Etch to remove defects from cutting: 40% Br_2 , before coating of crystals: 5% Br_2 , before coating of thin films: 2% Br_2 , (6) 30s etch, (7) degreasing: acetone and methanol, (8) 10s etch, rinsed with methanol, (9) 5min etch, (10) MeOH rinse before etch and post-etch degreasing with MeOH, Cl_3CH , acetone and MeOH, (11) rinsed with MeOH after etch, (12) 30s etch, rinsed with MeOH, (13) found 2% Br_2 and 0.5% Br_2 etch with MeOH too aggressive for thin films; also discusses etch rates, (14) at 60-70°C, *d* duplicate

Figure B.1 below shows the measured thicknesses of thin films on different chips taken from a single MBE-grown monocrystalline sample after etch with a methanol-bromine solution. The less concentrated solutions were prepared using the higher concentrated solutions. The measurements were taken within a time frame small enough to neglect the decrease in bromine concentration from the etching solution due to loss of bromine. Etching was interrupted by rinsing with pure methanol.

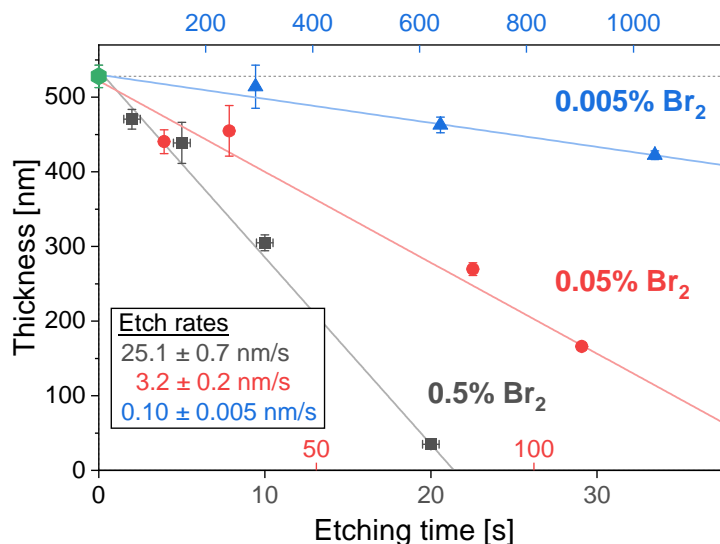


Figure B.1 – Etched thickness of a single monocrystalline thin film grown on InP for three methanol-bromine etching solutions, together with the etching rates of the solutions.

B.4.2 Materials joined with zinc phosphide

Nearly-exhaustive list of all materials joined to Zn_3P_2 reported in the literature:

- Ag (ohmic) [311, 445, 464, 489]. Electromigration of Ag at high electric fields may add acceptors into Zn_3P_2 (Reducing "n-type" doping [464] or increasing p-type doping [447])
- Al (Schottky) [485, 490]
- Al_2O_3 [408]
- Au (ohmic) [400, 435, 489, 491]
- Be (Schottky) [352]
- CdS [442, 491]
- (CdZn)S [491]
- Cr (Schottky) [259]
- Cu (ohmic) [259]
- Fe (Schottky) [259]
- Fe + Si (ohmic) [258]
- GaAs [252]
- graphene [492]
- In (Schottky OR ohmic) [259] VS [400, 435, 489]
- ITO (TBD) [493]
- InP (TBD) [494]
- Mg (Schottky) [258, 259, 420]
- Mn (Schottky) [259]
- Ni (ohmic) [259]
- Pt (ohmic?) [402]
- Zn (ohmic) [259]
- ZnO [442, 473, 474, 486, 491, 495, 496]
- ZnS (n-doped) [497]
- ZnSe [491, 498]

B.5 Other topics

Polaritons: [499, 500]

Excitons: [501]

B.6 Photoluminescence of zinc phosphide

Here, I will show a nearly exhaustive literature review of reports about the photoluminescence of zinc phosphide. I cannot exclude having missed a paper or other work mentioning the topic, but the vast majority of them, if not all, are included here. Works produced from our laboratory and briefly covering the topic (refs [260–263]), already mentioned in other parts of this work, will not be mentioned further. The works are separated in two categories, the first being those published between 1979 and 1996, and then those published in 2006 and after. No works have been published in the intermediate period. In the first period, focus has been on single crystals and thin films, while in the second, one-dimensional and zero-dimensional structures become more prevalent.

B.6.1 1979-1996

Photoluminescence of Zn_3P_2 has been the main topic of 4 papers, refs. [351, 356, 394, 502], and a mean of characterization in three others: [246, 255, 395].

The first paper reports the emission of Zn_3P_2 single crystals at temperature between 24 K and 75 K. [502] The authors observe a very intense peak centered between 1.0 eV and 1.1 eV, with a full width at half maximum (FWHM) and position nearly independent of the temperature and the crystal orientation. They also observe a small peak at 1.51 eV, at 24 K only. The authors hypothesized that the main emission peak was coming from defect transitions, and the radiative recombination was competing against a non-radiative recombination pathway with an activation energy of approximately 56 meV. The same authors published the year after a follow-up report, where they investigated thin films in addition to single crystals, at 100 K only. [394] In addition to the previously-mentioned 1.1 eV peak, they observe a peak at 0.636 eV in several samples (accompanied by a related peak at 0.52 eV, at a fixed 1:4 intensity ratio) and a peak at 0.8 eV in a couple of samples. Similarly to the first paper, the 0.64 eV appears to be competing with a non-radiative recombination process, with activation energy 84 meV. Annealing of the samples reduced the intensity of the 0.64 eV peak, but not the 1.1 eV peak.

One of the most extensive characterization of the photoluminescence of this semiconductor was done by Briones and co-authors in 1981. [351] Their two samples were grown by sublimation (sample 1) and by iodine transport (sample 2), and were cleaved before the measurement. The authors observed two large peaks, at 1.354 eV and 1.361 eV, in sample 1, and two large peaks at 1.278 eV and 1.320 eV in sample 2. Each peak is accompanied by a smaller

peak, shifted by 42 meV to lower energies, assumed to be a phonon replica. The temperature response of the peaks can be closely described by transitions between two defects, pair transitions. The activation energy of one of the two defects is always 1.5 meV, while for the other defect it is 7 meV, 15 meV and 20 meV for the characterized peaks. The authors conclude that the transitions occur between two defect levels across a 1.370 eV bandgap, with two defects near one band extremum separated by 8 meV. Interestingly, the authors also note a peak with a temperature dependence with opposite sign to all other peaks, which shift at the same rate as the temperature-induced bandgap widening, at $3.2 \times 10^{-4} \text{ eV K}^{-1}$.

In the fourth paper, the authors studied phosphorus-rich polycrystalline thin films grown by evaporation [356]. They measured the photoluminescence at 100 K and etched the films chemically. The spectrum they observe is made of two peaks, a very large peak at 1.23 eV, and a small one at 1.60 eV. Their assignment to a recombination mechanism are not supported by any measurements.

Then among the works using photoluminescence as a secondary tool, there is a paper depositing Zn_3P_2 with a photo-chemical vapor deposition method, decomposing the precursors with UV light. [255] They observe a single PL peak, at 1.53 eV. Then, Pangilinan and co-authors used photoluminescence to decide on the wavelength to use for resonant Raman spectroscopy [246]. They observe a single peak at 1.534 eV. They only observed this luminescence peak when illuminating with radiation from 730 nm to 900 nm. Otherwise they observed no emission.

Finally, Suda and co-authors also measured the photoluminescence of their claimed n-type Zn_3P_2 thin films grown by separate-source molecular beam epitaxy on GaAs [395]. Growing n-type Zn_3P_2 is a feat that would be very promising for the production of homojunction Zn_3P_2 solar cells since, other than in their paper, Zn_3P_2 is always intrinsically p-type. The authors mention that Hall measurements and thermoelectric measurements confirmed the n-type nature of their films, but they fail to show the data supporting these claims. Notwithstanding these gaps, the growth of n-type Zn_3P_2 , though difficult, is thought to be possible in Zn-rich conditions. Regarding photoluminescence, the authors observe a single peak centered at 1.41 eV, only shifting slightly with temperature. As in the early works discussed above, they observe a quenching of the peak at higher temperature, with an activation energy of the non-radiative recombination process of 46 meV.

B.6.2 2006-2021

During this period, photoluminescence has been a tool to characterize filamentary Zn_3P_2 nanocrystals (often nanowires) in five papers [495, 503–506], with a slightly more extensive investigation in a sixth [410]. One paper also studies Zn_3P_2 nanoparticles [409]. During this time period, only the group of Prof. H. A. Atwater studied the photoluminescence of bulk Zn_3P_2 [103, 311, 408].

The nanotrumpets in ref. [503] show a single broad room-temperature PL peak centered at

Appendix B. Additional properties of zinc phosphide

2.12 eV. The branched nanostructures in ref. [504] emit a room-temperature photoluminescence spectrum with a single peak centered at 1.61 eV. The nanowires in ref. [505] emit a broad peak (likely at room temperature) at 1.61 eV, tailing off on the low-energy side. A similar spectrum is observed from the nanowires in ref. [506] and ref. [495]. Lombardi et al. investigated the PL spectrum of chemical-vapor-deposition-grown nanowires in more detail [410]. At 3.8 K, they observe the biggest peak at 1.50 eV. They attribute peaks at 1.45 eV, 1.43 eV and 1.41 eV in the low-energy tail to recombinations with defects close to the VBM, with support from other measurements. They also observe a small peak at 1.30 eV, also attributed to recombination with a defect. Their emission also appears to have shoulders on the high-energy side, but they remain unfortunately unexplained. The authors also measured the dynamics of the recombinations leading to their biggest peak at 1.50 eV. They observe a monoexponential decrease with a time decay of 91 ps.

Ho et al. studied in detail Zn_3P_2 nanoparticles [409]. They observe a variety of spectra with a single peak centered at 2.27 eV to 2.64 eV, depending on the size of their nanocrystal. Time-resolved photoluminescence measurements on their structures were well fitted with bi-exponential decay, with time decays of 0.6 ns to 20.8 ns, which they attribute to recombinations from the band edge.

Regarding bulk Zn_3P_2 , Kimball and co-authors studied the photoluminescence of Zn_3P_2 wafers cut from polycrystalline boules [103, 311, 408]. Mirror-polished wafer show a single weak PL emission peak centered at 1.49 eV. Wafer etched with a bromine-methanol solution, with and without passivation with ammonium sulfide, show greatly increased emission, with emission at nearly the same energy. After several hours, however, the intensity of the signal went back to the level of unetched wafers [311].

At temperatures of 5 K to 20 K, the spectrum is made of a single large peak at 1.36 eV and a phonon replica 43 meV below. At temperature of 200 K to 310 K, the spectra are composed of a main peak near 1.4 eV with a shoulder at approximately 1.5 eV. They also observe a smaller feature, saturating at high power, at 1.37 eV. At room temperature, the two main peaks are located at 1.38 eV and 1.50 eV and blueshift with decreasing temperature at $3.8 \times 10^{-4} \text{ eV K}^{-1}$ and $4.5 \times 10^{-4} \text{ eV K}^{-1}$, respectively. Near cryogenic temperatures, their peaks blueshift with increasing laser power, whereas near room temperature, they do not. Time-resolved photoluminescence measurements at room temperature show a bi-exponential decay, with time constants of 4 ns and 20 ns. The authors explain this behavior as the bulk and surface recombination processes, with the surface processes dominating because of their use of strongly absorbed 355 nm light [103].

The authors showed that etching with a 2% bromine in methanol solution greatly increased the photoluminescence as compared to polished samples. The surface of the etched films were covered by less than one monolayer of oxidized zinc and oxidized phosphorus, as well as a few monolayers of elemental phosphorus. Etching with a 10%HF-0.25% H_2O_2 solution removed some of the elemental phosphorus, increased the steady-state photoluminescence and

B.6. Photoluminescence of zinc phosphide

reduced the surface recombination velocity, measured with time-resolved photoluminescence. Finally, leaving the Br-etched samples in air for a week likely produced some $\text{Zn}_x(\text{PO}_3)_y$ and reduced the surface recombination velocities even further. Native oxides on Br-etched Zn_3P_2 thus appears to passivate more than 90% of the electrically active surface recombination sites [408].

C Optical anisotropy of zinc phosphide

C.1 Literature review of the anisotropic optical properties of zinc phosphide

C.1.1 Birefringence

The birefringence of Zn_3P_2 at sub-bandgap energies has been measured by J. Misiewicz and coworkers by two different methods [412, 460]. The results, measured only in the 0.5 eV to 1.45 eV range, agree well. A typical measurement is shown for example in figure 6 of reference [460].

There are no reported measurements of the birefringence at energies higher than 1.45 eV (<855 nm) in the literature.

C.1.2 Dichroism

The dichroism of zinc phosphide has been measured by absorption measurements [247, 399, 412, 452] in the bandgap and sub-bandgap energy range (1.3 eV to 1.6 eV) and at energies up to 2.05 eV with different photoresponse techniques [247, 348, 399, 412, 452].

Representative graphs of the dichroism near the fundamental band edge are shown for example in figure 5 of reference [412] and figures 6 and 8 of reference [247].

Dichroism is defined here in the following way

$$\delta\alpha = \alpha_{\parallel} - \alpha_{\perp} \quad (\text{C.1})$$

where α_{\parallel} and α_{\perp} are the absorption coefficients for light polarized along and perpendicular to the optic axis. The photodichroism coefficient is a normalized measure of the dichroism, and is defined the following way:

$$P_{\alpha} \equiv \frac{\alpha_{\parallel} - \alpha_{\perp}}{\alpha_{\parallel} + \alpha_{\perp}} \quad (\text{C.2})$$

Appendix C. Optical anisotropy of zinc phosphide

We see a good agreement between the measurements of the fundamental edge anisotropy by comparing the photodichroism coefficient obtained from the absorption measurements reported in [412] and [247], shown in figure C.1.

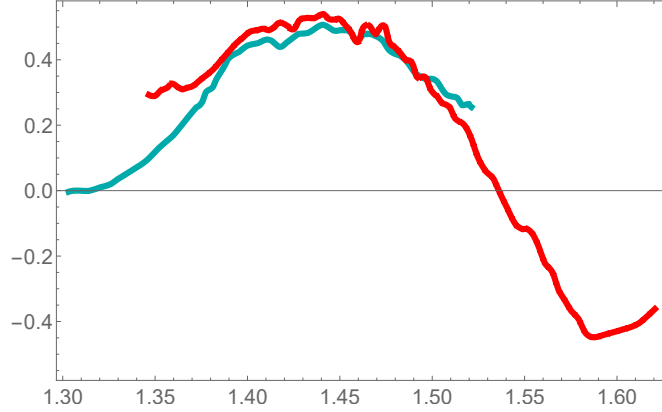


Figure C.1 – Photodichroism coefficient calculated from the absorption measurements at 300 K, reported in [412] (turquoise) and [247] (red). The difference in P_α below 1.38 eV likely comes from different defect-mediated absorption.

Misiewicz [247] showed that in Zn_3P_2 (space group D_{4h}^{15}), the smallest band transition at the Γ point (from valence band Γ_7^+ to conduction band Γ_6^+) is forbidden for light polarized parallel to the c -axis of the crystal. The first allowed transition for parallel-polarized light is at an energy larger by the crystal-field splitting, $\Delta_{cf} \approx 0.03$ eV. For this reason, the photodichroism coefficient is likely to be negative at the Γ band edge, as it is on the higher energy side of figure C.1. This seems to suggest that the dichroism in the range 1.3 eV to 1.5 eV is due either to the selection rules of indirect band transitions or that of defects. The DFT band structure calculations of Zn_3P_2 [343, 419] indicate that both the valence band maximum and conduction band minimum are at the Γ point, which would rule out the former option. The controversy regarding the existence of an indirect bandgap smaller than the direct bandgap still stands, however.

C.1.3 Dielectric tensor

Ultimately, both dichroism and birefringence are related to the difference between the two components of the complex dielectric tensor of Zn_3P_2 :

$$\bar{\epsilon} = \begin{pmatrix} \epsilon_\perp & 0 & 0 \\ 0 & \epsilon_\perp & 0 \\ 0 & 0 & \epsilon_\parallel \end{pmatrix} \quad (\text{C.3})$$

C.2 Determination of the optical anisotropy at all relevant energies

Knowing the optical anisotropy of Zn_3P_2 up to the energies relevant in spectroscopy (488 nm \Leftrightarrow 2.54 eV) is necessary to fully describe the laser-sample interaction and accurately apply the selection rules.

Furthermore, accurate optical anisotropy measurements at energies up to the far ultraviolet can be used to refine the band transitions identifications carried out by Misiewicz [247]. This could help resolve the controversy about the type of the fundamental band transition.

An option for measuring these properties for zinc phosphide would be by using the relations between the different optical properties (C.4, C.5) and the Kramers-Kronig (KK) relations (C.6), which would allow us to calculate the optical anisotropy up to the far ultraviolet in a manner similar to [398]. Extrapolation of polarized reflectivity [428] would provide us with the birefringence and dichroism over the whole energy spectrum.

$$r(\omega) \equiv \rho(\omega)e^{i\theta(\omega)} \quad (\text{C.4})$$

r is the angular-frequency-dependent reflectivity, with ρ its amplitude and θ is phase.

$$R = r^* \cdot r \quad (\text{C.5})$$

R is the reflectance and the asterisk indicates the complex conjugate.

$$\theta(\omega) = -\frac{1}{2\pi} \int_0^\infty \ln \left| \frac{s+\omega}{s-\omega} \right| \frac{d\ln(R(s))}{ds} ds \quad (\text{C.6})$$

The birefringence δn and the dichroism $\delta \alpha$ are directly related through the K-K relationships with the following formula [247]:

$$\delta n(E) = \frac{\hbar c}{\pi} \int_0^\infty \frac{\delta \alpha(x)}{x^2 - E^2} dx \quad (\text{C.7})$$

Polarized reflectivity data has only been published by Misiewicz, in the 80's [247, 428].

C.2.1 Correct identification of the band transitions

Several authors (Syrbu [398, 402, 416], Pawlikowski [418] and Misiewicz [247, 455]) have attempted to identify the near-bandgap and over-bandgap transitions (determined from polarized reflectivity measurements) using the band transitions selection rules and the calculated band diagram. While the approach is good, all of them have used the band diagram calculated using an overly-simplified cubic crystalline structure [440] instead of the full structure

calculation [419].

C.3 Polarization-resolved Raman spectroscopy of optically anisotropic zinc phosphide

Kranert et al. [507] have derived a detailed theory for optically anisotropic crystals. They focus on transparent semiconductors but their work is also applicable to absorbing semiconductors. They have not, however, considered dichroism.

C.3.1 Relative importance of birefringence

Because of the different phase velocities of the ordinary and extraordinary components of light in birefringent materials, the polarization direction of an initially linearly polarized beam will rotate with increasing travelling distance in the material.

The distance required for a full rotation of the polarization direction, $z^{2\pi}$, is given by

$$z^{2\pi} = \frac{\lambda_{air}}{\delta n} \quad (C.8)$$

where λ_{air} is the wavelength in air and δn is the birefringence

$$\delta n = n_e - n_o = n_{\parallel} - n_{\perp} \quad (C.9)$$

Assuming a negligible dichroism in comparison to the absorption coefficient, a comparison between $z^{2\pi}$ and the absorption depth $\alpha^{-1} \approx \alpha_{\perp}^{-1} \approx \alpha_{\parallel}^{-1}$ measures the importance of birefringence.

Case (1): If $z^{2\pi} \gg \alpha^{-1}$ the rotation of the polarization direction becomes negligible, as the light is absorbed much faster than the polarization rotates. The material is absorbing and non-birefringent but potentially dichroic.

Case (2): If $z^{2\pi} \ll \alpha^{-1}$, the light can be considered totally depolarized, as light polarized in all directions will contribute equally to the scattering process and the spectroscopic selection rules can not be used anymore. Dichroism is negligible.

Case (3): If $z^{2\pi} \approx \alpha^{-1}$, the spectroscopic selection rules can be derived, but birefringence plays an important role by rotating the polarization of light as it travels into the material. In addition to this, dichroism may need to be taken into account.

The work of Kranert et al. described above [507] treats the strongly absorbing case (1) and the birefringent case (3). They do not, however, take dichroism into account.

C.3. Polarization-resolved Raman spectroscopy of optically anisotropic zinc phosphide

In zinc phosphide, the birefringence of light at 850 nm is 0.02[412] and the absorption coefficient is approximately 200 cm^{-1} [391]. This makes the birefringence distance (43 000 nm) and the absorption distance (50 000 nm) approximately equal and the complex case (3) needs to be considered.

For light with wavelengths in the visible range, usually used in Raman and photoluminescence spectroscopy, the birefringence has not been directly measured. The birefringence can be calculated using the polarized dielectric function determined in [428] from reflectivity measurements in the range 1 eV to 5.4 eV. It is displayed in figure C.2. While the birefringence thus calculated contains errors compounded from the measurement, the incomplete K-K transformation and digitization, it shows that it remains well below unity in the whole range of interest. The absorption depth decreases by orders of magnitude as the fundamental edge is crossed, reaching approximately 60 nm at 532 nm. Therefore, we find ourselves most likely in case (1) and birefringence may be neglected in most visible light Raman and photoluminescence measurements.

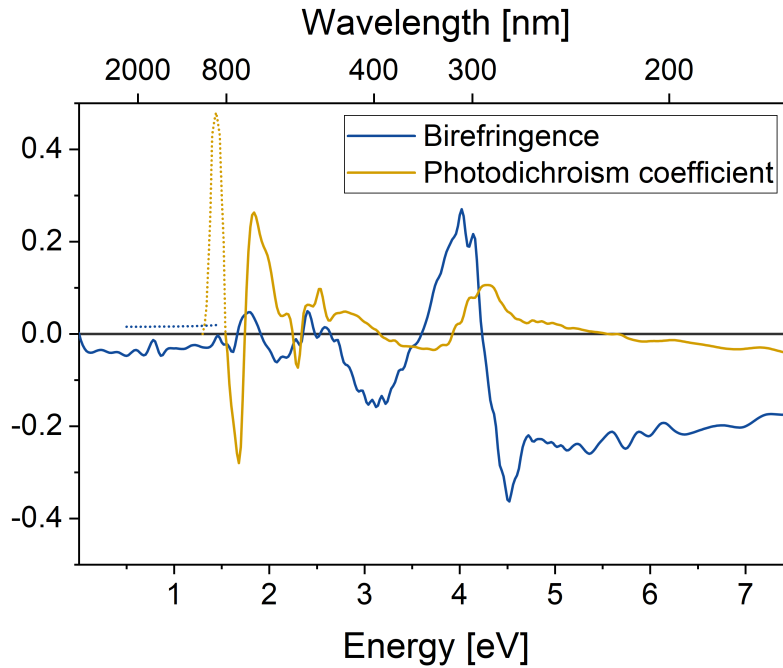


Figure C.2 – Calculated birefringence and photodichroism coefficients from data in [428]. The dotted curves are the experimental measures from [247] and from figure C.1.

We need to keep in mind that the anisotropic properties calculated this way contain multiple sources of errors. The range of energy over which polarized reflectivity was measured only goes from 1 eV to 5.4 eV approximately. For that reason, the higher energy features observed in unpolarized reflectivity measurements have not been taken into account. These approximations and errors in the polarized reflectivity are propagated through the Kramers-Kronig equations, which produce results very sensitive to the whole energy range. Finally, the dielectric function

Appendix C. Optical anisotropy of zinc phosphide

data is only available in a graph published in 1984.

In the table below, selected values of the different optical properties presented in figure C.2 are tabulated.

λ [nm]	E [eV]	α_{\perp} [cm^{-1}]	α_{\parallel} [cm^{-1}]	P_{α}	$\delta\alpha$ [cm^{-1}]	n_{\perp}	n_{\parallel}	δn
488	2.54	198 000	240 000	0.10	42 700	4.43	4.44	0.003
532	2.33	96 000	92 500	-0.02	-3 500	4.28	4.26	-0.023
633	1.96	29 700	42 800	0.18	13 100	3.97	3.95	-0.023

Table C.1 – Coefficient of absorption for light polarized perpendicularly to the c-axis (α_{\perp}), and parallel to the c-axis (α_{\parallel}), photodichroism coefficient (P_{α}), dichroism ($\delta\alpha$), ordinary index of refraction (n_{\perp}), extraordinary index of refraction (n_{\parallel}) and dichroism (δn) for light at the energies used in our Raman/PL setup. Calculated from data in [428].

D Additional zinc phosphide photoluminescence spectra

D.1 Changes due to composition

Large changes can be observed in the photoluminescence emission from samples of different compositions. Figure D.1 shows the impact on the low-energy emission of three monocrystalline samples with different compositions.

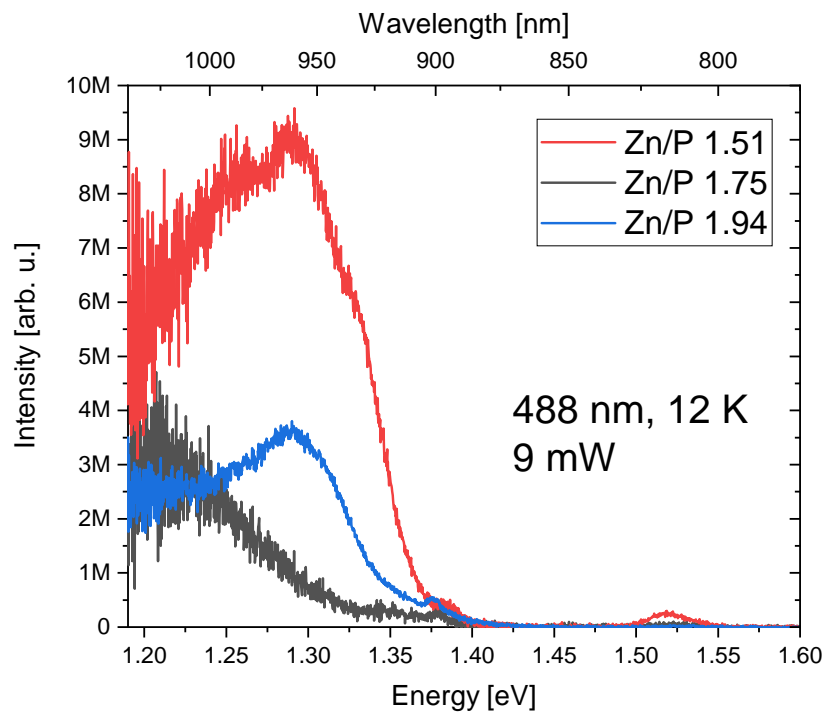


Figure D.1 – Photoluminescence spectra acquired from three Zn_3P_2 monocrystalline thin film samples with different zinc-to-phosphorus concentration ratios. The measurements were acquired at 12 K with a 488 nm laser. Incident power is approximately half of $9\mu\text{W}$ and the laser spot is about $1\mu\text{m}^2$. The large noise in the spectrum at low energy is due to the low responsivity of the detector at these energies.

Appendix D. Additional zinc phosphide photoluminescence spectra

Figure D.2 shows some differences observed near the direct bandgap energy from the same three monocrystalline thin film Zn_3P_2 samples.

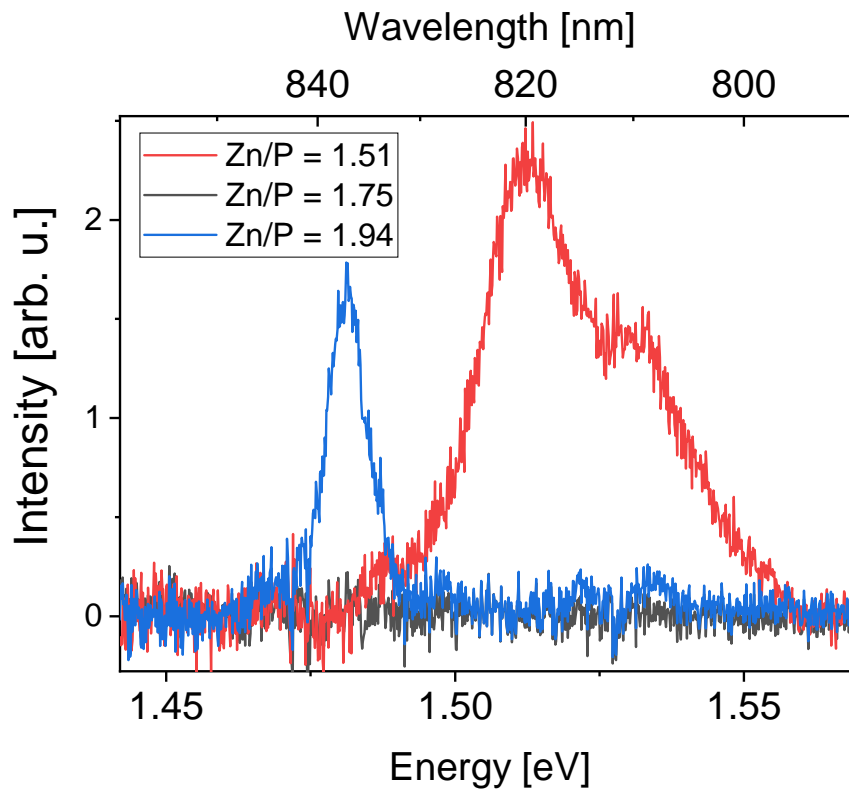


Figure D.2 – Photoluminescence spectra acquired from three Zn_3P_2 monocrystalline thin film samples with different zinc-to-phosphorus concentration ratios. The measurements were acquired at cryogenic temperatures with a 488 nm laser. Incident power is a few microwatt and the laser spot is about $1\ \mu\text{m}^2$.

D.2 High-energy emission

In one case, a sample also appeared to have several very-high-energy emission lines. These were not studied systematically or in detail, and were surprisingly observed much stronger using a particular spectrometer configuration ($600\ \text{mm}^{-1}$ grating instead of the usual $300\ \text{mm}^{-1}$). This change of configuration should not in itself explain the differences in observation. The broad background peaks shown in the spectra in figure D.3 were parasitic emission.

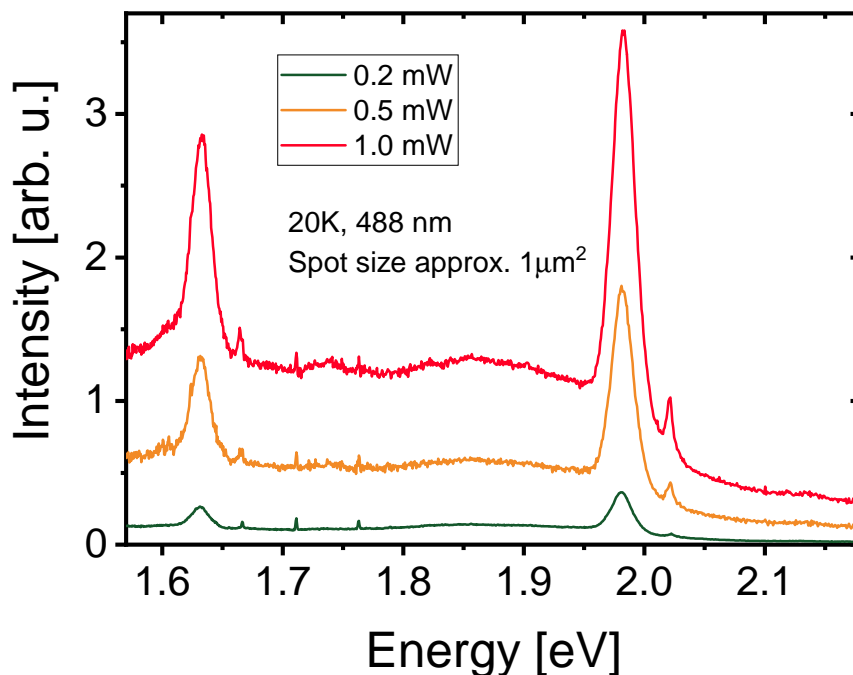


Figure D.3 – High energy photoluminescence spectrum of zinc phosphide. The measurements were acquired at 20 K with a 488 nm laser. Incident power is approximately half of the reported values and the laser spot is about $1 \mu\text{m}^2$. The broad background/peak from low energies to approximately 2 eV is parasitic emission not coming from Zn_3P_2 .

D.3 Irreversible changes

Finally, the figures D.4 and D.5 below show spectra acquired from another monocrystalline Zn_3P_2 thin film sample. The low-energy peaks are attributed to defect transitions, the high-energy peak to the direct bandgap transitions of Zn_3P_2 and, in this case, the peak near 1.44 eV is attributed to the InP substrate.

In figure D.4, the spectra measured on a single spot at increasing power densities are shown. As the power is increased, the measured spectrum increases homogeneously. After reaching a threshold, a large change is observed in the spectrum.

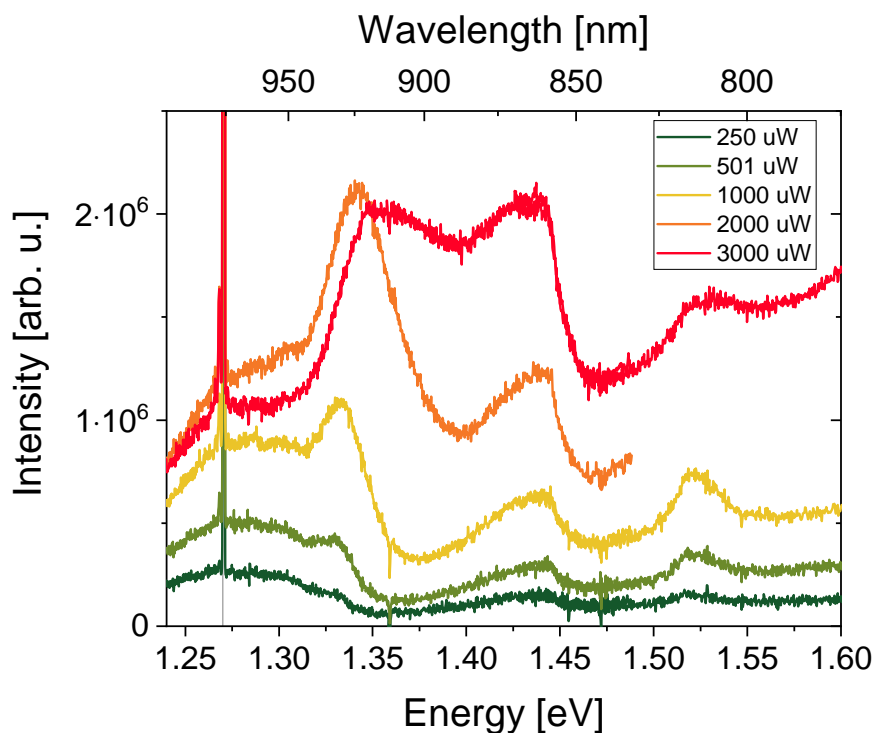


Figure D.4 – Power series on a monocrystalline Zn_3P_2 thin film sample. The measurements were acquired at 20 K with a 488 nm laser. Incident power is approximately half of the reported values and the laser spot is about $1\text{ }\mu\text{m}^2$. The sharp peak at 1.27 eV is the second-order diffraction peak of the 488 nm laser.

The spectra shown in figure D.5 were acquired on the same location as those shown in figure D.4, after the previous measurements were carried out. It can be observed that the abrupt change that occurred in the previous power series is still present even at low temperature, and thus appears to be irreversible.

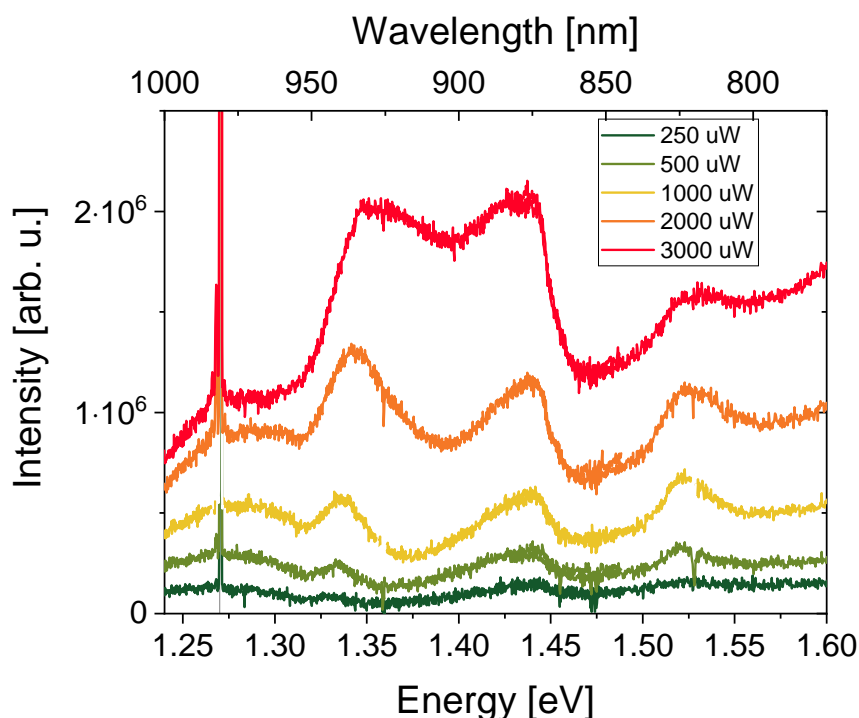


Figure D.5 – Power series on a monocrystalline Zn_3P_2 thin film sample, after a previous exposure to a high laser intensity. These measurements were carried out after the measurements shown in figure on the sample spot as the The measurements were acquired at 20 K with a 488 nm laser. Incident power is approximately half of the reported values and the laser spot is about $1\text{ }\mu\text{m}^2$. The sharp peak at 1.27 eV is the second-order diffraction peak of the 488 nm laser.

D.4 Recommendations

Given the spectra shown in these sections, a few recommendations for catching as much information from the photoluminescence spectra of Zn_3P_2 can be formulated: (1) capture emission in a range of energies from close to 0 to more than 2 eV and (2) look out for irreversible changes in the emission spectrum.

E Supplementary information for "Nanosails Showcasing Zn₃As₂ as an Optoelectronic-Grade Earth Abundant Semiconductor"

E.1 Nanosail growth parameters

As stated in the main text, a horizontal flow metal-organic vapor phase epitaxy system (Aixtron 200/4) was used to grow the Zn₃As₂ nanostructures on (111)B GaAs substrates similarly to Ref. [328]. The substrates were pre-treated with poly-l-lysine before the dispersion of 50 nm gold nanoparticles in colloidal solution. The growth was performed at 500 °C and 10 kPa under a total flow of 15 standard liters per minute using arsine and diethylzinc (DEZn) as precursors at molar fractions of 8.04×10^{-3} and 1.31×10^{-4} , respectively, giving a V/II ratio of approximately 60. The growth was carried out for 10 minutes.

E.2 Electrical contact fabrication and measurements

After growth, the nanoplatelets were detached by sonication in isopropanol and drop cast onto a silicon wafer with 200 nm of thermal oxide on it. The electrical contact pattern was written into a MMA/PMMA (400/150 nm) bilayer exposed at 100 keV with a dose of $1000 \mu\text{C cm}^{-2}$ in a Raith EBPG5000+ e-beam tool. It was found that without any surface pre-treatment, Schottky barriers at the contacts yielded unreproducible electrical measurements. Therefore both wet and dry etching approaches were employed to achieve ohmic contacts. As a result, the three ohmic devices presented here were contacted with slightly different processes summarized below:

Appendix E. Supplementary information for "Nanosails Showcasing Zn₃As₂ as an Optoelectronic-Grade Earth Abundant Semiconductor"

	BHF Wet Etch	In-situ Ar Milling	Metallization
Chip I	10 s	-	20/150 nm Cr/Au
Chip II	20 s	-	20/150 nm Cr/Au
Chip III	15 s	30 s	20/150 nm Cr/Au

Table E.1 – Processing conditions of three nanosails.

The last chip was additionally Ar milled in-situ to remove any oxide that may have re-grown before loading into the sputtering chamber, following a method known to work for InAs nanowires. [508, 509] The contacts were then deposited in the same Alliance-Concept DP-650 sputtering chamber.

All of the electrical measurements were performed in a liquid helium cryostat from Cryogenic Ltd. equipped with a 9 tesla magnet and a variable thermal insert (VTI) for temperature control. The connections to the sample were made through a homemade computer-controlled signal multiplexer and isolator in order to permute the sample connections during automated measurements. Electrical properties were measured with a Keithley 6221 current source combined with a Keithley 2182A nanovoltmeter in a delta mode measurement configuration.

The conductivity of the NPs was measured using the van der Pauw method. To reduce the measurement errors introduced by asymmetry of the platelet and the contacts, the resistances in the vertical and horizontal directions, R_v and R_h , respectively, were averaged between measurements in both polarities and flipped voltage/current contacts. The sheet resistance R_s was then obtained with the van der Pauw formula, $e^{-\pi R_v/R_s} + e^{-\pi R_h/R_s} = 1$. The conductivity σ of the NP was calculated using $\sigma = (R_s t)^{-1}$, where t is the thickness of the nanostructure determined by AFM. The mobility of the samples was measured using a standard Hall-effect measurement approach. In order to reduce the effects of sample and contact inhomogeneity, two measurements were performed using both possible contact configurations and averaged together. The resulting hall voltages obtained with this approach had the expected linear dependence of Hall voltage on magnetic field.

E.3 List of reported Raman peaks for α' -Zn₃As₂

Misiewicz [338] measured the Raman peak positions of a phase of Zn₃As₂. The space group used throughout that publication, C_{4v}^{14} , does not exist. Based on the author's previous publications and publications referenced in the article, [428, 510] the space group was likely C_{4v}^{12} (I4₁cd), which corresponds to the space group of α -Zn₃As₂. The room-temperature peak positions are listed in table E.2 below:

63	97	139	186	210	230	255	303	327	352	392
----	----	-----	-----	-----	-----	-----	-----	-----	-----	-----

Table E.2 – Observed room-temperature Raman frequencies of α -Zn₃As₂ reported in ref [338]. Units are cm⁻¹

In our work, no other peak than the first-order silicon Raman peak was detected between the 270 cm⁻¹ large Raman shift edge of the Raman spectrum shown in figure 3.2 in the main article and the 830 cm⁻¹ measurement limit.

E.4 Simulation of electron diffraction from the α'' -Zn₃As₂ phase

To the best of our knowledge, no crystal cell refinements have been carried out for α'' -Zn₃As₂. It is known that the space group of this phase is P4₂/nmc, but the exact displacements of the atoms with respect to the ideal anti-fluorite structure are unknown. As a first approximation, we assume that the atomic positions of α'' -Zn₃As₂ are the same as those in α/α'' Zn₃P₂. The lattice parameters of the tetragonal α'' -Zn₃As₂ phase are approximately a = 8.32 Å and c = 11.82 Å. [335] Thermal lattice expansion was ignored because it is likely insignificant and the measurement temperature is not clearly stated in [335]. Equivalent zone axes need to be compared in the different structures. Zone axes $\langle 221 \rangle$, $\langle 201 \rangle$, $\langle 241 \rangle$ and $\langle 111 \rangle$ in α -Zn₃As₂ and α' -Zn₃As₂ are equivalent to $\langle 201 \rangle$, $\langle 100 \rangle$, $\langle 101 \rangle$ and $\langle 311 \rangle$, respectively, in α'' -Zn₃As₂ and α/α'' -Zn₃P₂. This is assuming that the four-fold axis also changes direction during the $\alpha \rightleftharpoons \alpha''$ phase transition as it does in Cd₃As₂. [240]

Appendix E. Supplementary information for "Nanosails Showcasing Zn_3As_2 as an Optoelectronic-Grade Earth Abundant Semiconductor"

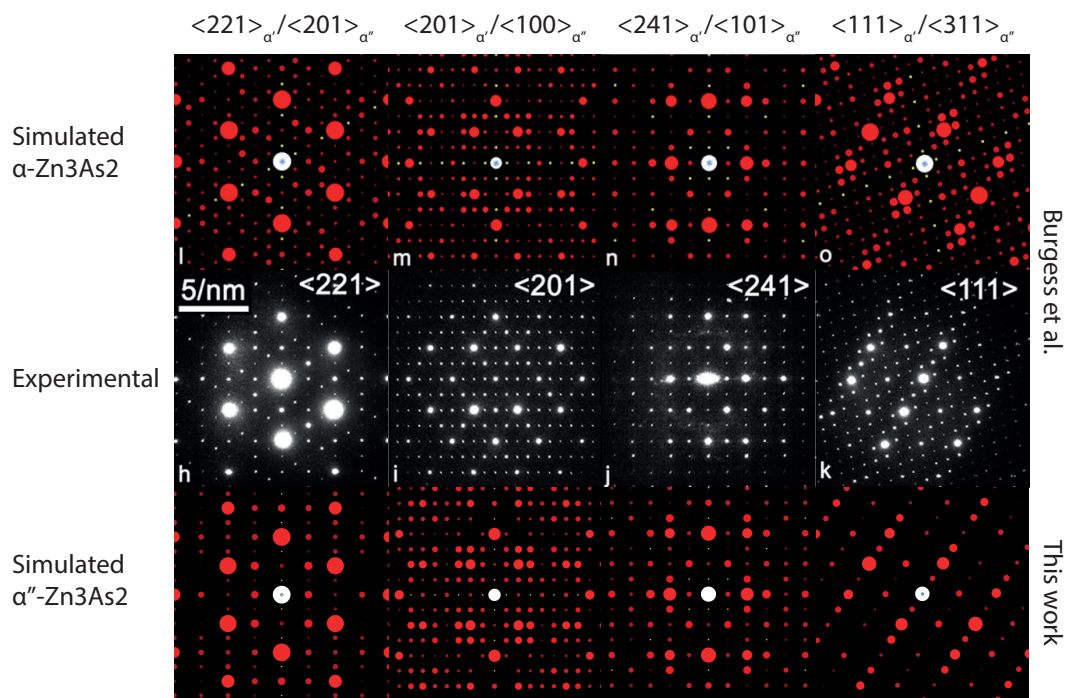


Figure E.1 – First and second rows: simulated $\alpha\text{-Zn}_3\text{As}_2$ and experimental diffraction patterns, adapted with permission from [328]. Copyright 2015 American Chemical Society. Third row: simulated $\alpha''\text{-Zn}_3\text{As}_2$ obtained by deriving the structure from $\alpha\text{-Zn}_3\text{P}_2$ and using the *jems* software (Pierre Stadelmann). The columns represent equivalent zone axes.

E.5 Fitting of the carrier concentration regime transition

The transition temperature between the nearly constant carrier concentration pure impurity band conduction regime and the thermal carrier generation regime has been determined by linear fitting of the two regimes in Log-vs-1/T plots. The transition temperatures are 31, 27 and 27 K for chips I, II and III, respectively.

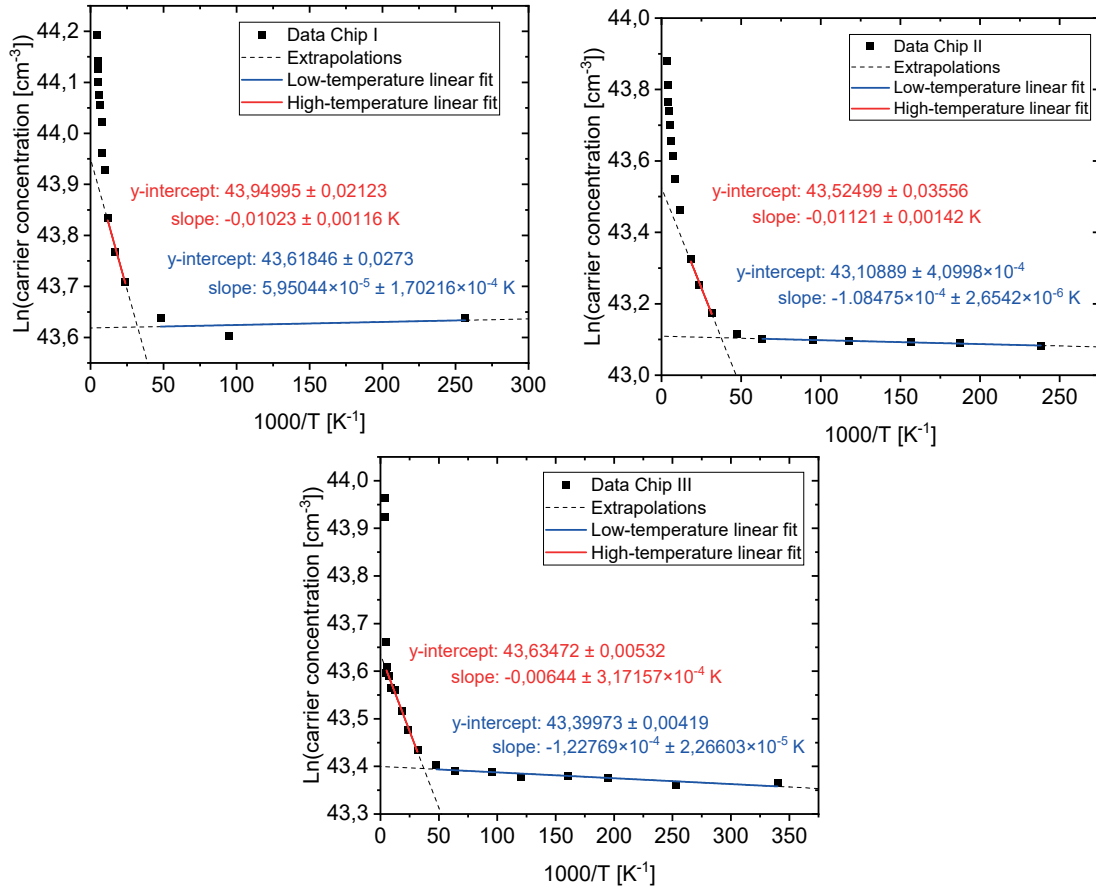


Figure E.2 – Arrhenius-type plot of the carrier concentration in the three studied nanosails. In each of them, the low-temperature and post-transition high-temperature linear parts are fitted. Dashed lines indicate extrapolations from the fitted range.

F Supplementary information for "Raman spectroscopy and lattice dynamics calculations of tetragonally-structured single crystal zinc phosphide (Zn_3P_2) nanowires"

F.1 Deconvolution procedure of Raman spectra

Identification of the Zn_3P_2 phonons was performed by the simultaneous deconvolution of the four Raman spectra measured in different polarization configurations (Figure 4.4 in the main text). Each peak was modeled with a Lorentzian curve characterized with peak position, peak width, and intensity. As the fitting procedure includes a large number of variables, rigorous restrictions were imposed on the fitting parameters in order to avoid correlation among the parameters, and obtain meaningful results. These include following:

- (i) peak positions of a certain Raman mode should not change under different polarization configurations, thus during the fitting procedure, peak positions of the same Raman modes were tied together for all four Raman spectra;
- (ii) as peak widths are mostly dependent on the phonon lifetime, which is determined by the crystal quality of the material, it is expected that all Raman modes have similar widths, regardless of the symmetry of the mode or polarization configurations under which the spectra were measured. This resulted in allowing only a narrow interval of change for the peak widths during the whole deconvolution process;
- (iii) peak intensity was considered as a free parameter in all cases.

Representative deconvolution of the Zn_3P_2 Raman spectra measured under $\langle -Y|ZZ|Y \rangle$ polarization configuration and in unpolarized conditions are presented in Figure F.1.

Appendix F. Supplementary information for "Raman spectroscopy and lattice dynamics calculations of tetragonally-structured single crystal zinc phosphide (Zn_3P_2) nanowires"

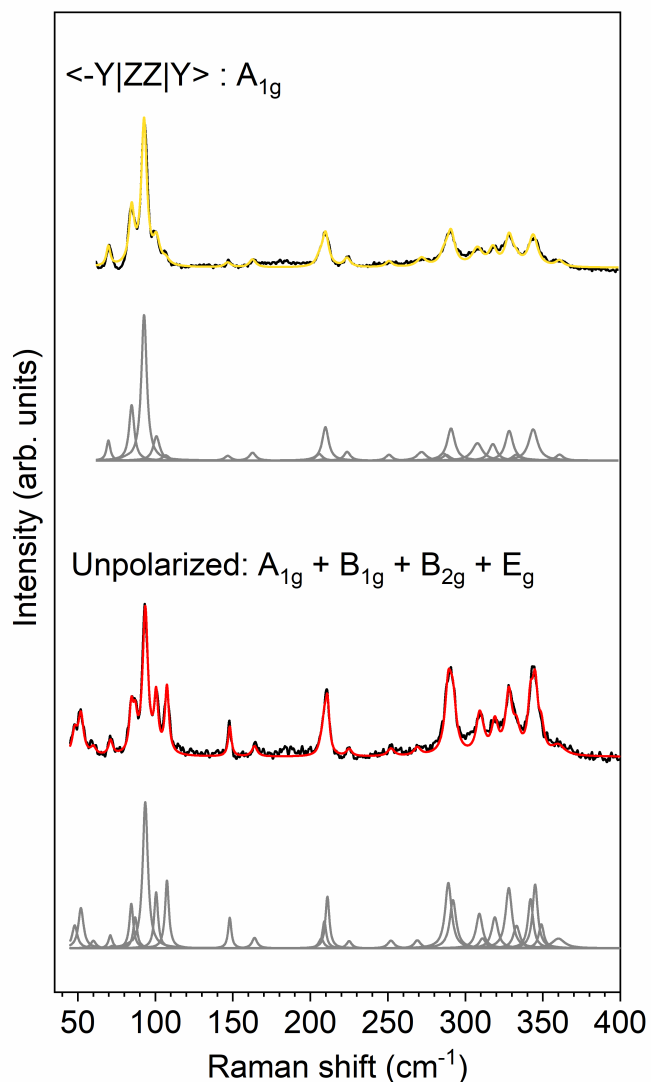


Figure E1 – Deconvoluted Raman spectra of Zn_3P_2 in polarized and unpolarized configurations measured at 12 K using 532 nm excitation wavelength. The polarization geometry is indicated above each spectrum, along with the labels of the specific phonons that are allowed in these conditions. Experimentally obtained spectra are drawn in black, while the fits obtained after the deconvolution are drawn in orange for $\langle -Y|ZZ|Y \rangle$ polarization configuration and in red for unpolarized Raman spectrum. The Lorentzian curves representing each Raman mode are drawn in gray.

G Supplementary information for "Showcasing the optical properties of monocrystalline zinc phosphide thin films as an earth-abundant pho- tovoltaic absorber"

G.1 Additional RBS data

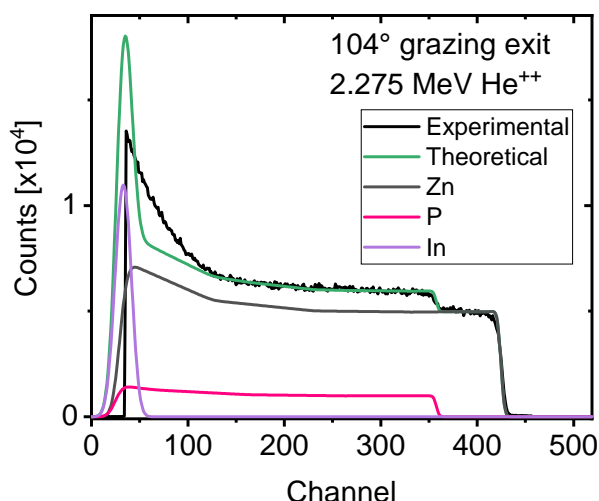


Figure G.1 – Rutherford backscattering spectrum acquired with a grazing exit detector at 104° from normally-impinging 2.275 MeV He⁺⁺. Elemental fits of the atoms in the Zn₃P₂ layer and InP substrate are shown.

G.2 Summary of photoluminescence peak properties

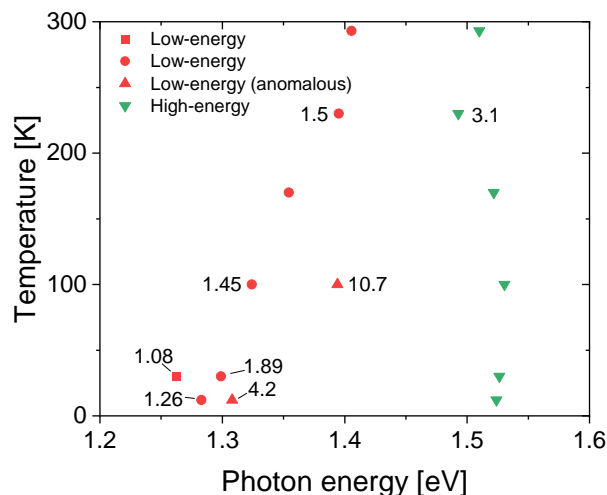


Figure G.2 – Peak center positions of the Gaussians best fitting the data. For the high-energy peaks (green), at 1 mW. For the low-energy peaks (red) at 30 K and below, extrapolated to 0 mW. For the low-energy peaks (red) at 100 K and above, averaged over the range of measurements. Numerical values indicate the exponent of the $I = P^k$ relationship, linking the peak intensity (I) to the laser power (P).

G.3 Variability of the photoluminescence spectrum

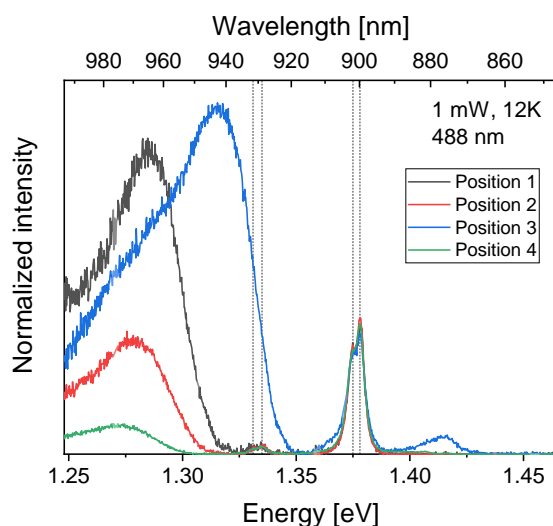


Figure G.3 – Photoluminescence spectra acquired with a 488 nm laser at 12 K at different positions. The defect peaks of the InP substrate and their phonon replicas are shown with vertical dotted lines. The spectra are normalized to the main InP peaks.

G.4 Fitting of the photoluminescence spectra

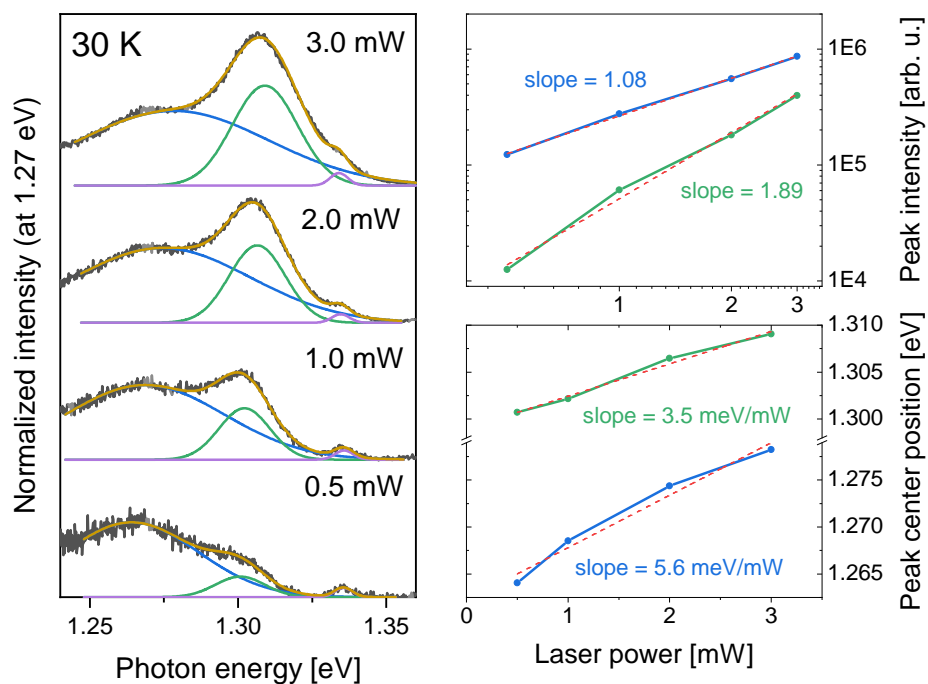


Figure G.4 – Detailed fitting of the sub-1.36 eV peaks in the spectra acquired at 30 K. The fit were carried out in the range from 1.24-1.25 eV to 1.36 eV with gaussians. No constraints were applied to the peaks besides their number, having a positive area, a baseline at $y = 0$ and the FWHM of the InP peak near 1.33 eV being constant.

Appendix G. Supplementary information for "Showcasing the optical properties of monocrystalline zinc phosphide thin films as an earth-abundant photovoltaic absorber"

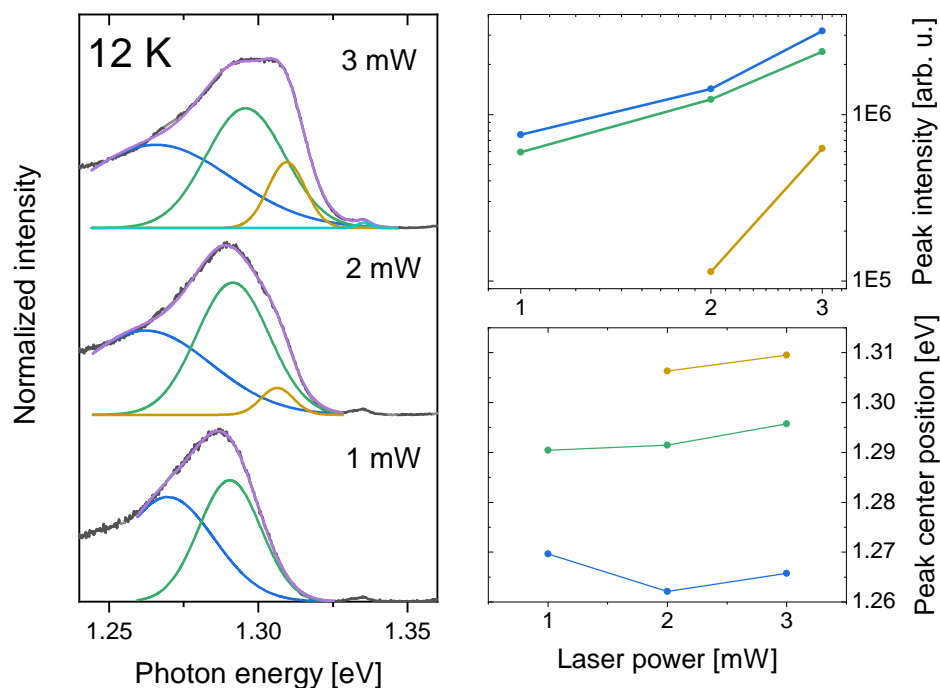


Figure G.5 – Detailed fitting of the sub-1.36 eV peaks in the spectra acquired at 12 K. The fit were carried out in the range from 1.24-1.25 eV to 1.36 eV with gaussians. No constraints were applied to the peaks besides their number, having a positive area and a baseline at $y = 0$.

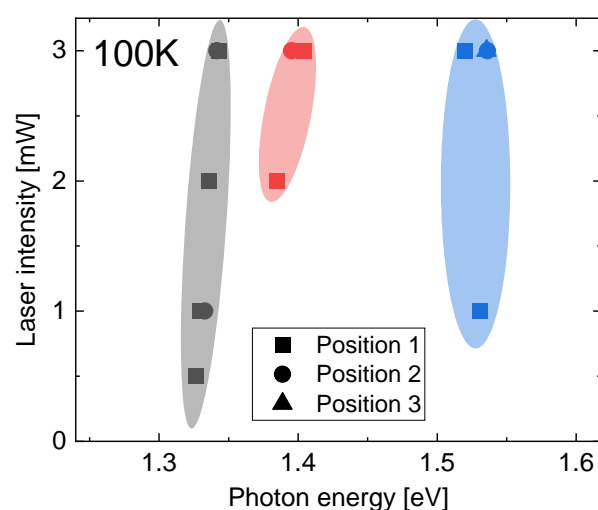


Figure G.6 – Best fit parameters (with two or three gaussians) of spectra acquired at 100 K. Data acquired at different positions on the same sample (data not shown).

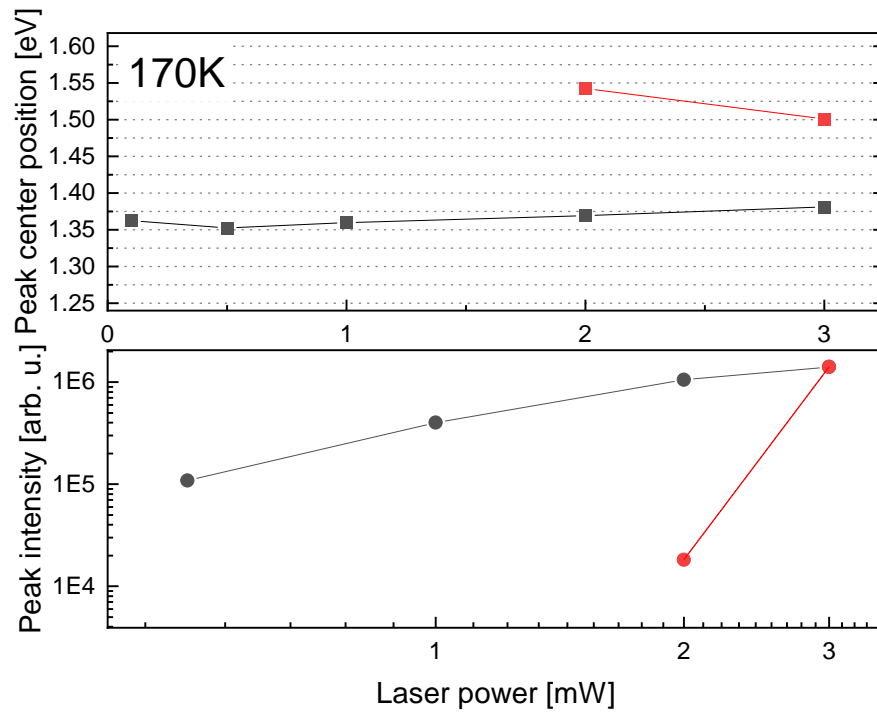


Figure G.7 – Best fit parameters (with two gaussians) of spectra acquired at 170 K. Top: peak center position. Bottom: peak intensity.

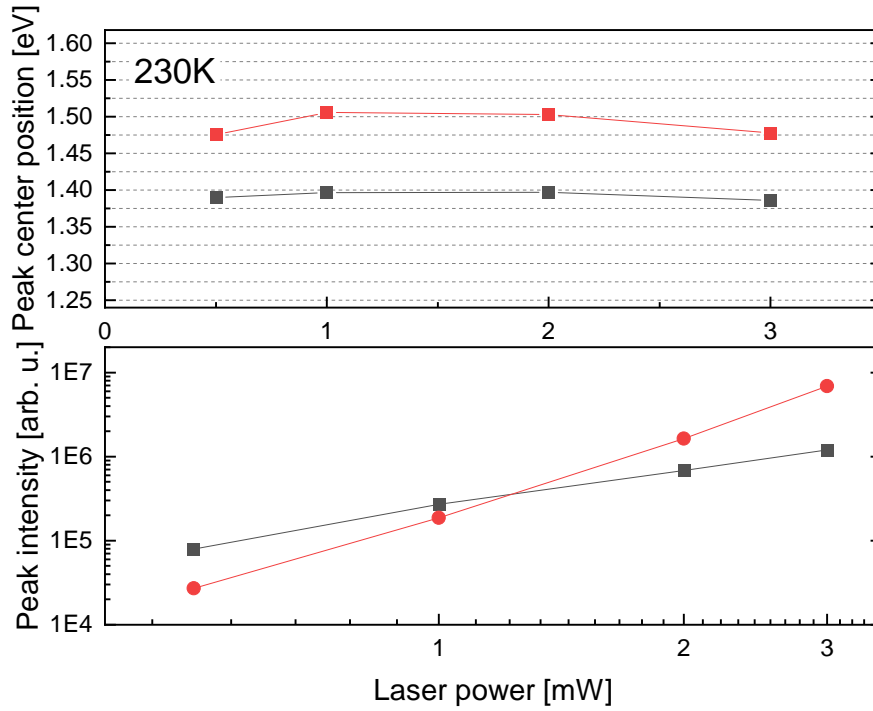


Figure G.8 – Best fit parameters (with two gaussians) of spectra acquired at 230 K. Top: peak center position. Bottom: peak intensity.

G.5 Optical pump terahertz probe spectroscopy fitting

For the reflection geometry used in the manuscript, the photoinduced change in THz reflected signal, ΔR is measured and referenced to the unphotoexcited THz reflected signal, R , as follows:

$$\frac{\Delta R}{R} = \frac{E_p - E_0}{E_0} = \frac{\Delta E_r}{E_r} \quad (\text{G.1})$$

where E_p is the measured reflected THz electric field when the sample is photoexcited and E_0 is the THz electric field measured in equilibrium (i.e. unphotoexcited case). R is therefore the sample reflectivity without photoexcitation and is equal to:

$$R = \frac{1 - n_0}{1 + n_0} \quad (\text{G.2})$$

where n_0 is the complex frequency-dependent refractive index of the unexcited sample at THz frequencies. This measured signal, $\frac{\Delta E_r}{E_r}$, is directly proportional to the effective photoinduced charge carrier density. The number of charge carriers induced by the pump beam is calculated

G.5. Optical pump terahertz probe spectroscopy fitting

using:

$$N = \varphi \frac{E\lambda}{hc} (1 - \exp(-\alpha d)) \quad (\text{G.3})$$

Where α is the absorption coefficient and d is the thickness of the thin film. E is the total energy and λ is the wavelength of the photoexcitation beam. φ is the ratio of free charge-carriers created per photon absorbed and is assumed to be unity ($\varphi=1$), to provide a maximum value for the number of photoinduced charge carriers.

To calculate the effective photoinduced charge density in the thin film, the overlapping area between the optical pump beam and THz probe beam is also taken account. Both beams are assumed to have 2D Gaussian profiles, so that the effective overlap area is given by:

$$A_{eff} = 2\pi(w_{pump}^2 + w_{THz}^2) \quad (\text{G.4})$$

where w_{pump} and w_{THz} are the beam waists of the pump and THz beam respectively. The effective photoinduced charge carrier density is therefore given by:

$$n = \frac{N}{A_{eff}} \quad (\text{G.5})$$

For this analysis, we used a measured value for the absorption coefficient of $1.85 \times 10^4 \text{ cm}^{-1}$ calculated from the extinction coefficient in reference [407]. This value is given for a photoexcitation with polarization perpendicular to the c-axis of the thin film, matching our experimental geometry. This value also coincides with other experimental studies [391, 511].

Figure G.9 shows the decay of the photoinduced charge carrier density as a function of time after photoexcitation.

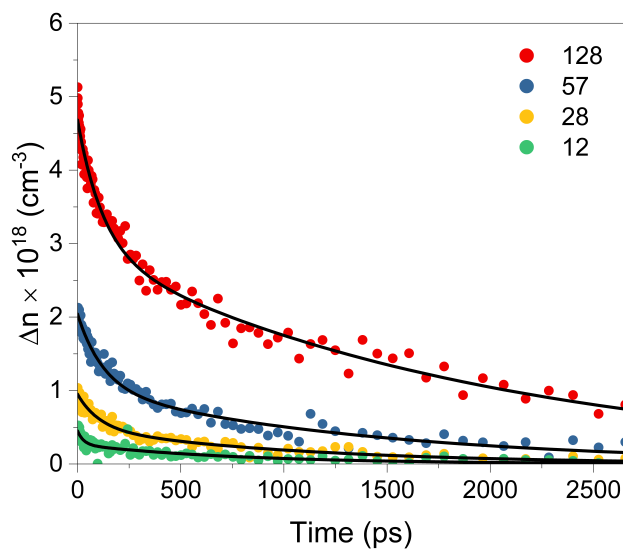


Figure G.9 – Decay of photoinduced carrier density as a function of time after photoexcitation.

For fluences of 128, 57, 28 and 12 $\mu\text{J cm}^{-2}$, the calculated photoinduced carrier density values at time = 0 ps after photoexcitation were (5.17, 2.3, 1.13, 0.49) $\cdot 10^{18} \text{ cm}^{-3}$.

G.6 Optical pump terahertz probe spectroscopy fitting

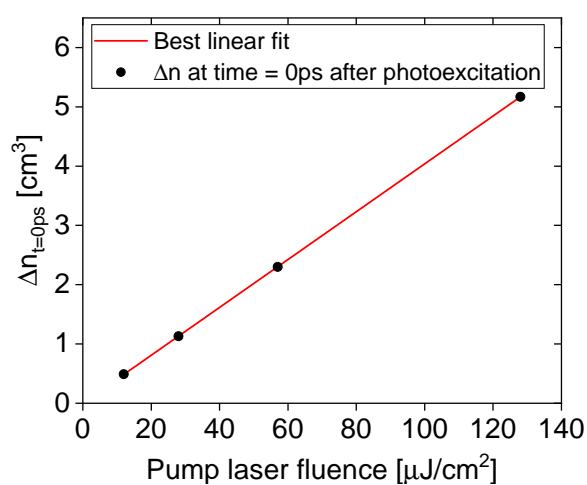


Figure G.10 – Maximum of the biexponential fit to the temporal OPTP data, versus pump fluence. The red curve is the best linear fit.

G.7 Optical pump terahertz probe data analysis - calculation of photoconductivity

To convert the transient photoinduced reflected THz signal into photoconductivity, the sample is modelled as a thin film on a thick bulk substrate. All multiple internal reflections of the probing THz pulse can therefore be separated by temporal windowing. The front face of the thin film is optically excited at a central wavelength of 750 nm and the thickness of the thin film is larger than the absorption depth of the material, so that the photoinduced THz response is dominated by the thin film with negligible contribution from the bulk substrate.

ΔE_r can be calculated via solving the wave equation, as demonstrated in ref. [512], so that the measured signal, ΔE_r is equal to:

$$\Delta E_r = \frac{Z_0 t_1^2 a^2}{2n_1} \left[\int_0^L \exp(2ikx) \Delta\sigma(x) dx + 2r_2 \exp(2ikL) \int_0^L \Delta\sigma(x) dx + (r_2 \exp(2ikL))^2 \int_0^L \exp(-2ikz) \Delta\sigma(x) dx \right] \quad (G.6)$$

where Z_0 is the vacuum impedance, $t_1 = 2n_1/(n_0 + n_1)$ is the transmission coefficient of the Zn_3P_2 thin film and $r_2 = (n_0 - n_1)/(n_0 + n_1)$ is the internal reflection coefficient at the interface between the thin film and InP substrate. For our sample geometry, n_1 is the refractive index of air ($n_1 = 1$), n_2 is the refractive index of InP ($n_2 = 3.2$); and n is the refractive index of the Zn_3P_2 thin film. The value for the refractive index of InP is an average of previously-reported values in the THz frequency range [513]. For the refractive index of Zn_3P_2 , the static dielectric constant was used ($n = \sqrt{33}$), which is consistent with other previous studies in the THz range [407, 511]. The parameter a takes into account the multiple internal reflection of the THz probe inside the sample and is equal to:

$$a = [1 - r_1 r_2 \exp(2ikL)]^{-1}. \quad (G.7)$$

No internal reflections of the THz probe beam were observed within the time-domain waveform, so $a = 1$. When the photoexcited part is much thinner than the sample thickness, the unexcited part of the sample can be considered as the substrate, so that $n_0 = n_2$ and $r_2 = 0$. The formula reduces to:

$$\frac{\Delta E_r}{E_r} = \frac{2Z_0 n_1}{n_0^2 - n_1^2} \int_0^L \exp(2ikx) \Delta\sigma(x) dx \quad (G.8)$$

This assumption is also valid for our case of a thin film on a highly conductive substrate when the substrate refractive index is comparable to that of the thin film [514], as r_2 reduces rendering the second and third terms in equation G.6 negligible. As the thin film is excited within the linear regime (see Figure G.10), the complex photoconductivity is assumed to follow

Appendix G. Supplementary information for "Showcasing the optical properties of monocrystalline zinc phosphide thin films as an earth-abundant photovoltaic absorber"

the Beer-Lambert absorption law as a result of an exponential excitation profile:

$$\Delta\sigma(x) = \Delta\sigma_s \exp(-\alpha x) \quad (\text{G.9})$$

Where $\Delta\sigma_s$ is the photoconductivity at the surface of the thin film. Therefore, the measured signal is equal to:

$$\frac{\Delta E_r}{E_r} = \frac{2Z_0 n_1}{n_0^2 - 1} \frac{\Delta\sigma_s}{\alpha} \frac{1}{1 - \frac{2i\omega n_0}{\alpha c}} \quad (\text{G.10})$$

The figure below shows the calculated frequency-averaged photoconductivity as a function of time after photoexcitation:

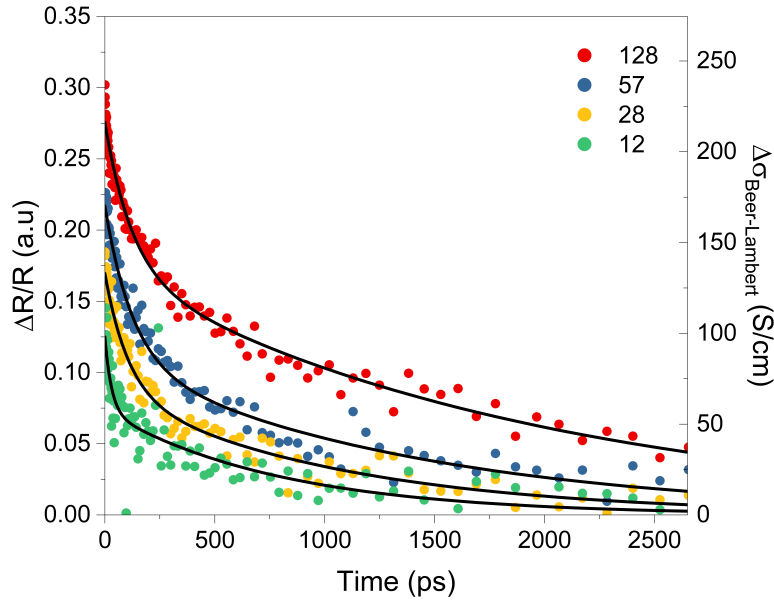


Figure G.11 – Frequency-averaged photoconductivity of the Zn_3P_2 thin film and the measured $\Delta R/R$ signal as a function of time after photoexcitation.

These values coincide with previously-reported values of $>100 \text{ Scm}^{-1}$ for photoexcitation above 1.55 eV.

G.8 Photoconductivity decay within the thin film

As the OPTP spectroscopic measurements were performed in reflection geometry, the observed photoinduced THz response is dominated by the photoconductivity at the surface of the Zn_3P_2 thin film. To illustrate this point, we model the expected photoconductivity from the InP substrate in our experimental configuration. Given the value of absorption coefficient used for the Zn_3P_2 , we calculate that 22% of the intensity of photoexcited excitation will reach the InP substrate. Taking into account absorption within the InP [513], this equates to an effective

G.8. Photoconductivity decay within the thin film

photoinduced carrier density on the order of $1 \times 10^{15} \text{ cm}^{-3}$, which is three orders of magnitude lower than the photoinduced carrier density in the Zn_3P_2 thin film and comparable to the equilibrium carrier concentration of InP.

The photoconductivity was calculated for this carrier density ($n = 1 \times 10^{15} \text{ cm}^{-3}$) using a Drude response. The intrinsic carrier concentration was taken as $n_0 = 3.79 \times 10^{15} \text{ cm}^{-3}$; the scattering time, $\tau = 0.21 \text{ ps}$; and the electron effective mass as $m_e^* = 0.08 m_e$ [513]. Figure G.11 shows the calculated photoconductivity response.

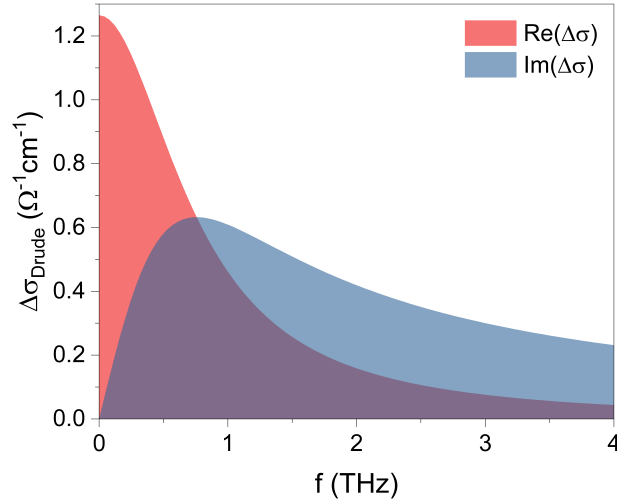


Figure G.12 – The calculated photoconductivity spectrum of the InP susbstrate when 22% of the photoexcited light intensity reaches its surface.

The magnitude of the photoconductivity for the InP susbstrate only reaches a maximum of $\approx 1.2 \text{ S cm}^{-1}$, which is significantly smaller than the photoconductivity of the Zn_3P_2 thin film and below the noise floor of our measurement. The measured photoinduced response can therefore be attributed solely to the Zn_3P_2 thin film.

Using the expression for the Beer-Lambert law, Figure G.12 shows the decay of the photoconductivity as a function of distance within the film.

Appendix G. Supplementary information for "Showcasing the optical properties of monocrystalline zinc phosphide thin films as an earth-abundant photovoltaic absorber"

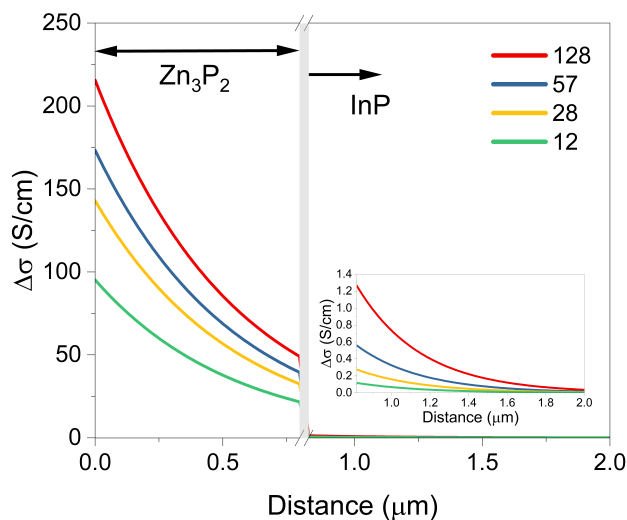


Figure G.13 – Change in photoconductivity as a function of distance within the Zn_3P_2 thin film and InP substrate.

The photoconductivity decays exponentially into the Zn_3P_2 thin film until it reaches the film thickness. At the film thickness, only 12% of the light intensity is absorbed by the InP substrate, leading to a reduced photoconductivity $< 1.2 \text{ S cm}^{-1}$. We therefore attribute the induced THz response solely due to the Zn_3P_2 thin film, with the dominant contribution from the surface of the thin film.

H Base concepts of solid-state physics

(Charge) carriers

Charge carriers are particles that transport electrical charge. They contribute to electrical current. In metals, they are typically electrons, with a negative charge. In semiconductors and insulator materials, the main charge carriers are electrons and *holes*, the absence of an electron, having a positive charge.

Bandgap/band gap

The *bandgap* of a material is the size of the interval of energies that electrons and holes may not have while in the material. Electrons with energies lower than the gap are bound to their atom and occupy the *valence band(s)*. Electrons with energies higher than the bandgap are in the *conduction band(s)* and contribute to electrical conduction by being free to travel through the crystal. When an electron received enough energy to cross the bandgap from the valence band to the conduction band, it is said that it is *excited*. Metals do not have a bandgap, their electrons can have any energy (within limits) and many contribute to conduction. Insulator materials have a very large bandgap. Because it is energetically very costly to have electrons in the conduction band, these materials are very poor electrical conductors. Semiconductors have a comparatively smaller bandgap than insulator materials. Ambient heat can excite electrons from the valence band to the conduction band, providing a few electrons for conduction. In addition, the electrical conduction of semiconductor can be accurately controlled and changed over many orders of magnitude by adding small amounts of impurities, other atoms, that add or remove electrons and holes able to contribute to conduction. This is *doping*. A semiconductor doped in a way as to have an excess of electrons in the conduction band is said to be *n-doped*, or *n-type*, and with an excess of holes it is *p-doped* or *p-type*. In some cases, ions, charged atoms, can also become charge carriers and contribute significantly to electrical current.

The bandgap of a semiconductor can be *direct* or *indirect*. The former means that electrons can travel between the valence band maximum and the conduction band minimum simply

Appendix H. Base concepts of solid-state physics

by gaining or losing energy. In photovoltaics, the gain of energy comes from a photon of light, which is absorbed. In indirect bandgap materials, the electrons need to change their momentum in order to cross the bandgap, in addition to losing or gaining energy. Photons cannot provide enough momentum to the electrons and the presence of another particle, with a significant momentum, is required to allow electrons to cross the gap. This particle is generally a phonon, a small unit (a quantum) of vibration of the crystalline lattice, also responsible for transporting heat. Because a phonon is required in addition to a photon, excitations of electrons across an indirect bandgap are less likely and the material is a worse absorber of light.

Bibliography

- [1] “World Population Prospects 2019: Highlights,” Tech. Rep. ST/ESA/SER.A/423, United Nations, Department of Economic and Social Affairs, Population Division, 2019. ISBN: 978-92-1-148316-1.
- [2] W. Lutz, A. Goujon, S. Kc, M. Stonawski, and N. Stilianakis, “Demographic and Human Capital Scenarios for the 21st Century: 2018 assessment for 201 countries,” Tech. Rep. JRC111148, EUR 29113 EN, Publications Office of the European Union, 2018. DOI:10.2760/835878, ISBN: 978-92-79-78024-0.
- [3] R. E. Smalley, “Future global energy prosperity: The terawatt challenge,” *MRS Bull.*, vol. 30, no. 6, pp. 412–417, 2005.
- [4] “International Energy Outlook 2020,” tech. rep., U.S. Energy Information Administration, 2020. [ieo2020.pdf](#).
- [5] E. Mearns, “Global Energy Forecast to 2100.” <http://euanmearns.com/global-energy-forecast-to-2100/>, 2018. Accessed: July 25th, 2021.
- [6] “Key World Energy Statistics 2020,” tech. rep., International Energy Agency, 2020. www.iea.org.
- [7] Unknown, “China moves forward with thorium molten salt reactor,” *Nuclear Engineering International*, 2021. <https://www.neimagazine.com/news/newschina-moves-forward-with-thorium-molten-salt-reactor-8919220>, Accessed: August 3rd, 2021.
- [8] “What is ITER?.” <https://www.iter.org/proj/inafewlines>. Accessed: August 3rd, 2021.
- [9] “Renewable energy explained.” <https://www.eia.gov/energyexplained/renewable-sources/>. Accessed: August 3rd, 2021.
- [10] “Geothermal Energy.” <https://www.nationalgeographic.org/encyclopedia/geothermal-energy/>. Accessed: August 3rd, 2021.
- [11] R. Lindsey, “Climate and Earth’s energy budget.” <https://earthobservatory.nasa.gov/features/EnergyBalance/page1.php>, 2009. Accessed: August 10th, 2021.
- [12] J. Jean, P. R. Brown, R. L. Jaffe, T. Buonassisi, and V. Bulović, “Pathways for solar photovoltaics,” *Energy Environ. Sci.*, vol. 8, no. 4, pp. 1200–1219, 2015.
- [13] “Renewable Power Generation Costs in 2020,” tech. rep., International Renewable Energy Agency, 2021. ISBN: 978-92-9260-348-9, <https://www.irena.org/publications/2021/Jun/Renewable-Power-Costs-in-2020>.

Bibliography

- [14] ourworldindata.org, “Solar PV module prices.” <https://ourworldindata.org/grapher/solar-pv-prices?time=earliest..latest>. Accessed: August 8th, 2021.
- [15] “World Energy Outlook 2020,” tech. rep., International Energy Agency, 2020. www.iea.org.
- [16] N. M. Haegel, H. A. Atwater, T. Barnes, C. Breyer, A. Burrell, Y.-M. Chiang, S. De Wolf, B. Dimmler, D. Feldman, S. Glunz, J. C. Goldschmidt, D. Hochschild, R. Inzunza, I. Kaizuka, B. Kroposki, S. Kurtz, S. Leu, R. Margolis, K. Matsubara, A. Metz, W. K. Metzger, M. Morjaria, S. Niki, S. Nowak, I. M. Peters, S. Philipps, T. Reindl, A. Richter, D. Rose, K. Sakurai, R. Schlatmann, M. Shikano, W. Sinke, R. Sinton, B. J. Stanbery, M. Topic, W. Tumas, Y. Ueda, J. van de Lagemaat, P. Verlinden, M. Vetter, E. Warren, M. Werner, M. Yamaguchi, and A. W. Bett, “Terawatt-scale photovoltaics: Transform global energy,” *Science* (80-.), vol. 364, no. 6443, pp. 836–838, 2019.
- [17] “Renewables 2020: Analysis and forecast to 2025,” tech. rep., International Energy Agency, 2020. <https://www.iea.org/reports/renewables-2020>.
- [18] “Renewables 2021 Global Status Report,” 2021. Paris, REN21 Secretariat, ISBN: 978-3-948393-03-8.
- [19] “Schweizerische Elektrizitätsstatistik 2020/Statistiques suisses de l’électricité 2020,” tech. rep., Swiss Federal Office of Energy, SFOE, 2021. <https://www.bfe.admin.ch/bfe/en/home/supply/statistics-and-geodata/energy-statistics/electricity-statistics.html>.
- [20] T. Tröndle, S. Pfenninger, and J. Lilliestam, “Home-made or imported: On the possibility for renewable electricity autarky on all scales in Europe,” *Energy Strateg. Rev.*, vol. 26, no. July, p. 100388, 2019.
- [21] M. Victoria, N. Haegel, I. M. Peters, R. Sinton, A. Jäger-Waldau, C. del Cañizo, C. Breyer, M. Stocks, A. Blakers, I. Kaizuka, K. Komoto, and A. Smets, “Solar photovoltaics is ready to power a sustainable future,” *Joule*, vol. 5, no. 5, pp. 1041–1056, 2021.
- [22] A. Fyke, “The Fall and Rise of Gravity Storage Technologies,” *Joule*, vol. 3, no. 3, pp. 625–630, 2019.
- [23] M. A. Green, “Third generation photovoltaics: Ultra-high conversion efficiency at low cost,” *Prog. Photovoltaics Res. Appl.*, vol. 9, no. 2, pp. 123–135, 2001.
- [24] S. Phillips and W. Warmuth, “Photovoltaics report,” tech. rep., Fraunhofer Institute for Solar Energy Systems, ISE, September 2020. <https://www.ise.fraunhofer.de/en/publications/studies/photovoltaics-report.html>.
- [25] F. Haase, C. Hollemann, S. Schäfer, A. Merkle, M. Rienäcker, J. Krügener, R. Brendel, and R. Peibst, “Laser contact openings for local poly-Si-metal contacts enabling 26.1%-efficient POLO-IBC solar cells,” *Sol. Energy Mater. Sol. Cells*, vol. 186, no. June, pp. 184–193, 2018.
- [26] M. Green, E. Dunlop, J. Hohl-Ebinger, M. Yoshita, N. Kopidakis, and X. Hao, “Solar cell efficiency tables (version 57),” *Prog. Photovoltaics Res. Appl.*, vol. 29, no. 1, pp. 3–15, 2021.
- [27] L. C. Andreani, A. Bozzola, P. Kowalczewski, M. Liscidini, and L. Redorici, “Silicon solar cells: Toward the efficiency limits,” *Adv. Phys. X*, vol. 4, no. 1, 2019.

-
- [28] T. Tiedje, E. Yablonovitch, G. Cody, and B. Brooks, "Limiting efficiency of silicon solar cells," *IEEE Trans. Electron Devices*, vol. 31, pp. 711–716, may 1984.
- [29] A. Goetzberger, J. Knobloch, and B. Voss, *Crystalline Silicon Solar Cells*. John Wiley and Sons, Ltd, 1998.
- [30] J. Svarc, "Most efficient solar panels 2021." <https://www.cleanenergyreviews.info/blog/most-efficient-solar-panels>. July 18, 2021, accessed: August 7th, 2021.
- [31] National Renewable Energy Laboratory, "Best research-cell efficiency chart." <https://www.nrel.gov/pv/cell-efficiency.html>, 2021. Accessed: May 25th, 2021.
- [32] B. Ehrler, E. Alarcón-Lladó, S. W. Tabernig, T. Veeken, E. C. Garnett, and A. Polman, "Photovoltaics Reaching for the Shockley–Queisser Limit," *ACS Energy Lett.*, vol. 5, pp. 3029–3033, sep 2020.
- [33] businesswire.com, "Alta Devices sets 29.1% solar efficiency record; NASA selects Alta Devices for International Space Station test." <https://www.businesswire.com/news/home/20181212005060/en/Alta-Devices-Sets-29.1-Solar-Efficiency-Record>, 2018. Accessed: May 25th, 2021.
- [34] W. Shockley and H. J. Queisser, "Detailed balance limit of efficiency of p-n junction solar cells," *J. Appl. Phys.*, vol. 32, no. 3, pp. 510–519, 1961.
- [35] J. F. Geisz, R. M. France, K. L. Schulte, M. A. Steiner, A. G. Norman, H. L. Guthrey, M. R. Young, T. Song, and T. Moriarty, "Six-junction III–V solar cells with 47.1% conversion efficiency under 143 Suns concentration," *Nat. Energy*, vol. 5, no. 4, pp. 326–335, 2020.
- [36] P. C. K. Vesborg and T. F. Jaramillo, "Addressing the terawatt challenge: Scalability in the supply of chemical elements for renewable energy," *RSC Adv.*, vol. 2, no. 21, pp. 7933–7947, 2012.
- [37] G. Kavlak, J. McNerney, R. L. Jaffe, and J. E. Trancik, "Metal production requirements for rapid photovoltaics deployment," *Energy Environ. Sci.*, vol. 8, no. 6, pp. 1651–1659, 2015.
- [38] European Commission, "Critical raw materials." https://ec.europa.eu/growth/sectors/raw-materials/specific-interest/critical_en. Accessed: May 25th, 2021.
- [39] European Commission, "The raw materials initiative: meeting our critical needs for growth and jobs in Europe." <https://eur-lex.europa.eu/legal-content/EN/TXT/?uri=CELEX:52008DC0699>. Accessed: August 8th, 2021.
- [40] European Commission, "Policy and strategy for raw materials." https://ec.europa.eu/growth/sectors/raw-materials/policy-strategy_en. Accessed: August 8th, 2021.
- [41] European Commission, "2017 list of Critical Raw Materials for the EU." <https://eur-lex.europa.eu/legal-content/EN/TXT/?uri=CELEX:52017DC0490>. Accessed: May 25th, 2021.
- [42] European Commission, "Critical Raw Materials Resilience: Charting a Path towards greater Security and Sustainability." <https://eur-lex.europa.eu/legal-content/EN/TXT/?uri=CELEX:52020DC0474>. Accessed: May 25th, 2021.
- [43] US Interior Department, *Final List of Critical Minerals 2018*. Fed. Reg. Vol. 83, p. 23295, 2018-05-18.
- [44] Y. Zhou, A. Xie, F. Lu, and K. Zhang, "The Belt and Road Initiative: An inclusive and

Bibliography

- symbiotic approach to shared global prosperity,” tech. rep., Boston Consulting Group, 2018.
- [45] Mission 2016 - The Future of Strategic Natural Resources, “Deep sea mining.” <https://web.mit.edu/12.000/www/m2016/finalwebsite/solutions/oceans.html>. Accessed: May 25th, 2021.
- [46] J. Brophy, F. Culick, and L. Friedman, “Asteroid retrieval feasibility study.” <https://commons.erau.edu/publication/893/>, 2012. Accessed: May 25th, 2021.
- [47] Sonter, Mark, “Asteroid mining: Key to the space economy.” <https://space.nss.org/asteroid-mining-key-to-the-space-economy/>, 2006. Accessed: May 25th, 2021.
- [48] Mission 2016 - The Future of Strategic Natural Resources, “Asteroid mining.” <https://web.mit.edu/12.000/www/m2016/finalwebsite/solutions/asteroids.html>. Accessed: May 25th, 2021.
- [49] J. R. Rumble, ed., *CRC Handbook of Chemistry and Physics*, ch. 14 Geophysics, Astronomy, and Acoustics: Abundance of Elements in the Earth’s Crust and in the Sea. Boca Raton, FL, USA: CRC Press/Taylor & Francis, 101st ed. Internet Version 2020.
- [50] W. Wang, M. T. Winkler, O. Gunawan, T. Gokmen, T. K. Todorov, Y. Zhu, and D. B. Mitzi, “Device characteristics of CZTSSe thin-film solar cells with 12.6% efficiency,” *Adv. Energy Mater.*, vol. 4, no. 7, pp. 1–5, 2014.
- [51] D. Tiwari, D. Alibhai, D. Cherns, and D. J. Fermin, “Crystal and Electronic Structure of Bismuth Thiophosphate, BiPS4: An Earth-Abundant Solar Absorber,” *Chem. Mater.*, vol. 32, no. 3, pp. 1235–1242, 2020.
- [52] C. Wadia, A. P. Alivisatos, and D. M. Kammen, “Materials Availability Expands the Opportunity for Large-Scale Photovoltaics Deployment,” *Environ. Sci. Technol.*, vol. 43, no. 6, pp. 2072–2077, 2009.
- [53] A. Zakutayev, J. D. Major, X. Hao, A. Walsh, J. Tang, T. K. Todorov, L. H. Wong, and E. Saucedo, “Emerging inorganic solar cell efficiency tables (version 2),” *JPhys Energy*, vol. 3, no. 3, 2021.
- [54] A. D. Martinez, B. R. Ortiz, N. E. Johnson, L. L. Baranowski, L. Krishna, S. Choi, P. C. Dippo, B. To, A. G. Norman, P. Stradins, V. Stevanovic, E. S. Toberer, and A. C. Tamboli, “Development of ZnSiP₂ for Si-Based Tandem Solar Cells,” *IEEE J. Photovoltaics*, vol. 5, no. 1, pp. 17–21, 2015.
- [55] J. L. Shay, B. Tell, E. Buehler, and J. H. Wernick, “Band structure of ZnGeP₂ and ZnSiP₂ - Ternary compounds with pseudodirect energy gaps,” *Phys. Rev. Lett.*, vol. 30, no. 20, pp. 983–986, 1973.
- [56] L. Yu and A. Zunger, “Identification of potential photovoltaic absorbers based on first-principles spectroscopic screening of materials,” *Phys. Rev. Lett.*, vol. 108, no. 6, pp. 1–5, 2012.
- [57] Y. Hinuma, T. Hatakeyama, Y. Kumagai, L. A. Burton, H. Sato, Y. Muraba, S. Iimura, H. Hiramatsu, I. Tanaka, H. Hosono, and F. Oba, “Discovery of earth-abundant nitride semiconductors by computational screening and high-pressure synthesis,” *Nat. Commun.*, vol. 7, no. May, pp. 1–2, 2016.

- [58] J. Kangsabanik and A. Alam, "High-performance ternary alkali nitrides for renewable energy applications," *Phys. Rev. Mater.*, vol. 3, no. 10, p. 105405, 2019.
- [59] A. Swarnkar, W. J. Mir, R. Chakraborty, M. Jagadeeswararao, T. Sheikh, and A. Nag, "Are Chalcogenide Perovskites an Emerging Class of Semiconductors for Optoelectronic Properties and Solar Cell?," *Chem. Mater.*, vol. 31, no. 3, pp. 565–575, 2019.
- [60] S. J. S. Flora and N. Dwivedi, "A toxicochemical review of gallium arsenide," *Def. Sci. J.*, vol. 62, no. 2, pp. 95–104, 2012.
- [61] R. Nechache, C. Harnagea, S. Li, L. Cardenas, W. Huang, J. Chakrabartty, and F. Rosei, "Bandgap tuning of multiferroic oxide solar cells," *Nat. Photonics*, vol. 9, no. 1, pp. 61–67, 2014.
- [62] B. D. Yuhas and P. Yang, "Nanowire-Based All-Oxide Solar Cells," *J. Am. Chem. Soc.*, vol. 131, pp. 3756–3761, 2009.
- [63] T. K. Todorov, S. Singh, D. M. Bishop, O. Gunawan, Y. S. Lee, T. S. Gershon, K. W. Brew, P. D. Antunez, and R. Haight, "Ultrathin high band gap solar cells with improved efficiencies from the world's oldest photovoltaic material," *Nat. Commun.*, vol. 8, no. 1, 2017.
- [64] U. S. D. o. E. Solar Energy Technologies Office, "Cadmium telluride." <https://www.energy.gov/eere/solar/cadmium-telluride>. Accessed: May 31st, 2021.
- [65] K. A. Dick, P. Caroff, J. Bolinsson, M. E. Messing, J. Johansson, K. Deppert, L. R. Wallenberg, and L. Samuelson, "Control of III-V nanowire crystal structure by growth parameter tuning," *Semicond. Sci. Technol.*, vol. 25, no. 2, 2010.
- [66] M. L. Cohen and J. R. Chelikowsky, *Chalcopyrite Structure Semiconductors*, pp. 161–171. Berlin, Heidelberg: Springer Berlin Heidelberg, 1988.
- [67] P. St-Jean, G. A. Seryogin, and S. Francoeur, "Band gap of sphalerite and chalcopyrite phases of epitaxial ZnSnP₂," *Appl. Phys. Lett.*, vol. 96, no. 23, pp. 10–13, 2010.
- [68] S. Schorr, "The crystal structure of kesterite type compounds: A neutron and X-ray diffraction study," *Sol. Energy Mater. Sol. Cells*, vol. 95, no. 6, pp. 1482–1488, 2011.
- [69] J. Breternitz and S. Schorr, "What Defines a Perovskite?," *Adv. Energy Mater.*, vol. 8, p. 1802366, 2018.
- [70] M. Ghasemi, E. Z. Stutz, S. Escobar Steinvall, M. Zamani, and A. Fontcuberta i Morral, "Thermodynamic re-assessment of the Zn–P binary system," *Materialia*, vol. 6, p. 100301, jun 2019.
- [71] V. Y. Rud, Y. V. Rud, A. A. Vaipolin, I. V. Bodnar, M. A. Osipiva, and T. N. Ushakova, "Photosensitive structures based on ZnP₂ single crystals of monoclinic and tetragonal modifications: Fabrication and properties," *Semiconductors*, vol. 43, no. 7, pp. 858–864, 2009.
- [72] H. Okamoto, "The As-Zn (arsenic-zinc) system," *J. Phase Equilibria*, vol. 13, no. 2, pp. 155–161, 1992.
- [73] B. Sujak-Cyrul, B. Kolodka, J. Misiewicz, and J. M. Pawlikowski, "Intraband and interband optical transitions in Zn₃As₂," *J. Phys. Chem. Solids*, vol. 43, no. 11, pp. 1045–1051, 1982.
- [74] J. R. Botha, G. J. Scriven, J. A. A. Engelbrecht, and A. W. R. Leitch, "Photoluminescence properties of metalorganic vapor phase epitaxial Zn₃As₂," *J. Appl. Phys.*, vol. 86, no. 10, pp. 5614–5618, 1999.

Bibliography

- [75] H. S. Im, K. Park, D. M. Jang, C. S. Jung, J. Park, S. J. Yoo, and J. G. Kim, "Zn₃P₂-Zn₃As₂ solid solution nanowires," *Nano Lett.*, vol. 15, no. 2, pp. 990–997, 2015.
- [76] V. M. Trukhan, S. F. Marenkin, and V. A. Rubtsov, "Solid Solutions and Phase Relations in the Cd-Zn-As-P System," *Inorg. Mater.*, vol. 34, no. 7, pp. 642–651, 1998.
- [77] J.-B. Li, M.-C. Record, and J.-C. Tedenac, "A thermodynamic assessment of the Sb-Zn system," *J. Alloys Compd.*, vol. 438, no. 1-2, pp. 171–177, 2007.
- [78] G. J. Snyder, M. Christensen, E. Nishibori, T. Caillat, and B. B. Iversen, "Disordered zinc in Zn₄Sb₃ with phonon-glass and electron-crystal thermoelectric properties," *Nat. Mater.*, vol. 3, no. 7, pp. 458–463, 2004.
- [79] J. Lin, X. Li, G. Qiao, Z. Wang, J. Carrete, Y. Ren, L. Ma, Y. Fei, B. Yang, L. Lei, and J. Li, "Unexpected high-temperature stability of β -Zn₄Sb₃ opens the door to enhanced thermoelectric performance," *J. Am. Chem. Soc.*, vol. 136, no. 4, pp. 1497–1504, 2014.
- [80] K. Niedziółka and P. Jund, "Influence of the Exchange–Correlation Functional on the Electronic Properties of ZnSb as a Promising Thermoelectric Material," *J. Electron. Mater.*, vol. 44, no. 6, pp. 1540–1546, 2015.
- [81] J. M. Goicoechea and S. C. Sevov, "[Zn₉Bi₁₁]5- A Ligand-Free Intermetalloid Cluster," *Angew. Chemie - Int. Ed.*, vol. 45, pp. 5147–5150, 2006.
- [82] P. Narang, S. Chen, N. C. Coronel, S. Gul, J. Yano, L. W. Wang, N. S. Lewis, and H. A. Atwater, "Bandgap tunability in Zn(Sn,Ge)N₂ semiconductor alloys," *Adv. Mater.*, vol. 26, no. 8, pp. 1235–1241, 2014.
- [83] T. D. Veal, N. Feldberg, N. F. Quackenbush, W. M. Linhart, D. O. Scanlon, L. F. J. Piper, and S. M. Durbin, "Band Gap Dependence on Cation Disorder in ZnSnN₂ Solar Absorber," *Adv. Energy Mater.*, vol. 5, no. 24, pp. 1–5, 2015.
- [84] A. D. Martinez, A. N. Fioretti, E. S. Toberer, and A. C. Tamboli, "Synthesis, structure, and optoelectronic properties of II-IV-V₂ materials," *J. Mater. Chem. A*, vol. 5, no. 23, pp. 11418–11435, 2017.
- [85] Y. Ye, R. Lim, and J. M. White, "High mobility amorphous zinc oxynitride semiconductor material for thin film transistors," *J. Appl. Phys.*, vol. 106, no. 7, 2009.
- [86] E. Lee, A. Benayad, T. Shin, H. Lee, D.-S. Ko, T. S. Kim, K. S. Son, M. Ryu, S. Jeon, and G.-S. Park, "Nanocrystalline ZnON; High mobility and low band gap semiconductor material for high performance switch transistor and image sensor application," *Sci. Rep.*, vol. 4, pp. 1–8, 2014.
- [87] Y. Kumagai, K. Harada, H. Akamatsu, K. Matsuzaki, and F. Oba, "Carrier-Induced Band-Gap Variation and Point Defects in Zn₃N₂ from First Principles," *Phys. Rev. Appl.*, vol. 8, no. 1, pp. 27–30, 2017.
- [88] T. Suda and K. Kakishita, "Band-gap energy and electron effective mass of polycrystalline Zn₃N₂," *J. Appl. Phys.*, vol. 99, no. 7, pp. 2–5, 2006.
- [89] G. Z. Xing, D. D. Wang, B. Yao, L. F. N. Ah Qune, T. Yang, Q. He, J. H. Yang, and L. L. Yang, "Structural and electrical characteristics of high quality (100) orientated-Zn₃N₂ thin films grown by radio-frequency magnetron sputtering," *J. Appl. Phys.*, vol. 108, no. 8, p. 083710, 2010.

- [90] M. Futsuhara, K. Yoshioka, and O. Takai, "Structural, electrical and optical properties of zinc nitride thin films prepared by reactive rf magnetron sputtering," *Thin Solid Films*, vol. 322, no. 1-2, pp. 274–281, 1998.
- [91] F. Zong, H. Ma, W. Du, J. Ma, X. Zhang, H. Xiao, F. Ji, and C. Xue, "Optical band gap of zinc nitride films prepared on quartz substrates from a zinc nitride target by reactive rf magnetron sputtering," *Appl. Surf. Sci.*, vol. 252, no. 22, pp. 7983–7986, 2006.
- [92] K. Kuriyama, Y. Takahashi, and F. Sunohara, "Optical band gap of Zn₃N₂ films," *Phys. Rev. B*, vol. 48, no. 4, pp. 2781–2782, 1993.
- [93] R. Ayouchi, C. Casteleiro, L. Santos, and R. Schwarz, "RF-plasma assisted PLD growth of Zn₃N₂ thin films," *Phys. Status Solidi Curr. Top. Solid State Phys.*, vol. 7, no. 9, pp. 2294–2297, 2010.
- [94] M. Ullah, G. Murtaza, M. Yaseen, and S. A. Khan, "Band structure features, chemical bonding and optical properties of Zn₃X₂ (X = N, P, As) compounds," *J. Alloys Compd.*, vol. 728, pp. 1226–1234, 2017.
- [95] A. Kolodziejczak-Radzimska and T. Jesionowski, "Zinc oxide-from synthesis to application: A review," *Materials (Basel)*, vol. 7, no. 4, pp. 2833–2881, 2014.
- [96] M. Futsuhara, K. Yoshioka, and O. Takai, "Optical properties of zinc oxynitride thin films," *Thin Solid Films*, vol. 317, no. 1-2, pp. 322–325, 1998.
- [97] H.-S. Kim, S. H. Jeon, J. S. Park, T. S. Kim, K. S. Son, J.-B. Seon, S.-J. Seo, S.-J. Kim, E. Lee, J. G. Chung, H. Lee, S. Han, M. Ryu, S. Y. Lee, and K. Kim, "Anion control as a strategy to achieve high-mobility and high-stability oxide thin-film transistors," *Sci. Rep.*, vol. 3, pp. 1–7, 2013.
- [98] X. Cao, A. Sato, Y. Ninomiya, and N. Yamada, "Oxygen-doped zinc nitride as a high-mobility nitride-based semiconductor," *J. Phys. Chem. C*, vol. 119, no. 10, pp. 5327–5333, 2015.
- [99] E. Brechtel, G. Cordier, and H. Schäfer, "Neue ternäre erdalkali-übergangselementpnictide," *J. Less-Common Met.*, vol. 79, no. 1, pp. 131–138, 1981.
- [100] E. Brechtel, G. Cordier, and H. Schäfer, "Darstellung und Kristallstruktur von Ca₉Mn₄Bi₉ und Ca₉Zn₄Bi₉," *Zeitschrift für Naturforsch.*, vol. 34B, pp. 1229–1233, 1979.
- [101] C. Tiburtius and H.-U. Schuster, "LiBeSb und LiZnBi, ternäre Verbindungen mit Wurtz-iterüst," *Zeitschrift für Naturforsch. - Sect. B J. Chem. Sci.*, vol. 33, no. 1, pp. 35–38, 1978.
- [102] G. Cordier, B. Eisenmann, and H. Schäfer, "Darstellung und Kristallstruktur von SrCu₂Sb₂ und SrZnBi₂," *Zeitschrift für Anorg. und Allg. Chemie*, vol. 426, pp. 205–214, 1976.
- [103] G. M. Kimball, A. M. Müller, N. S. Lewis, and H. A. Atwater, "Photoluminescence-based measurements of the energy gap and diffusion length of Zn₃P₂," *Appl. Phys. Lett.*, vol. 95, no. 11, p. 112103, 2009.
- [104] M. Bhushan and A. Catalano, "Polycrystalline Zn₃P₂ Schottky barrier solar cells," *Appl. Phys. Lett.*, vol. 38, no. 1, pp. 39–41, 1981.
- [105] H. Coelho-Júnior, B. G. Silva, C. Labre, R. P. Loreto, and R. L. Sommer, "Room-

Bibliography

- temperature synthesis of earth-abundant semiconductor ZnSiN₂ on amorphous carbon,” *Sci. Rep.*, vol. 11, no. 1, pp. 2–7, 2021.
- [106] A. N. Fioretti, A. Zakutayev, H. Moutinho, C. Melamed, J. D. Perkins, A. G. Norman, M. Al-Jassim, E. S. Toberer, and A. C. Tamboli, “Combinatorial insights into doping control and transport properties of zinc tin nitride,” *J. Mater. Chem. C*, vol. 3, no. 42, pp. 11017–11028, 2015.
- [107] P. C. Quayle, K. He, J. Shan, and K. Kash, “Synthesis, lattice structure, and band gap of ZnSnN₂,” *MRS Commun.*, vol. 3, no. 3, pp. 135–138, 2013.
- [108] I. S. Khan, K. N. Heinselman, and A. Zakutayev, “Review of ZnSnN₂ semiconductor material,” *J. Phys. Energy*, vol. 2, p. 032007, 2020.
- [109] S. Akari, J. Chantana, S. Nakatsuka, Y. Nose, and T. Minemoto, “ZnSnP₂ solar cell with (Cd,Zn)S buffer layer: Analysis of recombination rates,” *Sol. Energy Mater. Sol. Cells*, vol. 174, no. June 2017, pp. 412–417, 2018.
- [110] P. Sivakumar, P. Peranantham, V. V. Siva Kumar, K. Asokan, and Y. L. Jeyachandran, “Structure, composition and photoconductivity analysis of zinc tin phosphide ternary compound nanoparticles synthesized by chemical method,” *J. Mater. Sci. Mater. Electron.*, vol. 32, no. 7, pp. 8767–8777, 2021.
- [111] E. Arca, J. D. Perkins, S. Lany, A. Mis, B.-R. Chen, P. Dippo, J. L. Partridge, W. Sun, A. Holder, A. C. Tamboli, M. F. Toney, L. T. Schelhas, G. Ceder, W. Tumas, G. Teeter, and A. Zakutayev, “Zn₂SbN₃ : growth and characterization of a metastable photoactive semiconductor,” *Mater. Horizons*, 2019.
- [112] K. Kuriyama, T. Kato, and T. Tanaka, “Optical band gap of the filled tetrahedral semiconductor LiZnN,” *Phys. Rev. B*, vol. 49, no. 7, pp. 4511–4513, 1994.
- [113] *Appendix F Properties of Important Semiconductors*, pp. 789–789. John Wiley and Sons, Ltd, 2006.
- [114] R. Chandramohan, C. Sanjeeviraja, and T. Mahalingam, “Preparation of Zinc Selenide Thin Films by Electrodeposition Technique for Solar Cell Applications,” *Phys. Status Solidi*, vol. 163, 1997.
- [115] A. Zhussupbekova, D. Caffrey, K. Zhussupbekov, C. M. Smith, I. V. Shvets, and K. Fleischer, “Low-Cost, High-Performance Spray Pyrolysis-Grown Amorphous Zinc Tin Oxide: The Challenge of a Complex Growth Process,” *ACS Appl. Mater. Interfaces*, vol. 12, no. 41, pp. 46892–46899, 2020.
- [116] Z.-L. Tseng, C.-H. Chiang, S.-H. Chang, and C.-G. Wu, “Surface engineering of ZnO electron transporting layer via Al doping for high efficiency planar perovskite solar cells,” *Nano Energy*, vol. 28, pp. 311–318, 2016.
- [117] R. B. Hall, R. W. Birkmire, J. E. Phillips, and J. D. Meakin, “Thin-film polycrystalline Cu₂S/Cd_{1-x}Zn_xS solar cells of 10% efficiency,” *Appl. Phys. Lett.*, vol. 38, pp. 925–926, 1981.
- [118] A. Zakutayev, C. M. Caskey, A. N. Fioretti, D. S. Ginley, J. Vidal, V. Stevanovic, E. Tea, and S. Lany, “Defect tolerant semiconductors for solar energy conversion,” *J. Phys. Chem. Lett.*, vol. 5, no. 7, pp. 1117–1125, 2014.

- [119] A. Ścigała, E. Szlyk, L. Dobrzańska, D. H. Gregory, and R. Szczęsny, "From binary to multinary copper based nitrides – Unlocking the potential of new applications," *Coord. Chem. Rev.*, vol. 436, p. 213791, 2021.
- [120] A. Zakutayev, A. J. Allen, X. Zhang, J. Vidal, Z. Cui, S. Lany, M. Yang, F. J. Disalvo, and D. S. Ginley, "Experimental synthesis and properties of metastable CuNbN₂ and theoretical extension to other ternary copper nitrides," *Chem. Mater.*, vol. 26, no. 17, pp. 4970–4977, 2014.
- [121] N. J. Szymanski, L. N. Walters, O. Hellman, D. Gall, and S. V. Khare, "Dynamical stabilization in delafossite nitrides for solar energy conversion," *J. Mater. Chem. A*, vol. 6, no. 42, pp. 20852–20860, 2018.
- [122] M. Yang, A. Zakutayev, J. Vidal, X. Zhang, D. S. Ginley, and F. J. DiSalvo, "Strong optical absorption in CuTaN₂ nitride delafossite," *Energy Environ. Sci.*, vol. 6, no. 10, pp. 2994–2999, 2013.
- [123] S. Bugarinovic, M. Rajcic-Vujasinovic, Z. Stevic, and V. Grekulovic, "Cuprous oxide as an active material for solar cells," in *Solar Cells* (L. A. Kosyachenko, ed.), ch. 8, Rijeka: IntechOpen, 2011.
- [124] Y. Wu, C. Wadia, W. Ma, B. Sadtler, and A. P. Alivisatos, "Synthesis and photovoltaic application of copper(I) sulfide nanocrystals," *Nano Lett.*, vol. 8, no. 8, pp. 2345–2350, 2008.
- [125] J.-H. Choi and Y.-K. Han, "Structural, electronic, and optical properties of bulk Cu₂Se," *Curr. Appl. Phys.*, vol. 15, no. 11, pp. 1417–1420, 2015.
- [126] L. Frazer, K. B. Chang, K. R. Poeppelmeier, and J. B. Ketterson, "Cupric oxide inclusions in cuprous oxide crystals grown by the floating zone method," *Sci. Technol. Adv. Mater.*, vol. 16, no. 3, 2015.
- [127] M. Ozga, J. Kaszewski, A. Seweryn, P. Sybilski, M. Godlewski, and B. S. Witkowski, "Ultra-fast growth of copper oxide (II) thin films using hydrothermal method," *Mater. Sci. Semicond. Process.*, vol. 120, no. February, p. 105279, 2020.
- [128] R. N. Briskman, "A study of electrodeposited cuprous oxide photovoltaic cells," *Sol. Energy Mater. Sol. Cells*, vol. 27, no. 4, pp. 361–368, 1992.
- [129] T. Minami, Y. Nishi, and T. Miyata, "Efficiency enhancement using a Zn_{1-x}GexO thin film as an n-type window layer in Cu₂O-based heterojunction solar cells," *Appl. Phys. Express*, vol. 9, no. 5, 2016.
- [130] S. Giraldo, Z. Jehl, M. Placidi, V. Izquierdo-Roca, A. Pérez-Rodríguez, and E. Saucedo, "Progress and Perspectives of Thin Film Kesterite Photovoltaic Technology: A Critical Review," *Adv. Mater.*, vol. 31, no. 16, p. 1806692, 2019.
- [131] A. W. Welch, L. L. Baranowski, H. Peng, H. Hempel, R. Eichberger, T. Unold, S. Lany, C. Wolden, and A. Zakutayev, "Trade-Offs in Thin Film Solar Cells with Layered Chalcostibite Photovoltaic Absorbers," *Adv. Energy Mater.*, vol. 7, no. 11, 2017.
- [132] A. Penezko, M. Kauk-Kuusik, O. Volobujeva, R. Traksmaa, and M. Grossberg, "Observation of photoluminescence edge emission in CuSbSe₂ absorber material for photovoltaic applications," *Appl. Phys. Lett.*, vol. 115, no. 9, 2019.

Bibliography

- [133] T. J. Whittles, T. D. Veal, C. N. Savory, A. W. Welch, F. W. De Souza Lucas, J. T. Gibbon, M. Birkett, R. J. Potter, D. O. Scanlon, A. Zakutayev, and V. R. Dhanak, "Core Levels, Band Alignments, and Valence-Band States in CuSbS₂ for Solar Cell Applications," *ACS Appl. Mater. Interfaces*, vol. 9, no. 48, pp. 41916–41926, 2017.
- [134] D. M. Berg, R. Djemour, L. Gütay, G. Zoppi, S. Siebentritt, and P. J. Dale, "Thin film solar cells based on the ternary compound Cu₂SnS₃," *Thin Solid Films*, vol. 520, no. 19, pp. 6291–6294, 2012.
- [135] A. Kanai, K. Toyonaga, K. Chino, H. Katagiri, and H. Araki, "Fabrication of Cu₂SnS₃ thin-film solar cells with power conversion efficiency of over 4%," *Jpn. J. Appl. Phys.*, vol. 54, no. 8, pp. 3–7, 2015.
- [136] J. A. Marquez Prieto, S. Levchenko, J. Just, H. Hampel, I. Forbes, N. M. Pearsall, and T. Unold, "Earth abundant thin film solar cells from co-evaporated Cu₂SnS₃ absorber layers," *J. Alloys Compd.*, vol. 689, pp. 182–186, 2016.
- [137] N. Aihara and K. Tanaka, "Photoluminescence characterization of Cu₂Sn_{1-x}GexS₃ bulk single crystals," *AIP Adv.*, vol. 8, no. 9, 2018.
- [138] D. Shin, B. Saparov, and D. B. Mitzi, "Defect Engineering in Multinary Earth-Abundant Chalcogenide Photovoltaic Materials," *Adv. Energy Mater.*, vol. 7, no. 11, 2017.
- [139] D. Shin, B. Saparov, T. Zhu, W. P. Huhn, V. Blum, and D. B. Mitzi, "BaCu₂Sn(S,Se)₄: Earth-abundant chalcogenides for thin-film photovoltaics," *Chem. Mater.*, vol. 28, no. 13, pp. 4771–4780, 2016.
- [140] T. Gershon, Y. S. Lee, P. Antunez, R. Mankad, S. Singh, D. Bishop, O. Gunawan, M. Hopstaken, and R. Haight, "Photovoltaic materials and devices based on the alloyed kesterite absorber (Ag_xCu_{1-x})₂ZnSnSe₄," *Adv. Energy Mater.*, vol. 6, no. 10, pp. 1–7, 2016.
- [141] M. Grossberg, K. Timmo, T. Raadik, E. Kärber, V. Mikli, and J. Krustok, "Study of structural and optoelectronic properties of Cu₂Zn(Sn_{1-x}Gex)Se₄ (x = 0 to 1) alloy compounds," *Thin Solid Films*, vol. 582, pp. 176–179, 2015.
- [142] S. Giraldo, E. Saucedo, M. Neuschitzer, F. Oliva, M. Placidi, X. Alcobé, V. Izquierdo-Roca, S. Kim, H. Tampo, H. Shibata, A. Pérez-Rodríguez, and P. Pistor, "How small amounts of Ge modify the formation pathways and crystallization of kesterites," *Energy Environ. Sci.*, vol. 11, no. 3, pp. 582–593, 2018.
- [143] H. Du, F. Yan, M. Young, B. To, C.-S. Jiang, P. Dippo, D. Kuciauskas, Z. Chi, E. A. Lund, C. Hancock, W. M. Hlaing Oo, M. A. Scarpulla, and G. Teeter, "Investigation of combinatorial coevaporated thin film Cu₂ZnSnS₄. I. Temperature effect, crystalline phases, morphology, and photoluminescence," *J. Appl. Phys.*, vol. 115, no. 17, 2014.
- [144] C. Yan, J. Huang, K. Sun, S. Johnston, Y. Zhang, H. Sun, A. Pu, M. He, F. Liu, K. Eder, L. Yang, J. M. Cairney, N. J. Ekins-Daukes, Z. Hameiri, J. A. Stride, S. Chen, M. A. Green, and X. Hao, "Cu₂ZnSnS₄ solar cells with over 10% power conversion efficiency enabled by heterojunction heat treatment," *Nat. Energy*, vol. 3, no. 9, pp. 764–772, 2018.
- [145] Y. Liu, B. Yang, M. Zhang, B. Xia, C. Chen, X. Liu, J. Zhong, Z. Xiao, and J. Tang, "Bournonite CuPbSbS₃: An electronically-3D, defect-tolerant, and solution-processable semiconductor for efficient solar cells," *Nano Energy*, vol. 71, no. February, p. 104574, 2020.

- [146] M. Zhang, Y. Liu, B. Yang, X. Lin, Y. Lu, J. Zheng, C. Chen, and J. Tang, "Efficiency Improvement of Bournonite CuPbSbS_3 Solar Cells via Crystallinity Enhancement," *ACS Appl. Mater. Interfaces*, vol. 13, no. 11, pp. 13273–13280, 2021.
- [147] A. Crovetto, Z. Xing, M. Fischer, R. Nielsen, C. N. Savory, T. Rindzevicius, N. Stenger, D. O. Scanlon, I. Chorkendorff, and P. C. K. Vesborg, "Experimental and First-Principles Spectroscopy of $\text{Cu}_2\text{SrSnS}_4$ and $\text{Cu}_2\text{BaSnS}_4$ Photoabsorbers," *ACS Appl. Mater. Interfaces*, vol. 12, no. 45, pp. 50446–50454, 2020.
- [148] D. K. Chaudhary, A. Ghosh, R. Thangavel, and L. Kumar, "Bulk-heterojunction hybrid solar cells with non-toxic, earth abundant stannite phase $\text{CuZn}_2\text{AlS}_4$ nanocrystals," *Thin Solid Films*, vol. 649, no. April 2017, pp. 202–209, 2018.
- [149] J. Ge and Y. Yan, "Synthesis and characterization of photoelectrochemical and photovoltaic $\text{Cu}_2\text{BaSnS}_4$ thin films and solar cells," *J. Mater. Chem. C*, vol. 5, no. 26, pp. 6406–6419, 2017.
- [150] M. Morihama, F. Gao, T. Maeda, and T. Wada, "Crystallographic and optical properties of $\text{Cu}_2\text{Zn}(\text{Sn}-x\text{Gex})\text{Se}_4$ solid solution," *Jpn. J. Appl. Phys.*, vol. 53, p. 04ER09, jan 2014.
- [151] S. Bag, O. Gunawan, T. Gokmen, Y. Zhu, and D. B. Mitzi, "Hydrazine-processed Ge-substituted CZTSe solar cells," *Chem. Mater.*, vol. 24, no. 23, pp. 4588–4593, 2012.
- [152] D. Shin, T. Zhu, X. Huang, O. Gunawan, V. Blum, and D. B. Mitzi, "Earth-Abundant Chalcogenide Photovoltaic Devices with over 5% Efficiency Based on a $\text{Cu}_2\text{BaSn}(\text{S},\text{Se})_4$ Absorber," *Adv. Mater.*, vol. 29, no. 24, pp. 1–7, 2017.
- [153] B. Teymur, S. Levenco, H. Hempel, E. Bergmann, J. A. Márquez, L. Choubrac, I. G. Hill, T. Unold, and D. B. Mitzi, "Optoelectronic and material properties of solution-processed Earth-abundant $\text{Cu}_2\text{BaSn}(\text{S}, \text{Se})_4$ films for solar cell applications," *Nano Energy*, vol. 80, no. August 2020, 2021.
- [154] Y. Qi, Q. Tian, Y. Meng, D. Kou, Z. Zhou, W. Zhou, and S. Wu, "Elemental Precursor Solution Processed $(\text{Cu}_{1-x}\text{Ag}_x)_2\text{ZnSn}(\text{S},\text{Se})_4$ Photovoltaic Devices with over 10% Efficiency," *ACS Appl. Mater. Interfaces*, vol. 9, no. 25, pp. 21243–21250, 2017.
- [155] W.-J. Yin, T. Shi, and Y. Yan, "Unique properties of halide perovskites as possible origins of the superior solar cell performance," *Adv. Mater.*, vol. 26, no. 27, pp. 4653–4658, 2014.
- [156] W.-J. Yin, T. Shi, and Y. Yan, "Unusual defect physics in $\text{CH}_3\text{NH}_3\text{PbI}_3$ perovskite solar cell absorber," *Appl. Phys. Lett.*, vol. 104, no. 6, 2014.
- [157] W. Meng, B. Saparov, F. Hong, J. Wang, D. B. Mitzi, and Y. Yan, "Alloying and Defect Control within Chalcogenide Perovskites for Optimized Photovoltaic Application," *Chem. Mater.*, vol. 28, no. 3, pp. 821–829, 2016.
- [158] S. Perera, H. Hui, C. Zhao, H. Xue, F. Sun, C. Deng, N. Gross, C. Milleville, X. Xu, D. F. Watson, B. Weinstein, Y.-Y. Sun, S. Zhang, and H. Zeng, "Chalcogenide perovskites - an emerging class of ionic semiconductors," *Nano Energy*, vol. 22, pp. 129–135, 2016.
- [159] S. Niu, H. Huyan, Y. Liu, M. Yeung, K. Ye, L. Blankemeier, T. Orvis, D. Sarkar, D. J. Singh, R. Kapadia, and J. Ravichandran, "Bandgap Control via Structural and Chemical Tuning of Transition Metal Perovskite Chalcogenides," *Adv. Mater.*, vol. 29, no. 9, pp. 16–21, 2017.

Bibliography

- [160] Y. Nishigaki, T. Nagai, M. Nishiwaki, T. Aizawa, M. Kozawa, K. Hanzawa, Y. Kato, H. Sai, H. Hiramatsu, H. Hosono, and H. Fujiwara, "Extraordinary Strong Band-Edge Absorption in Distorted Chalcogenide Perovskites," *Sol. RRL*, vol. 4, no. 5, pp. 1–8, 2020.
- [161] X. Wei, H. Hui, S. Perera, A. Sheng, D. F. Watson, Y.-Y. Sun, Q. Jia, S. Zhang, and H. Zeng, "Ti-Alloying of BaZrS₃ Chalcogenide Perovskite for Photovoltaics," *ACS Omega*, vol. 5, no. 30, pp. 18579–18583, 2020.
- [162] S. F. Hoefler, G. Trimmel, and T. Rath, "Progress on lead-free metal halide perovskites for photovoltaic applications: a review," *Monatshefte fur Chemie*, vol. 148, no. 5, pp. 795–826, 2017.
- [163] N. C. Miller and M. Bernechea, "Research Update: Bismuth based materials for photovoltaics," *APL Mater.*, vol. 6, no. 8, 2018.
- [164] M. Pazoki and T. Edvinsson, "Metal replacement in perovskite solar cell materials: Chemical bonding effects and optoelectronic properties," *Sustain. Energy Fuels*, vol. 2, no. 7, pp. 1430–1445, 2018.
- [165] Q. Xu, D. Yang, J. Lv, Y.-Y. Sun, and L. Zhang, "Perovskite Solar Absorbers: Materials by Design," *Small Methods*, vol. 2, no. 5, pp. 1–19, 2018.
- [166] L. Theofylaktos, K. O. Kosmatos, E. Giannakaki, H. Kourti, D. Deligiannis, M. Konstantakou, and T. Stergiopoulos, "Perovskites with d-block metals for solar energy applications," *Dalt. Trans.*, vol. 48, no. 26, pp. 9516–9537, 2019.
- [167] V. M. Fridkin, "Bulk Photovoltaic Effect in Noncentrosymmetric Crystals," *Crystallogr. Reports*, vol. 46, no. 4, pp. 722–726, 2001.
- [168] W. Ji, K. Yao, and Y. C. Liang, "Bulk photovoltaic effect at visible wavelength in epitaxial ferroelectric BiFeO₃ thin films," *Adv. Mater.*, vol. 22, no. 15, pp. 1763–1766, 2010.
- [169] M. Alexe and D. Hesse, "Tip-enhanced photovoltaic effects in bismuth ferrite," *Nat. Commun.*, vol. 2, no. 1, 2011.
- [170] Y. Guo, B. Guo, W. Dong, H. Li, and H. Liu, "Evidence for oxygen vacancy or ferroelectric polarization induced switchable diode and photovoltaic effects in BiFeO₃ based thin films," *Nanotechnology*, vol. 24, no. 27, 2013.
- [171] S. Gupta, M. Tomar, and V. Gupta, "Ferroelectric photovoltaic response to structural transformations in doped BiFeO₃ derivative thin films," *Mater. Des.*, vol. 105, pp. 296–300, 2016.
- [172] Z. Fan, W. Ji, T. Li, J. Xiao, P. Yang, K. P. Ong, K. Zeng, K. Yao, and J. Wang, "Enhanced photovoltaic effects and switchable conduction behavior in BiFe_{0.6}Sc_{0.4}O₃ thin films," *Acta Mater.*, vol. 88, pp. 83–90, 2015.
- [173] C. Wang, X. Liu, S. Sheng, Y. Zhou, H. Liu, and Y. Sun, "Photovoltaic mechanism in Na-substituted BiFeO₃ films," *J. Phys. D. Appl. Phys.*, vol. 47, no. 35, 2014.
- [174] W. Cai, C. Fu, R. Gao, W. Jiang, X. Deng, and G. Chen, "Photovoltaic enhancement based on improvement of ferroelectric property and band gap in Ti-doped bismuth ferrite thin films," *J. Alloys Compd.*, vol. 617, pp. 240–246, 2014.
- [175] S. Gupta, R. Medwal, T. B. Limbu, R. K. Katiyar, S. P. Pavunny, M. Tomar, G. Morell, V. Gupta, and R. S. Katiyar, "Graphene/semiconductor silicon modified BiFeO₃/indium

- tin oxide ferroelectric photovoltaic device for transparent self-powered windows,” *Appl. Phys. Lett.*, vol. 107, no. 6, 2015.
- [176] T. Shi, J. Wang, W. Yan, X. Shao, and Z.-L. Hou, “Enhanced photovoltaic property based on reduced leakage current and band gap in Nd-doped BiFeO₃ films,” *Mater. Res. Express*, vol. 6, no. 8, 2019.
- [177] Y. Ukai, S. Yamazaki, T. Kawae, and A. Morimoto, “Polarization-induced photovoltaic effects in Nd-doped BiFeO₃ ferroelectric thin films,” *Jpn. J. Appl. Phys.*, vol. 51, no. 9 PART 2, 2012.
- [178] R. Agarwal, Y. Sharma, S. Hong, and R. S. Katiyar, “Modulation of oxygen vacancies assisted ferroelectric and photovoltaic properties of (Nd, V) co-doped BiFeO₃ thin films,” *J. Phys. D: Appl. Phys.*, vol. 51, no. 27, 2018.
- [179] V. S. Puli, D. K. Pradhan, R. K. Katiyar, I. Coondoo, N. Panwar, P. Misra, D. B. Chrisey, J. E. Scott, and R. S. Katiyar, “Photovoltaic effect in transition metal modified polycrystalline BiFeO₃ thin films,” *J. Phys. D: Appl. Phys.*, vol. 47, no. 7, 2014.
- [180] Z.-W. Peng, Y.-L. Wang, and B.-T. Liu, “Enhanced open circuit voltage in photovoltaic effect of polycrystalline La and Ni co-doped BiFeO₃ film,” *Funct. Mater. Lett.*, vol. 8, no. 1, p. 1550002, 2015.
- [181] S. Li, L. Xu, X. Kong, T. Kusunose, N. Tsurumachi, and Q. Feng, “Bismuth chalcogenide iodides Bi₁₃S₁₈I₂ and BiSI: Solvothermal synthesis, photoelectric behavior, and photovoltaic performance,” *J. Mater. Chem. C*, vol. 8, no. 11, pp. 3821–3829, 2020.
- [182] J. Xiong, Z. You, S. Lei, K. Zhao, Q. Bian, Y. Xiao, and B. Cheng, “Solution Growth of BiSI Nanorod Arrays on a Tungsten Substrate for Solar Cell Application,” *ACS Sustain. Chem. Eng.*, vol. 8, no. 35, pp. 13488–13496, 2020.
- [183] M. Wu, X. Lou, T. Li, J. Li, S. Wang, W. Li, B. Peng, and G. Gou, “Ni-doped SrBi₂Nb₂O₉ – Perovskite oxides with reduced band gap and stable ferroelectricity for photovoltaic applications,” *J. Alloys Compd.*, vol. 724, pp. 1093–1100, 2017.
- [184] L. Peedikakkandy, S. Chatterjee, and A. J. Pal, “Bandgap Engineering and Efficient Conversion of a Ternary Perovskite (Cs₃Bi₂I₉) to a Double Perovskite (Cs₂NaBiI₆) with the Aid of Alkali Metal Sulfide,” *J. Phys. Chem. C*, vol. 124, no. 20, pp. 10878–10886, 2020.
- [185] M. B. Johansson, B. Philippe, A. Banerjee, D. Phuyal, S. Mukherjee, S. Chakraborty, M. Cameau, H. Zhu, R. Ahuja, G. Boschloo, H. Rensmo, and E. M. J. Johansson, “Cesium Bismuth Iodide Solar Cells from Systematic Molar Ratio Variation of CsI and BiI₃,” *Inorg. Chem.*, vol. 58, no. 18, pp. 12040–12052, 2019.
- [186] H. Zhang, Y. Xu, Q. Sun, J. Dong, Y. Lu, B. Zhang, and W. Jie, “Lead free halide perovskite Cs₃Bi₂I₉ bulk crystals grown by a low temperature solution method,” *CrystEngComm*, vol. 20, no. 34, pp. 4935–4941, 2018.
- [187] R. Waykar, A. Bhorde, S. Nair, S. Pandharkar, B. Gabhale, R. Aher, S. Rondiya, A. Waghmare, V. Doiphode, A. Punde, P. Vairale, M. Prasad, and S. Jadkar, “Environmentally stable lead-free cesium bismuth iodide (Cs₃Bi₂I₉) perovskite: Synthesis to solar cell application,” *J. Phys. Chem. Solids*, vol. 146, no. October 2019, p. 109608, 2020.
- [188] F. Bai, Y. Hu, Y. Hu, T. Qiu, X. Miao, and S. Zhang, “Lead-free, air-stable ultrathin Cs₃Bi₂I₉

- perovskite nanosheets for solar cells,” *Sol. Energy Mater. Sol. Cells*, vol. 184, no. April, pp. 15–21, 2018.
- [189] P. Sebastia-Luna, M. C. Gélvez-Rueda, C. Dreessen, M. Sessolo, F. C. Grozema, F. Palazon, and H. J. Bolink, “Potential and limitations of CsBiI₃ as a photovoltaic material,” *J. Mater. Chem. A*, vol. 8, no. 31, pp. 15670–15674, 2020.
- [190] H. Zhu, M. B. Johansson, and E. M. J. Johansson, “The Effect of Dopant-Free Hole-Transport Polymers on Charge Generation and Recombination in Cesium–Bismuth–Iodide Solar Cells,” *ChemSusChem*, vol. 11, no. 6, pp. 1114–1120, 2018.
- [191] P. Mariyappan, T. H. Chowdhury, S. Subashchandran, I. Bedja, H. M. Ghaithan, and A. Islam, “Fabrication of lead-free CsBiI₃ based compact perovskite thin films by employing solvent engineering and anti-solvent treatment techniques: an efficient photo-conversion efficiency up to 740 nm,” *Sustain. Energy Fuels*, vol. 4, no. 10, pp. 5042–5049, 2020.
- [192] Q. Wei, J. Chen, P. Ding, B. Shen, J. Yin, F. Xu, Y. Xia, and Z. Liu, “Synthesis of Easily Transferred 2D Layered BiI₃ Nanoplates for Flexible Visible-Light Photodetectors,” *ACS Appl. Mater. Interfaces*, vol. 10, no. 25, pp. 21527–21533, 2018.
- [193] A. J. Lehner, H. Wang, D. H. Fabini, C. D. Liman, C. A. Hébert, E. E. Perry, M. Wang, G. C. Bazan, M. L. Chabinyc, and R. Seshadri, “Electronic structure and photovoltaic application of BiI₃,” *Appl. Phys. Lett.*, vol. 107, no. 13, pp. 1–5, 2015.
- [194] B. Yoo, D. Ding, J. M. Marin-Beloqui, L. Lanzetta, X. Bu, T. Rath, and S. A. Haque, “Improved Charge Separation and Photovoltaic Performance of BiI₃ Absorber Layers by Use of an in Situ Formed BiSI Interlayer,” *ACS Appl. Energy Mater.*, vol. 2, no. 10, pp. 7056–7061, 2019.
- [195] M. Masroor, T. Yan, J. McRae, E. P. Mostland, R. Rivas, E. R. Ruano, A. McClelland, and P. M. Rao, “Controlling crystal growth of non-toxic Bismuth iodide (BiI₃) semiconducting material for efficient photovoltaics,” in *Proc. SPIE* (A. Freundlich, M. Sugiyama, and S. Collin, eds.), no. March 2020, p. 16, SPIE, mar 2020.
- [196] Y. Hu, F. Bai, X. Liu, Q. Ji, X. Miao, T. Qiu, and S. Zhang, “Bismuth Incorporation Stabilized α -CsPbI₃ for Fully Inorganic Perovskite Solar Cells,” *ACS Energy Lett.*, vol. 2, no. 10, pp. 2219–2227, 2017.
- [197] M. Roy, S. Ghorui, Bhawna, J. Kangsabanik, R. Yadav, A. Alam, and M. Aslam, “Enhanced Visible Light Absorption in Layered Cs₃Bi₂Br₉ Halide Perovskites: Heterovalent Pb²⁺ Substitution-Induced Defect Band Formation,” *J. Phys. Chem. C*, vol. 124, no. 36, pp. 19484–19491, 2020.
- [198] C. F. J. Lau, Z. Wang, N. Sakai, J. Zheng, C. H. Liao, M. Green, S. Huang, H. J. Snaith, and A. Ho-Baillie, “Fabrication of Efficient and Stable CsPbI₃ Perovskite Solar Cells through Cation Exchange Process,” *Adv. Energy Mater.*, vol. 9, no. 36, pp. 1–7, 2019.
- [199] B. Zhang, Y. Lei, R. Qi, H. Yu, X. Yang, T. Cai, and Z. Zheng, “An in-situ room temperature route to CuBiI₄ based bulk-heterojunction perovskite-like solar cells,” *Sci. China Mater.*, vol. 62, no. 4, pp. 519–526, 2019.
- [200] Z. Hu, Z. Wang, G. Kapil, T. Ma, S. Iikubo, T. Minemoto, K. Yoshino, T. Toyoda, Q. Shen,

- and S. Hayase, "Solution-Processed Air-Stable Copper Bismuth Iodide for Photovoltaics," *ChemSusChem*, vol. 11, no. 17, pp. 2930–2935, 2018.
- [201] H. Wu, X. Huang, J. Lv, L. Sheng, B. Gao, C. Jiang, T. Wang, and J. He, "Effect of Halogen-Doping on Properties of Bismuth Iodide (BiI₃) Optical Absorption Layer," *Phys. Status Solidi Appl. Mater. Sci.*, vol. 218, no. 11, pp. 3–9, 2021.
- [202] B. Saparov, F. Hong, J.-P. Sun, H.-S. Duan, W. Meng, S. Cameron, I. G. Hill, Y. Yan, and D. B. Mitzi, "Thin-Film Preparation and Characterization of Cs₃Sb₂I₉: A Lead-Free Layered Perovskite Semiconductor," *Chem. Mater.*, vol. 27, no. 16, pp. 5622–5632, 2015.
- [203] S. Lo Piano, A. Saltelli, and J. P. van der Sluijs, "Silver as a constraint for a large-scale development of solar photovoltaics? Scenario-making to the year 2050 supported by expert engagement and global sensitivity analysis," *Front. Energy Res.*, vol. 7, no. JUN, pp. 1–13, 2019.
- [204] M. Bernechea, N. Cates Miller, G. Xercavins, D. So, A. Stavrinadis, and G. Konstantatos, "Solution-processed solar cells based on environmentally friendly AgBiS₂ nanocrystals," *Nat. Photonics*, vol. 10, no. 8, pp. 521–525, 2016.
- [205] Y. Kim, Z. Yang, A. Jain, O. Voznyy, G.-H. Kim, M. Liu, L. N. Quan, F. P. García de Arquer, R. Comin, J. Z. Fan, and E. H. Sargent, "Pure Cubic-Phase Hybrid Iodobismuthates AgBi₂I₇ for Thin-Film Photovoltaics," *Angew. Chemie - Int. Ed.*, vol. 55, no. 33, pp. 9586–9590, 2016.
- [206] H. Zhu, A. Erbing, H. Wu, G. J. Man, S. Mukherjee, C. Kamal, M. B. Johansson, H. Rensmo, M. Odelius, and E. M. J. Johansson, "Tuning the Bandgap in Silver Bismuth Iodide Materials by Partly Substituting Bismuth with Antimony for Improved Solar Cell Performance," *ACS Appl. Energy Mater.*, vol. 3, no. 8, pp. 7372–7382, 2020.
- [207] H. Wu, H. Zhu, A. Erbing, M. B. Johansson, S. Mukherjee, G. J. Man, H. Rensmo, M. Odelius, and E. M. J. Johansson, "Bandgap Tuning of Silver Bismuth Iodide via Controllable Bromide Substitution for Improved Photovoltaic Performance," *ACS Appl. Energy Mater.*, vol. 2, no. 8, pp. 5356–5362, 2019.
- [208] R. L. Z. Hoye, L. Eyre, F. Wei, F. Brivio, A. Sadhanala, S. Sun, W. Li, K. H. L. Zhang, J. L. MacManus-Driscoll, P. D. Bristowe, R. H. Friend, A. K. Cheetham, and F. Deschler, "Fundamental Carrier Lifetime Exceeding 1 μ s in Cs₂AgBiBr₆ Double Perovskite," *Adv. Mater. Interfaces*, vol. 5, no. 15, pp. 2–9, 2018.
- [209] E. M. Hutter, M. C. Gélvez-Rueda, D. Bartesaghi, F. C. Grozema, and T. J. Savenije, "Band-Like Charge Transport in Cs₂AgBiBr₆ and Mixed Antimony-Bismuth Cs₂AgBi_{1-x}Sb_xBr₆ Halide Double Perovskites," *ACS Omega*, vol. 3, no. 9, pp. 11655–11662, 2018.
- [210] Q. Zhang, C. Wu, X. Qi, F. Lv, Z. Zhang, Y. Liu, S. Wang, B. Qu, Z. Chen, and L. Xiao, "Photovoltage Approaching 0.9 V for Planar Heterojunction Silver Bismuth Iodide Solar Cells with Li-TFSI Additive," *ACS Appl. Energy Mater.*, vol. 2, no. 5, pp. 3651–3656, 2019.
- [211] Z. Yi, T. Zhang, H. Ban, H. Shao, X. Gong, M. Wu, G. Liang, X. L. Zhang, Y. Shen, and M. Wang, "AgBi₃I₁₀ ruddersite for photovoltaic application," *Sol. Energy*, vol. 206, no. February, pp. 436–442, 2020.
- [212] N. Pai, J. Lu, T. R. Gengenbach, A. Seeber, A. S. R. Chesman, L. Jiang, D. C. Senevirathna, P. C. Andrews, U. Bach, Y.-B. Cheng, and A. N. Simonov, "Silver Bismuth Sulfoiodide

- Solar Cells: Tuning Optoelectronic Properties by Sulfide Modification for Enhanced Photovoltaic Performance,” *Adv. Energy Mater.*, vol. 9, no. 5, pp. 1–11, 2019.
- [213] S. Hosseini and M. Adelifard, “The Impact of Cesium and Antimony Alloying on the Photovoltaic Properties of Silver Bismuth Iodide Compounds,” *Phys. Status Solidi Appl. Mater. Sci.*, vol. 218, no. 7, pp. 1–7, 2021.
- [214] A. Ennaoui, S. Fiechter, C. Pettenkofer, N. Alonso-Vante, K. B  ker, M. Bronold, C. H  pfner, and H. Tributsch, “Iron disulfide for solar energy conversion,” *Sol. Energy Mater. Sol. Cells*, vol. 29, no. 4, pp. 289–370, 1993.
- [215] P. Sinsermsuksakul, L. Sun, S. W. Lee, H. H. Park, S. B. Kim, C. Yang, and R. G. Gordon, “Overcoming Efficiency Limitations of SnS-Based Solar Cells,” *Adv. Energy Mater.*, vol. 4, no. 15, pp. 1–7, 2014.
- [216] J. A. Andrade-Arvizu, M. Courel-Piedrahita, and O. Vigil-Gal  n, “SnS-based thin film solar cells: perspectives over the last 25 years,” *J. Mater. Sci. Mater. Electron.*, vol. 26, no. 7, pp. 4541–4556, 2015.
- [217] N. Koteeswara Reddy, M. Devika, and E. S. R. Gopal, “Review on Tin (II) Sulfide (SnS) Material: Synthesis, Properties, and Applications,” *Crit. Rev. Solid State Mater. Sci.*, vol. 40, no. 6, pp. 359–398, 2015.
- [218] O. Reckeweg, C. Lind, A. Simon, and F. J. DiSalvo, “Rietveld Refinement of the Crystal Structure of α -Be₃N₂ and the Experimental Determination of Optical Band Gaps for Mg₃N₂, Ca₃N₂ and CaMg₂N₂,” *Zeitschrift fur Naturforsch. - Sect. B J. Chem. Sci.*, vol. 58, pp. 159–162, 2003.
- [219] A. W. Harzing, “Publish or perish,” 2007. Available from <https://harzing.com/resources/publish-or-perish>. Search carried out on the 18th of August, 2021, with software version 7.33.3388.7819.
- [220] M. V. Stackelberg and R. Paulus, “Untersuchungen   ber die Kristallstruktur der Nitride und Phosphide zweiwertiger Metalle,” *Zeitschrift f  r Phys. Chemie*, vol. 22B, no. 1, pp. 305–322, 1933.
- [221] M. Zamani, *Crystalline Order in Compound Semiconductors in Nanoscale Structures and Thin Films*. PhD thesis,   cole Polytechnique F  d  rale de Lausanne, EPFL, 2021. DOI: 10.5075/epfl-thesis-8456.
- [222] S. Escobar Steinvall, *Growth and characterisation of earth-abundant semiconductor nanostructures for solar energy harvesting*. PhD thesis,   cole Polytechnique F  d  rale de Lausanne, EPFL, 2020. DOI: 10.5075/epfl-thesis-8213.
- [223] R. Katsube, *Investigation on properties of zinc phosphide related materials and interfaces for optoelectronic devices*. PhD thesis, Kyoto University, 2018. DOI: 10.14989/doctor.k21104.
- [224] T. Burgess, *From Dopant to Source: The Use of Zinc as an Enabler in the Synthesis of Nanostructures by Metalorganic Vapour Phase Epitaxy*. PhD thesis, Australian National University, 2017. DOI: 10.25911/5d67b4bc30821.
- [225] J. P. Bosco, *Rational Design of Zinc Phosphide Heterojunction Photovoltaics*. PhD thesis, California Institute of Technology, 2014. DOI: 10.7907/09NG-5E90.

- [226] G. M. Kimball, *Zn₃P₂ and Cu₂O Substrates for Solar Energy Conversion*. PhD thesis, California Institute of Technology, 2012. DOI: 10.7907/Q4F1-H538.
- [227] L. Gerward, J. S. Olsen, and A. Waśkowska, “Thermoelastic properties of Zn₃P₂,” *High Press. Res.*, vol. 31, no. 1, pp. 39–42, 2011.
- [228] Y. Tang, H. Liang, S. Guan, M. Huang, W. Wang, Q. Wang, D. He, and F. Peng, “Elucidating the Phase Transformation and Metallization Behavior of Zinc Phosphide under High Pressure,” *Inorg. Chem.*, 2021.
- [229] Y. Tanaka, “Chemical reaction at high temperature and high pressure VI: polymorphic transition in ZnP₂ at high temperature and high pressure,” *Rev. Phys. Chem. Japan*, vol. 38, no. 2, pp. 151–169, 1968.
- [230] V. M. Trukhan, S. F. Marenkin, and T. V. Shoukavaya, “Compounds and solid solutions in the Zn-P, Zn-As, and Cd-As systems formed under high pressures and temperatures,” *Crystallogr. Reports*, vol. 59, no. 1, pp. 53–59, 2014.
- [231] A. Mokhtari, “High pressure study of the zinc phosphide semiconductor compound in two different phases,” *J. Phys. Condens. Matter*, vol. 21, no. 27, 2009.
- [232] X.-J. Zhang and B.-G. Liu, “Two-dimensional wide-band-gap II-V semiconductors with a dilated graphene-like structure,” *Semicond. Sci. Technol.*, vol. 31, no. 12, p. 125002, 2016.
- [233] M. V. Stackelberg and R. Paulus, “Untersuchungen an den Phosphiden und Arseniden des Zinks und Cadmiums. Das Zn₃P₂-Gitter,” *Zeitschrift für Phys. Chemie*, vol. B28, pp. 427–460, jan 1935.
- [234] J. Dutkiewicz, “The P-Zn (Phosphorus-Zinc) System,” *J. Phase Equilibria*, vol. 12, no. 4, pp. 435–438, 1991.
- [235] C. W. F. T. Pistorius, J. B. Clark, J. Coetzer, G. J. Kruger, and O. A. Kunze, “High-pressure phase relations and crystal structure determination for zinc phosphide Zn₃P₂ and cadmium phosphide Cd₃P₂,” *High Temp. - High Press.*, vol. 9, pp. 471–482, 1977.
- [236] I. J. Hegyi, E. E. Loebner, E. W. Poor Jr., and J. G. White, “Two crystal forms of ZnP₂, their preparation, structure, and optoelectronic properties,” *J. Phys. Chem. Solids*, vol. 24, pp. 333–337, 1963.
- [237] W. Zdanowicz, F. Królicki, and P. Plenkiewicz, “Preparation and semiconducting properties of pseudobinary solid solutions Zn₃As₂-Zn₃P₂,” *Acta Phys. Pol. A*, vol. 44, no. 3, pp. 447–454, 1973.
- [238] T. Z. Vitkina, L. K. Orlik, E. M. Smolyarenko, and V. M. Trukhan, “Interatomic interaction in Zn₃P_xAs_{1-x} solid solutions,” *Cryst. Res. Technol.*, vol. 21, no. 11, pp. 1409–1412, 1986.
- [239] L. E. Soshnikov, V. M. Trukhan, and S. F. Marenkin, “Temperature-dependent elastic constants and dielectric properties of (Zn_{1-x}Cd_x)₃(P_{1-y}As_y)₂ crystals,” *Inorg. Mater.*, vol. 39, no. 4, pp. 317–322, 2003.
- [240] A. Pietraszko and K. Lukaszewicz, “Thermal Expansion and Phase Transitions of Cd₃As₂ and Zn₃As₂,” *Phys. Status Solidi*, vol. 18, pp. 723–730, 1973.
- [241] G. Pangilinan, R. Sooryakumar, B. Chelluri, and T. Y. Chang, “Raman spectroscopy of the II-V vacancy ordered semiconductor Zn₃As₂,” *SPIE Proc.*, vol. 1336, pp. 31–42, 1990.

Bibliography

- [242] A. D. Izotov, V. P. Sanygin, and V. F. Ponomarev, "Genetic relationship of crystal-structures of polymorphic modification of AlI3BV2 type compounds," *Kristallografiya*, vol. 23, no. 4, pp. 764–767, 1978.
- [243] V. J. Shevchenko, "Physical and Chemical Properties and Application of Semiconductor Compounds of the AlIBV System," in *Proc. first Int. Symp. Phys. Chem. II-V Compd.*, pp. 15–32, 1980.
- [244] H. Okamoto, "The As-Cd (arsenic-cadmium) system," *J. Phase Equilibria*, vol. 13, no. 2, pp. 147–154, 1992.
- [245] G. Pangilinan, R. Sooryakumar, B. Chelluri, and T. Y. Chang, "New Long-Range Atomic Order and Heteroepitaxy of Single-Crystal Zn3As2," *Phys. Rev. Lett.*, vol. 62, no. 5, pp. 551–554, 1989.
- [246] G. Pangilinan, R. Sooryakumar, and J. Misiewicz, "Raman activity of Zn3P2," *Phys. Rev. B*, vol. 44, no. 6, pp. 2582–2588, 1991.
- [247] J. Misiewicz, "Inter-band transitions in Zn3P2," *J. Phys. Condens. Matter*, vol. 2, pp. 2053–2072, 1990.
- [248] I. E. Zanin, K. B. Aleinikova, M. Y. Antipin, and M. M. Afanasiev, "Analysis of chemical bonding in Zn3P2 crystals from X-ray diffraction data," *Crystallogr. Reports*, vol. 49, no. 4, pp. 579–584, 2004.
- [249] I. E. Zanin, K. B. Aleinikova, M. M. Afanasiev, and M. Y. Antipin, "Structure of Zn3P2," *J. Struct. Chem.*, vol. 45, no. 5, pp. 844–848, 2004.
- [250] S. Escobar Steinvall, L. Ghisalberti, R. R. Zamani, N. Tappy, F. S. Hage, E. Z. Stutz, M. Zamani, R. Paul, J.-B. Leran, Q. M. Ramasse, W. C. Carter, and A. Fontcuberta i Morral, "Heterotwin Zn3P2 superlattice nanowires: the role of indium insertion in the superlattice formation mechanism and their optical properties," *Nanoscale*, 2020.
- [251] L. Güniat, P. Caroff, and A. Fontcuberta i Morral, "Vapor Phase Growth of Semiconductor Nanowires: Key Developments and Open Questions," *Chem. Rev.*, vol. 119, pp. 8958–8971, aug 2019.
- [252] S. Jeon, J. P. Bosco, S. S. Wilson, S. J. Rozeveld, H. Kim, and H. A. Atwater, "Growth Mechanism and Electronic Structure of Zn3P2 on the Ga-Rich GaAs(001) Surface," *J. Phys. Chem. C*, vol. 118, no. 24, pp. 12717–12726, 2014.
- [253] S. Montanari, "Fabrication and characterization of planar gunn diodes for monolithic microwave integrated circuits," 2005.
- [254] H. Föll, "Wavelength engineering." https://www.tf.uni-kiel.de/matwis/amat/semi_en/kap_5/backbone/r5_1_4.html. Accessed: August 19th, 2021.
- [255] Y. Kato, S. Kurita, and T. Suda, "Photoenhanced chemical vapor deposition of zinc phosphide," *J. Appl. Phys.*, vol. 62, no. 9, pp. 3733–3739, 1987.
- [256] V. Kumar and B. S. Sastry, "Thermal expansion coefficient of binary semiconductors," *Cryst. Res. Technol.*, vol. 36, no. 6, pp. 565–569, 2001.
- [257] J. Long, "The Growth of Zn3P2 by Metalorganic Chemical Vapor Deposition," *J. Electrochem. Soc.*, vol. 130, pp. 725–728, 1983.
- [258] S. Hava, "Polycrystalline Zn3P2 Schottky photodiode: vacuum surface effects," *J. Appl. Phys.*, vol. 78, no. 4, pp. 2808–2810, 1995.

- [259] N. Convers Wyeth and A. Catalano, “Barrier heights of evaporated metal contacts on Zn₃P₂,” *J. Appl. Phys.*, vol. 51, no. 4, pp. 2286–2288, 1980.
- [260] M. Zamani, E. Z. Stutz, S. Escobar Steinvall, R. R. Zamani, R. Paul, J.-B. Leran, M. Dimitrievska, and A. Fontcuberta i Morral, “The path towards 1 μ m monocrystalline Zn₃P₂ films on InP: substrate preparation, growth conditions and luminescence properties,” *J. Phys. Energy*, vol. 3, no. 3, p. 034011, 2021.
- [261] R. Paul, N. Humblot, S. Escobar Steinvall, E. Z. Stutz, S. S. Joglekar, J.-B. Leran, M. Zamani, C. Cayron, R. Log  , A. Granados del Aguila, Q. Xiong, and A. Fontcuberta I Morral, “Van der Waals Epitaxy of Earth-Abundant Zn₃P₂ on Graphene for Photovoltaics,” *Cryst. Growth Des.*, vol. 20, no. 6, pp. 3816–3825, 2020.
- [262] S. Escobar Steinvall, N. Tappy, M. Ghasemi, R. R. Zamani, T. Lagrange, E. Z. Stutz, J.-B. Leran, M. Zamani, R. Paul, and A. Fontcuberta i Morral, “Multiple morphologies and functionality of nanowires made from earth-abundant zinc phosphide,” *Nanoscale Horizons*, vol. 5, pp. 274–282, 2020.
- [263] S. Escobar Steinvall, E. Z. Stutz, R. Paul, M. Zamani, N. Y. Dzade, V. Piazza, M. Friedl, V. de Mestral, J.-B. Leran, R. R. Zamani, and A. Fontcuberta i Morral, “Towards defect-free thin films of the earth-abundant absorber zinc phosphide by nanopatterning,” *Nanoscale Adv.*, vol. 3, no. 2, pp. 326–332, 2021.
- [264] C. V. Raman and K. S. Krishnan, “A new type of secondary radiation,” *Nature*, vol. 121, no. 3048, pp. 501–502, 1928.
- [265] G. Landsberg and L. Mandelstam, “  ber die Lichtzerstreuung in Kristallen,” *Zeitschrift f  r Phys.*, vol. 50, no. 11-12, pp. 769–780, 1928.
- [266] P. Moch, A. T. Abdalian, and B. Briat, “Raman scattering studies of optical magnons and of high-energy magnetic excitons,” in *Magnetic Excitations and Fluctuations II* (U. Balucani, S. W. Lovesey, M. G. Rasetti, and V. Tognetti, eds.), (Berlin, Heidelberg), pp. 191–195, Springer Berlin Heidelberg, 1987.
- [267] F. Amaduzzi, E. Alarc  n-Llad  , H. Hautmann, R. Tanta, F. Matteini, G. T  t  nc  o  lu, T. Vosch, J. Nyg  rd, T. S. Jespersen, E. Uccelli, and A. Fontcuberta I Morral, “Tuning the response of non-allowed Raman modes in GaAs nanowires,” *J. Phys. D: Appl. Phys.*, vol. 49, no. 9, pp. 1–7, 2016.
- [268] M. Brewster, O. Schimek, S. Reich, and S. Grade  ak, “Exciton-phonon coupling in individual GaAs nanowires studied using resonant Raman spectroscopy,” *Phys. Rev. B - Condens. Matter Mater. Phys.*, vol. 80, no. 20, pp. 5–8, 2009.
- [269] E. Burstein, S. Ushioda, and A. Pinczuk, “Raman scattering by polaritons,” *Solid State Commun.*, vol. 6, pp. 407–411, 1968.
- [270] G. Irmer, C. R  der, C. Himcinschi, and J. Kortus, “Phonon polaritons in uniaxial crystals: A Raman scattering study of polaritons in α -GaN,” *Phys. Rev. B - Condens. Matter Mater. Phys.*, vol. 88, no. 10, 2013.
- [271] D. A. Long, *Raman spectroscopy*. New York: McGraw-Hill, 1977.
- [272] R. W. Boyd, *Nonlinear Optics*, ch. The Nonlinear Optical Susceptibility. Elsevier, 3rd ed., 2008. DOI: 10.1016/B978-0-12-369470-6.00001-0.

Bibliography

- [273] M. Grundmann, *The Physics of Semiconductors: An Introduction Including Nanophysics and Applications*. Graduate Texts in Physics, Springer International Publishing, 3rd ed., 2015.
- [274] J. W. Strutt, “On the Light from the Sky, its Polarization and Colour,” *London, Edinburgh, Dublin Philos. Mag. J. Sci.*, vol. 41, no. 271, pp. 107–120, 1871.
- [275] A. T. Young, “Rayleigh scattering,” *Phys. Today*, vol. 35, no. 1, pp. 42–48, 1982.
- [276] G. F. Koster, *Space Groups and their Representations*. Academic Press, 1957.
- [277] WebQC.org, “D4h - point group symmetry character tables.” www.webqc.org/symmetrypointgroup-d4h.html. Accessed: May 24rd, 2021.
- [278] E. W. Weisstein, “Mulliken symbols.” From MathWorld—A Wolfram Web Resource. Accessed: June 7th, 2021.
- [279] L. Piela, “Appendix C - group theory in spectroscopy,” in *Ideas of Quantum Chemistry (Second Edition)* (L. Piela, ed.), pp. e17–e64, Oxford: Elsevier, second edition ed., 2014.
- [280] P. Yu and M. Cardona, *Fundamentals of Semiconductors: Physics and Materials Properties*, ch. 2.3: A Pedestrian’s Guide to Group Theory. Graduate Texts in Physics, Springer Berlin Heidelberg, 4th ed., 2010.
- [281] M. Dresselhaus, G. Dresselhaus, and A. Jorio, *Group Theory: Application to the Physics of Condensed Matter*. Springer, 2008.
- [282] C. Bradley and A. Cracknell, *The Mathematical Theory of Symmetry in Solids: Representation Theory for Point Groups and Space Groups*. Oxford University Press, 2010.
- [283] D. M. Bishop, *Group Theory and Chemistry*. New York: Dover Publications, 1973.
- [284] Shimadzu Corp., “Diffraction efficiency and relationship between diffraction efficiency and polarization.” <https://www.shimadzu.com/opt/guide/diffraction/08.html>. Accessed: May 20th, 2021.
- [285] D. M. Berg, M. Arasimowicz, R. Djemour, L. Gütay, S. Siebentritt, S. Schorr, X. Fontané, V. Izquierdo-Roca, A. Pérez-Rodríguez, and P. J. Dale, “Discrimination and detection limits of secondary phases in Cu₂ZnSnS₄ using X-ray diffraction and Raman spectroscopy,” *Thin Solid Films*, vol. 569, no. C, pp. 113–123, 2014.
- [286] E. Garcia-Llamas, M. Guc, I. V. Bodnar, X. Fontané, R. Caballero, J. M. Merino, M. León, and V. Izquierdo-Roca, “Multiwavelength excitation Raman scattering of Cu₂ZnSn_{1-x}Gex(S,Se)₄ single crystals for earth abundant photovoltaic applications,” *J. Alloys Compd.*, vol. 692, pp. 249–256, 2017.
- [287] M. Dimitrievska, F. Oliva, M. Guc, S. Giraldo, E. Saucedo, A. Pérez-Rodríguez, and V. Izquierdo-Roca, “Defect characterisation in Cu₂ZnSnSe₄ kesterites: Via resonance Raman spectroscopy and the impact on optoelectronic solar cell properties,” *J. Mater. Chem. A*, vol. 7, no. 21, pp. 13293–13304, 2019.
- [288] K.-J. Yang, J.-H. Sim, D.-H. Son, D.-H. Kim, G. Y. Kim, W. Jo, S. Song, J. Kim, D. Nam, H. Cheong, and J.-K. Kang, “Effects of the compositional ratio distribution with sulfurization temperatures in the absorber layer on the defect and surface electrical characteristics of Cu₂ZnSnS₄ solar cells,” *Prog. Photovoltaics Res. Appl.*, vol. 23, pp. 1771–1784, dec 2015.

- [289] K.-J. Yang, D.-H. Son, S.-J. Sung, J.-H. Sim, Y.-I. Kim, S.-N. Park, D.-H. Jeon, J. Kim, D.-K. Hwang, C.-W. Jeon, D. Nam, H. Cheong, J.-K. Kang, and D.-H. Kim, "A band-gap-graded CZTS_{Se} solar cell with 12.3% efficiency," *J. Mater. Chem. A*, vol. 4, no. 26, pp. 10151–10158, 2016.
- [290] J. Tao, J. Liu, L. Chen, H. Cao, X. Meng, Y. Zhang, C. Zhang, L. Sun, P. Yang, and J. Chu, "7.1% efficient co-electroplated Cu₂ZnSnS₄ thin film solar cells with sputtered CdS buffer layers," *Green Chem.*, vol. 18, no. 2, pp. 550–557, 2016.
- [291] J. Tao, L. Chen, H. Cao, C. Zhang, J. Liu, Y. Zhang, L. Huang, J. Jiang, P. Yang, and J. Chu, "Co-electrodeposited Cu₂ZnSnS₄ thin-film solar cells with over 7% efficiency fabricated via fine-tuning of the Zn content in absorber layers," *J. Mater. Chem. A*, vol. 4, no. 10, pp. 3798–3805, 2016.
- [292] R. Sun, M. Zhao, D. Zhuang, Q. Gong, L. Guo, L. Ouyang, and Y. Wei, "High-sulfur Cu₂ZnSn(S,Se)₄ films by sulfurizing as-deposited CZTSe film: The evolutions of phase, crystallinity and S/(S+Se) ratio," *J. Alloys Compd.*, vol. 695, pp. 3139–3145, 2017.
- [293] Z. Zhang, L. Yao, Y. Zhang, J. Ao, J. Bi, S. Gao, Q. Gao, M.-J. Jeng, G. Sun, Z. Zhou, Q. He, and Y. Sun, "Modified Back Contact Interface of CZTSe Thin Film Solar Cells: Elimination of Double Layer Distribution in Absorber Layer," *Adv. Sci.*, vol. 5, no. 2, pp. 1–9, 2018.
- [294] J. J. S. Scragg, L. Choubrac, A. Lafond, T. Ericson, and C. Platzer-Björkman, "A low-temperature order-disorder transition in Cu₂ZnSnS₄ thin films," *Appl. Phys. Lett.*, vol. 104, no. 4, pp. 2–6, 2014.
- [295] T. Schmidt, K. Lischka, and W. Zulehner, "Excitation-power dependence of the near-band-edge photoluminescence of semiconductors," *Phys. Rev. B*, vol. 45, no. 16, pp. 8989–8994, 1992.
- [296] A. Dorodnyy, E. Alarcón-Lladó, V. Shklover, C. Hafner, A. Fontcuberta i Morral, and J. Leuthold, "Efficient Multiterminal Spectrum Splitting via a Nanowire Array Solar Cell," *ACS Photonics*, vol. 2, no. 9, pp. 1284–1288, 2015.
- [297] R. H. Bube, *Photoelectronic Properties of Semiconductors*. Cambridge University Press, 1992.
- [298] S. S. Li, *Semiconductor Physical Electronics*. Springer-Verlag New York, 2nd ed., 2006.
- [299] H. Fujiwara and R. W. Collins, eds., *Spectroscopic Ellipsometry for Photovoltaics. Volume 1: Fundamental Principles and Solar Cell Characterization*. Springer, 2018.
- [300] J. Opsal, J. Fanton, J. Chen, J. Leng, L. Wei, C. Uhrich, M. Senko, C. Zaiser, and D. E. Aspnes, "Broadband spectral operation of a rotating-compensator ellipsometer," *Thin Solid Films*, vol. 313-314, pp. 58–61, 1998.
- [301] G. E. Jellison Jr., "Ellipsometry data analysis: a tutorial." <https://web.eecs.umich.edu/~fredty/wise2000/jellison.pdf>, 2000. Accessed: May 23rd, 2021.
- [302] M. A. McKay, J. Li, J. Y. Lin, and H. X. Jiang, "Anisotropic index of refraction and structural properties of hexagonal boron nitride epilayers probed by spectroscopic ellipsometry," *J. Appl. Phys.*, vol. 127, no. 5, 2020.
- [303] P. D. Paulson and X. Mathew, "Spectroscopic ellipsometry investigation of optical and interface properties of CdTe films deposited on metal foils," *Sol. Energy Mater. Sol. Cells*, vol. 82, no. 1-2, pp. 279–290, 2004.

Bibliography

- [304] P. D. Paulson, B. E. McCandless, and R. W. Birkmire, "Optical properties of $\text{Cd}_{1-x}\text{Zn}_x\text{Te}$ films in a device structure using variable angle spectroscopic ellipsometry," *J. Appl. Phys.*, vol. 95, no. 6, pp. 3010–3019, 2004.
- [305] S.-Y. Li, C. Hägglund, Y. Ren, J. J. S. Scragg, J. K. Larsen, C. Frisk, K. Rudisch, S. Englund, and C. Platzer-Björkman, "Optical properties of reactively sputtered $\text{Cu}_2\text{ZnSnS}_4$ solar absorbers determined by spectroscopic ellipsometry and spectrophotometry," *Sol. Energy Mater. Sol. Cells*, vol. 149, pp. 170–178, 2016.
- [306] T. Begou, J. D. Walker, D. Attygalle, V. Ranjan, R. W. Collins, and S. Marsillac, "Real time spectroscopic ellipsometry of CuInSe_2 : Growth dynamics, dielectric function, and its dependence on temperature," *Phys. Status Solidi - Rapid Res. Lett.*, vol. 5, no. 7, pp. 217–219, 2011.
- [307] P. Koirala, D. Attygalle, P. Aryal, P. Pradhan, J. Chen, S. Marsillac, A. S. Ferlauto, N. J. Podraza, and R. W. Collins, "Real time spectroscopic ellipsometry for analysis and control of thin film polycrystalline semiconductor deposition in photovoltaics," *Thin Solid Films*, vol. 571, no. P3, pp. 442–446, 2014.
- [308] S.-H. Han, F. S. Hasoon, H. A. Al-Thani, A. M. Hermann, and D. H. Levi, "Effect of Cu deficiency on the defect levels of $\text{Cu}_{0.86}\text{In}_{1.09}\text{Se}_{2.05}$ determined by spectroscopic ellipsometry," *Appl. Phys. Lett.*, vol. 86, no. 2, pp. 3–6, 2005.
- [309] P. Aryal, D. Attygalle, P. Pradhan, N. J. Podraza, S. Marsillac, and R. W. Collins, "Large-area compositional mapping of $\text{Cu}(\text{In}_{1-x}\text{Ga}_x)\text{Se}_2$ materials and devices with spectroscopic ellipsometry," *IEEE J. Photovoltaics*, vol. 3, no. 1, pp. 359–363, 2013.
- [310] E. Pascual, A. Lousa, and E. Bertrán, "Ellipsometric Characterization of Surface Oxidation in Polycrystalline Zn_3P_2 Thin-Films," *Thin Solid Films*, vol. 214, no. 1, pp. 74–77, 1992.
- [311] G. M. Kimball, N. S. Lewis, and H. A. Atwater, "Synthesis and surface chemistry of Zn_3P_2 ," *PVSC 33rd IEEE Photovolt. Spec. Conf.*, 2008.
- [312] E. Z. Stutz, M. Friedl, T. Burgess, H. H. Tan, P. Caroff, C. Jagadish, and A. Fontcuberta i Morral, "Nanosails Showcasing Zn_3As_2 as an Optoelectronic-Grade Earth Abundant Semiconductor," *Phys. status solidi - Rapid Res. Lett.*, vol. 13, p. 1900084, mar 2019.
- [313] J. Szatkowski and K. Sierański, "Electrical Conductivity of Zn_3As_2 ," *J. Phys. Chem. Solids*, vol. 51, no. 3, pp. 249–251, 1990.
- [314] G. Chen, Z. Liu, B. Liang, G. Yu, Z. Xie, H. Huang, B. Liu, X. Wang, D. Chen, M. Q. Zhu, and G. Shen, "Single-crystalline p-type Zn_3As_2 nanowires for field-effect transistors and visible-light photodetectors on rigid and flexible substrates," *Adv. Funct. Mater.*, vol. 23, no. 21, pp. 2681–2690, 2013.
- [315] G. A. Castellion and L. C. Beegle, "The Preparation and Properties of Cd_3As_2 - Zn_3As_2 Alloys," *J. Phys. Chem. Solids*, vol. 26, pp. 767–773, 1965.
- [316] H. Lu, X. Zhang, Y. Bian, and S. Jia, "Topological Phase Transition in Single Crystals of $(\text{Cd}_{1-x}\text{Zn}_x)_3\text{As}_2$," *Sci. Rep.*, vol. 7, no. 1, pp. 1–10, 2017.
- [317] B. Chelluri, T. Y. Chang, A. Ourmazd, A. H. Dayem, J. L. Zyskind, and A. Srivastava, "Molecular beam epitaxial growth of II–V semiconductor Zn_3As_2 and II–IV–V chalcopyrite ZnGeAs_2 ," *J. Cryst. Growth*, vol. 81, pp. 530–535, feb 1987.

- [318] B. Chelluri, T. Y. Chang, A. Ourmazd, A. H. Dayem, J. L. Zyskind, and A. Srivastava, "Molecular beam epitaxial growth of the II-V semiconductor compound Zn_3As_2 ," *Appl. Phys. Lett.*, vol. 49, no. 24, pp. 1665–1667, 1986.
- [319] S. Sudhakar, V. Ganesh, I. Sulania, P. K. Kulriya, and K. Baskar, "Liquid phase epitaxial growth of II-V semiconductor compound Zn_3As_2 ," *J. Phys. D: Appl. Phys.*, vol. 40, no. 17, pp. 5071–5074, 2007.
- [320] J. A. A. Engelbrecht, G. J. Scriven, J. H. Neethling, and M. C. Wagener, "Crack formation in Zn_3As_2 epilayers grown by MOVPE," *J. Cryst. Growth*, vol. 216, pp. 235–244, 2000.
- [321] F. Glas, "Critical dimensions for the plastic relaxation of strained axial heterostructures in free-standing nanowires," *Phys. Rev. B - Condens. Matter Mater. Phys.*, vol. 74, no. 12, pp. 2–5, 2006.
- [322] M. T. Björk, B. J. Ohlsson, T. Sass, A. I. Persson, C. Thelander, M. H. Magnusson, K. Depert, L. R. Wallenberg, and L. Samuelson, "One-dimensional Steeplechase for Electrons Realized," *Nano Lett.*, vol. 2, no. 2, pp. 87–89, 2002.
- [323] M. Glaser, A. Kitzler, A. Johannes, S. Prucnal, H. Potts, S. Conesa-Boj, L. Filipovic, H. Kosina, W. Skorupa, E. Bertagnolli, C. Ronning, A. Fontcuberta i Morral, and A. Lugstein, "Synthesis, Morphological, and Electro-optical Characterizations of Metal/Semiconductor Nanowire Heterostructures," *Nano Lett.*, vol. 16, no. 6, pp. 3507–3513, 2016.
- [324] L. C. Chuang, M. Moewe, K. W. Ng, T.-T. D. Tran, S. Crankshaw, R. Chen, W. S. Ko, and C. Chang-Hasnain, "GaAs nanoneedles grown on sapphire," *Appl. Phys. Lett.*, vol. 98, no. 12, pp. 2009–2012, 2011.
- [325] K.-W. Kwon and M. Shim, " γ - Fe_2O_3 /II-VI sulfide nanocrystal heterojunctions," *J. Am. Chem. Soc.*, vol. 127, no. 29, pp. 10269–10275, 2005.
- [326] N. Kouklin, S. Sen, and M. Gajdardziska-Josifovska, "Self-driven formation and structure of single crystal platelets of Zn_3As_2 ," *Appl. Phys. Lett.*, vol. 89, p. 071901, aug 2006.
- [327] J. Y. Li, L.-S. Wang, D. B. Buchholz, and R. P. H. Chang, "Simultaneous Growth of Pure Hyperbranched Zn_3As_2 Structures and Long Ga_2O_3 Nanowires," *Nano Lett.*, vol. 9, no. 5, pp. 1764–1769, 2009.
- [328] T. Burgess, P. Caroff, Y. Wang, B. H. Badada, H. E. Jackson, L. M. Smith, Y. Guo, H. H. Tan, and C. Jagadish, " Zn_3As_2 nanowires and nanoplatelets: Highly efficient infrared emission and photodetection by an earth abundant material," *Nano Lett.*, vol. 15, no. 1, pp. 378–385, 2015.
- [329] M. de la Mata, R. Leturcq, S. R. Plissard, C. Rolland, C. Magén, J. Arbiol, and P. Caroff, "Twin-Induced InSb Nanosails: A Convenient High Mobility Quantum System," *Nano Lett.*, vol. 16, no. 2, pp. 825–833, 2016.
- [330] S. Conesa-Boj, E. Russo-Averchi, A. Dalmau-Mallorquí, J. Trevino, E. F. Pecora, C. Forestiere, A. Handin, M. Ek, L. Zweifel, L. R. Wallenberg, D. Ruffer, M. Heiss, D. Troadec, L. Dal Negro, P. Caroff, and A. Fontcuberta i Morral, "Vertical "III-V" V-shaped nanomembranes epitaxially grown on a patterned Si[001] substrate and their enhanced light scattering," *ACS Nano*, vol. 6, no. 12, pp. 10982–10991, 2012.

Bibliography

- [331] C.-Y. Chi, C.-C. Chang, S. Hu, T.-W. Yeh, S. B. Cronin, and P. D. Dapkus, "Twin-free GaAs nanosheets by selective area growth: Implications for defect-free nanostructures," *Nano Lett.*, vol. 13, no. 6, pp. 2506–2515, 2013.
- [332] G. Tütüncüoglu, M. De La Mata, D. Deiana, H. A. Potts, F. Matteini, J. Arbiol, and A. Fontcuberta i Morral, "Towards defect-free 1-D GaAs/AlGaAs heterostructures based on GaAs nanomembranes," *Nanoscale*, vol. 7, no. 46, pp. 19453–19460, 2015.
- [333] P. Blanc, M. Heiss, C. Colombo, A. Dalmau-Mallorquí, T. Saberi Safaei, P. Krogstrup, J. Nygård, and A. Fontcuberta i Morral, "Electrical contacts to single nanowires: a scalable method allowing multiple devices on a chip. Application to a single nanowire radial p-i-n junction," *Int. J. Nanotechnol.*, vol. 10, no. 5/6/7, pp. 419–432, 2013.
- [334] L. J. van der Pauw, "A Method of Measuring Specific Resistivity and Hall Effect of Discs of Arbitrary Shape," *Philips Res. Reports*, vol. 13, no. 1, pp. 1–9, 1958.
- [335] W. Zdanowicz, K. Lukaszewicz, and W. Trzebiatowski, "Crystal Structure of the Semi-conducting System Cd₃As₂-Zn₃As₂," *Bull. l'Académie Pol. des Sci. Série des Sci. Chim.*, vol. 12, no. 3, pp. 169–176, 1964.
- [336] V. N. Yakimovich, V. A. Rubtsov, and V. M. Trukhan, "Phase equilibria in the Zn-P-As-Cd System," *Inorg. Mater.*, vol. 32, no. 7, pp. 705–709, 1996.
- [337] J. Hanuza, A. Lemiec, and J. Misiewicz, "Molecular model of lattice vibrations in Zn₃P₂," *Vib. Spectrosc.*, vol. 17, no. 1, pp. 93–103, 1998.
- [338] J. Misiewicz, "The Raman Scattering of Zn₃As₂," *Infrared Phys. Technol.*, vol. 35, no. 6, pp. 781–783, 1994.
- [339] M. Iwami, K. Fujishima, and K. Kawabe, "Magnetoresistance Effect in p-Zn₃As₂ Single Crystals," *J. Phys. Soc. Japan*, vol. 41, no. 2, pp. 521–525, 1976.
- [340] G. J. Scriven, A. W. R. Leitch, J. H. Neethling, V. V. Kozyrkov, and V. J. Watters, "The growth of Zn₃As₂ on InP by atmospheric pressure MOVPE," *J. Cryst. Growth*, vol. 170, no. 1-4, pp. 813–816, 1997.
- [341] S. F. Marenkin, N. S. Zhalilov, A. V. Mudryi, A. I. Patuk, and I. A. Shakin, "Optical Properties of Single Crystals and Films of Semiconducting Compound Zn₃As₂," *Inorg. Mater.*, vol. 28, no. 10-11, pp. 1659–1661, 1992.
- [342] J. Szatkowski and K. Sierański, "Electronic energy levels of an ideal vacancy in II₃-V₂ compounds," *Solid State Commun.*, vol. 93, no. 7, pp. 595–598, 1995.
- [343] W.-J. Yin and Y. Yan, "The electronic properties of point defects in earth-abundant photovoltaic material Zn₃P₂: A hybrid functional method study," *J. Appl. Phys.*, vol. 113, no. 1, p. 013708, 2013.
- [344] B. Kolodka, J. Misiewicz, and J. M. Pawlikowski, "Optical Transitions in Zn₃As₂ Thin Films and Single Crystals," *Acta Phys. Pol. A*, vol. 62, no. 1-2, pp. 63–81, 1982.
- [345] I. Aberg, G. Vescovi, D. Asoli, U. Naseem, J. P. Gilboy, C. Sundvall, A. Dahlgren, K. E. Svensson, N. Anttu, M. T. Björk, and L. Samuelson, "A GaAs nanowire array solar cell with 15.3% efficiency at 1 sun," *IEEE J. Photovoltaics*, vol. 6, no. 1, pp. 185–190, 2016.
- [346] S. Gazibegovic, G. Badawy, T. L. J. Buckers, P. Leubner, J. Shen, F. K. de Vries, S. Koelling, L. P. Kouwenhoven, M. A. Verheijen, and E. P. A. M. Bakkers, "Bottom-Up Grown 2D InSb Nanostructures," *Adv. Mater.*, p. 1808181, 2019.

- [347] E. Z. Stutz, S. Escobar Steinvall, A. P. Litvinchuk, J.-B. Leran, M. Zamani, R. Paul, A. Fontcuberta i Morral, and M. Dimitrievska, "Raman spectroscopy and lattice dynamics calculations of tetragonally-structured single crystal zinc phosphide (Zn₃P₂) nanowires," *Nanotechnology*, vol. 32, p. 085704, feb 2021.
- [348] J. Misiewicz, L. Bryja, K. Jezierski, J. Szatkowski, N. Mirowska, Z. Gumieny, and E. Placzek-Popko, "Zn₃P₂ - a new material for optoelectronic devices," *Microelectronics J.*, vol. 25, pp. 1–6, 1994.
- [349] M. Y. Swinkels, A. Campo, D. Vakulov, W. Kim, L. Gagliano, S. Escobar Steinvall, H. Detz, M. De Luca, A. Lugstein, E. Bakkers, A. Fontcuberta I Morral, and I. Zardo, "Measuring the Optical Absorption of Single Nanowires," *Phys. Rev. Appl.*, vol. 14, no. 2, p. 024045, 2020.
- [350] J. M. Pawlikowski, "Band Structure and Properties of Zn₃P₂-Promising New Infrared Material," *Infrared Phys.*, vol. 21, pp. 181–187, 1981.
- [351] F. Briones, F.-C. Wang, and R. H. Bube, "Pair transitions in Zn₃P₂," *Appl. Phys. Lett.*, vol. 39, no. 10, pp. 805–807, 1981.
- [352] N. Convers Wyeth and A. Catalano, "Spectral response measurements of minority-carrier diffusion length in Zn₃P₂," *J. Appl. Phys.*, vol. 50, no. 3, pp. 1403–1407, 1979.
- [353] T. L. Chu, S. S. Chu, K. Murthy, E. D. Stokes, and P. E. Russell, "Deposition and properties of zinc phosphide films," *J. Appl. Phys.*, vol. 54, no. 4, pp. 2063–2068, 1983.
- [354] A. Catalano and R. B. Hall, "Defect dominated conductivity in Zn₃P₂," *J. Phys. Chem. Solids*, vol. 41, no. 6, pp. 635–640, 1980.
- [355] N. Mirowska and J. Misiewicz, "Defect-related transitions in Zn₃P₂ studied by means of photovoltaic effect spectroscopy," *Semicond. Sci. Technol.*, vol. 7, no. 11, pp. 1332–1336, 1992.
- [356] A. Nayak and D. R. Rao, "Photoluminescence spectra of Zn₃P₂-Cd₃P₂ thin films," *Appl. Phys. Lett.*, vol. 63, no. 5, pp. 592–593, 1993.
- [357] P. Panpech, S. Vijarnwannahuk, S. Sanorpim, W. Ono, F. Nakajima, R. Katayama, and K. Onabe, "Correlation between Raman intensity of the N-related local vibrational mode and N content in GaAsN strained layers grown by MOVPE," *J. Cryst. Growth*, vol. 298, no. SPEC. ISS, pp. 107–110, 2007.
- [358] N. Kazemi-Zanjani, E. Kergrene, L. Liu, T.-K. Sham, and F. Lagugné-Labarthe, "Tip-enhanced Raman imaging and nano spectroscopy of etched silicon nanowires," *Sensors*, vol. 13, no. 10, pp. 12744–12759, 2013.
- [359] L. G. Cançado, A. Jorio, E. H. Martins Ferreira, F. Stavale, C. A. Achete, R. B. Capaz, M. V. O. Moutinho, A. Lombardo, T. S. Kulmala, and A. C. Ferrari, "Quantifying defects in graphene via Raman spectroscopy at different excitation energies," *Nano Lett.*, vol. 11, no. 8, pp. 3190–3196, 2011.
- [360] M. Dimitrievska, A. Fairbrother, A. Pérez-Rodríguez, E. Saucedo, and V. Izquierdo-Roca, "Raman scattering crystalline assessment of polycrystalline Cu₂ZnSnS₄ thin films for sustainable photovoltaic technologies: Phonon confinement model," *Acta Mater.*, vol. 70, pp. 272–280, 2014.

Bibliography

- [361] M. Placidi, M. Dimitrievska, V. Izquierdo-Roca, X. Fontané, A. Castellanos-Gomez, A. Pérez-Tomás, N. Mestres, M. Espíndola-Rodríguez, S. López-Marino, M. Neuschitzer, V. Bermudez, A. Yaremko, and A. Pérez-Rodríguez, "Multiwavelength excitation Raman scattering analysis of bulk and two-dimensional MoS₂: Vibrational properties of atomically thin MoS₂ layers," *2D Mater.*, vol. 2, no. 3, 2015.
- [362] M. Dimitrievska, F. Boero, A. P. Litvinchuk, S. Delsante, G. Borzone, A. Perez-Rodriguez, and V. Izquierdo-Roca, "Structural Polymorphism in "Kesterite" Cu₂ZnSnS₄: Raman Spectroscopy and First-Principles Calculations Analysis," *Inorg. Chem.*, vol. 56, no. 6, pp. 3467–3474, 2017.
- [363] S. B. Demers and A. Van De Walle, "Intrinsic defects and dopability of zinc phosphide," *Phys. Rev. B - Condens. Matter Mater. Phys.*, vol. 85, no. 19, pp. 1–10, 2012.
- [364] N. Y. Dzade, "Unravelling the early oxidation mechanism of zinc phosphide (Zn₃P₂) surfaces by adsorbed oxygen and water: a first-principles DFT-D3 investigation," *Phys. Chem. Chem. Phys.*, vol. 22, pp. 1444–1456, 2020.
- [365] N. Y. Dzade, "First-Principles Insights into the Interface Chemistry between 4-Aminothiophenol and Zinc Phosphide (Zn₃P₂) Nanoparticles," *ACS Omega*, vol. 5, no. 2, pp. 1025–1032, 2020.
- [366] D. M. Ceperley and B. J. Alder, "Ground state of the electron gas by a stochastic method," *Phys. Rev. Lett.*, vol. 45, no. 7, pp. 566–569, 1980.
- [367] J. P. Perdew and A. Zunger, "Self-interaction correction to density-functional approximations for many-electron systems," *Phys. Rev. B*, vol. 23, no. 10, pp. 5048–5079, 1981.
- [368] S. J. Clark, M. D. Segall, C. J. Pickard, P. J. Hasnip, M. I. J. Probert, K. Refson, and M. C. Payne, "First principles methods using CASTEP," *Zeitschrift fur Krist.*, vol. 220, no. 5-6, pp. 567–570, 2005.
- [369] M. I. Aroyo, J. M. Perez-Mato, D. Orobengoa, E. Tasci, G. De La Flor, and A. Kirov, "Crystallography online: Bilbao crystallographic server," *Bulg. Chem. Commun.*, vol. 43, no. 2, pp. 183–197, 2011.
- [370] M. I. Aroyo, J. M. Perez-Mato, C. Capillas, E. Kroumova, S. Ivantchev, G. Madariaga, A. Kirov, and H. Wondratschek, "Bilbao Crystallographic Server: I. Databases and crystallographic computing programs," *Zeitschrift fur Krist.*, vol. 221, no. 1, pp. 15–27, 2006.
- [371] M. I. Aroyo, A. Kirov, C. Capillas, J. M. Perez-Mato, and H. Wondratschek, "Bilbao Crystallographic Server. II. Representations of crystallographic point groups and space groups," *Acta Crystallogr. Sect. A Found. Crystallogr.*, vol. 62, no. 2, pp. 115–128, 2006.
- [372] J. He, K. Hummer, and C. Franchini, "Stacking effects on the electronic and optical properties of bilayer transition metal dichalcogenides MoS₂, MoSe₂, WS₂, and WSe₂," *Phys. Rev. B - Condens. Matter Mater. Phys.*, vol. 89, no. 7, pp. 1–11, 2014.
- [373] J. Menéndez and M. Cardona, "Interference effects: A key to understanding forbidden Raman scattering by LO phonons in GaAs," *Phys. Rev. B*, vol. 31, no. 6, pp. 3696–3704, 1985.
- [374] E. Poliani, M. R. Wagner, A. Vierck, F. Herziger, C. Nenstiel, F. Gannott, M. Schweiger, S. Fritze, A. Dadgar, J. Zaumseil, A. Krost, A. Hoffmann, and J. Maultzsch, "Breakdown

- of Far-Field Raman Selection Rules by Light-Plasmon Coupling Demonstrated by Tip-Enhanced Raman Scattering," *J. Phys. Chem. Lett.*, vol. 8, no. 22, pp. 5462–5471, 2017.
- [375] M. Takase, H. Ajiki, Y. Mizumoto, K. Komeda, M. Nara, H. Nabika, S. Yasuda, H. Ishihara, and K. Murakoshi, "Selection-rule breakdown in plasmon-induced electronic excitation of an isolated single-walled carbon nanotube," *Nat. Photonics*, vol. 7, no. 7, pp. 550–554, 2013.
- [376] B. Ketterer, E. Uccelli, and A. Fontcuberta i Morral, "Mobility and carrier density in p-type GaAs nanowires measured by transmission Raman spectroscopy," *Nanoscale*, vol. 4, no. 5, p. 1789, 2012.
- [377] A. P. Litvinchuk and M. Y. Valakh, "Raman and infrared phonons in tetragonal ZnP2 and CdP2 crystals: A density functional study," *J. Phys. Condens. Matter*, vol. 32, no. 44, 2020.
- [378] M. Dimitrievska, A. Fairbrother, X. Fontané, T. Jawhari, V. Izquierdo-Roca, E. Saucedo, and A. Pérez-Rodríguez, "Multiwavelength excitation Raman scattering study of polycrystalline kesterite Cu₂ZnSnS₄ thin films," *Appl. Phys. Lett.*, vol. 104, no. 2, 2014.
- [379] S. Davidsson and M. Höök, "Material requirements and availability for multi-terawatt deployment of photovoltaics," *Energy Policy*, vol. 108, no. December 2016, pp. 574–582, 2017.
- [380] E. A. Fagen, "Optical properties of Zn₃P₂," *J. Appl. Phys.*, vol. 50, no. 10, pp. 6505–6515, 1979.
- [381] A. Catalano, J. V. Masi, and N. Convers Wyeth, "Schottky Barrier Grid Devices on Zn₃P₂," in *Proc. 1979 Photovolt. Energy Conf.*, (Berlin), p. 440, 1979.
- [382] A. J. Ferguson, R. Farshchi, P. K. Paul, P. Dippo, J. Bailey, D. Poplavskyy, A. Khanam, F. Tuomisto, A. R. Arehart, and D. Kuciauskas, "Defect-mediated metastability and carrier lifetimes in polycrystalline (Ag,Cu)(In,Ga)Se₂ absorber materials," *J. Appl. Phys.*, vol. 127, no. 21, 2020.
- [383] S. K. Wallace, D. B. Mitzi, and A. Walsh, "The steady rise of kesterite solar cells," *ACS Energy Lett.*, vol. 2, no. 4, pp. 776–779, 2017.
- [384] T. Unold and L. Gütay, "Photoluminescence Analysis of Thin-Film Solar Cells," in *Adv. Charact. Tech. Thin Film Sol. Cells Second Ed.*, vol. 1-2, pp. 275–297, John Wiley & Sons, Ltd, 2016.
- [385] M. Stolterfoht, C. M. Wolff, J. A. Márquez, S. Zhang, C. J. Hages, D. Rothhardt, S. Albrecht, P. L. Burn, P. Meredith, T. Unold, and D. Neher, "Visualization and suppression of interfacial recombination for high-efficiency large-area pin perovskite solar cells," *Nat. Energy*, vol. 3, no. 10, pp. 847–854, 2018.
- [386] M. Dimitrievska, S. Giraldo, P. Pistor, E. Saucedo, A. Pérez-Rodríguez, and V. Izquierdo-Roca, "Raman scattering analysis of the surface chemistry of kesterites: Impact of post-deposition annealing and Cu/Zn reordering on solar cell performance," *Sol. Energy Mater. Sol. Cells*, vol. 157, pp. 462–467, 2016.
- [387] M. Monti, S. X. Tao, M. Staniforth, A. Crocker, E. Griffin, A. Wijesekara, R. A. Hatton, and J. Lloyd-Hughes, "Efficient Intraband Hot Carrier Relaxation in the Perovskite Semiconductor Cs_{1-x}Rb_xSnI₃ Mediated by Strong Electron-Phonon Coupling," *J. Phys. Chem. C*, vol. 122, no. 36, pp. 20669–20675, 2018.

Bibliography

- [388] J. Lloyd-Hughes and T.-I. Jeon, "A review of the terahertz conductivity of bulk and nano-materials," *J. Infrared, Millimeter, Terahertz Waves*, vol. 33, no. 9, pp. 871–925, 2012.
- [389] H. J. Joyce, J. L. Boland, C. L. Davies, S. A. Baig, and M. B. Johnston, "A review of the electrical properties of semiconductor nanowires: Insights gained from terahertz conductivity spectroscopy," *Semicond. Sci. Technol.*, vol. 31, no. 10, 2016.
- [390] M. Flór, E. Z. Stutz, A. P. Litvinchuk, S. P. Ramanandan, M. Zamani, R. Paul, J.-B. Leran, A. Fontcuberta i Morral, and M. Dimitrievska, "Raman tensor elements of zinc-phosphide (Zn3P2): from experiments to simulation of Raman spectra (in preparation),"
- [391] J. M. Pawlikowski, "Zn3P2 as infrared-to-ultraviolet photoconverter," *Infrared Phys.*, vol. 28, no. 3, pp. 177–182, 1988.
- [392] J. U. Fischbach, G. Benz, N. Stath, and M. H. Pilkuhn, "Free and bound electron transitions to acceptors in indium phosphide," *Solid State Commun.*, vol. 11, pp. 725–728, 1972.
- [393] M. Dimitrievska, F. S. Hage, S. Escobar Steinvall, A. P. Litvinchuk, E. Z. Stutz, Q. M. Ramasse, and A. Fontcuberta i Morral, "The Advantage of Nanowire Configuration in Band Structure Determination," *Adv. Funct. Mater.*, p. 2105426, jul 2021.
- [394] B. O. Sundström, N. G. Nilsson, L. Hultdt, and W. Zdanowicz, "Extrinsic photoluminescence in Zn3P2," in *Proc. first Int. Symp. Phys. Chem. II-V Compd.* (M. J. Gelten and L. Zdanowicz, eds.), (Mogilany, Poland), pp. 175–178, 1980.
- [395] T. Suda, K. Kakishita, H. Sato, and K. Sasaki, "N-type zinc phosphide grown by molecular beam epitaxy," *Appl. Phys. Lett.*, vol. 69, no. 16, pp. 2426–2428, 1996.
- [396] A. P. Levanyuk and V. V. Osipov, "Edge Luminescence of Direct-Gap Semiconductors," *Sov. Phys. - Uspekhi*, vol. 24, no. 3, pp. 187–215, 1981.
- [397] J. Krustok, H. Collan, M. Yakushev, and K. Hjelt, "The Role of Spatial Potential Fluctuations in the Shape of the PL Bands of Multinary Semiconductor Compounds," *Phys. Scr. T*, vol. 79, pp. 179–182, 1999.
- [398] I. G. Stamov, N. N. Syrbu, and A. V. Dorogan, "Energetic band structure of Zn3P2 crystals," *Phys. B Condens. Matter*, vol. 408, no. 1, pp. 29–33, 2013.
- [399] V. Munoz, D. Decroix, A. Chevy, and J. M. Besson, "Optical properties of zinc phosphide," *J. Appl. Phys.*, vol. 60, no. 9, pp. 3282–3288, 1986.
- [400] J. M. Pawlikowski, J. Misiewicz, and N. Mirowska, "Direct and indirect Optical Transitions in Zn3P2," *J. Phys. Chem. Solids*, vol. 40, pp. 1027–1033, 1979.
- [401] G. P. Chuiko, "Mott transitions in disordered A3IIB2V compounds," *Ukr. Fiz. Zhurnal*, vol. 29, no. 5, pp. 787–789, 1984.
- [402] V. V. Sobolev and N. N. Syrbu, "Optical Properties and Energy Band Structure of Zn3P2 and Cd3P2 Crystals," *Phys. Status Solidi*, vol. 64, pp. 423–429, 1974.
- [403] J. Misiewicz and J. A. Gaj, "Optical Anisotropy in the Zn3P2 Band Gap Region," *Phys. Status Solidi*, vol. 105, no. 1, pp. K23–K25, 1981.
- [404] M. C. Spadaro, S. Escobar Steinvall, N. Y. Dzade, S. Marti-Sanchez, P. Torres-Vila, E. Z. Stutz, M. Zamani, R. Paul, J.-B. Leran, A. Fontcuberta i Morral, and J. Arbiol, "Rotated do-

- mains in selective area epitaxy grown Zn₃P₂: formation mechanism and functionality,” *ACS Nano*, *Submitt.*
- [405] S. G. Bishop, W. J. Moore, and E. M. Swiggard, “Optically pumped Cd₃P₂ laser,” *Appl. Phys. Lett.*, vol. 16, pp. 459–461, 1970.
 - [406] A. Nayak, D. R. Rao, and H. D. Banerjee, “Derivative spectra of polycrystalline Zn₃P₂ thin films,” *Solid State Commun.*, vol. 78, no. 2, pp. 149–151, 1991.
 - [407] J. Misiewicz and K. Jezierski, “Zinc Phosphide (Zn₃P₂),” in *Handb. Opt. Constants Solids* (E. D. Palik, ed.), vol. 2, pp. 609–635, Academic Press, 1997.
 - [408] G. M. Kimball, J. P. Bosco, A. M. Müller, S. F. Tajdar, B. S. Brunschwig, H. A. Atwater, and N. S. Lewis, “Passivation of Zn₃P₂ substrates by aqueous chemical etching and air oxidation,” *J. Appl. Phys.*, vol. 112, no. 10, pp. 1–4, 2012.
 - [409] M. Q. Ho, R. J. A. Esteves, G. Kedarnath, and I. U. Arachchige, “Size-Dependent Optical Properties of Luminescent Zn₃P₂ Quantum Dots,” *J. Phys. Chem. C*, vol. 119, no. 19, pp. 10576–10584, 2015.
 - [410] G. A. Lombardi, F. M. de Oliveira, M. D. Teodoro, and A. J. Chiquito, “Investigation of trapping levels in p-type Zn₃P₂ nanowires using transport and optical properties,” *Appl. Phys. Lett.*, vol. 112, no. 19, p. 193103, 2018.
 - [411] G. Elert, “Refraction.” <https://physics.info/refraction/>. Accessed: August 23rd, 2021.
 - [412] J. Misiewicz and J. A. Gaj, “Optical anisotropy of Zn₃P₂ in the band gap region,” in *Proc. first Int. Symp. Phys. Chem. II-V Compd.* (M. J. Gelten and L. Zdanowicz, eds.), (Mogilany, Poland), pp. 163–167, 1980.
 - [413] B. Dowgiałło-Plenkiewicz and P. Plenkiewicz, “Spin-Orbit and Crystal Field Splittings of the Valence Band in II₃V₂ Semiconducting Compounds,” *Phys. Status Solidi*, vol. 87, pp. 309–315, 1978.
 - [414] P. Plenkiewicz and B. Dowgiałło-Plenkiewicz, “Energy band structure of Cd₃P₂ for real D_{4h}15 symmetry: I. Energy Bands,” *Phys. Status Solidi*, vol. 92, pp. 379–387, 1979.
 - [415] P. Plenkiewicz and B. Dowgiałło-Plenkiewicz, “Energy band structure of Cd₃P₂ for real D_{4h}15 symmetry: II. Symmetry Properties,” *Phys. Status Solidi*, vol. 95, pp. 29–37, 1979.
 - [416] N. N. Syrbu, I. G. Stamov, V. I. Morozova, V. K. Kiossev, and L. G. Peev, “Energy band structure of Zn₃P₂, ZnP₂ and CdP₂ crystals on wavelength modulated photoconductivity and photoresponse spectra of Schottky diodes investigation,” in *Proc. first Int. Symp. Phys. Chem. II-V Compd.* (M. J. Gelten and L. Zdanowicz, eds.), (Mogilany, Poland), pp. 237–242, 1980.
 - [417] J. Cisowski, “Level Ordering in II₃-V₂ Semiconducting Compounds,” *Phys. Status Solidi*, vol. 111, pp. 289–293, 1982.
 - [418] J. M. Pawlikowski, “Comments on Zn₃P₂ band structure,” *J. Appl. Phys.*, vol. 53, no. 5, pp. 3639–3642, 1982.
 - [419] J. Andrzejewski and J. Misiewicz, “Energy band structure of Zn₃P₂-type semiconductors: Analysis of the crystal structure simplifications and energy band calculations,” *Phys. Status Solidi Basic Res.*, vol. 227, no. 2, pp. 515–540, 2001.
 - [420] G. M. Kimball, N. S. Lewis, and H. A. Atwater, “Mg doping and alloying in Zn₃P₂ heterojunction solar cells,” *PVSC IEEE Photovolt. Spec. Conf.*, pp. 1039–1043, 2010.

Bibliography

- [421] G. M. Kimball, N. S. Lewis, and H. A. Atwater, "Direct evidence of Mg-Zn-P alloy formation in Mg/Zn₃P₂ solar cells," *PVSC 37th IEEE Photovolt. Spec. Conf.*, pp. 003381–003381, 2011.
- [422] M. Mushrush, M. Sharma, S. Rozeveld, R. Wright, A. Cimaroli, N. Paudel, and Y. Yan, "Interfaces of Zinc Phosphide Magnesium Schottky Diodes," *IEEE J. Photovoltaics*, vol. 4, pp. 1680–1682, nov 2014.
- [423] R. Katsube, K. Kazumi, T. Tadokoro, and Y. Nose, "Reactive Epitaxial Formation of a Mg-P-Zn Ternary Semiconductor in Mg/ZnP Solar Cells," *ACS Appl. Mater. Interfaces*, vol. 10, pp. 36102–36107, oct 2018.
- [424] R. Katsube and Y. Nose, "Thermodynamic considerations on interfacial reactivity concerning carrier transport characteristics in metal/p-Zn₃P₂ junctions," *J. Mater. Chem. C*, vol. 5, no. 22, pp. 5538–5543, 2017.
- [425] V. Vasiraju, Y. Kang, and S. Vaddiraju, "Non-conformal decoration of semiconductor nanowire surfaces with boron nitride (BN) molecules for stability enhancement: degradation-resistant Zn₃P₂, ZnO and Mg₂Si nanowires.," *Phys. Chem. Chem. Phys.*, vol. 16, no. 30, pp. 16150–16157, 2014.
- [426] M. H. Mobarok and J. M. Buriak, "Elucidating the surface chemistry of zinc phosphide nanoparticles through ligand exchange," *Chem. Mater.*, vol. 26, pp. 4653–4661, aug 2014.
- [427] G. Ramos-Sanchez, M. Albornoz, Y. H. Yu, Z. Cheng, V. Vasiraju, S. Vaddiraju, F. El Mellouhi, and P. B. Balbuena, "Organic molecule-functionalized Zn₃P₂ nanowires for photochemical H₂ production: DFT and experimental analyses," *Int. J. Hydrogen Energy*, vol. 39, no. 35, pp. 19887–19898, 2014.
- [428] J. Misiewicz, J. M. Wróbel, and K. Jezierski, "Optical constants and band transitions of Zn₃P₂ and Zn₃As₂," *J. Phys. C Solid State Phys.*, vol. 17, pp. 3091–3099, 1984.
- [429] J. Misiewicz, J. M. Wróbel, and B. P. Clayman, "Lattice modes of Zn₃P₂," *Solid State Commun.*, vol. 66, no. 7, pp. 747–750, 1988.
- [430] J. Misiewicz, "Optical vibrations in the Zn₃P₂ lattice," *J. Phys. Condens. Matter*, vol. 1, pp. 9283–9299, 1989.
- [431] J. Misiewicz, J. M. Wróbel, and B. P. Clayman, "An investigation of optical vibrations in Zn₃P₂," *Acta Phys. Pol. A*, vol. 79, no. 2-3, pp. 405–409, 1991.
- [432] J. Misiewicz, A. Lemiec, K. Jezierski, J. M. Wróbel, and B. P. Clayman, "A classical oscillators model for infrared reflectance spectra of Zn₃P₂," *Infrared Phys. Technol.*, vol. 35, no. 6, pp. 775–779, 1994.
- [433] A. Weber, P. Sutter, and H. von Känel, "Optical, electrical, and photoelectrical properties of sputtered thin amorphous Zn₃P₂ films," *J. Appl. Phys.*, vol. 75, no. 11, pp. 7448–7455, 1994.
- [434] F.-C. Wang and R. H. Bube, "Spectral response of ac photoconductivity in Zn₃P₂," *J. Appl. Phys.*, vol. 53, no. 4, pp. 3335–3338, 1982.
- [435] J. M. Pawlikowski, N. Mirowska, P. Becla, and F. Krolicki, "Photoelectric properties of Zn₃P₂," *Solid. State. Electron.*, vol. 23, no. 7, pp. 755–758, 1980.
- [436] A. J. Nelson, L. L. Kazmerski, M. Engelhardt, and H. Hochst, "Valence-band electronic

- structure of Zn₃P₂ as a function of annealing as studied by synchrotron radiation photoemission," *J. Appl. Phys.*, vol. 67, no. 3, pp. 1393–1396, 1990.
- [437] J. M. Pawlikowski, "Absorption edge of Zn₃P₂," *Phys. Rev. B*, vol. 26, no. 8, pp. 4711–4713, 1982.
- [438] J. M. Pawlikowski, J. Misiewicz, N. Mirowska, and P. Becla, "Absorption edge of Zn₃P₂ at 5, 80 and 300 K," *Phys. Status Solidi*, vol. 88, no. 2, pp. K153–K156, 1978.
- [439] L. N. Kurbatov, A. I. Dirochka, E. V. Sinitsyn, V. B. Lazarev, V. J. Shevchenko, and S. E. Kozlov, "Luminescence of cadmium and zinc phosphides," *Sov. J. Quantum Electron.*, vol. 6, no. 2, pp. 166–168, 1976.
- [440] P. J. Lin-Chung, "Energy Band Structures of Cd₃P₂ and Zn₃P₂," *Phys. Status Solidi*, vol. 47, pp. 33–39, 1971.
- [441] A. Hupfer, D. Hirsch, and S. Schulze, "Photoemission on A₃B₂V Semiconductor Material - Cd₃As₂, Zn₃As₂, Cd₃P₂, Zn₃P₂ Crystals and Thin Films," *Phys. Status Solidi*, vol. 152, pp. 505–517, 1989.
- [442] J. P. Bosco, D. O. Scanlon, G. W. Watson, N. S. Lewis, and H. A. Atwater, "Energy-band alignment of II-VI/Zn₃P₂ heterojunctions from x-ray photoemission spectroscopy," *J. Appl. Phys.*, vol. 113, no. 20, 2013.
- [443] K. Sierański, J. Szatkowski, and J. Misiewicz, "Semiempirical tight-binding band structure of II₃V₂ semiconductors: Cd₃P₂, Zn₃P₂, Cd₃As₂, and Zn₃As₂," *Phys. Rev. B*, vol. 50, no. 11, pp. 7331–7337, 1994.
- [444] G. P. Chuiko and N. M. Chuiko, "Specific features of band spectra of A₃B₂V semiconductors," *Sov. Phys. Semicond.*, vol. 15, no. 7, pp. 739–741, 1981.
- [445] J. Lagrenaudie, "Propriétés du phosphure de zinc P₂Zn₃ en cristaux," *J. Phys. le Radium*, vol. 16, no. 3, pp. 234–235, 1955.
- [446] V. J. Shevchenko, L. R. Babarina, S. E. Kozlov, and V. B. Lazarev, "Electrical properties of zinc phosphide (in russian)," *Neorg. Mater.*, vol. 11, no. 9, p. 1719, 1975.
- [447] F.-C. Wang, A. L. Fahrenbruch, and R. H. Bube, "Electrical properties of Zn₃P₂ single crystals," *J. Electron. Mater.*, vol. 11, no. 1, pp. 75–88, 1982.
- [448] D. P. Saha, P. S. Basak, and R. P. Singh, "Electrical conduction in n-type polycrystalline Zn₃P₂ films," *Indian J. Pure Appl. Phys.*, vol. 32, no. 2, pp. 171–175, 1994.
- [449] M. Bhushan, J. A. Turner, and B. A. Parkinson, "Photoelectrochemical Investigation of Zn₃P₂," *J. Electrochem. Soc.*, vol. 133, no. 3, p. 536, 1986.
- [450] J. Lagrenaudie, "Proprietes semi-conductrices du phosphure de zinc (P₂Zn₃)," *J. Chim. Phys.*, vol. 50, pp. 545–547, 1953.
- [451] R. W. Fessenden, J. Sobhanadri, and V. Subramanian, "Minority carrier lifetime in thin films of Zn₃P₂ using microwave and optical transient measurements," *Thin Solid Films*, vol. 266, no. 2, pp. 176–181, 1995.
- [452] J. Misiewicz, N. Mirowska, and Z. Gumieny, "Fundamental Optical and Photoelectric Properties of Poly- and Mono-Crystals of Zn₃P₂," *Phys. Status Solidi*, vol. 83, no. 1, pp. K51–K56, 1984.
- [453] K. Jezierski, J. Misiewicz, and J. M. Pawlikowski, "Kramers-Kronig analysis for Zn₃P₂,"

Bibliography

- in *Proc. first Int. Symp. Phys. Chem. II-V Compd.* (M. J. Gelten and L. Zdanowicz, eds.), (Mogilany, Poland), pp. 193–197, 1980.
- [454] K. Jezierski, J. Misiewicz, J. Wnuk, and J. M. Pawlikowski, “Kramers-Kronig analysis of the optical constants of Zn₃As₂ and Zn₃P₂,” *Opt. Appl.*, vol. 12, no. 1, pp. 107–118, 1982.
- [455] J. Misiewicz and K. Jezierski, “Reflectivity, optical constants and interband transitions in Zn₃P₂,” *Solid State Commun.*, vol. 70, no. 4, pp. 465–469, 1989.
- [456] J. P. Bosco, G. M. Kimball, N. S. Lewis, and H. A. Atwater, “Pseudomorphic growth and strain relaxation of α -Zn₃P₂ on GaAs(001) by molecular beam epitaxy,” *J. Cryst. Growth*, vol. 363, pp. 205–210, 2013.
- [457] A. Catalano, V. Dalal, W. E. Devaney, E. A. Fagen, R. B. Hall, J. V. Masi, J. D. Meakin, G. Warfield, N. Convers Wyeth, and A. M. Barnett, “Zn₃P₂: a promising photovoltaic material,” in *Conf. Rec. 13th IEEE Photovolt. Spec. Conf.*, (Washington, DC), pp. 288–293, 1978.
- [458] K. Jezierski, J. Misiewicz, and F. Królicki, “Influence of the Surface Quality on the Reflectance of Zn₃P₂,” *Phys. Status Solidi*, vol. 112, no. 3, pp. K135–K137, 1989.
- [459] J. M. Pawlikowski, “Comments on the determination of the absorption coefficient of thin semiconductor films,” *Thin Solid Films*, vol. 127, no. 1-2, pp. 29–38, 1985.
- [460] Z. Gumienny and J. Misiewicz, “New methods of determination of the birefringence of the crystal-application to Zn₃P₂,” *Opt. Appl.*, vol. 15, no. 1, pp. 63–68, 1985.
- [461] W. Zdanowicz and Z. Henkie, “Some Electric Properties of Zn₃P₂,” *Bull. l’Académie Pol. des Sci. Série des Sci. Chim.*, vol. 12, no. 10, pp. 729–734, 1964.
- [462] A. Catalano and M. Bhushan, “Evidence of p/n homojunction formation in Zn₃P₂,” *Appl. Phys. Lett.*, vol. 37, no. 6, pp. 567–569, 1980.
- [463] M. Bhushan, “Mg diffused zinc phosphide n/p junctions,” *J. Appl. Phys.*, vol. 53, no. 1, pp. 514–519, 1982.
- [464] R. P. Singh and S. L. Singh, “Vacuum-evaporated zinc phosphide films and their characterization,” *Phys. Status Solidi*, vol. 100, no. 2, pp. 493–500, 1987.
- [465] R. P. Singh and S. L. Singh, “Photoelectrochemical Solar Cells Using Vacuum-Evaporated Zinc Phosphide Films,” *Phys. Status Solidi*, vol. 101, no. 1, pp. 129–135, 1987.
- [466] D. P. Saha and R. P. Singh, “Characterization of Zn₃P₂ thin films,” *Indian J. Pure Appl. Phys.*, vol. 32, no. 11, pp. 912–914, 1994.
- [467] S. M. Thurgate and G. N. Raikar, “Auger line shape analysis of Zn₃P₂,” *Appl. Surf. Sci.*, vol. 26, pp. 51–60, 1986.
- [468] L. Szaro, F. Królicki, and M. Lewicki, “Surface photovoltage on Zn₃P₂ monocrystals,” in *Proc. first Int. Symp. Phys. Chem. II-V Compd.* (M. J. Gelten and L. Zdanowicz, eds.), (Mogilany, Poland), pp. 205–208, 1980.
- [469] A. Catalano and M. Bhushan, “P/N junction formation in Zn₃P₂,” in *Proc. first Int. Symp. Phys. Chem. II-V Compd.* (M. J. Gelten and L. Zdanowicz, eds.), (Mogilany, Poland), pp. 169–174, 1980.
- [470] T. Suda and R. H. Bube, “Deep levels in zinc phosphide,” *Appl. Phys. Lett.*, vol. 45, no. 7, pp. 775–777, 1984.

- [471] S. Fuke, Y. Takatsuka, K. Kuwahara, and T. Imai, "Growth and characterization of zinc phosphide crystals," *J. Cryst. Growth*, vol. 87, pp. 567–570, 1988.
- [472] M. Bhushan, "Schottky solar cells on thin polycrystalline Zn₃P₂ films," *Appl. Phys. Lett.*, vol. 40, no. 1, pp. 51–53, 1982.
- [473] P. S. Nayar and A. Catalano, "Zinc phosphide-zinc oxide heterojunction solar cells," *Appl. Phys. Lett.*, vol. 39, no. 1, pp. 105–107, 1981.
- [474] P. S. Nayar, "Properties of zinc phosphide/zinc oxide heterojunctions," *J. Appl. Phys.*, vol. 53, no. 2, pp. 1069–1075, 1982.
- [475] J. Misiewicz, "Optical and electrical investigations of imperfection levels in Zn₃P₂," *J. Phys. Chem. Solids*, vol. 50, no. 10, pp. 1013–1022, 1989.
- [476] K. Sierański, J. Szatkowski, and J. M. Pawlikowski, "Persistent photoconductivity in high resistive Zn₃P₂," *J. Appl. Phys.*, vol. 115, no. 8, pp. 2–5, 2014.
- [477] K. Sierański, J. Szatkowski, and A. Hajdusianek, "Deep levels in low resistive Zn₃P₂," *Phys. Status Solidi*, vol. 4, no. 5, pp. 1–4, 2017.
- [478] T. Suda, M. Kobayashi, A. Kuroyanagi, and S. Kurita, "Zn₃P₂/ITO Heterojunction Solar Cells," *Jpn. J. Appl. Phys.*, vol. 21, no. Suppl. 21-2, pp. 63–66, 1982.
- [479] T. Suda, M. Suzuki, and S. Kurita, "Polycrystalline Zn₃P₂/Indium-Tin Oxide Solar Cells," *Jpn. J. Appl. Phys.*, vol. 22, no. 10, pp. L656–L658, 1983.
- [480] M. S. Casey, A. L. Fahrenbruch, and R. H. Bube, "Properties of zinc-phosphide junctions and interfaces," *J. Appl. Phys.*, vol. 61, no. 8, pp. 2941–2946, 1987.
- [481] F.-C. Wang, A. L. Fahrenbruch, and R. H. Bube, "Transport mechanisms for Mg/Zn₃P₂ junctions," *J. Appl. Phys.*, vol. 53, no. 12, pp. 8874–8879, 1982.
- [482] J. M. Pawlikowski, "Optical band gap of Cd₃P₂-Zn₃P₂ semiconductor solid solutions," *J. Phys. C*, vol. 18, pp. 5605–5616, 1985.
- [483] K. Sierański and J. Szatkowski, "Electrical Conductivity of Zn₃P₂," *Phys. Status Solidi*, vol. 94, pp. K133–K135, 1986.
- [484] N. Mirowska and M. Adamczyk, "Influence of semiconductor surface condition on electrical and photoelectric properties of Al-Zn₃P₂ contacts," in *Proc. Int. Conf. Solid State Cryst. '98 Epilayers Heterostruct. Optoelectron. Semicond. Technol.* (A. Rogalski and J. Rutkowski, eds.), vol. 3725, (Zakopane, Poland), pp. 168–173, apr 1999.
- [485] N. Mirowska and J. Misiewicz, "Influence of semiconductor surface preparation on photoelectric properties of Al-Zn₃P₂ contacts," *Mater. Sci. Eng. B Solid-State Mater. Adv. Technol.*, vol. 130, pp. 49–56, 2006.
- [486] M. Ginting and J. D. Leslie, "Preparation and electrical properties of heterojunctions of ZnO on Zn₃P₂ and CdTe," *Can. J. Phys.*, vol. 67, no. 4, pp. 448–455, 1989.
- [487] W. Zdanowicz, K. Kloc, A. Kalińska, E. Cisowska, and A. Burian, "The morphology of Zn₃P₂ single crystals grown from the vapour phase," *J. Cryst. Growth*, vol. 31, pp. 56–59, 1975.
- [488] Y. A. Ugai, O. Y. Gukov, E. P. Domashevskaya, and L. A. Ozerov, "Phase Diagrams of the Zn-Zn₃P₂ and Cd-Cd₃P₂ Systems," *Neorg. Mater.*, vol. 4, no. 1, pp. 147–148, 1968.
- [489] J. M. Pawlikowski, N. Mirowska, and F. Królicki, "Photoconductivity and Dember Effect in Zn₃P₂," *Infrared Phys.*, vol. 18, pp. 343–346, 1978.

Bibliography

- [490] R. Sathyamoorthy, C. Sharmila, P. Sudhagar, S. Chandramohan, and S. Velumani, "Electrical conduction in zinc phosphide thin films," *Mater. Charact.*, vol. 58, pp. 730–734, 2007.
- [491] M. Bhushan, J. D. Meakin, A. Catalano, V. Dalal, E. A. Fagen, R. B. Hall, J. V. Masi, G. Warfield, A. M. Barnett, W. E. Devaney, and N. Convers Wyeth, "Zn₃P₂ as an improved semiconductor for photovoltaic solar cells," tech. rep., 1985.
- [492] O. Vazquez-Mena, J. P. Bosco, O. Ergen, H. I. Rasool, A. Fathalizadeh, M. Tosun, M. Crommie, A. Javey, H. A. Atwater, and A. Zettl, "Performance Enhancement of a Graphene-Zinc Phosphide Solar Cell Using the Electric Field-Effect," *Nano Lett.*, vol. 14, pp. 4280–4285, 2014.
- [493] T. Suda, "Zinc Phosphide Thin Films Grown by Plasma Assisted Vapor Phase Deposition," *J. Cryst. Growth*, vol. 99, pp. 625–629, 1990.
- [494] M.-H. Park, L. C. Wang, J. Y. Cheng, F. Deng, S. S. Lau, and C. J. Palmstrom, "Low resistance Zn₃P₂/InP heterostructure Ohmic contact to p-InP," *Appl. Phys. Lett.*, vol. 68, no. 7, pp. 952–954, 1995.
- [495] P. Wu, T. Sun, Y. Dai, Y. Sun, Y. Ye, and L. Dai, "Novel Type-II Zn₃P₂/ZnO Core/Shell Nanowires: Synthesis, Characteristic, and Photoluminescence Properties," *Cryst. Growth Des.*, vol. 11, no. 5, pp. 1417–1421, 2011.
- [496] E. J. Lubber, M. H. Mobarok, and J. M. Buriak, "Solution-Processed Zinc Phosphide Colloidal Semiconducting Nanocrystals for Thin Film Photovoltaic Applications," *ACS Nano*, vol. 7, pp. 8136–8146, sep 2013.
- [497] G. Shen, C. Ye, D. Golberg, J. Hu, and Y. Bando, "Structure and cathodoluminescence of hierarchical Zn₃P₂ ZnS nanotube/nanowire heterostructures," *Appl. Phys. Lett.*, vol. 90, no. 7, pp. 1–4, 2007.
- [498] K. Kakishita, K. Aihara, and T. Suda, "Zinc phosphide epitaxial growth by photo-MOCVD," *Appl. Surf. Sci.*, vol. 79 pt 80, no. 1-4, pp. 281–286, 1994.
- [499] E. F. Venger, T. Barlas, and K. V. Shportko, "Surface polaritons in zinc phosphide," *Spectroscopy*, vol. 30, no. 2, 2015.
- [500] K. V. Shportko, T. Barlas, E. F. Venger, H. M. El-Nasser, and V. Ponomarenko, "Influence of the temperature on the dispersion of the surface polaritons in Zn₃P₂- Material for the photovoltaic applications," *Curr. Appl. Phys.*, vol. 16, no. 1, pp. 8–11, 2016.
- [501] D. M. Stepanchikov, "Calculation of exciton energy levels in (Zn_xCd_{1-x})₃P₂ alloy system," *Bull. Kherson Natl. Tech. Univ.*, vol. 4, no. 63, pp. 11–18, 2017.
- [502] L. Hultdt, N. G. Nilsson, B. O. Sundström, and W. Zdanowicz, "Photoluminescence of Zinc Phosphide - Zn₃P₂," *Phys. Status Solidi*, vol. 53, no. 1, pp. K15–K18, 1979.
- [503] G. Shen, Y. Bando, J. Q. Hu, and D. Golberg, "Single-crystalline trumpetlike zinc phosphide nanostructures," *Appl. Phys. Lett.*, vol. 88, no. 14, pp. 1–4, 2006.
- [504] R. Yang, Y. L. Chueh, J. R. Morber, R. Snyder, L. J. Chou, and Z. L. Wang, "Single-crystalline branched zinc phosphide nanostructures: Synthesis, properties, and optoelectronic devices," *Nano Lett.*, vol. 7, no. 2, pp. 269–275, 2007.
- [505] C. Liu, L. Dai, L. P. You, W. J. Xu, R. M. Ma, W. Q. Yang, Y. F. Zhang, and G. G. Qin,

- “Synthesis of high quality p-type Zn₃P₂ nanowires and their application in MISFETs,” *J. Mater. Chem.*, vol. 18, no. 33, p. 3912, 2008.
- [506] P. Wu, Y. Dai, Y. Ye, Y. Yin, and L. Dai, “Fast-speed and high-gain photodetectors of individual single crystalline Zn₃P₂ nanowires,” *J. Mater. Chem.*, vol. 21, no. 8, p. 2563, 2011.
- [507] C. Kranert, C. Sturm, R. Schmidt-Grund, and M. Grundmann, “Raman Tensor Formalism for Optically Anisotropic Crystals,” *Phys. Rev. Lett.*, vol. 116, no. 12, pp. 1–5, 2016.
- [508] M. J. L. Sourribes, I. Isakov, M. Panfilova, and P. A. Warburton, “Minimization of the contact resistance between InAs nanowires and metallic contacts,” *Nanotechnology*, vol. 24, no. 4, 2013.
- [509] H. A. Potts, M. Friedl, F. Amaduzzi, K. Tang, G. Tütüncüoğlu, F. Matteini, E. Alarcón-Lladó, P. C. McIntyre, and A. Fontcuberta I Morral, “From Twinning to Pure Zincblende Catalyst-Free InAs(Sb) Nanowires,” *Nano Lett.*, vol. 16, no. 1, pp. 637–643, 2016.
- [510] J. Misiewicz, J. M. Wróbel, and K. Jezierski, “Interband transitions in Zn₃As₂,” *Solid State Commun.*, vol. 86, no. 8, pp. 509–511, 1993.
- [511] “Zinc phosphide (Zn₃P₂) optical properties, dielectric constant,” in *Non-Tetrahedrally Bond. Elem. Bin. Compd. I* (O. Madelung, U. Rössler, and M. Schulz, eds.), Springer-Verlag Berlin Heidelberg, 1998.
- [512] F. D’Angelo, H. Němec, S. H. Parekh, P. Kužel, M. Bonn, and D. Turchinovich, “Self-referenced ultra-broadband transient terahertz spectroscopy using air-photonics,” *Opt. Express*, vol. 24, no. 9, p. 10157, 2016.
- [513] C. Zhang, B. Jin, J. Chen, P. Wu, and M. Tonouchi, “Noncontact evaluation of nondoped InP wafers by terahertz time-domain spectroscopy,” *J. Opt. Soc. Am. B*, vol. 26, pp. A1–A5, sep 2009.
- [514] H. Hempel, T. Unold, and R. Eichberger, “Measurement of charge carrier mobilities in thin films on metal substrates by reflection time resolved terahertz spectroscopy,” *Opt. Express*, vol. 25, no. 15, p. 17227, 2017.

Glossary

LED light emitting diode. 62

nanosail nanometer-scale sail-like structure. 69, 71, 72, 73, 74, 75, 76, 77, 147

NP nanoplatelet, nanometer-scale platelets. Sometimes interchangeably used instead of nanosail. 144

phonon Collective excitation of the atomic lattice. Quasi-particle and quantization of the lattice vibrations.. 47

Acronyms

- AFM** atomic force microscopy. 71
- CBM** conduction band minimum. 60, 62, 111
- CIGS** copper indium gallium sulfide. 6, 8, 16, 22
- CIGSSe** copper indium gallium sulfide/selenide. 12, 17, 23, 24, 59
- CTE** coefficient of thermal expansion. 41, 70
- CZTS** copper zinc tin sulfide. 13, 16, 22, 70
- CZTSSe** copper zinc tin sulfide/selenide. 12, 17, 23, 24, 58, 59
- DFT** density-functional theory. 21, 76, 81, 82, 88, 91, 93, 109, 112
- EC** European Commission. 9, 10
- EDX** energy-dispersive x-ray spectroscopy. 82, 85, 86
- EU** European Union. 15
- FCC** face-centered cubic. 17
- FWHM** full width at half maximum. 126
- IB** impurity band. 76
- IR** infrared. 55
- MBE** molecular beam epitaxy. 82
- MOCVD** metal-organic chemical vapor deposition. 74, 78
- MOVPE** metal-organic vapor phase epitaxy. 71, 109
- NMR** nuclear magnetic resonance. 59

Acronyms

OPTP optical pump terahertz probe. 97, 106, 108, 158, 160

PCE power conversion efficiency. 7, 25

PDOS phonon density of states. 82, 91, 93

PL photoluminescence. 45, 59, 60, 61, 96, 127

PV photovoltaic. 8, 13, 31, 66, 70, 80, 81

RBS Rutherford backscattering spectrometry. 100, 108

SE spectroscopic ellipsometry. 66, 67

SEM scanning electron microscopy. 71, 82, 85

SNSF Swiss National Science Foundation. 78, 94, 108

TEM transmission electron microscopy. 82, 85

TW terawatt. 1, 15, 17

UV ultraviolet. 27, 127

VBM valence band maximum. 76, 111, 128

XRD X-ray diffraction. 58, 59, 69

Elias Stutz

Chemin du Motte 35
1020 Renens
Switzerland
Nationality: Swiss

ezstutz@gmail.com
+41 78/895 73 21
www.linkedin.com/in/eliasstutz
ORCID: 0000-0003-1079-8063

Strengths

- Materials scientist specialized in semiconductors, photovoltaics and optical spectroscopy
- Advanced operation and maintenance of an optical spectrometer
- Good language and communication skills, project management and pupil supervision

Education

- **École Polytechnique Fédérale de Lausanne, EPFL** Lausanne, Switzerland
Doctoral studies. Thesis director: Prof. Anna Fontcuberta i Morral Oct. 2017 - Nov. 2021
- **Lawrence Berkeley National Laboratory, LBNL** Berkeley, CA, USA
Participating Guest Researcher, Master Project Feb. 2015 - Aug. 2015
 - Part of the Joint Center for Artificial Photosynthesis. Supervized by Dr. Le Chen, Prof. Ian Sharp and Dr. Joel W. Ager.
 - Optimized plasma-assisted atomic layer deposition process for the deposition of thin-films of NiCo₂O₄ transparent conductive oxides. Photoelectrochemical cell characterization.
 - Synchrotron beam time at SLAC National Accelerator Laboratory
- **École Polytechnique Fédérale de Lausanne, EPFL** Lausanne, Switzerland
Master of Science (MSc), Materials Science and Engineering Sep. 2013 - Sep. 2015
 - Specialization: Materials for electronics
- **Carnegie Mellon University, CMU** Pittsburgh, PA, USA
Year of studies abroad. Aug. 2012 - May 2013
- **École Polytechnique Fédérale de Lausanne, EPFL** Lausanne, Switzerland
Bachelor of Science (BSc), Materials Science and Engineering Sep. 2010 - Sep. 2013

Professional Experience

- **École Polytechnique Fédérale de Lausanne, EPFL** Lausanne, Switzerland
Research Intern at the Laboratory of Semiconductor Materials Apr. 2017 - Sep. 2017
- **eOde** Neuchâtel, Switzerland
Scientific collaborator Jan. 2017 - Mar. 2017
 - Developed code in R from ground up to calculate custom building pollution hazards from soil pollution maps, with a graphical interface.

- **EMPA, Laboratory for Advanced Materials Processing** Thun, Switzerland
Research Intern Jul. 2014 - Dec. 2014
 - Optimized mesoporous alumina slip casting procedure and post-sintering processing
 - Characterized mechanical properties following industry standards
- **École Polytechnique Fédérale de Lausanne, EPFL** Lausanne, Switzerland
Teaching Assistant Sep. 2013 - Jun. 2014

Institutional responsibilities

- Responsible for maintenance and upkeep of a triple Raman spectrometer and a photoluminescence spectrometer on a customized optical table, as well as training and assisting users and writing user manuals.
- Organizing outreach and visits:
 - Laboratory booth for EPFL's 50 Years Open Day
 - High-schooler class visits, multiple times
 - Organization of multiple-day student visit
- Teaching assistant for bachelor courses. Running exercise sessions.
- Supervision and coaching of student research projects
 - Bachelor Semester Project: 3
 - Master Semester Project: 4
 - Master Thesis or long-term project: 2
 - Remote project: 3
- Research collaborations with groups internal and external to EPFL

Skills

Languages: French (native), English (fluent), German (intermediate), Swiss-german (basic)

Programming languages: Python, L^AT_EX, R

Applications: Mathematica, Origin (OriginLab), ImageJ, LabVIEW, L^AT_EX, Office Suite

Lab Skills: Vacuum systems, cryogenic systems, lasers and optical systems.

Characterization Skills: Wide array of materials characterization skills of **mechanical** (hardness, tensile and flexural testing, rheometer, etc.), **electrical** (PEC cell, Hall, 4-point, etc.) and **chemical** (XPS, EDX) properties. **Microscopic characterization** with AFM, SEM, and optical microscopy.

Extensive optical spectroscopy experience including characterization, analysis, maintenance and support. Optical techniques including Raman, Photoluminescence, ellipsometry, Infrared and UV-Vis-IR

Other: X-ray diffraction, DSC

Growth and Fabrication Skills: PLD, (PE-)ALD, sputtering, evaporation, sputtering deposition and MBE (minor). Photolithography, wet etch, dry etch, ellipsometry

Soft skills: Strong verbal, presentation and written communication skills. Project and pupil management.

Peer-reviewed Publications

141 citations (Google scholar)

1. Dimitrievska, M., Hage, F. S., Escobar Steinvall, S., Litvinchuk, A. P., **Stutz, E. Z.**, Ramasse, Q. M. and Fontcuberta i Morral, A. (2021). "The Advantage of Nanowire Configuration in Band Structure Determination". *Advanced Functional Materials*, 2105426. <https://doi.org/10.1002/adfm.202105426>
2. Dubrovskii, V. G., Escobar Steinvall, S., de Mestral, V., Paul, R., Leran, J.-B., Zamani, M., **Stutz, E. Z.** and Fontcuberta i Morral, A. (2021). "Modeling the Shape Evolution of Selective Area Grown Zn₃P₂ Nanoislands". *Crystal Growth and Design*. <https://doi.org/10.1021/acs.cgd.1c00569>
3. Zamani, M., **Stutz, E. Z.**, Escobar Steinvall, S., Zamani, R. R., Paul, R., Leran, J.-B., Dimitrievska, M. and Fontcuberta i Morral, A. (2021). "The path towards 1 μ m monocrystalline Zn₃P₂ films on InP: substrate preparation, growth conditions and luminescence properties". *Journal of Physics: Energy*, 3(3), 034011. <https://doi.org/10.1088/2515-7655/abf723>
4. **Stutz, E. Z.**, Escobar Steinvall, S., Litvinchuk, A. P., Leran, J.-B., Zamani, M., Paul, R., Fontcuberta i Morral, A. and Dimitrievska, M. (2021). "Raman spectroscopy and lattice dynamics calculations of tetragonally-structured single crystal zinc phosphide (Zn₃P₂) nanowires". *Nanotechnology*, 32(8), 085704. <https://doi.org/10.1088/1361-6528/abc91b>
5. Escobar Steinvall, S., **Stutz, E. Z.**, Paul, R., Zamani, M., Dzade, N. Y., Piazza, V., Friedl, M., de Mestral, V., Leran, J.-B., Zamani, R. R. and Fontcuberta i Morral, A. (2021). "Towards defect-free thin films of the earth-abundant absorber zinc phosphide by nanopatterning". *Nanoscale Advances*, 3(2), 326–332. <https://doi.org/10.1039/D0NA00841A>
6. Escobar Steinvall, S.*, Ghisalberti, L.*, Zamani, R. R.*, Tappy, N., Hage, F. S., **Stutz, E. Z.**, Zamani, M., Paul, R., Leran, J.-B., Ramasse, Q. M., Carter, W. C. and Fontcuberta I Morral, A. (2020). "Heterotwin Zn₃P₂ superlattice nanowires: the role of indium insertion in the superlattice formation mechanism and their optical properties". *Nanoscale*. <https://doi.org/10.1039/d0nr05852a>
7. Paul, R., Humblot, N., Escobar Steinvall, S., **Stutz, E. Z.**, Joglekar, S. S., Leran, J.-B., Zamani, M., Cayron, C., Logé, R., Granados del Aguila, A., Xiong, Q. and Fontcuberta I Morral, A. (2020). "Van der Waals Epitaxy of Earth-Abundant Zn₃P₂ on Graphene for

Photovoltaics". *Crystal Growth and Design*, 20(6), 3816–3825.
<https://doi.org/10.1021/acs.cgd.0c00125>

8. Escobar Steinvall, S., Tappy, N., Ghasemi, M., Zamani, R. R., Lagrange, T., **Stutz, E. Z.**, Leran, J.-B., Zamani, M., Paul, R. and Fontcuberta i Morral, A. (2020). "Multiple morphologies and functionality of nanowires made from earth-abundant zinc phosphide". *Nanoscale Horizons*, 5, 274–282. <https://doi.org/10.1039/c9nh00398c>
9. Ghasemi, M., **Stutz, E. Z.**, Escobar Steinvall, S., Zamani, M. and Fontcuberta i Morral, A. (2019). "Thermodynamic re-assessment of the Zn–P binary system". *Materialia*, 6, 100301. <https://doi.org/10.1016/j.mtla.2019.100301>
10. **Stutz, E. Z.***, Friedl, M.*, Burgess, T., Tan, H. H., Caroff, P., Jagadish, C. and Fontcuberta i Morral, A. (2019). "Nanosails Showcasing Zn₃As₂ as an Optoelectronic-Grade Earth Abundant Semiconductor". *Physica Status Solidi (RRL) - Rapid Research Letters*, 13(7), 1900084. <https://doi.org/10.1002/pssr.201900084>
11. von Gastrow, G., Savin, H., Calle, E., Ortega, P., Alcubilla, R., Daniil, A., **Stutz, E. Z.**, Fontcuberta i Morral, A., Husein, S., Nietzold, T. and Bertoni, M. (2017). "Metallized Boron-Doped Black Silicon Emitters For Front Contact Solar Cells". In 2017 IEEE 44th Photovoltaic Specialist Conference (PVSC) (pp. 944–947). Washington, DC: IEEE. <https://doi.org/10.1109/PVSC.2017.8366010>
12. Xu, X., Bullock, J., Schelhas, L. T., **Stutz, E. Z.**, Fonseca, J. J., Hettick, M., Pool, V. L., Tai, K. F., Toney, M. F., Fang, X., Javey, A., Wong, L. H. and Ager, J. W. (2016). "Chemical Bath Deposition of p-Type Transparent, Highly Conducting (CuS)_x:(ZnS)_{1-x} Nanocomposite Thin Films and Fabrication of Si Heterojunction Solar Cells." *Nano Letters*, 16(3). <https://doi.org/10.1021/acs.nanolett.5b05124>

* equal contribution

Publications under peer-review or under preparation

1. Escobar Steinvall, S., **Stutz, E. Z.**, Paul, E., Zamani, M., Leran, J.-B., Dimitrievska, M. and Fontcuberta i Morral, A. "Nanoscale growth initiation as a pathway to improve the earth abundant absorber zinc phosphide", *ACS Applied Energy Materials*, (submitted)
2. Spadaro, M. C.*, Escobar Steinvall, S.*, Dzade, N. Y., Marti-Sanchez, S., Torres-Vila, P., **Stutz, E. Z.**, Zamani, M., Paul, R., Leran, J.-B., Fontcuberta i Morral, A. and Arbiol, J., "Rotated domains in selective area epitaxy grown Zn₃P₂: formation mechanism and functionality", *ACS Nano*, (submitted)
3. **Stutz, E. Z.**, Zamani, M., Damry, D., Buswell, L., Paul, R., Escobar Steinvall, S., Leran, J.-B., Boland, J. L., Dimitrievska, M. and Fontcuberta i Morral, A., "Showcasing the optical properties of monocrystalline zinc phosphide thin films as an earth-abundant photovoltaic absorber", (under preparation)
4. Flór, M., **Stutz, E. Z.**, Litvinchuk, A. P., Ramanandan, S. P., Zamani, M., Paul, R., Leran, J.-B., Fontcuberta i Morral, A., Dimitrievska, M., "Raman tensor elements of zinc-phosphide (Zn₃P₂): from experiments to simulation of Raman spectra", (under preparation)

* equal contribution

Conferences & Workshops

- [Virtual Material Research Society \(MRS\) Spring Meeting](#), online, 19th of April, 2021
- Live and recorded talk, titled: "Defect identification and full lattice dynamics of zinc phosphide, an earth-abundant semiconductor for photovoltaics"
- [EDMX Research Day](#), online, 10th of February, 2021
- Short presentation, titled: "Functional properties of zinc phosphide for earth-abundant photovoltaics"
- [CIME Day](#), Lausanne, Switzerland, 6th of March, 2020
- Poster, titled: "Spectroscopic characterization of zinc phosphide thin films for photovoltaics"
- [EDMX Research Day](#), Lausanne, Switzerland, 29th of November, 2019
- Poster, titled: "Passivation of earth-abundant nanostructures and thin films"
- [Nanowire Week](#), Pisa, Italy, 23rd - 27th of September, 2019
- Poster, titled: "Functional properties of earth-abundant nanowires and nanosails"
- [International Conference on Amorphous and Nano-crystalline Semiconductors, ICANS28](#), Palaiseau, France, 5th - 9th of August, 2019
- Poster, titled: "Surface passivation of zinc phosphide thin films and nanowires"
- [European Materials Research Society \(E-MRS\) Spring Meeting](#), Nice, France, 27th - 31st of May, 2019
- Talk, titled: "Surface passivation of zinc phosphide thin films and nanowires"
- [Winterschool on "Quantum effects and miniaturization of Mechanics, Fluidics, Optics and Electronics"](#), Tegernsee, Germany, 7th - 11th of January, 2019
- Poster, titled: "Spectroscopic characterization and passivation of zinc phosphide for photovoltaic applications"
- [EDMX Research Day](#), Lausanne, Switzerland, 12th of December, 2018
- Poster, titled: "Spectroscopic characterization and passivation of zinc phosphide for photovoltaic applications"
- [ICPS 2018](#), Montpellier, France, 29th of July - 3rd of August, 2018
- Poster, titled: "Determination of the growth direction of zinc phosphide nanowires using Raman spectroscopy"
- [NRG 2018 Winter School](#), Crans-Montana, Switzerland, 5th - 9th of March, 2018
- Poster, titled: "Investigation of zinc phosphide as a novel earth abundant material for photovoltaics"

Interests

Academic: Materials for energy, Photovoltaics, Solid state physics and devices, nanotechnology, optical spectroscopy

Sports: Dancing: Ballroom dancing (Swissdance medaltest Silver in Standard and Latin), West Coast Swing, Disco Fox, Rock'n'roll and more. Collegiate dancesport competitions.